Particle Acceleration and Detection

Yacouba Diawara *Editor*

Neutron Detectors for Scattering Applications

Springer

Particle Acceleration and Detection

The series “Particle Acceleration and Detection” is devoted to monograph texts dealing with all aspects of particle acceleration and detection research and advanced teaching. The scope also includes topics such as beam physics and instrumentation as well as applications. Presentations should strongly emphasize the underlying physical and engineering sciences. Of particular interest are

- contributions which relate fundamental research to new applications beyond the immediate realm of the original field of research

- contributions which connect fundamental research in the aforementioned fields to fundamental research in related physical or engineering sciences

- concise accounts of newly emerging important topics that are embedded in a broader framework in order to provide quick but readable access of very new material to a larger audience

The books forming this collection will be of importance to graduate students and active researchers alike.

Yacouba Diawara
Editor

Neutron Detectors for Scattering Applications

Springer

Editor
Yacouba Diawara
Detector Group
Oak Ridge National Laboratory
Oak Ridge, TN, USA

ISSN 1611-1052 ISSN 2365-0877 (electronic)
Particle Acceleration and Detection
ISBN 978-3-031-36545-4 ISBN 978-3-031-36546-1 (eBook)
https://doi.org/10.1007/978-3-031-36546-1

This Springer imprint is published by the registered company Springer Nature Switzerland AG
The registered company address is: Gewerbestrasse 11, 6330 Cham, Switzerland

The neutron's neutral charge, near-zero electric dipole moment, and interactions with atoms via nuclear reactions are exceptional properties justifying its use as a probe tool in materials research and analysis. At the same time and for the same reasons, these properties make this particle detection very arduous. What a challenge for detector scientists!

—Yacouba Diawara, PhD

Foreword

If you have ever done a neutron scattering experiment and wondered how the neutrons scattered by your sample were detected, this short textbook will tell you the detailed physics of how that happens. Because neutrons pass through many materials rather easily, they are not simple to detect and only a few isotopes are able to intercept enough neutrons and generate the nuclear reactions suitable for this purpose. In the early chapters of this book, you will come to understand the logic behind the choice of materials as well as the various constraints that neutron detectors must respect to be useful. Some of these constraints, such as efficiency and gamma-ray sensitivity, are common to all neutron counters while others, like timing resolution, dynamic range and peak counting rate, depend on the applications.

As neutron fluences have increased over the past few decades so too have demands for ever finer positional resolution for the detection of neutrons, challenging detector developers as well as engineers who design electronic read-outs. Instrument-specific trade-offs between detector parameters are often required when all the desired functional specifications cannot be achieved simultaneously: there really is no one-size-fits-all when it comes to neutron detectors.

Not surprisingly given the authors' affiliation, this book concentrates on detectors in use at the High Flux Isotope Reactor (HFIR) and the Spallation Neutron Source (SNS) at Oak Ridge National Laboratory (ORNL). Since many types of neutron-scattering instruments are represented at one or other of these sources, this does not exclude any major topics. However, in one respect, ORNL is quite unique: it has access to a large stock of ^{3}He, a rare isotope available only from the decay of tritium produced in a few specialized nuclear reactors. It turns out, as explained clearly in this book, that ^{3}He is a very convenient material for making neutron detectors: it has a large neutron absorption cross section; it can be used at high pressure where the density of atoms is high; it is relatively gamma insensitive; it can be deployed in detectors of various shapes and sizes, and it is suitable for detectors with moderate spatial resolution.

Despite the advantage conferred by a plentiful supply of ^{3}He, not every detector at ORNL uses this isotope, for a variety of instrument specific reasons that are described in detail in the book. Pictures of actual neutron spectrometers help the reader get a better idea of the size and complexity of detector configurations on several ORNL neutron instruments. Readers looking for precise information about detector specifications will find more than enough detail to satisfy their curiosity or professional interest. The physics of so-called *stopping* and *quench gasses* are described in detail, taking the mystery out of these terms often bandied about at neutron facilities.

Of course, the nuclear reactions within the detector that give rise to ionization are only the first step in the process of neutron detection. Designing electronics that can use the ionization clouds to determine that a neutron (as opposed to a gamma ray) has been detected and to localize the position of the nuclear detection event is complicated. Nevertheless, this book guides the reader through the physical processes and the required electronics in a way that is accessible for those not professionally involved in designing electronic circuits. Various sources of distortion of the neutron signal are described along with various electronic "tricks" and calibration procedures. If, like me, you are not a detector expert, you will not need the level of information supplied here about sources of noise in detectors, but some of that knowledge will allow you to have an intelligent conversation with whoever you call to fix the noisy detector on your neutron instrument. On the other hand, if you do want to design detectors, you will find all you need to get started, with fairly complete technical specifications for all of the neutron detectors in use at both the SNS and at the HFIR.

The book covers, for the first time, the most common neutron detectors used in neutron scattering facilities and all of those in use at Oak Ridge National Lab. The first two chapters describe the facilities, instruments and the critical detector parameters needed by various instruments. The third chapter focuses on the key components of the ^{3}He-based linear position sensitive detectors as well as on their electronics, which require particular attention to signal-processing and noise reduction. The fourth chapter is dedicated to the ^{3}He alternatives where scintillators play a critical role. Finally, fifth chapter covers emerging neutron detection technologies including semiconductors, vacuum-based devices and their associated readouts, which will be required in the future for high rate and high-resolution neutron detectors.

Physics Department, Indiana University,
Bloomington, IN, USA

Roger Pynn

Acknowledgments

A very special thanks goes to Dr. Ronald Cooper and Dr. Richard Riedel. They have been pioneers in neutron detector development and inspiring leaders for the group.

Writing this book on neutron detectors has been rewarding and more arduous than we anticipated. We benefited from the support of our technical team, especially Vladislav Sedov, Dr. Jason Hodges, Dr. Lowell Crow, Cornelius Donahue Jr., Theodore Visscher, Christopher Montcalm, Bruce Hannan, William Reynolds, and Brad Bochenek, who have made outstanding contributions to the detectors described in this book.

We also extend our gratitude to Rachel Brooks, Rebekah Ellis, Erica Heinrich, and Laurie Varma, the ORNL technical editors who provided valuable support during this endeavor.

Finally, we have benefited from the support of Professor Roger Pynn for the book introduction, as well as technical reviews from Dr. Georg Ehlers and Dr. Anton Khaplanov.

To all of them, we would like to express our gratitude.

Contents

Abbreviations

ACPC	Anger camera position calculator
ADC	Analog to digital converter
AROC	Anger camera readout control
BL	SNS beamline location
BNL	Brookhaven National Laboratory
CCD	Charge-coupled device
CG	HFIR Cold Guide Hall beamline location
CMOS	Complementary metal–oxide–semiconductor
CP	Chicago Pile reactor
cps	Counts per second
CYCLOPS	Cylindrical CCD Laue Octagonal Photo Scintillator
DAC	Digital to analog converter
DC	Direct current
DSP	Data stream packetizer
e–h	Electron–hole
FALCON	Fast Acquisition Laue Camera for Neutrons
FPGA	Field-programmable gate array
FWHM	Full width at half maximum
Gen	Generation
HB-	HFIR horizontal beamline location
HFIR	High Flux Isotope Reactor
HN	High voltage Type N connector
I-layer	Intrinsic layer
LC	Inductor/capacitor
LG	Lithium glass
LPSD	Linear position-sensitive ^{3}He gas detector
LVDS	Low voltage differential signal
MCP	Microchannel plate
MHV	Miniature high voltage connector
MWPC	Multiwire proportional chamber

NRSF2	Neutron Residual Stress Mapping Facility, 2nd generation
NRU	National Research Universal reactor
NRX	National Research Experimental reactor
OPI	Operator interface
ORNL	Oak Ridge National Laboratory
PC	Personal computer
PE	Photoelectric effect
P-I-N	(or PIN) P-type, intrinsic, and N-type junction
PMT	Photomultiplier tube
P-N	P-N-type junction
PP	Pair production
RMS	(or rms) root mean square
ROC	Readout card
RTG	Radioisotope thermoelectric generator
SANS	Small-angle neutron scattering
SHV	Safe high voltage connector
SiPM	Silicon photomultiplier
SNS	Spallation Neutron Source
STS	Second Target Station
TAX	(or TAS) Triple-axis spectrometry, triple-axis spectrometer
TOF	Time-of-flight
WLSF	Wavelength shifting fiber

HFIR and SNS Instrument Names

ARCS	Wide Angular-Range Chopper Spectrometer
BASIS	Backscattering Spectrometer
BIO-SANS	Biological Small-Angle Neutron Scattering Instrument
CNCS	Cold Neutron Chopper Spectrometer
CORELLI	Elastic Diffuse Scattering Spectrometer
CTAX	Cold Neutron Triple-Axis Spectrometer
DEMAND	Dimensional Extreme Magnetic Neutron Diffractometer
EQ-SANS	Extended Q-Range Small-Angle Neutron Scattering Diffractometer
FIE-TAX	Fixed-Incident-Energy Triple-Axis Spectrometer (former name for VERITAS)
GP-SANS	General-Purpose Small-Angle Neutron Scattering Instrument
HIDRA	High Intensity Diffractometer for Residual stress Analysis
HYSPEC	Hybrid Spectrometer
IMAGINE	Quasi-Laue Diffractometer
IMAGING	Neutron Imaging Facility (former name for MARS)
LIQREF	Liquids Reflectometer
MANDI	Macromolecular Neutron Diffractometer
MAGREF	Magnetism Reflectometer
MARS	Multimodal Advanced Radiography Station (formerly known as Imaging)
NOMAD	Nanoscale-Ordered Materials Diffractometer
NSE	Neutron Spin Echo Spectrometer
POWDER	Neutron Powder Diffractometer
POWGEN3	Powder Diffractometer, 3rd generation
PTAX	Polarized Triple-Axis Spectrometer
SEQUOIA	Fine-Resolution Fermi Chopper Spectrometer
SNAP	Spallation Neutrons and Pressure Diffractometer
TAX	Triple-Axis Spectrometer
TOPAZ	Single-Crystal Diffractometer
USANS	Ultra-Small-Angle Neutron Scattering Instrument

VENUS	Versatile Neutron Imaging Instrument at SNS
VERITAS	Versatile Intense Triple-Axis Spectrometer (formerly known as FIE-TAX)
VISION	Vibrational Spectrometer
VULCAN	Engineering Materials Diffractometer
WAND	Wide-Angle Neutron Diffractometer, 1st generation
$WAND^2$	Wide-Angle Neutron Diffractometer, 2nd generation

Chapter 1
Neutron Scattering, Sources, and Instruments

Kevin D. Berry

Abstract This chapter begins with an introduction to neutron scattering and its application to condensed matter research. The role of the neutron as a probe of matter is described. The processes of fission and spallation, the two primary methods for large-scale neutron production at neutron scattering facilities, are discussed. The High Flux Isotope Reactor and the Spallation Neutron Source, both at the Oak Ridge National Laboratory, are covered in more detail, including a description of the neutron scattering beam lines at those facilities. Finally, a typical neutron scattering beam line is discussed, along with a survey of commonly encountered beam line components.

1.1 Neutron Scattering: Introduction and Description

Neutron scattering is an extremely useful and versatile experimental technique researchers can employ to study the structure and dynamics of matter. It finds application in a wide variety of broad scientific disciplines including biology, chemistry, geology, physics, and engineering materials. Samples can be in the form of single crystals or powders, bulk polycrystalline or amorphous solids, glasses, liquids, thin films and interfaces, and composite or aggregate structures or solutions. Practical sample sizes range from around 0.1 mm^3 to several cm^3. Smaller samples are certainly possible, though scattered intensity generally decreases with volume of material in the neutron beam. Larger samples may also be studied, even those exceeding the dimensions of the neutron beam, by passing the sample through the beam, mapping smaller regions one at a time.

As a probe of matter, the neutron can provide information about crystalline or molecular structure, grain size and distribution, phases and inclusions, defects, and many other structural features of interest. In some instances, the experiment may be tailored to give dynamical results over a range of time scales (e.g., phonon or

K. D. Berry (✉)
Neutron Sciences Directorate, Oak Ridge National Laboratory, Oak Ridge, TN, USA
e-mail: berrykd@ornl.gov

Y. Diawara (ed.), *Neutron Detectors for Scattering Applications*, Particle Acceleration and Detection, https://doi.org/10.1007/978-3-031-36546-1_1

magnon excitations, phase transformations, diffusion, and other kinetic processes). Often, researchers may want to study a sample under extreme or changing conditions. Furnaces, cryostats, high-field magnets, and pressure cells are among the many types of sample environments that have been developed over the years to provide researchers with a variety of options.

Neutron scattering is but one of many experimental techniques that scientists use to study the properties of matter. It is complementary to other scattering or imaging techniques (e.g., charged particle or x-ray diffraction, electron microscopy) and, owing to the unique properties of the neutron, it has the capability of providing information where other methods may be limited. Charged particles and x-rays primarily interact with atomic electrons in matter. Since electron density increases with increasing atomic number, samples with moderate to high atomic number may attenuate a sufficient fraction of the beam that penetration depth is confined to the near-surface region. Thus, for samples that are too thick, bulk sampling or transmission experiments with charged particle or x-ray beams may not be feasible.

Neutrons have no net electric charge, so their main mode of interaction with atoms is through the strong nuclear force. This is a short-range force that acts over nuclear distances (approximately 10^{-15} m) and only exists between nucleons in the atomic nucleus. Because nuclear diameters are roughly five orders of magnitude smaller than typical atomic diameters, the probability of a neutron scattering from a nucleus is considerably less than for charged particle or x-ray beams. For this reason, neutrons are able to penetrate much further into materials and consequently are a much better probe of bulk matter.

Another characteristic property of the neutron that has been exploited to great benefit in scattering experiments is that the neutron possesses a magnetic moment. This magnetic moment provides an interaction mechanism with externally applied magnetic fields or with intrinsic magnetic moments that exist in some materials. Polarized neutron beams are a very powerful tool to probe the magnetic structure and dynamics of matter and is an area of research that has seen rapid growth and development in recent years.

The neutron can be described using both the classical (particle) and quantum (wave) formulations common to quantum physics, and both are regularly employed in the study of neutrons and neutron scattering. The classical kinetic theory of gases can also be applied to neutrons, and it is convenient at times to associate neutron wavelengths and kinetic energies with their thermal energy or temperature. Equations (1.1) and (1.2) are useful for converting between neutron energy, velocity, wavelength, and temperature:

$$E_{\mathrm{K}} = \frac{1}{2} m_{\mathrm{n}} v^2 = k_{\mathrm{B}} T \tag{1.1}$$

$$\lambda = \frac{h}{m_{\mathrm{n}} v} \tag{1.2}$$

where E_K is neutron kinetic energy, m_n is neutron mass (1.675×10^{-27} kg), v is velocity, k_B is Boltzmann's constant (1.38×10^{-23} J/K), λ is the neutron wavelength, and h is Planck's constant (6.626×10^{-34} J s).

For example, a neutron distribution in thermal equilibrium at room temperature (300 K) will have an associated thermal energy k_BT of 0.0258 eV, a velocity v of $(2E_K/m_n)^{1/2}$ equal to 2223 m/s, and a wavelength λ of $h/m_nv = 1.78 \times 10^{-10}$ m, or approximately 1.8 Å (1 Å $= 10^{-10}$ m).

Equations (1.1) and (1.2) indicate an inverse square relationship between neutron energy E and neutron wavelength λ, given by Eq. (1.3):

$$E = \frac{1}{2}\left(\frac{h^2}{m_n}\right)\left(\frac{1}{\lambda^2}\right) \tag{1.3}$$

Substituting the values for the constants h and m_n and changing energy units from Joules to electron volts eV, (1 eV $= 1.6 \times 10^{-19}$ J) gives the useful conversion in Eq. (1.4):

$$E = \frac{0.0818}{\lambda^2} \tag{1.4}$$

where neutron energy is measured in electron volts, and wavelength is measured in angstroms. A nomogram for quick conversion between neutron kinetic energy, velocity, and wavelength is shown in Fig. 1.1.

Neutrons for scattering applications are often grouped into broad temperature regions, which are referred to as ultracold, cold, thermal, or epithermal neutrons. Thermal and cold neutrons have wavelengths in the ranges that correspond to the atomic or molecular distances in most condensed matter materials. Thus, they are the optimal choice for use in neutron scattering experiments. Neutron scattering user facilities are designed with this in mind, providing researchers with neutrons in thermal, cold, and, in some cases, epithermal energy and wavelength ranges. This broad temperature classification is also shown in Fig. 1.1.

Figure 1.2 shows a diagram of a typical neutron scattering experiment in perhaps its simplest form. A sample is placed in a neutron beam, with some fraction of neutrons scattering from the sample at some angle or angles, and others passing directly through unperturbed. It is the measurement of this scattered intensity as a function of scattering angle, more correctly called the *differential scattering cross section*, that is of interest to the researcher in a neutron scattering experiment.

The expression for the differential scattering cross section is given by Eq. (1.5):

$$\frac{d\sigma}{d\Omega} = \frac{dN}{\varphi d\Omega} \tag{1.5}$$

where φ is the total incident neutron flux (number of incident neutrons per unit area per second), N is the total scattered neutron flux (number of neutrons scattered per

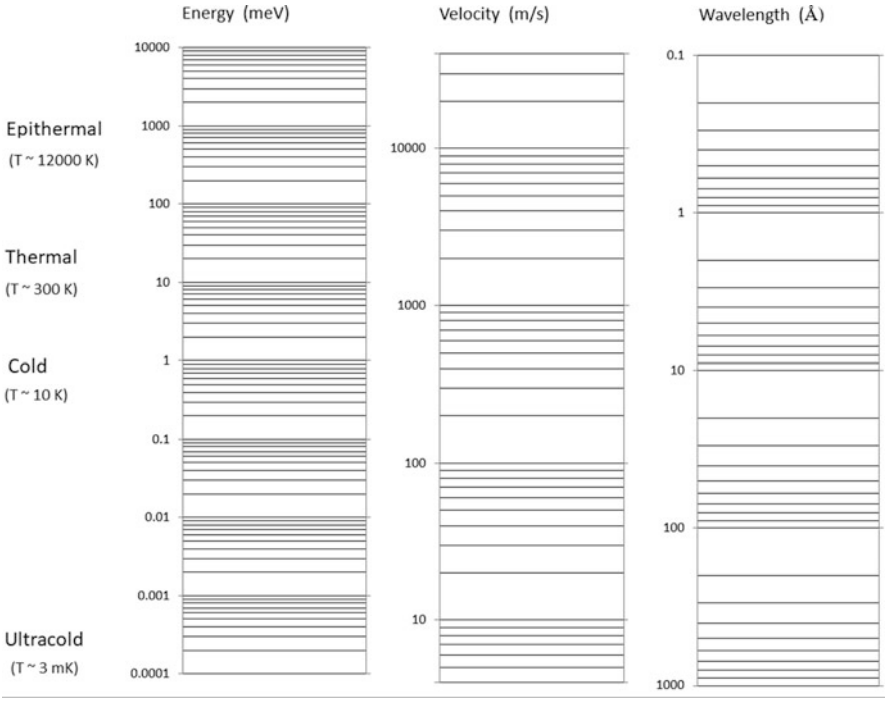

Fig. 1.1 Nomogram of neutron energy (meV), neutron velocity (m/s), and neutron wavelength (Å). The broad classifications based on neutron equilibrium temperature are also shown

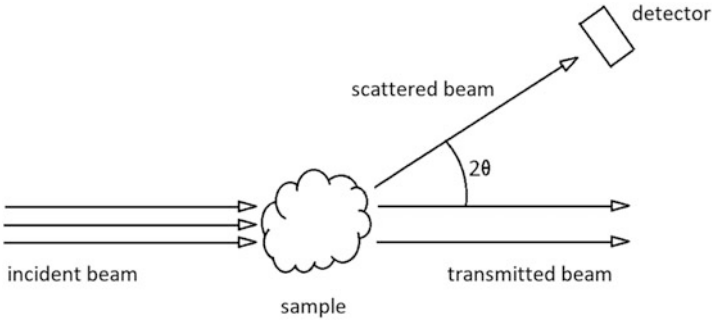

Fig. 1.2 A simplistic diagram of a neutron scattering experiment. Some neutrons from the incident beam interact with the sample and are scattered; the rest are unperturbed and comprise the transmitted beam. A neutron detector records the neutron intensity as a function of scattering angle 2θ

unit area per second), and $\sigma = N/\varphi$ is the total scattered neutron flux/total incident neutron flux. The differential scattering cross section $d\sigma/d\Omega$ is the fraction of the incident neutron flux that is scattered into differential solid angle element $d\Omega$.

By invoking the mathematics of scattering theory, the differential scattering cross section provides the information necessary to determine the structure and dynamics of the sample under study. A researcher must be able to measure these scattered neutrons—this is the role of the neutron detector.

The differential scattering cross section is wavelength dependent; that is, the neutron wavelength must be known to properly evaluate it. In some experiments, the incident and scattered wavelengths have the same magnitude. In others, they may be different, and the researcher must be able to determine both. The former is an elastic experiment, with no energy exchange between the neutron and the sample. Instruments of this type are generally referred to as diffractometers. The latter is an inelastic experiment, and these instruments, where neutron-sample energy exchange is involved, whether exothermic or endothermic, are called spectrometers. Fortunately, practical techniques to determine these neutron wavelengths exist. The three methods that are most often employed are neutron beam choppers, monochromators, and velocity selectors, which are described in Sect. 1.5.

1.2 Neutron Sources and Neutron Production

Large-scale neutron scattering user facilities exist throughout the world, providing researchers with access to a wide variety of scattering instruments with high flux (approximately 10^7–10^8 neutrons/cm^2/s) neutron beams. The neutron sources at these user facilities are based on one of two techniques capable of high-intensity neutron production: either the fission process at research reactors or the spallation process using charged particle beams (most often these are pulsed beams) from accelerators. Reactor-based neutron sources were developed first, beginning in the 1940s with the Chicago Piles CP-1 and CP-2 and the X-10 Graphite Reactor in the United States, and the National Research Experimental (NRX) and subsequent National Research Universal (NRU) reactors at Chalk River Laboratories in Canada. The 1994 Nobel Prize in Physics was jointly awarded to Clifford G. Shull (United States) and Bertram Brockhouse (Canada) for their pioneering work in the development of neutron scattering techniques, much of which occurred at these early facilities.

The 1960s and 1970s saw the construction of higher-power research reactors, notably the High Flux Beam Reactor, the High Flux Isotope Reactor (HFIR), and the National Bureau of Standards Reactor, all in the United States, and the High Flux Reactor at the Institut Laue-Langevin in Grenoble, France. An aerial view of HFIR at the US Department of Energy's Oak Ridge National Laboratory (ORNL) is shown Fig. 1.3. The table in Appendix A lists the major research reactor user facilities currently in operation and available for neutron scattering.

Research reactors produce neutrons for scattering through the fission process, most often using highly enriched (>90%) ^{235}U as the nuclear fuel. This process is described by Eq. (1.6) and shown diagrammatically in Fig. 1.4. In this process, a ^{235}U atom absorbs a neutron (n), then breaks apart into (usually two) smaller fission

Fig. 1.3 The High Flux Isotope Reactor. The reactor building is in the center of the photo [1]

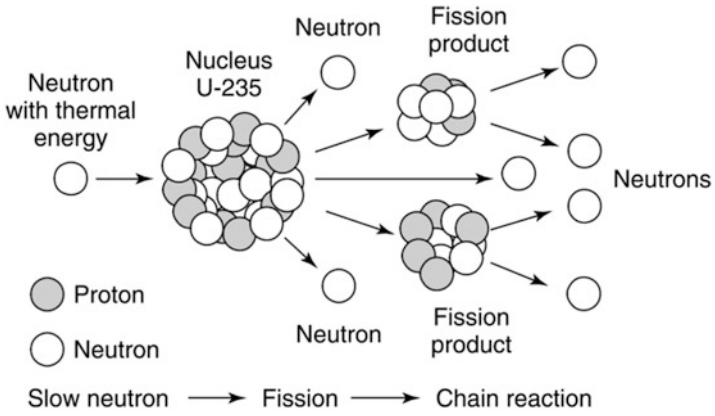

Fig. 1.4 Diagram of the fission process in ^{235}U [2]

fragments X and Y, releasing approximately 2.5 neutrons on average per fission. However, because one of these neutrons is required to sustain the chain reaction, a typical average of only 1–1.5 neutrons per fission are available for a neutron scattering experiment.

$$\mathrm{n} + {}^{235}\mathrm{U} \rightarrow \text{fission products } (X + Y + \cdots) + 2.5\mathrm{n} + \text{gamma rays} \tag{1.6}$$

The total energy released in a fission event is approximately 200 MeV, which is imparted to the neutrons and the much larger fission products. The emitted neutron energy spectrum peaks in the megaelectron volt (MeV) range. As previously mentioned, this energy is much too high for practical neutron scattering experiments with condensed matter. Thus, the neutrons must be moderated, or slowed, to the thermal or cold energy ranges. Most research reactors use the reactor cooling water as the

neutron moderating medium, resulting in a neutron energy spectrum in the thermal range. Some reactors also employ a separate dedicated cold source, usually using liquid hydrogen, to further reduce the neutron thermal energy for use in cold neutron experiments.

The modern era of pulsed spallation neutron sources began in the 1980s with the construction of the KEK Neutron Source in Japan, the Intense Pulsed Neutron Source and the Los Alamos Neutron Science Center in the United States, and the ISIS facility in the United Kingdom. Several higher-power spallation sources have been built since the early 2000s, advancing the technological challenges of increased accelerator power. These new high-power pulsed sources include the Spallation Neutron Source (SNS) at ORNL, ISIS Target Station 2, the China Spallation Neutron Source, the Japan Spallation Neutron Source, and the European Spallation Source. Current spallation-based neutron sources and their operating parameters are listed in Appendix B. Figure 1.5 shows a photo of SNS at ORNL.

In the spallation process, high-energy particles (usually protons) bombard the nuclei of heavy atoms (e.g., lead, mercury, tungsten), resulting in the release of fragment particles, typically 20–30 neutrons (n) per proton (p), and gamma rays. This process is described by Eq. (1.7) and illustrated in Fig. 1.6.

$$\text{p} + \text{heavy nucleus} \rightarrow \text{spallation fragments} + (20 \text{ to } 30)\text{n} + \text{gamma rays} \quad (1.7)$$

Neutron production efficiency is greatest when the proton energy is at least 1 GeV; therefore, particle accelerators are necessary to generate these very high energy beams (with proton speeds approaching 90% of the speed of light). Although not a requirement, most proton beams at spallation sources are pulsed, allowing for extremely high instantaneous neutron fluxes, which are much greater than what

Fig. 1.5 The Spallation Neutron Source. The target building (also known as the experiment hall) is just above center in the photo, and the laboratory and office complex is in the foreground. The linear accelerator can be seen just above the target building, extending approximately 330 m into the background [3]

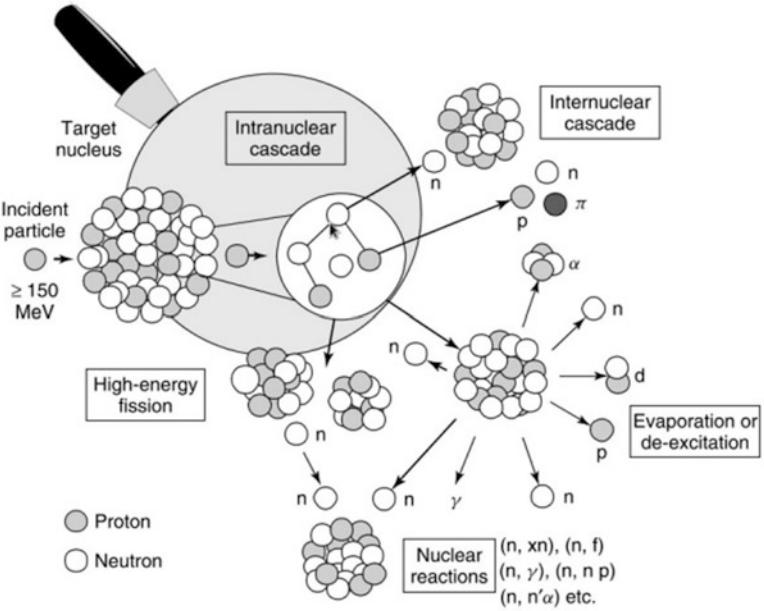

Fig. 1.6 Diagram of the spallation process. In this diagram, n stands for neutron, p stands for proton Spallation products may include fission fragments (f), pions (π), alpha particles (α), deuterons (d), tritons (t), and gamma rays (γ) [2]

reactors can produce. Modern spallation-based neutron sources provide the highest time-averaged thermal neutron fluxes. Like with fission sources, the neutron energy spectrum resulting from spallation events is also in the MeV range, far too high to be useful for scattering experiments. Neutron moderators are necessary to slow the neutrons to thermal or cold energies.

1.3 The High Flux Isotope Reactor

HFIR is an 85 MW research reactor located at ORNL. It is a beryllium-reflected light-water reactor that uses highly enriched ^{235}U (93% enrichment in the form of a U_3O_8/Al cermet) as the fuel. Construction began in 1961, and it first achieved criticality in 1965. As the name implies, its original mission was to produce transuranic isotopes, but its potential as a high-flux source for neutron scattering was recognized early, and four neutron beam tubes were installed during construction. Isotope production remains one of its primary missions in addition to neutron scattering. HFIR produces approximately 70% of the world's supply of ^{252}Cf as well as ^{238}Pu, which NASA uses in radioisotope thermoelectric generators (RTGs) to power deep space missions. HFIR's other core missions are irradiation materials testing and neutron activation analysis. The reactor is now in its seventh decade of

operation and has completed over 500 operational run cycles as a bright source of neutrons for scattering experiments, with a peak thermal neutron flux greater than 2×10^{15} neutrons/cm^2/s.

Figure 1.7 shows the locations and orientations of the four beam tubes relative to the reactor core. Three of these tubes deliver high-flux thermal neutron beams to instruments in the beam room. The fourth beam tube (HFIR beamline HB-4) was replaced by a liquid hydrogen moderator in 2007, which acts as a neutron cold source extending available neutron wavelengths into the 4–12 Å range. The Cold Guide Hall was built to house instruments specifically designed to take advantage of the new high flux of cold neutrons. The instrument layout at HFIR is illustrated in Fig. 1.8. The thermal beam room and associated instruments are shown in the left side of the figure, and the Cold Guide Hall instruments are to the right in the figure. Plans are underway for facility upgrades beginning in 2028. These upgrades will likely lead to an expansion of the Cold Guide Hall, a new instrument layout, and several new instruments.

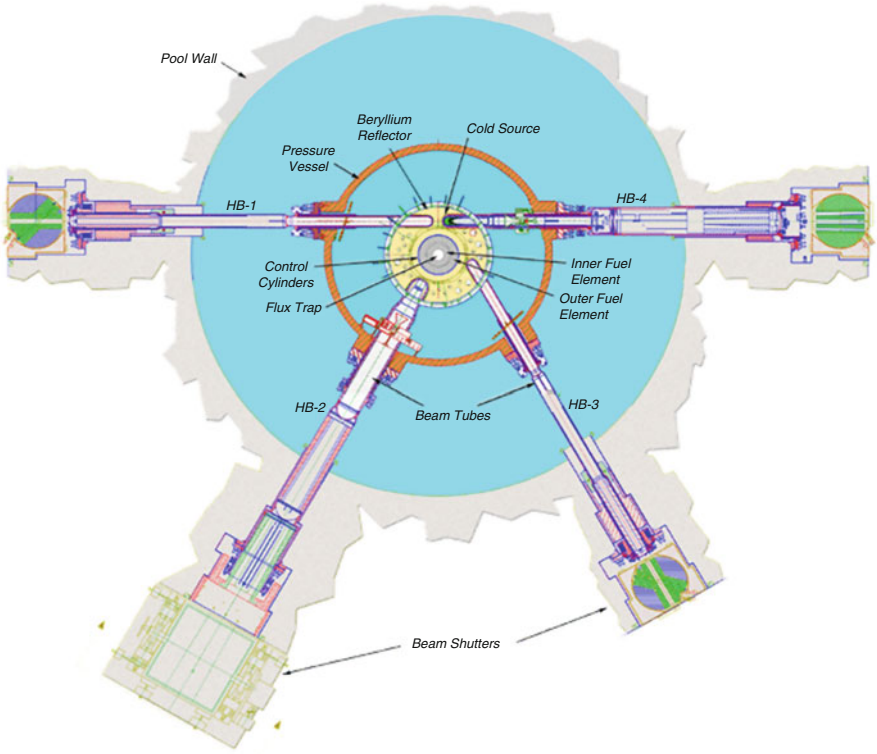

Fig. 1.7 Beam tube placement near the reactor core at HFIR. The horizontal beam at HB-4 was replaced with a liquid hydrogen cold source in 2007, supplying cold neutrons to the instruments in the Cold Guide Hall [4]

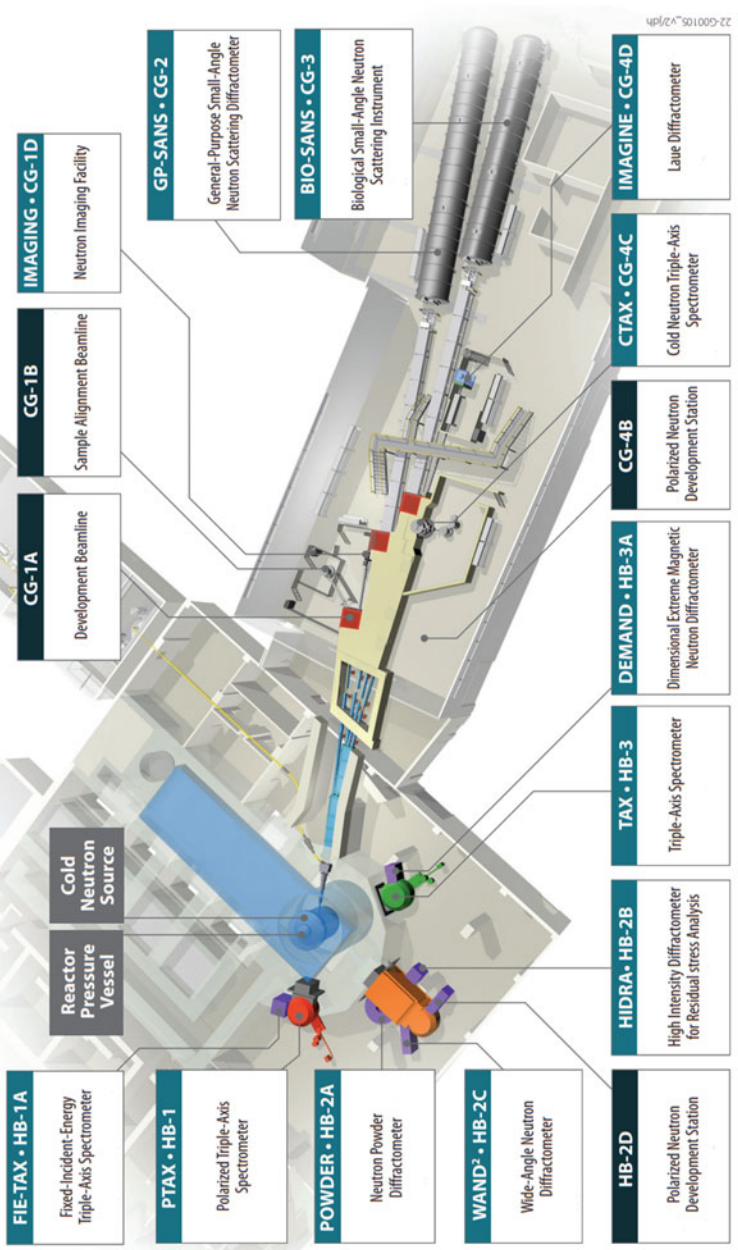

Fig. 1.8 HFIR instrument layout [5]

1.4 Spallation Neutron Source

SNS is a 1.4 MW pulsed neutron source that sits atop Chestnut Ridge, also located at ORNL. The project was a collaborative effort between six different US national laboratories, with each facility contributing effort based on their own unique expertise. The layout of the SNS site is shown in Fig. 1.9, along with the areas of contribution of the six laboratories.

A 900 m long linac and accumulator ring combine to provide an intense pulsed beam of 1 GeV protons, which generates spallation neutrons upon collision with a liquid mercury target. The proton beam is pulsed at 60 Hz, and each pulse contains approximately 1.5×10^{14} protons confined within a pulse width below 700 ns. The energy spectrum of spallation neutrons peaks around 2 MeV (with some emitted at the maximum energy of approximately 1 GeV), and, as previously mentioned, the neutrons must be slowed to be of practical use for neutron scattering. At SNS, four different moderators are used for the 18 beam ports: one ambient water moderator provides thermal neutron beams to 6 beam ports, and three moderators contain liquid hydrogen, providing colder neutrons to the other 12 beam ports. Neutron beam guide systems direct the pulsed neutrons outward to the array of instruments. The SNS instrument layout is shown in Fig. 1.10.

Construction at the SNS site began in 1999, and the first spallation neutrons were produced in 2006. At that time, only three instruments were complete enough to be able to accommodate a neutron beam. Subsequent instrument buildout occurred over the next several years at a frenetic pace: the 17th and 18th instruments (USANS, or Ultra-Small-Angle Neutron Scattering Instrument, and CORELLI, the Elastic Diffuse Scattering Spectrometer) entered the user program in 2014. A neutron imaging

Fig. 1.9 Layout of the SNS facility at ORNL. Six different laboratories participated in the project, each according to their own area of expertise [6]

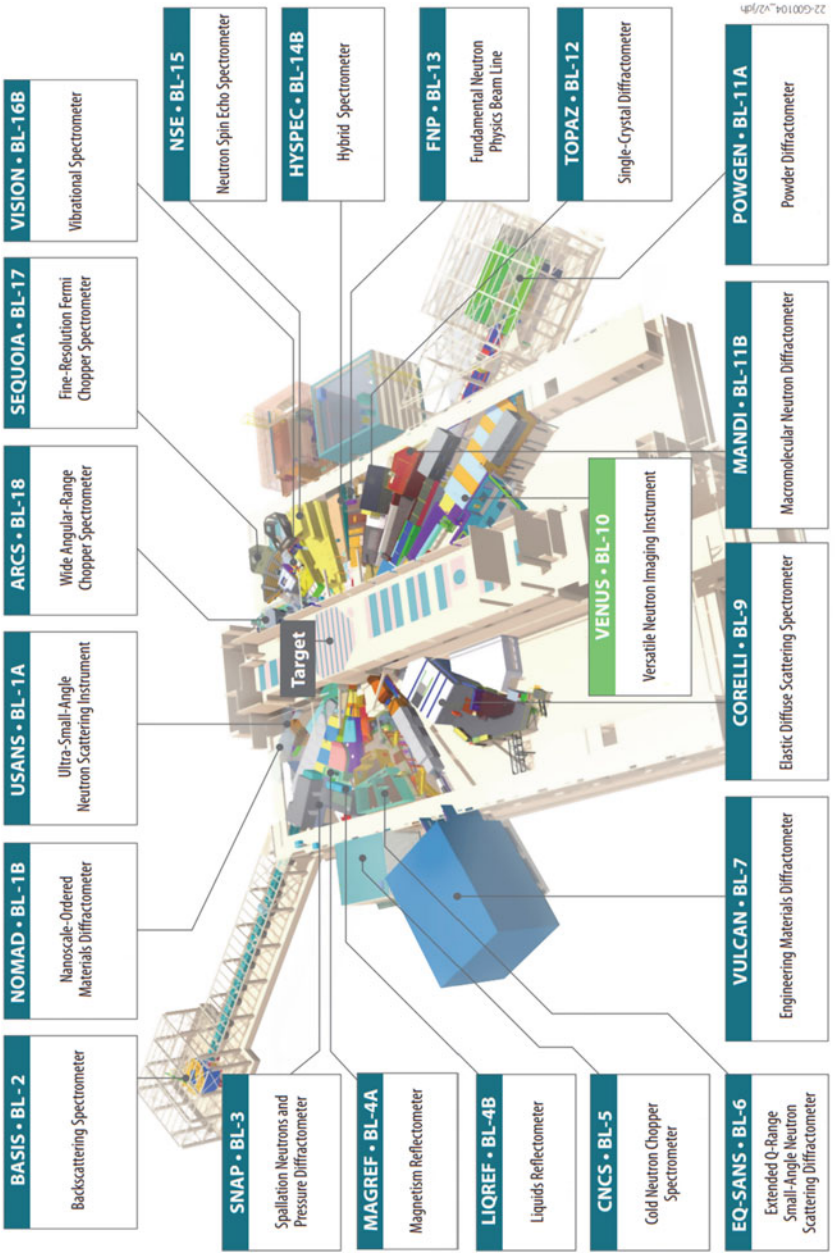

Fig. 1.10 SNS instrument layout. BL stands for beamline, and it is followed by its location [7]

beamline called VENUS (the Versatile Neutron Imaging Instrument, currently under construction at SNS beamline BL-10), will be the first new instrument at SNS since 2014.

SNS is operating at its current full design power of 1.4 MW, making it the most powerful pulsed neutron source in the world (and listed in the *Guinness Book of World Records*). With its current configuration, the time-averaged neutron production rate is approximately 2×10^{17} neutrons/s. A project is underway to further increase the proton beam power on target. The Proton Power Upgrade project, once completed in 2024, will increase the power to 2.8 MW. Most of this power increase (2.0 MW) will go to the SNS, and 0.8 MW will be directed to a new scattering instrument facility that is being designed, called the Second Target Station (STS). The STS will consist of 22 beam ports for all-new instruments. STS construction is scheduled to begin in 2028.

1.5 Neutron Instrument Components

The time distribution of neutrons emitted from pulsed spallation sources is quite different from that of neutrons emitted from research reactors. The fission process in reactors produces an essentially constant neutron flux, whereas neutrons at pulsed spallation sources are generated at specific frequencies with repetition rates that are typically in the range of tens of hertz. This is shown qualitatively in Fig. 1.11.

This leads to several practical design aspects for instruments at the two different types of neutron sources. The most obvious of these is the ability to utilize the time-of-flight (TOF) technique at pulsed sources to determine neutron velocities, and therefore energies or wavelengths. TOF refers to the time difference between when the neutron was produced at the source and when it was recorded in the detector. Knowledge of the TOF combined with the known flight path length L gives the neutron velocity v, from $v = L/TOF$. Knowledge of the neutron velocity allows one to determine the neutron wavelength using Eq. (1.2).

Neutron beam choppers are one method for producing neutron beams within narrow wavelength ranges. Neutron beam choppers are rotating disks constructed of neutron-absorbing material with a small aperture that only allows neutrons to pass during specific times in the rotation (i.e., when the aperture is aligned with the beam). With appropriate placement along the beam, as well as proper phasing of the beam choppers to the neutron pulse frequency, the instrument can chop the beam into small pulses, allowing only specific neutron velocities, and therefore wavelengths, to pass through to reach the sample. Figure 1.12 illustrates how a pair of neutron choppers slices a continuous neutron beam into smaller pulses, effectively producing a “monochromatic” pulse.

Monochromators are another instrument component used to generate neutron beams at specific wavelengths. Monochromators are single crystals that reflect neutrons via the process of Bragg reflection. In Bragg reflection, illustrated in Fig. 1.13, the atomic planes in a crystal lattice (spaced a distance d apart) act as

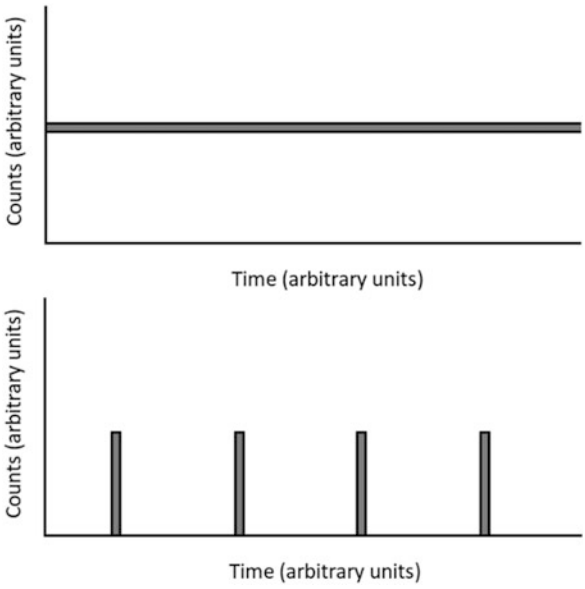

Fig. 1.11 Neutron intensity diagrams. (*top*) steady-state neutron intensity from reactor-based source vs. (*bottom*) pulsed intensity at spallation source

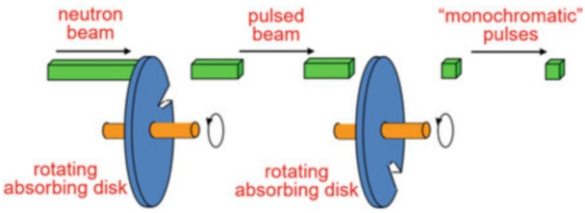

Fig. 1.12 Illustration of the role of neutron choppers in producing pulses within a narrow wavelength bandwidth, essentially monochromatic pulses [8]

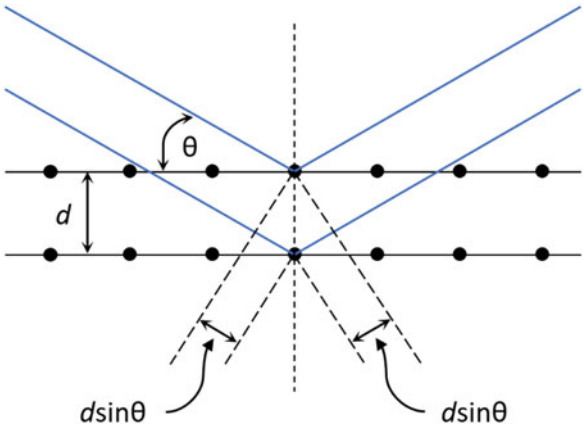

Fig. 1.13 Geometry of Bragg's law for the scattering of plane waves from a crystal lattice. Constructive interference occurs when the path length $2d\sin\theta$ is equal to an integral number of wavelengths $n\lambda$

reflecting surfaces to incident plane waves. Constructive interference between waves occurs when the total increase in path length between scattering planes, $2d\sin\theta$, is equal to an integral number of wavelengths $n\lambda$ (n is an integer and λ is the neutron wavelength). Reflection is most intense when this criterion (the Bragg condition) is met. The reflected angle θ is identical to the incident angle; thus, the total scattered angle is 2θ. The Bragg condition is defined by Eq. (1.8).

$$n\lambda = 2d\sin\theta \tag{1.8}$$

Single-crystal monochromators may be located before the sample, where they are used to determine the incident neutron wavelength, and after the sample, where they determine the final scattered wavelength. In the latter case, they are referred to as analyzers.

Another common technique to determine the neutron wavelength uses a device called a velocity selector. These are often employed at reactor-based sources. A velocity selector is a rotating drum that contains a spiral pattern of neutron absorbing blades, as shown in Fig. 1.14. The spiral pattern is designed to allow only neutrons of a specific velocity to pass all the way through unobstructed. Neutrons with a velocity either too slow or too fast will be blocked by the rotating blades.

In practice, many other components comprise a typical neutron scattering beamline, and each component plays its own unique and important role. Figure 1.15 shows a layout of SNS BL-7, the engineering materials instrument named VULCAN, illustrating the placement of some of these components in a typical neutron beamline.

A moderator is necessary to slow high-energy neutrons (coming directly from the source) to lower kinetic energies that are more appropriate for neutron scattering

Fig. 1.14 Velocity selector [9]

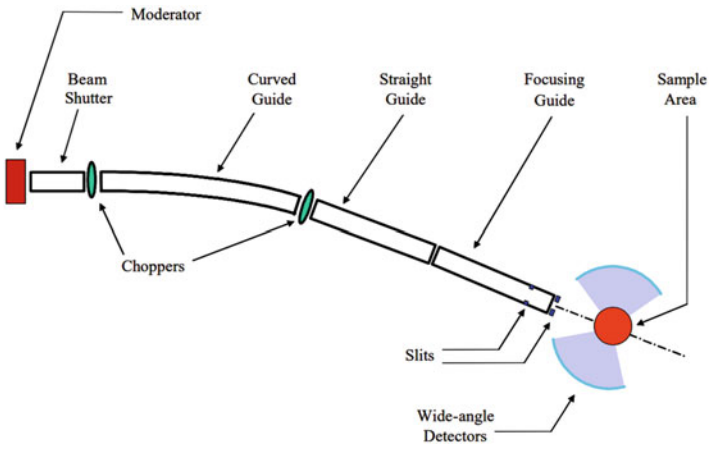

Fig. 1.15 Layout of the major beamline components for the SNS BL-7 instrument VULCAN. The role of the individual components is described in the text [10]

experiments. Water moderators produce a thermal spectrum, and liquid hydrogen moderators produce a cold neutron spectrum.

Neutron beam shutters block the neutron beam when it is not needed (e.g., when changing the sample or the sample environment or during beamline maintenance activities). They are composed of highly effective neutron- and gamma-absorbing material so personnel can safely work in the vicinity of the beam in a radiation-free environment.

Neutron beam guides direct neutrons from their source toward the sample area. Neutron trajectories cannot be altered in the same way as charged-particle beams, but neutron beam guides with reflecting inner surfaces can act as neutron mirrors, if only for small or glancing angles. They are usually evacuated to minimize air scatter. In some cases, they may be constructed with a large radius of curvature. These are called *bent* or *curved beam guides* and are useful if the sample position must be shielded from a direct line of sight to the source. Some beam guides have an internal taper, which has a focusing effect on neutron beams as they exit the guide systems.

Other components that play a major role in neutron scattering experiments include beam collimators and vertical and horizontal slits, which control beam size and beam divergence at the sample.

Radiation shielding, for neutrons and for gamma rays, is a significant part of any neutron scattering beamline. Shielding plays the dual role of (1) reducing radiation levels outside the beamline area, minimizing unnecessary radiation exposure to the researcher, and (2) reducing background levels near the detectors, thereby minimizing unwanted background in the detector response.

This chapter provides a brief summary of the benefits of using neutrons as a probe of condensed matter and describes the main components of a typical neutron scattering instrument. Neutron production at both steady state and pulsed sources is discussed, with special emphasis on the two facilities that are the subject of this

book (SNS and HFIR). The following chapters will cover materials selection for neutron detection, the fundamentals of the neutron detection process, and a detailed description of the specific neutron detection systems that comprise the scattering instruments in the user programs at SNS and HFIR.

References

1. Oak Ridge National Laboratory, *High Flux Isotope Reactor|Neutron Sciences Directorate*. https://neutrons.ornl.gov/hfir
2. D. Filges, F. Goldenbaum, *Handbook of Spallation Research: Theory, Experiments and Applications* (Wiley, 2010)
3. Oak Ridge National Laboratory. *Spallation Neutron Source|Neutron Sciences Directorate*. https://neutrons.ornl.gov/sns
4. D.L. Selby, A.B. Jones, L. Crow, In *European Research Reactor Conference (RRFM)/International Group Operating Research Reactors (IGORR) 2012 Conference Transactions*, Prague, Czech Republic, March 18–22, 2012
5. Oak Ridge National Laboratory, *HFIR Instrument Layout* (2022). https://neutrons.ornl.gov/sites/default/files/HFIR_instrument_layout_061622.pdf
6. M. Hagen, *Time of Flight Inelastic Scattering* (2007)
7. Oak Ridge National Laboratory, *SNS Instrument Layout* (2022). https://neutrons.ornl.gov/sites/default/files/SNS_instrument_layout_061622.pdf
8. R.K. Crawford, *Neutron Scattering Instrument Components* (2010)
9. Reprinted with permission. https://mirrotron.com/en
10. Oak Ridge National Laboratory, *Vulcan Design Criteria Document*; SNS VULC07-03-DC0001-R00

Chapter 2
Neutron Detection Materials, Detector Properties, and Selection

Kevin D. Berry and Yacouba Diawara

Abstract This chapter focuses on the properties of thermal neutron detectors at neutron scattering facilities. It begins with a discussion of materials selection for neutron detection and describes in detail the relevant properties of the three isotopes most often used (helium-3, boron-10, and lithium-6). This is followed by a discussion of the key detector defining properties that should be considered when selecting the appropriate detector for a given application or instrument. These include neutron and gamma ray detection efficiency, spatial and timing resolution, and count rate related performance. Finally, the variety of neutron scattering beam lines are discussed, and a rationale is provided for detector selection at those instruments at the High Flux Isotope Reactor and the Spallation Neutron Source.

2.1 Neutron Detection Materials

A neutron detector in a scattering instrument must be able to measure and record neutron counts as a function of scattering angle and wavelength. Because neutrons are only weakly interacting with most materials, one might correctly assume that the very reasons that make neutrons a good probe of bulk matter might also make their presence very difficult to detect. Most neutron beams in fact pass through most materials with very little interaction.

So, how does a neutron detector detect neutrons, and what materials can be used to construct an effective neutron detector? Neutron interaction with atomic electrons is not possible as it is with x-rays, gamma rays, or charged particles. We must instead rely on the only interaction available—the nuclear reaction with an atomic nucleus. As will be seen below, we cannot directly measure the neutron energy from these types of reactions. We must instead measure the energy of the reaction products. Ideally, these reaction product energies can be converted into electrical signals,

K. D. Berry (✉) · Y. Diawara
Neutron Sciences Directorate, Oak Ridge National Laboratory, Oak Ridge, TN, USA
e-mail: berrykd@ornl.gov; diawaray@ornl.gov

Y. Diawara (ed.), *Neutron Detectors for Scattering Applications*, Particle Acceleration and Detection, https://doi.org/10.1007/978-3-031-36546-1_2

which then allow us to take advantage of conventional detection technologies and signal processing electronics.

The probability of a neutron–nucleus reaction is not the same for all atoms, or even for all isotopes. It is characterized by a parameter called the neutron absorption cross section (alternatively the neutron capture cross section) usually represented by the Greek symbol σ, which can be interpreted as the effective area the atomic nucleus presents to the neutron for the nuclear absorption reaction to occur. Thus, σ has dimensions of area, and, for processes that occur at the nuclear length scale, it is useful to use the unit called the *barn* (where one 1 barn = 10^{-24} cm^2).

The concept of cross section is illustrated in Fig. 2.1. In this figure, atomic spacing is represented by the distance between circle centers, and the absorption cross sections are represented by the areas of the circles. The material represented on the right in the figure has a much larger cross section than the material represented on the left; thus, it has a much greater interaction probability. (The relative circle sizes in this image are much larger than they would be for most materials in practice. They are only drawn this size for illustration. A cross section of 1 barn would be imperceptible on this scale of atomic spacing.)

Identifying suitable materials for neutron detectors first requires selecting isotopes with absorption cross sections that are sufficiently large to give a reasonable probability of neutron capture. For most materials, σ is on the order of a few barns, or maybe a few tens of barns. These materials would not make practical neutron detectors since the barn is much too small a unit for effective neutron capture.

Thermal neutron absorption cross sections have been tabulated in *The Neutron Data Booklet* [1]. Examination of this list reveals 20 isotopes with cross sections above 500 barns, a somewhat arbitrary but not unreasonable selection criterion for neutron capture cross section. These cross sections are shown in the graph in Fig. 2.2, and except for ^{113}Cd near the center of the plot, they are otherwise clustered into two groups. The three isotopes on the left side of the graph (^{3}He, ^{6}Li, and ^{10}B) all result in charged-particle reaction products, and those on the right side (mostly from the lanthanide series on the periodic table) have more complicated de-excitations, typically emitting moderate- to high-energy gamma rays and conversion electrons after neutron capture. Cadmium-113 behaves like the isotopes to the

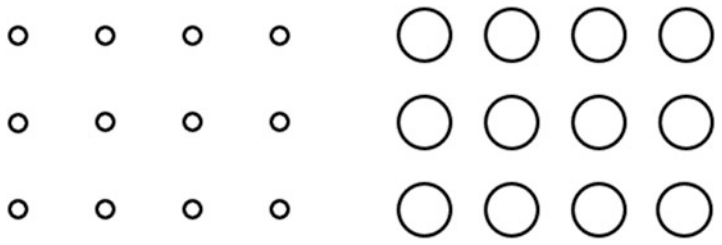

Fig. 2.1 Illustration showing the cross sections of two different materials. (*left*) A material with a relatively smaller cross section and (*right*) another with a relatively larger cross section

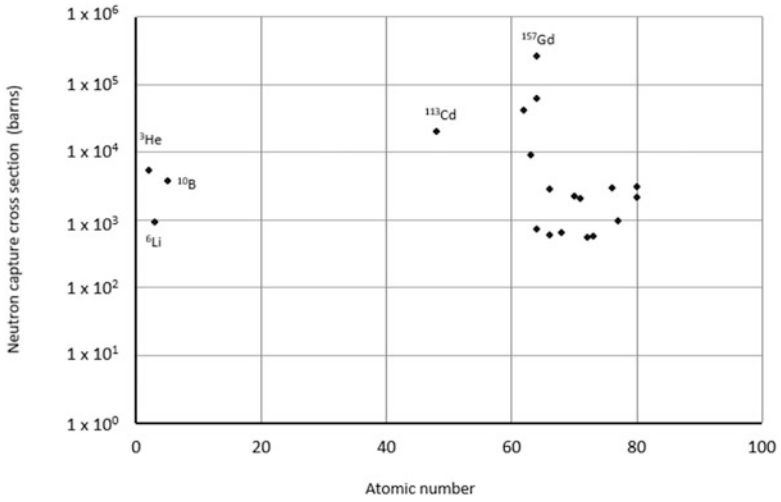

Fig. 2.2 Thermal neutron capture cross section σ for materials with σ > 500 barns

right: its emission spectrum predominantly consists of 96, 558, and 651 keV gamma rays, as well as conversion electrons.

Gamma rays are generally considered a source of unwanted background around neutron detectors, so unless measuring gamma rays is an intended part of the detection process, the isotopes that primarily result in prompt gamma emission are not preferred materials for neutron detectors.

Thus, considering all the available isotopes, we are left with three practical options that produce charged particles as their primary reaction products. Consequently, thermal neutron detection technology to date has largely revolved around ^{3}He, ^{6}Li, and ^{10}B. This textbook mainly considers neutron detectors constructed from these three isotopes because they comprise the detector materials of choice at neutron scattering instruments, including those at Spallation Neutron Source (SNS) and High Flux Isotope Reactor (HFIR).

Nevertheless, a few of the isotopes in the right-hand cluster in Fig. 2.2 do see application in some instances primarily due to their extremely high cross sections. Natural gadolinium, for example, has a capture cross section of 49,700 barns (^{157}Gd has a cross section of 259,000 barns), and thin neutron conversion layers of gadolinium can be deposited on top of conventional semiconductor diode detectors, whereby the conversion electron energy is converted into electron–hole pairs and measured by conventional means in the semiconductor.

It is also worth mentioning that because these materials are reasonable neutron absorbers, they also make good neutron shielding material. Neutron shielding is used for personal radiation safety as well as reduction of neutron background at the instruments, particularly around the detectors. Cadmium metal (containing approximately 12% ^{113}Cd); naturally occurring or isotopically enriched ^{10}B, usually in the form of B_4C or incorporated into aluminum or other alloys; and various lithium

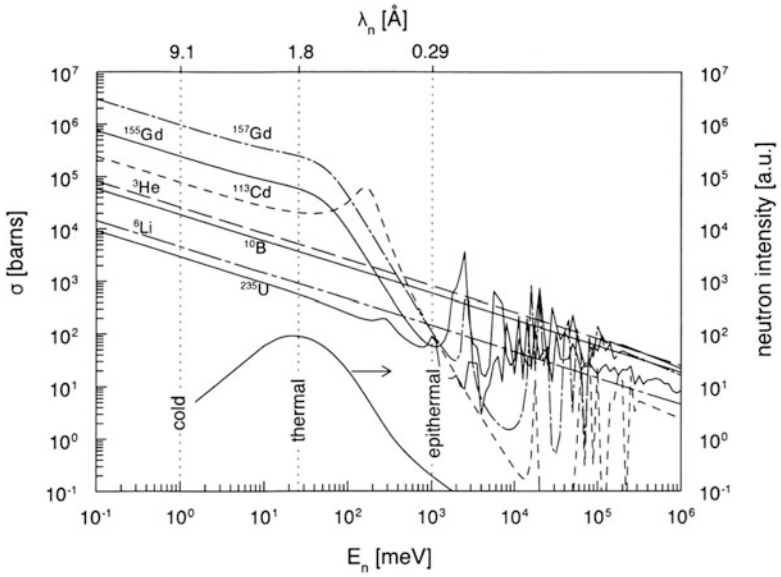

Fig. 2.3 Neutron absorption cross section for isotopes relevant to neutron detection [2]

compounds are commonly employed as neutron shielding materials at scattering instruments. Likewise, gadolinium paint is occasionally used as a high-efficiency neutron absorber for shielding purposes.

Figure 2.3 shows a plot of the neutron absorption cross sections for several isotopes of interest to neutron scattering and neutron detectors [2]. In Fig. 2.3, in the thermal and cold regions applicable to neutron scattering, cross section increases with wavelength (although not obvious from the plot, cross section in this region is proportional to $1/v$, where v is neutron velocity). Furthermore, cadmium and gadolinium exhibit a sharp decrease in cross section below approximately 0.9 Å. This decrease means the effectiveness of those materials to absorb neutrons decreases accordingly, which is a significant practical design consideration if they are to be used as detector or shielding material in that wavelength region.

Because cross section is proportional to $1/v$ in the thermal and cold regions, cross sections can be easily calculated at different wavelengths with knowledge of the cross section at some other specific wavelength using Eq. (2.1) (recall from Eq. (1.2) that λ is inversely proportional to v):

$$\sigma(\lambda) = \lambda\left[\frac{\sigma(\lambda_i)}{\lambda_i}\right] \tag{2.1}$$

To give an example of Eq. (2.1) for ^{3}He,

$$\sigma(\lambda = 4\ \text{Å}) = 4\ \text{Å} \times \left[\frac{5{,}330\ \text{barns}}{1.8\ \text{Å}}\right] = 11{,}844\ \text{barns}$$

The following sections describe in more detail the nuclear reactions that occur in the neutron detector materials ^{3}He, ^{10}B, and ^{6}Li.

2.1.1 Helium-3

Helium-3 is perhaps the most widely used neutron converter material for neutron detectors worldwide and is generally considered the best choice for many instruments, due to its advantageous detector properties. It has the largest capture cross section of the three materials under discussion, and high neutron capture efficiencies (>80%) are readily achievable in reasonable detector geometries. Helium-3 detectors have spatial and timing resolutions that are acceptable for most neutron scattering applications, and the detectors have exceptionally low sensitivity to gamma rays, which is particularly important for small-angle neutron scattering (SANS), reflectometry, and inelastic spectrometers for which high dynamic range and low background are essential detector requirements. Each of these detector performance parameters is described in more detail later in this chapter. In addition to its use in detectors, ^{3}He also finds application, albeit in much smaller volumes, in neutron polarization cells and in ^{3}He/^{4}He dilution refrigerators capable of achieving very low millikelvin temperatures for extreme sample cooling.

Helium-3 is an inert gas at standard temperature and pressure (STP), thus is always in the gaseous state in neutron detection applications. It is a stable isotope, but it has an extremely low natural isotopic abundance, as seen in Table 2.1. However, ^{3}He is a byproduct of tritium (tritium decays into ^{3}He with a half-life of approximately 12.3 years), which was produced in large quantities during the Cold War era. Hence, ^{3}He neutron detectors first saw use beginning in the early 1950s. Although ^{3}He was considered undesirable contamination, it was separated from the tritium during the purification process. (Ironically, ^{3}He converts back into tritium following neutron capture.)

The neutron (n) reaction with a ^{3}He nucleus is described by Eq. (2.2) and is represented by the diagram in Fig. 2.4.

$$^{1}\mathrm{n} + {}^{3}\mathrm{He} \rightarrow {}^{3}\mathrm{H} + {}^{1}\mathrm{H} + 0.764\ \mathrm{MeV} \tag{2.2}$$

Equation (2.2) is an exothermic reaction releasing an energy of 0.764 MeV (referred to as the Q value of the reaction), which is imparted as kinetic energy to the two reaction products: one proton and one tritium atom (triton). The Q value is

Table 2.1 Absorption cross section and natural isotopic abundance for ^{3}He, ^{6}Li, and ^{10}B

Isotope	Absorption cross section at 1.8 Å (barns)	Natural abundance (%)
^{3}He	5333	0.000137
^{6}Li	940	7.5
^{10}B	3835	19.9

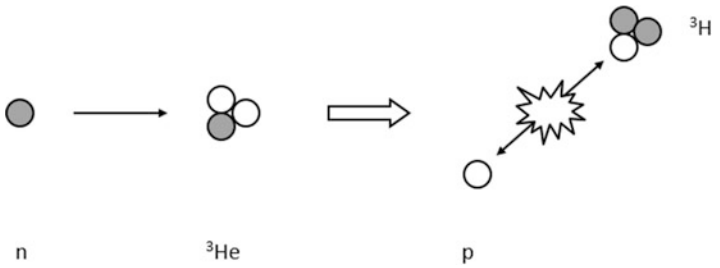

Fig. 2.4 Diagram illustrating the neutron reaction with a ^{3}He nucleus. In the figure, n is neutron, p is proton

determined by examining the mass excess (nuclear binding energy) of each component in the reaction and then comparing the initial with the final states. Equation (2.3) shows these binding energy values (in parentheses, units of MeV) used to find Q in Eq. (2.2) [3].

$$^1\text{n}\,(8.0713) + {}^3\text{He}\,(14.9312) - {}^3\text{H}(14.9498) - {}^1\text{H}(7.2889) = 0.7638\ \text{MeV} \quad (2.3)$$

The Q value of the reaction is considerably larger than the typical thermal neutron kinetic energy (0.026 eV). Thus, the neutron energy is imperceptible in the reaction energetics analysis. It is for this reason that neutron kinetic energy cannot be directly measured, and why we must instead measure the energy of the reaction products to 'detect' the neutron.

Since there are exactly two reaction products, they move in anti-parallel trajectories away from the site of the reaction. The exothermic energy (764 keV) is distributed between the two reaction products according to their masses. This quantity can be evaluated by consideration of the principle of conservation of linear momentum. The derivation follows:

Let subscript T refer to the tritium atom, and subscript P refer to proton. M is mass, V is velocity, and E is kinetic energy.

Using the approximation that the proton and neutron masses are the same, $M_\text{P} = M_\text{T}/3$, and combining this equation with the conservation of linear momentum $M_\text{T}V_\text{T} = M_\text{P}V_\text{P}$ gives Eq. (2.4):

$$V_\text{P} = 3V_\text{T} \quad (2.4)$$

Applying the definition of kinetic energy $E = (1/2)MV^2$ to Eq. (2.4) yields Eq. (2.5):

$$E_\text{P} = \frac{1}{2}M_\text{P}V_\text{P}^2 = \frac{1}{2}\left(\frac{M_\text{T}}{3}\right)(3V_\text{T})^2 = \frac{1}{2}\left(3M_\text{T}V_\text{T}^2\right) \quad (2.5)$$

Thus, using $E_P = 3E_T$ yields Eq. (2.6):

$$E_P + E_T = 4E_T = 764 \text{ keV} \tag{2.6}$$

to give $E_T = 191$ keV and $E_P = 573$ keV.

The proton and triton reaction products scatter from and ionize atoms as they travel through the gas, producing an electron–ion charge distribution, which can subsequently be measured to detect the presence of the neutron. This process is described in greater detail in Chap. 3.

2.1.2 Boron-10

Naturally occurring boron is comprised of approximately 20% ^{10}B which has a high thermal neutron capture cross section of 3835 barns. The remaining 80% is ^{11}B, which has a very low capture cross section of 0.006 barns. Both are stable isotopes. So, although effective neutron detectors can be constructed from natural boron, boron enriched as ^{10}B is often used to dramatically increase the neutron detection efficiency. Boron-based neutron detectors can be constructed in gaseous form (BF_3) or in various solid forms, most often as thin film conversion layers. Semiconductors using various boron compounds (e.g., BN, B_4C) have also been developed, albeit on a much smaller scale.

The neutron (n) reaction with ^{10}B is given by Eqs. (2.7) and (2.8):

$$^1n + {}^{10}B \rightarrow {}^7Li^* + {}^4He \rightarrow {}^7Li + {}^4He + 0.48 \text{ MeV gamma rays} + 2.31 \text{ MeV } (93\%) \tag{2.7}$$

$$^1n + {}^{10}B \rightarrow {}^7Li^* + {}^4He \rightarrow {}^7Li + {}^4He + 2.79 \text{ MeV } (7\%) \tag{2.8}$$

The reaction products are an excited-state $^7Li^*$ atom and an alpha particle (^4He). Two possible de-excitation paths exist for excited state $^7Li^*$. The first path (in 93% of occurrences) results in the emission of a 0.48 MeV gamma ray, and as a result, the Q value is 2.31 MeV. Equation (2.7) represents this radiative de-excitation path. The second path (7% of occurrences) results in no gamma emission, thus Q assumes the full value of 2.79 MeV. Equation (2.8) represents the non-radiative de-excitation path.

Just like with Eq. (2.3) for ^3He, the energy equivalent of the mass excesses resulting in the 2.79 MeV Q value are given in Eq. (2.9).

$$n\ (8.0713) + {}^{10}B\ (12.0506) - {}^7Li\ (14.9071) - {}^4He\ (2.4249) = 2.7899 \text{ MeV} \tag{2.9}$$

Following the conservation of momentum derivations for ^{3}He above, the resulting kinetic energies of the ^{7}Li and the ^{4}He particles in the most predominant (93%) branch are 0.84 MeV and 1.47 MeV, respectively.

The first use of BF_3 gas-proportional detectors predates that of ^{3}He by about a decade. Compared with ^{3}He, the smaller capture cross section leads to a lower intrinsic efficiency, but the larger Q value (2.79 MeV) allows for better gamma rejection. There are, however, a few detrimental properties associated with BF_3 gas detectors. For one, practical gas pressures are limited to less than 2 atm owing to a loss of signal charge with increasing pressure. Not only does this present a limitation on tube efficiency (by contrast, ^{3}He detectors at pressures up to 30 atm are not uncommon), but substantially higher operating voltages are required to overcome the loss of signal intensity. Perhaps the most significant argument against the installation and operation of BF_3 detectors in the user facilities at the SNS and HFIR is that BF_3 is a toxic and corrosive gas and an irritant to the eyes and lungs. The potential health risks associated with BF_3 detectors are difficult to justify from a facility operations perspective.

The most common detector application of boron in the solid state is as thinly deposited layers of the compound B_4C, either natural or enriched, on the inside walls of gas-proportional detectors. The proportional gas in this instance does not need to be a neutron absorbing material since neutron conversion takes place in the boron itself. Thin layers are necessary due to the short particle ranges of the reaction products in B_4C (the mean ranges for ^{7}Li and ^{4}He in B_4C are approximately 1.5 and 3 μm, respectively). With particle ranges this short, only those reaction products created within approximately 1 μm of the surface have a significant probability of escaping into the gas, thus generating a signal charge; all others would be fully absorbed within the B_4C layer. As a result, detectors constructed from B_4C layers necessarily have low capture efficiencies: for example, the capture efficiency for 2 Å neutrons in a 1-μm-thick layer of B_4C is just under 5%. To compensate for this low intrinsic efficiency, B_4C detectors are usually stacked several units deep to provide a cumulative efficiency that is acceptable for neutron scattering applications.

Because the reaction products for ^{10}B travel in antiparallel trajectories (again, following the conservation of linear momentum), only one of the two particles would be expected to escape the solid surface and enter the proportional gas volume. This has ramifications on the shape of the pulse amplitude spectrum, as the signal charge associated with the neutron detection event is never representative of the full Q value energy. Notwithstanding this, very effective neutron detectors have been constructed and deployed utilizing this thin layer B_4C technology, both in neutron scattering and in national security applications. To date, no detectors utilizing B_4C conversion layers have been installed in the neutron scattering instruments at SNS or HFIR, as these applications have largely been fulfilled by ^{3}He.

As previously mentioned, boron-loaded materials also make excellent neutron absorbers, and that is by far the single largest application of ^{10}B at SNS and HFIR, whether it be in the form of shielding plates, beam size defining slits, or neutron beam collimators.

2.1.3 Lithium-6

Lithium exists in two isotopic forms: ^{6}Li with approximately 7.5% natural abundance, and ^{7}Li with approximately 92.5% abundance. Both are stable isotopes, but only ^{6}Li has a meaningful neutron capture cross section (940 barns). As with boron, natural lithium can be used as a neutron detection material, but isotopically enriched lithium is preferred for greater capture efficiency. Lithium is a highly reactive alkali metal that only exists in nature in compound form. In neutron detector applications, lithium compounds are most often employed as the neutron-sensitive component in scintillation materials. Two such scintillators, cerium-doped lithium glass (GS20) and ZnS(Ag)/^{6}LiF, are the neutron convertors in use in the detectors at the SNS and HFIR beamlines. Hence, these are the scintillators which will be covered in this section.

Figure 2.5 is a list of scintillator materials that have been studied for use in neutron detectors along with some properties relevant to their role in neutron detection.

The neutron (n) reaction with ^{6}Li is given by Eq. (2.10):

$$^{1}\mathrm{n} + {}^{6}\mathrm{Li} \rightarrow {}^{4}\mathrm{He} + {}^{3}\mathrm{H} + 4.78\ \mathrm{MeV} \tag{2.10}$$

The resulting reaction products are an alpha particle (^{4}He) and a tritium atom (^{3}H). Like with ^{3}He and ^{10}B, the Q value for this reaction (4.78 MeV) is split between the two particles based on their relative masses. Thus, the alpha particle is emitted with initial kinetic energy 2.05 MeV and the tritium atom with the remaining 2.73 MeV. No gamma rays result from the neutron conversion reaction with ^{6}Li atoms.

The energetics associated with deriving the Q value are shown in Eq. (2.11):

$$\begin{aligned} &^{1}\mathrm{n}\ (8.0713) + {}^{6}\mathrm{Li}\ (14.0868) - {}^{4}\mathrm{He}\ (2.4249) - {}^{3}\mathrm{H}\ (14.9498) \\ &= 4.7834\ \mathrm{MeV} \end{aligned} \tag{2.11}$$

In scintillation materials, the absorption of kinetic energy from particle interaction with the material lattice results in the emission of photons (light). In scintillator

Traditional and new thermal-neutron scintillators

Host	Dopant (conc mol%)	Density ρ (g/cm^3)	ρZ^4_{eff} ($\times 10^{-6}$)[a]	Abs. Length at 1.8Å (mm)	Light yield photons per		α/β Ratio	λ_{em} (nm)	τ (ns)
					Neutron	MeV gamma			
^{6}Li-glass	Ce	2.5		0.52	~6000	~4000	0.3	395	75
^{6}LiI	Eu	4.1	31	0.54	50,000	12,000	0.87	470	1400
^{6}LiF/ZnS	Ag	2.6	1.2	0.8	160,000	75,000	0.44	450	>1000
$LiBaF_3$	Ce,K	5.3	35		3500	5000	0.14	190–330	1/34/2100
$LiBaF_3$	Ce,Rb	5.3	35		3600	4500	0.17	190–330	1/34/2400
$^{6}Li^{nat}Gd(^{11}BO_3)_3$	Ce	3.5	25	0.35	40,000	25,000	0.32	385,415	200/800
$^{6}Li^{nat}Gd(^{11}BO_3)_3$ + Y_2SiO_5	Ce	3.9		1	40,000 —	30,000 30,000		420 420	200/800 70
$Cs^{6}_{2}LiYCl_6$	Ce (0.1)	3.3		3.2	70,000 —	22,000 700	0.66	380 255–470	~1000 3
$Cs^{6}_{2}LiYBr_6$	Ce (1)	4.1		3.7	88,000	23,000	0.76	389,423	89/2500

[a] As an indication of gamma-ray detection efficiency by photoelectric effect ρZ^4_{eff} values are presented

Fig. 2.5 Table of properties of neutron sensitive scintillators [4]

detectors, this light is measured and converted into an electrical current for subsequent signal processing.

Neutron detection in ^{6}Li-based scintillators is a multistep process:

- The neutron is absorbed by a ^{6}Li atom, resulting in the two reaction products, as described by Eq. (2.10).
- As the reaction products travel through the material (again in antiparallel trajectories), they lose kinetic energy through interactions with the lattice, creating electron–hole pairs (exciting electrons across the energy band gap) along their path. The particle ranges are specific to the scintillator material and determine the spatial extent of the electron–hole pair distribution.
- Electron–hole pair recombination results in photon emission. The photon energy is also a material property. Often, dopant atoms are included in the scintillator material to introduce energy levels within the bandgap, facilitating the processes of energy absorption and emission. These dopant atoms are called activators.
- The photons that escape the scintillator are measured by a light sensor (e.g., photomultiplier tube). The output of the light sensor (electrical signal) is recorded as the measurement of the 'detection' of the neutron.

For each of these steps, there is an associated efficiency, thus the overall detection efficiency for scintillator detectors is not the same as, and is always less than, the neutron conversion efficiency in the scintillator material. For example, the scintillator material may not be completely transparent to the emission photons, resulting in a photon yield that is less than the emission yield. Another example where inefficiencies may occur is in the matching of the photon emission spectrum (wavelength) with that of the light-sensitive photocathode element in the photomultiplier tube.

Two types of neutron-sensitive scintillators are used in the SNS and HFIR detectors:

- GS20 lithium glass—this is a ^{6}Li-doped silicate glass with Ce(III) as activator [5]. The Li_2O content is 18% by weight, with 95% ^{6}Li enrichment. The emission wavelength is 395 nm, and the photon yield is approximately 7000 photons per neutron. It is the scintillator of choice for the Anger camera style detectors. These are described in greater detail in Chap. 4.
- ZnS(Ag)/^{6}LiF—^{6}Li enriched LiF combined with ZnS in an epoxy binder. Silver as Ag(II) is a substitutional activator impurity, replacing some fraction of the Zn (II) in the ZnS lattice. The emission wavelength is 450 nm, and the photon yield is approximately 160,000 photons per neutron. This scintillator is only semitransparent to its emission wavelength, resulting in a significant photon loss available to the photomultiplier tubes. Nevertheless, these scintillators make a capable neutron detection material. Large area screens (77 × 38 cm) are used in the wavelength shifting fiber style detectors, which are also discussed in Chap. 4.

Solid scintillator materials have atomic densities 2–3 orders of magnitude larger than gaseous detectors (approximately 10^{22} versus 10^{19}–10^{20} atoms/cm^3). Additionally, these scintillator materials are composed of materials with substantially higher atomic numbers than ^{3}He. They are therefore expected to have a greater absorption

efficiency for gamma rays, and this is generally found to be the case. Gamma sensitivity and gamma discrimination are significant considerations when selecting scintillator materials for neutron detection.

Like with ^{10}B, compounds containing ^{6}Li (e.g., $^{6}Li_2CO_3$) are also used to construct neutron shielding materials. One advantage they have over boron is there is no associated prompt gamma ray emission following neutron capture.

2.2 Detector Properties

Although the charge neutrality of the neutron makes it extremely useful in materials research and analysis, it also makes detecting the same particle hard. Interactions with the chargeless neutron take place either via the nuclear force or its magnetic moment. Certain neutron detectors make use of the recoil effect in hydrogen or resonance interactions, but these techniques are of limited use at neutron scattering instruments, where typical neutron energies are below 0.5 eV. Thermal and cold neutron detectors use a conversion reaction where the captured neutron is converted to one or more high-energy daughter products, which then produce charged secondary particles including ionized particles and then are detected directly via the process of scintillation or after further amplification via avalanche processes. For example, thermal neutron capture in ^{3}He produces approximately 31,000 ionized helium atoms, or approximately 4.96 fC of charge, given its 24.58 eV ionization energy [6]. In the case of ionization mode detectors or further amplified in proportional detectors, this charge is then measured directly. As shown in Table 2.2, ^{3}He, ^{6}Li, ^{10}B, ^{155}Gd, and ^{157}Gd comprise the known conversion elements used in thermal neutron detectors used at scattering facilities where high detector efficiencies are normally required.

The conversion of the neutron and the detection of the conversion products form the basis for most operational neutron detectors. Various implementations in the use of these conversion elements allow a researcher to broadly categorize neutron detectors as based on a gas, scintillator, convertor foil/film, or semiconductor. Each neutron detector category has seen active research and development over the last decade that has greatly expanded the suite of possible solutions for future scientific studies in crystallography and materials science. The following sections discuss some of the neutron detector requirement drivers for neutron sources and instruments.

Generally, the detector parameters are determined from a detailed analysis of the neutron scattering instrument's design with the goal that the detector should not significantly influence the accuracy when determining a material's scattering functions. Various critical parameters need to be considered for the neutron detector design, including time and spatial resolution, distortion, efficiency, count rate, gamma ray sensitivity, uniformity, and active area. In addition to these parameters, other requirements for a specific application must be considered. For example, in the case of a magnetism reflectometer, sensitivity to stray magnetic fields should be

Table 2.2 The most useful neutron-absorbing isotopes and the key features of the neutron interactions at 25 meV. Neutron absorption length was calculated assuming the elemental density if a specific density was not given. The approximate particle lengths were calculated using SRIM software (found at http://www.srim.org/). The values for ^{6}Li glass were calculated using a generic composition aluminosilicate glass with 7.7% Li by weight; exact particle ranges depend on the specific composition of the sample. Electron range was calculated using ESTAR [10]

Isotope	State	Cross section (barns)	Neutron absorption length	Particle energies (keV)		Approximate particle range *R*
^{3}He	Gas	5333	77 mm. atm pure ^{3}He	*p*: 573	*t*: 191	*p:* 2.8 mm for 6 atm ^{3}He and 1 atm C_3H_8
^{6}Li (elemental)	Solid	940	230 μm	*t*: 2727	*a*: 2055	*t*: 134 μm *a*: 23 μm
95% enriched ^{6}Li glass	Solid	893	673 μm	*t*: 2727	*a*: 2055	*t*: 36 μm *a*: 6 μm
^{10}B	Solid	3835	20 μm	*a*: 1472	^{7}Li: 840	*a*: 3 μm ^{7}Li: 1.7 μm
$^{10}BF_3$	Gas	3835	97 mm.atm	*a*: 1472	^{7}Li: 840	4.2 mm.atm
Gd (natural)	Solid	49,700	6.7 μm	Conversion electrons: ~30–200		5–100 μm
^{157}Gd	Solid	259,000	1.3 μm	Conversion electrons: ~30–200		5–100 μm

a: alpha particle, *p:* proton, *t:* triton

considered. For pulsed neutron sources, the use of a single event detector (counter) is required for time stamping.

The following sections discuss some general drivers of detector requirements that are imposed by either the neutron source or the type of neutron scattering instrument.

2.2.1 *Efficiency*

The detector efficiency, ε, is defined as the ratio of the number of neutrons recorded per unit time (N_r) to the number of neutrons incident to the detector per unit time (N_i) and is given by Eq. (2.12):

$$\varepsilon = \frac{N_r}{N_e} = \frac{\text{number of counts recorded}}{\text{total number of particles emitted}} = \varepsilon_{\text{geometric}} \times \varepsilon_{\text{intrinsic}} \tag{2.12}$$

The detector efficiency is affected by the geometric efficiency ($\varepsilon_{\text{geometric}}$), intrinsic efficiency ($\varepsilon_{\text{intrinsic}}$), the fraction of output signals from the detector that falls within the pulse-height analyzer window, and a factor for absorption and scatter occurring between the source and detector.

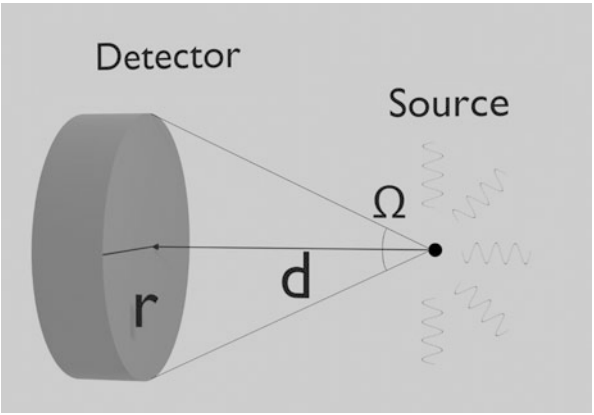

Fig. 2.6 Illustration of a point-source geometric efficiency for a circular area detector positioned close to the detector. The detector radius is represented by *r*, and *d* is the source-to-detector distance

Considering an isotopic emission, the geometric efficiency is the fraction of particles that are emitted by the source and arrive at the detector surface. Therefore, it is the ratio of the number of photons emitted toward the detector divided by the number of photons emitted by the source, given by Eq. (2.13):

$$\varepsilon_{\text{geometric}} = \frac{\Omega}{4\pi} \tag{2.13}$$

where Ω is the solid angle between source and detector in steradians. Notably, $\varepsilon_{\text{geometric}}$ depends only on the source–detector geometry, as shown in Fig. 2.6.

Equation (2.14) is used for a point source:

$$\Omega = 2\pi\left(1 - \frac{d}{\sqrt{d^2 + r^2}}\right) \tag{2.14}$$

where *r* is the detector radius, and *d* the source-to-detector distance [7].

$\varepsilon_{\text{geometric}}$ equals 0.5 when the detector encloses half of the source and equals 1.0 when it fully encloses the source.

Intrinsic efficiency is the ratio of the number of counts recorded by a detector to the total number of particles incident on the detector, given by Eq. (2.15):

$$\varepsilon_{\text{intrinsic}} = \frac{\text{number of counts recorded}}{\text{number of neutrons incident to detector}} = 1 - \exp\{-N\Sigma(\lambda)d\} \tag{2.15}$$

where Σ(λ) is the absorption cross section (function of wavelength), *N* the number density of the absorber, and *d* is the thickness [8].

For example, for a 1 cm absorption length in ^{3}He ($N = 2.7 \times 10^{19}$ cm^{-3} atm^{-1} at 300 K) and 1.8 Å, $\varepsilon_{\text{intrinsic}}$ is 13%.

2.2.2 Counting Rate

Most detector systems operate in pulse mode. The objective of pulse mode is to record the number of pulses that occur over a given measurement time or, alternatively, to indicate the rate at which these pulses are occurring. Therefore, the count rate is the number of collected counts divided by the acquisition time. The detector counting rate is generally limited by the charge drift time (gaseous or semiconductor) or by the light decay time (scintillator).

One example of the complicated nature of determining detector requirements is the detector's count rate capability. Global rate (i.e., the average rate over the detector's sensitive area) and local rate requirements are not always the same, especially in the case of single-crystal instruments, for which the local count rate from a Bragg peak can be orders of magnitude greater than areas of the detector that only count the background. Because of this discrepancy, care must be taken so that the detector performance is not compromised by higher local count rates. Likewise, peak rates at time-of-flight (TOF) pulsed neutron sources can be 3–10 times greater than the time-averaged rate. In the case of single-crystal instruments, the local count rate at a particular TOF can be many orders of magnitude higher. The change in neutron flux as a function of time at a TOF source occurs because of the way neutrons are produced. Unlike a steady-state reactor, which produces a relatively constant thermal neutron flux, neutron production at a TOF source occurs in a short, high-flux burst typically less than 1 μs in duration. This production burst is periodic and, depending on the neutron source, occurs anywhere between 1 and 60 times per second. The neutrons produced by this burst are moderated and then travel the length of an instrument's flight path. These moderated neutrons are detected at a later time that is proportional to the neutron's wavelength. A typical thermal neutron spectrum from a TOF source is shown in the left chart in Fig. 2.7.

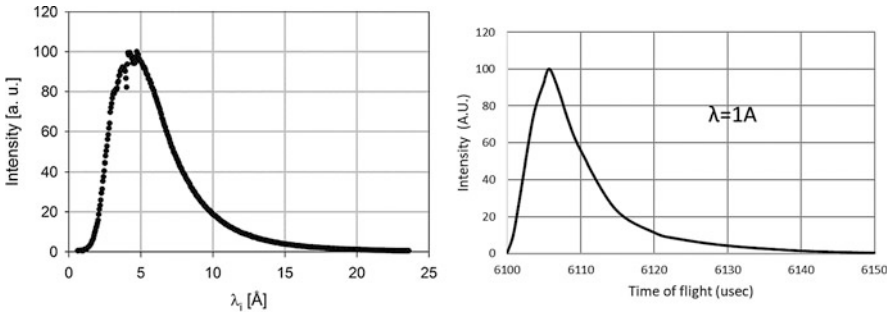

Fig. 2.7 Counting rate. (*left*) A typical rate profile for an elastic instrument at a spallation source. Multiplication of the horizontal axis by a scale factor (which is dependent upon the instrument geometry) gives the TOF. (*right*) The time profile of the count rate from a spatially localized Bragg peak at a single-crystal instrument is nomially zero except near the TOF value that meets the Bragg condition

The peak flux in this example is approximately four times the average flux over useful wavelengths. In most cases, the peak flux determines the operational rate requirement of the detector. To change the units of the horizontal axis in Fig. 2.7 from wavelength to time, multiply the wavelength values by a scale factor that depends upon the geometry of the beamline. As an example, for a very short beamline with a flight path of approximately 4 m, the horizonal axis of the left chart in Fig. 2.7 would be the TOF in milliseconds, with the peak flux occurring near 5 ms (the neutron production burst occurring at time zero). Depending upon the type of neutron moderator and the scattering instrument's flight path, the peak in the neutron flux can occur milliseconds to even hundreds of milliseconds later than the production pulse. The right chart in Fig. 2.7 shows the even more dramatic situation with a single-crystal TOF instrument. In that case, a Bragg peak occurs within a very short time window and at a specific, localized region of the detector. The Bragg condition is met at this position and time. In this scenario, the average count rate seen by the detector may be only tens of counts per second, and the instantaneous peak rate at the Bragg condition could be hundreds of thousands of counts per second. These examples are illustrative of the complications that occur when deciding upon an appropriate detector technology to use.

2.2.3 *Dead Time*

The dead time of a detector (τ) is defined as the minimum time interval between two consecutive resolved events. The Fig. 2.8 shows that the fraction of counts lost to dead time will depend on these three parameters:

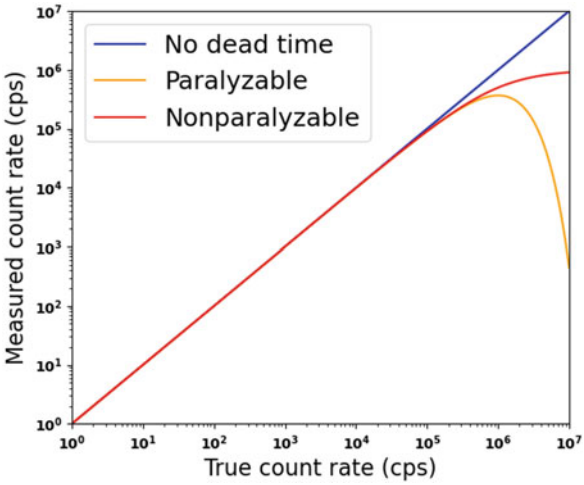

Fig. 2.8 Illustration of the observable detector count rate as a function of true count rate. The ideal, paralyzable ($m = n\exp\{-n\tau\}$), and nonparalyzable ($n = m/[1 - m\tau]$) cases are shown. For an ideal detector ($\tau = 0$), the registered count rate (m) is equal to the true count rate (n)

- the dead time (τ) duration,
- the rate of countable events at the detector, and
- whether the detector is paralyzable or nonparalyzable.

Most detectors follow the ideal curve at low count rates but start to lose counts owing to pileup as the intensity increases. For a nonparalyzable detector, the measured count rate increases slowly toward an asymptotic value, whereas for a paralyzable detector, the measured count rate reaches a peak value and then drops again.

If a detector used to monitor counting rates has dead time, then the measured counting rate is lower than the real counting rate. However, the real counting rate can be calculated from the measured rate if the dead time of the detector is known.

2.2.4 Dynamic Range

The detector's dynamic range is the ratio between the strongest and the weakest intensities that the detector can measure. It is the detector's ability to measure simultaneously weakly and strongly diffracted beams, as shown in Fig. 2.9. In practice, the noise may not originate solely from the detector's intrinsic noise because it includes any other background noise (i.e., all unwanted events).

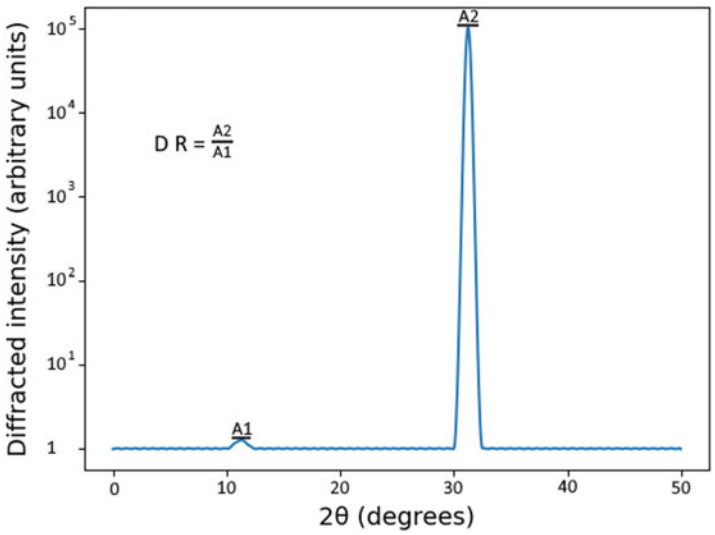

Fig. 2.9 Illustration of the dynamic range (DR) with the strongest and weakest reflected beams. A2 represents the highest measurable intensity, and A1 represents the smallest intensity (above the noise floor)

For reflectometry instruments, a dynamic range greater than 10^7 is required for some experiments. High-counting detectors and the test environment play important roles in achieving this requirement.

2.2.5 Position Resolution

The detector's spatial, or *position*, resolution is defined as the measurement of the smallest feature that it can resolve.

Generally, when the signal is collected in a single strip or pixel, the resolution, σ, measured as the root mean square of the residual distribution, can be approximated [7] by Eq. (2.16):

$$\sigma = \frac{p}{\sqrt{12}} \tag{2.16}$$

where p is the readout pitch. In some cases, spatial resolution can also be significantly improved by interpolating the position based on the signal measured on two neighboring strips or pixels. For detectors in which the signal-to-noise ratio (S/N) of the signal amplitude measurement on each cell dominates the resolution, the resolution is given by the simple formula in Eq. (2.17) [7]:

$$\sigma \propto \frac{p}{S/N} \tag{2.17}$$

For most current instruments, the required spatial resolution from neutron detectors varies from the millimeter range (powder diffraction) to a few micrometers (neutron imaging).

Neutron detectors, such as the linear position–sensitive ^{3}He gas detector (LPSD), demonstrate the complexity of the effects of measurement and experimental conditions on the position resolution under operational conditions. Spatial resolution of an LPSD strongly depends on count rate and the position along the tube, as shown in Fig. 2.10.

Detectors certified with low-flux neutron sources are unlikely to give the quoted resolution under operational conditions in which the neutron flux might be orders of magnitude higher. Furthermore, depending upon the design of the electronics, the resolution at the tube ends can be substantially poorer than that at the middle of the tube [8]. Variations in resolution as a function of position will almost invariably be found in any detector that relies upon signal interpolation.

For a given position along the tube, such as in the center, the position resolution varies with detector bias, as shown in Fig. 2.11, where higher spatial resolution (4.8 mm) can be obtained as the bias voltage (hence, the internal gain) increases.

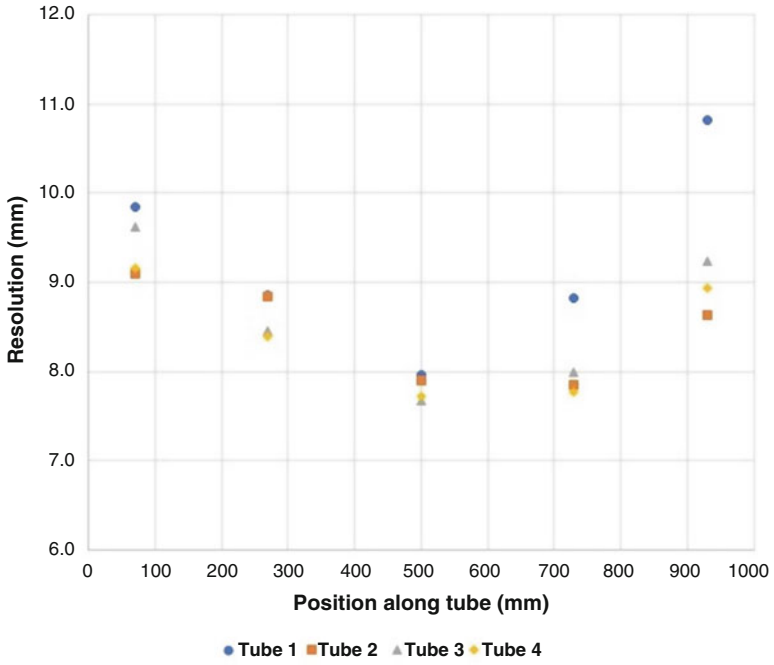

Fig. 2.10 Helium-3–based spatial resolution as a function of the position along the long tube for four tubes of a detector operating at 1850 V bias. At 10 atm, 100 cm long, and 2.5 cm diameter

At a higher rate, the electric field inside the tube is distorted, which reduces the signal amplitude. Smaller signal amplitudes reduce the S/N and thus reduces the position resolution, as shown in Fig. 2.12.

Generally, the positional dependence of resolution is not the only misperception associated with the discussion of a detector's resolution. The value itself may be quoted as a full width at half maximum (FWHM) value, a variance, or the line-pair dimension that achieves a 10% modulation value. All these numbers have a useful meaning depending on the information a researcher is attempting to extract from the experiment. If a researcher is trying to determine whether a peak has magnetic splitting in it, then the researcher might be interested in the FWHM resolution. Alternatively, if a researcher is interested in discerning features in imaging, then a 10% modulation value might be the more relevant number. Care must also be taken not to confuse detector pixelization with detector resolution. In certain pixelated detectors, pixelation and detector resolution might be the same. However, in many detectors, the pixelization is much finer than the spatial resolution of the detector. Operational neutron detectors may have spatial resolutions (FWHM) from 10 μm to 10 cm. Generally, detectors with the highest resolutions are used for imaging or radiography, and the lowest-resolution detectors are used in inelastic instruments.

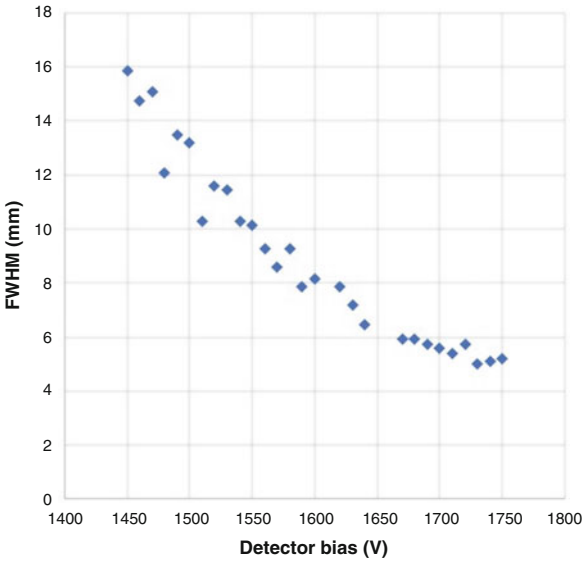

Fig. 2.11 Position resolution as a function of the bias of a detector tube. At 20 atm, 100 cm long, and 0.8 cm diameter. FWHM means full width at half maximum

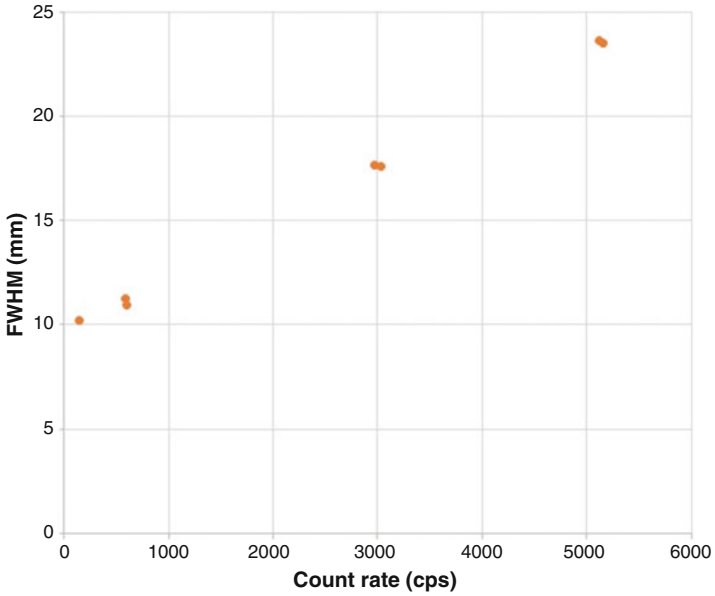

Fig. 2.12 Illustration of the resolution vs. intensity rate of a detector tube. At 15 atm, 84 cm long, and 1.3 cm diameter. The tube was illuminated through a slit 2 mm wide with the rate altered by changing an aperture size far upstream on the beamline. Along with the resolution decrease, the peak shape increasingly deviated from a Gaussian shape as the rate increased

2.2.6 Time Resolution

The detector's time resolution is defined by how accurately the time at which a neutron crossing the detector can be determined. High time resolution in (gaseous or scintillator-based) detectors is important in most applications in scattering facilities because of the interest in TOF information. For example, the time response of neutron scintillating materials, mainly their luminescence response, may limit the time resolution of scintillation detectors. Faster scintillation decay times such as those observed in GS20 neutron scintillators are attractive because their integration in silicon photomultipliers (SiPMs) offers high–time resolution neutron detectors.

2.2.7 Uniformity and Distortion

Reviewing detector uniformity and distortion requirements for a single-crystal diffractometer in detail is illustrative of how complex both requirements are in crystallography applications. Single-crystal diffractometers make use of Bragg peaks to determine structural factors, including the Debye–Waller factor of the lattice. To determine these factors accurately, the position, shape, and intensity of each Bragg peak must be measured accurately by the detector. Distortions in the measured peak shape invariably affect the position and shape estimates created by various software fitting routines, and variations in detection efficiency over the active area of the detector lead to increased error in the calculated peak intensity. In the case of Anger cameras, distortions and uniformities below 0.1 mm are required for very good correlation coefficients (R^2 values close to 1) [8]. The uniformity of detector efficiency is also important to meet the requirements for the identification of diffuse scattering processes.

Generally, diffuse scattering is characterized by a spatially periodic background structure (in many cases, weak) that is considered separately from the much stronger Bragg peaks. Analyzing a weakly spatially periodic background structure imposes an additional requirement on detector uniformity—that no significant components should appear in the Fourier transform of the detector's corrected flood response. Because most detectors that achieve the position resolution required for single-crystal instruments use interpolation schemes, in which the underlying pixelization of the sensor has spatial periodicity, care must be taken to ensure this periodicity (shown in the uncorrected flood response in Fig. 2.13) is precisely corrected. If the periodicity is not corrected, then the residual periodic may appear in the background analysis used to identify the presence of diffuse scattering processes.

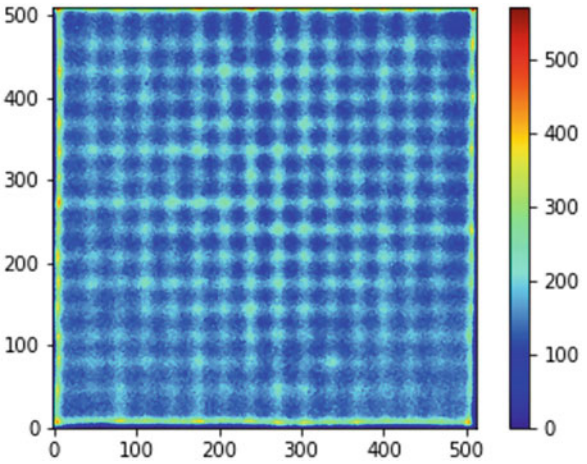

Fig. 2.13 Illustration of the diffuse scattering from a molecular solid. Uncorrected flood image from an Anger camera. Incorrect or incomplete correction of the flood response can lead to periodic artifacts that can interfere with the interpretation of diffuse scattering backgrounds

2.2.8 Gamma Rejection

Gamma rays are one of the pervasive background signals in neutron scattering. Although gamma rays can be produced by a variety of mechanisms, background gamma rays that arise as products of neutron interactions with various materials are pervasive at neutron scattering instruments, as shown in Fig. 2.14. This type of gamma ray can be used to nondestructively (such as prompt gamma ray activation analysis) identify the component elements. In neutron scattering, these gamma rays are generally considered a component of noise in the collected data. The two primary sources of these gamma rays are prompt or delayed gamma rays:

- Gamma rays that arise from neutrons interacting with instrument material, such as shielding and sample environment equipment
- Gamma rays that arise from neutron interactions with the sample

For example, boron, which is used extensively in thermal neutron shielding, emits a prompt gamma ray of approximately 480 KeV. These gamma rays, depending upon the location of the shielding relative to the detector, can create a very large gamma ray background. Other neutron shielding materials, such as gadolinium, produce a broad range of hard gamma rays and can eliminate entire classes of detectors from being useful at a beamline when used in slit assemblies, especially near the detector.

Gamma rays from the sample can also be a source of background noise in neutron scattering experiments. For example, samples containing hydrogen, which are ubiquitous in life science neutron scattering, emit prompt gamma rays with an energy of 2.2 MeV. Further complicating the design of detectors is that high gamma fluxes, even if they can be discriminated against, can have secondary effects on detector performance, such as reduced spatial resolution or reduced count rate capability. These secondary effects are well known, and in security applications, certain detector parameters must be shown to be immune to large gamma flux [9]. Gamma

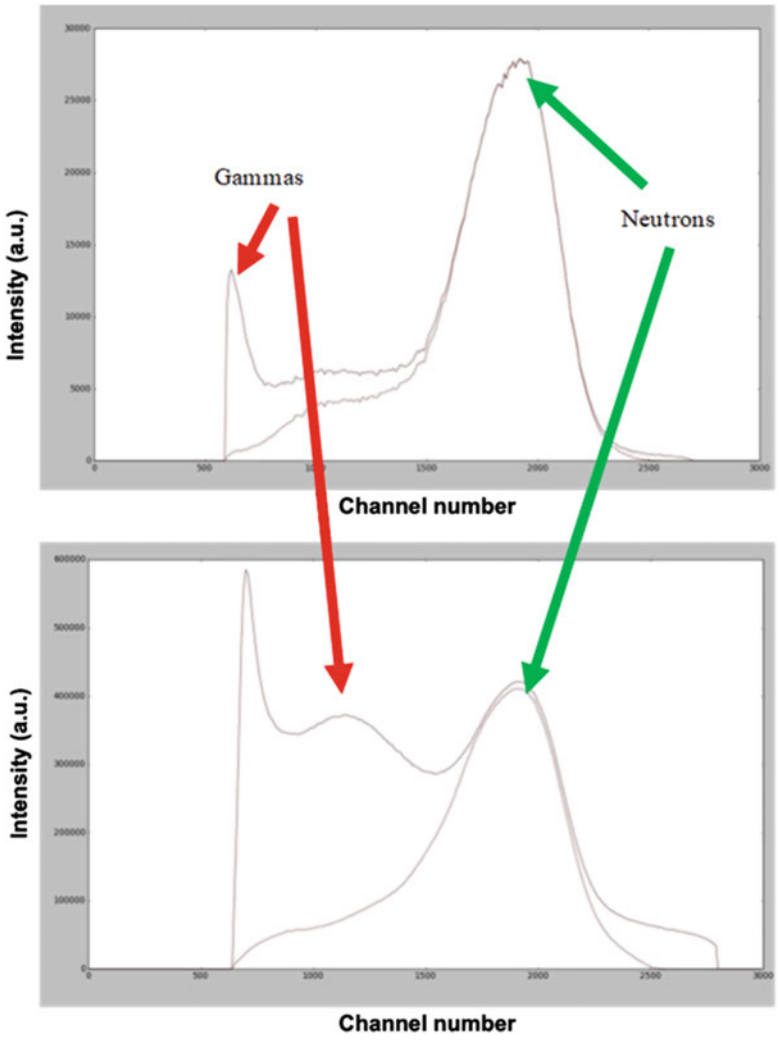

Fig. 2.14 Pulse height spectrum of the same Anger camera in two different beamlines. The gamma rays distribution is a good illustration of how the environment can affect its spectrum for the same detector

rejection values for neutron detectors are often reported as either gamma ray detection efficiency using a gamma ray source of known energy spectrum (^{60}Co and ^{137}Cs are typical) or as a gamma rejection ratio, which is the gamma ray detection efficiency divided by the neutron detection efficiency at a given neutron wavelength. The gamma rejection ratio needed for an instrument depends strongly upon the science being investigated. For example, an imaging instrument can operate with ratios near 10^{-3}, but inelastic instruments generally require rejection

ratios closer to 10^{-6}. As with many parameters, the gamma rejection ratio is strongly related to other detector parameters, such as neutron detection efficiency. In some scintillator-based detectors (e.g., an Anger camera), using the adjustment of operational parameters, a researcher can improve the gamma rejection by an order of magnitude, with a reduction in thermal neutron detection efficiency of 10% or less. Even though the detector efficiency may fall slightly below a desired operational specification, the order of magnitude improvement in gamma rejection might allow the exploration of new scientific discoveries. This coupling of detector parameters is a prime example of why it is critical to examine the entire suite of detector requirements before deciding upon a detector technology.

2.2.9 Scintillation Decay Time

To measure light decay time, scintillation light pulses (flashes) are usually characterized by a fast increase of the intensity in time (pulse rise time) followed by an exponential decrease, as shown in Fig. 2.15. The decay time of a scintillator is defined by the time after which the intensity of the light pulse has returned to 1/e of its maximum value.

Most scintillators are characterized by more than one decay time, and usually, the effective average decay time is mentioned. The decay time is important for fast counting or timing applications.

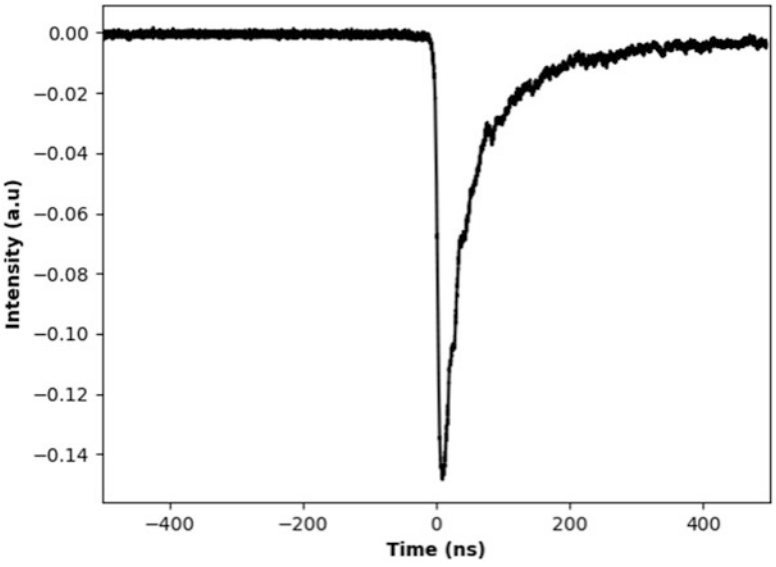

Fig. 2.15 Illustration of a GS20 scintillator luminescence response to a neutron

2.3 Detector Selection for Instruments

Different neutron detection materials necessitate different detector configurations. As one might expect, neutron detectors with gas as the conversion medium have a different construction and operation than those that generate scintillation light, or where the neutron conversion takes place in a thin surface layer or bulk solid. For example, gas-based detectors require some type of containment or pressure vessel, and the signal charge is generated and drifts through a gas, while scintillating materials utilize a two-step process in which neutrons are first converted into photons in the scintillator, and these photons are then collected by a photosensitive device, such as a photomultiplier tube.

This understandably results in a range of performance characteristics that depend on the choice of detection material and detector design. Spatial resolution, neutron capture efficiency, gamma ray sensitivity, and many of the other performance parameters outlined in Sect. 2.2 generally depend on the conversion material, detector configuration (i.e., size, shape, design), and the form of signal processing electronics employed. Some detectors have good spatial and timing resolution and acceptable efficiency, but they have poor gamma ray rejection. Others may have a different set of advantageous or disadvantageous properties. It is usually the case that there are performance trade-offs when attempting to select the best detector type for a particular instrument. In other words, there is no 'one size fits all', no ideal detector to suit all applications or instrument requirements. Appropriate detector selection requires an understanding of the specific instrument design and specifications.

Section 2.3.1 presents an overview of the basic detector requirements by instrument type, as well as the selection of detectors for the instruments at SNS and HFIR to best meet those requirements.

2.3.1 Instrument Classifications for Neutron Scattering

Neutron scattering is applicable to a broad range of sample material types, shapes, sizes, and environments. In the earliest implementations, neutron diffraction was used to determine the structure of single crystals or powder samples. This was followed by the development of the triple axis technique to study inelastic—or *energy-exchange*—interactions, which measure excitation modes within the sample.

These early experiments were conducted at research reactors. With the advent of pulsed sources, the TOF technique became feasible, and along with it, many new instrument concepts and technologies were realized. *TOF* refers to the measurement of the total neutron transit time down the flight path, and from this the neutron velocity, and thus the wavelength, can be determined. The TOF technique, combined with large area detector coverage and event mode data acquisition, where the pixel and TOF for each neutron is recorded individually, allows for faster data collection using broad bandwidth neutron scattering. Instrument designs continue to evolve at

Table 2.3 Table of representative detector performance requirements by instrument type

	Resolution (FWHM)	Efficiency (2 Å)	Count rate (time averaged)	Gamma sensitivity (^{60}Co)	Active area
Single crystal diffractometers	0.5–1 mm	60–80%	500 kcps/m^2	$<1 \times 10^{-6}$–1×10^{-5}	0.5–4 m^2
Powder diffractometers	0.5 × 1–5 cm	60%	20 kcps/m^2	$<1 \times 10^{-6}$	10 m^2
Direct geometry spectrometers	1–2 cm	80%	50 kcps/m^2	$<5 \times 10^{-7}$	40 m^2
Indirect geometry spectrometers	1 cm	80%	100 cps/cm^2	$<1 \times 10^{-6}$	0.5 m^2
Small angle neutron scattering	5–8 mm	70%	1 Mcps/m^2	$<1 \times 10^{-6}$–1×10^{-5}	1 m^2
Reflectometry	1–2 mm	70%	10 kcps/cm^2	$<1 \times 10^{-6}$	100 cm^2
Neutron imaging	10–100 μm	40%	5 Mcps/cm^2	$<1 \times 10^{-3}$	1–100 cm^2

cps: counts per second

both reactor-based and pulsed sources, with designs generally revolving around the form of the samples to be studied. Accordingly, optimal detector selection depends to a large degree on instrument design.

Neutron scattering instruments can be classified by instrument type:

- Diffractometers—structural determination via elastic scattering
- Spectrometers—excitations and dynamical studies via inelastic scattering
- Small-angle neutron scattering (SANS)—structure and function of samples with features over relatively large length scales
- Reflectometry—structure and kinetics of surfaces, thin films, and interfaces
- Neutron imaging—structure and kinetics of bulk samples using neutron radiography and tomography

Table 2.3 lists the typical range of values as a function of instrument type for some of the detector performance parameters described in Sect. 2.2. The subdivisions for diffractometers (e.g., single crystal, powder) and spectrometers (direct versus indirect geometry) are explained in the subsequent text.

2.3.2 Diffractometers

Diffractometer instruments can be further subdivided into two main types: single-crystal diffractometers and powder diffractometers. This subdivision has important ramifications for detector selection. The diffraction pattern from single crystals predominantly consists of Bragg reflections—that is, strong scatter peaks highly localized in space (and time, for TOF instruments). Detectors for single-crystal diffractometers must have good spatial resolution and high local count rate

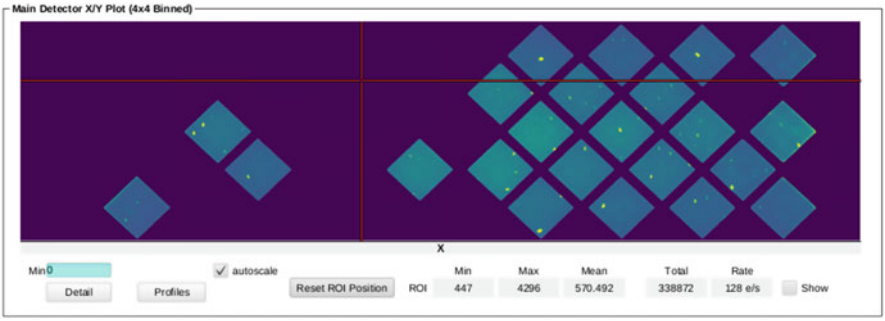

Fig. 2.16 Image showing Bragg peaks from single-crystal YMn_6Sn_6 recorded in multiple Anger camera detectors at TOPAZ at SNS

capability. Large area detector coverage is preferred to collect as many Bragg reflections as possible. Figure 2.16 shows an image of Bragg peaks from a YMn_6Sn_6 sample.

Anger cameras constructed with GS20 lithium glass scintillator and multi-anode photomultiplier tubes (operating in Anger mode) are capable of <1 mm FWHM spatial resolution and local count rates of approximately 10–20 kcps (cps means counts per second). These detector types were selected for the single-crystal instruments at SNS: SNAP (Spallation Neutrons and Pressure Diffractometer), TOPAZ (Single-Crystal Diffractometer), and MANDI (Macromolecular Neutron Diffractometer). Figure 2.17 shows the arrangement of Anger camera detectors surrounding the sample position at the MANDI instrument at SNS. Anger camera–type detectors are described in Sect. 4.1.

In recent years, an upgraded version of the Anger camera was developed using silicon photomultipliers. This detector was installed on the four-circle diffractometer single-crystal instrument at HFIR, rechristened DEMAND (Dimensional Extreme Magnetic Neutron Diffractometer; HB-3A). The quasi-Laue diffractometer IMAGINE (also at HFIR) utilizes a high spatial resolution (<500 μm) neutron sensitive image plate in a vertical cylindrical geometry surrounding the sample position.

The diffraction pattern from powder samples can be visualized as a quasi-continuous distribution of Bragg reflections at fixed scattering angle 2θ (for a given lattice spacing d) about the neutron beam axis. These are referred to as Debye–Scherrer cones, examples of which are illustrated in Fig. 2.18. They display a circular pattern on a 2D or area detector in transmission (or small-angle scattering), or as curved sections of the cone in detectors located at higher scattering angles. Debye–Scherrer cones can be projected forward, at 90-degrees, or backscattered, as shown in the figure, depending on the combination of the crystal lattice parameters and neutron wavelength.

Because the scattering pattern from powders is distributed over larger regions, detectors for powder instruments often comprise banks with large areal coverage at longer sample-to-detector distances. For this reason, they generally have more

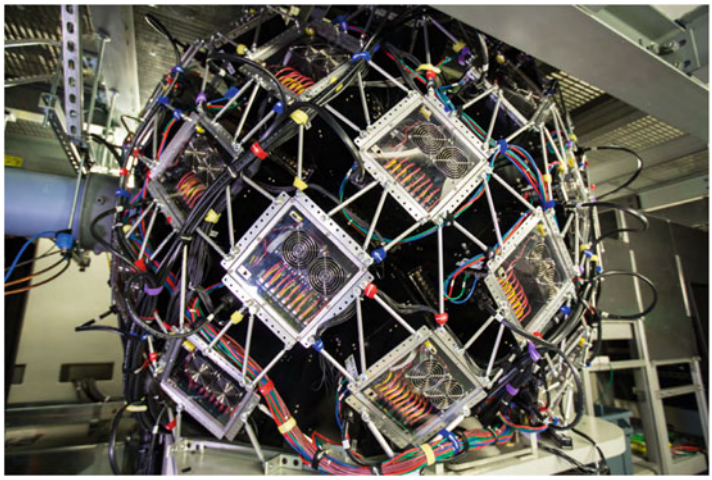

Fig. 2.17 Anger camera detectors installed to surround the sample at MANDI (SNS)

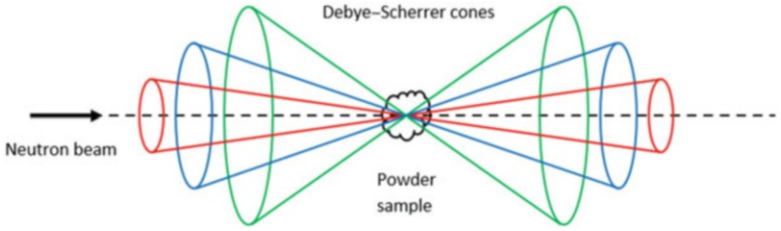

Fig. 2.18 Illustration of the Debye–Scherrer geometry in powder scattering

modest resolution and rate requirements. Thus, ^{3}He gas–based detectors or wavelength shifting fiber (WLSF) detectors were considered viable options for the powder instruments. Two of the powder diffractometers at SNS, VULCAN and POWGEN, were designed for large area detector coverage in air. The larger pixel sizes (5 × 50 mm) and moderate rate capability made the ZnS(Ag)/^{6}LiF scintillator-based WLSF detectors attractive choices for those instruments. (The detector array at VULCAN has since been replaced with banks of LPSDs because of the improvements in science that the higher resolution and uniformity gas-based detectors were found to provide.) Figure 2.19 shows the placement of some of the WLSF detectors in the POWGEN SNS instrument. The WLSF detectors are described in Sect. 4.2.

Although the Nanoscale-Ordered Materials Diffractometer (NOMAD) was also designed for modest resolution and rate and for large areal coverage, the detectors for this instrument are placed in vacuum. The scintillator-based detectors available at the time were not vacuum-capable, so ^{3}He LPSDs were selected for this instrument.

Two of the powder diffractometers at HFIR, POWDER and WAND (Wide-Angle Neutron Diffractometer), were originally instrumented with curved arrays of ^{3}He detectors, providing 1D position resolution in the horizontal plane. The detectors for

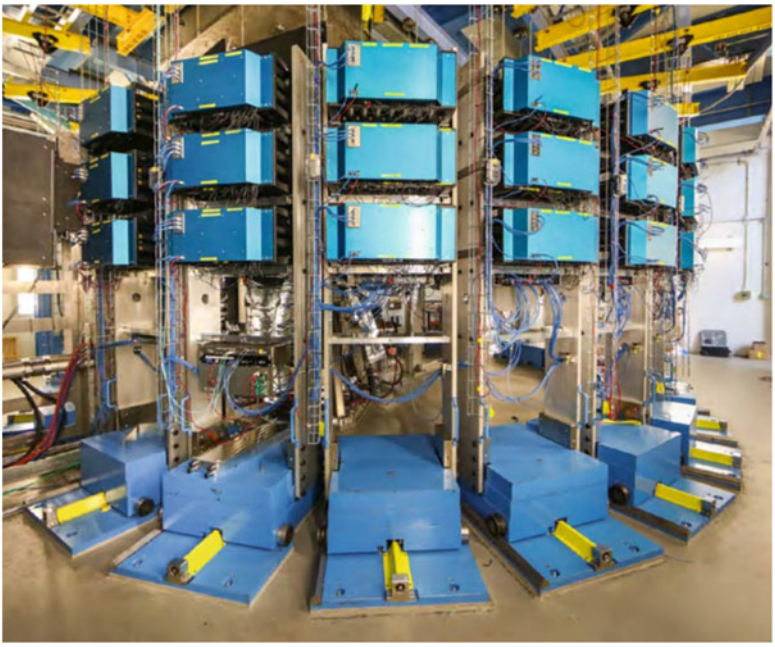

Fig. 2.19 Scintillator-based WLSF detectors at POWGEN (SNS)

the POWDER instrument comprise 44 individual vertically oriented single-output tubes. The original 1D detector at WAND was replaced in 2017 with a 2D detector and renamed WAND^2 (indicating the upgrade to 2D capability). The single output detectors for POWDER are described in Sect. 3.3, the WAND^2 detector is covered in Sect. 3.5.

The detector for the Neutron Residual Stress Mapping Facility (NRSF2) was upgraded in 2018, replacing the previous arrangement of seven horizontally oriented 1D detectors with a 2D detector of larger active area. This detector is a ^{3}He multiwire proportional chamber design with delay line readout and 2 × 2 mm spatial resolution. The high resolution is necessary because this instrument uses fine slits and collimation to define small gauge volumes for bulk strain mapping. This instrument was renamed HIDRA (High Intensity Diffractometer for Residual Stress Analysis) following the upgrade, and its detector is described in Sect. 3.6.

2.3.3 Spectrometers

Spectrometers measure the energy exchange between the neutron and the sample. This type of interaction, referred to as *inelastic scattering*, produces a much weaker signal and of slightly higher or lower energy than that which results from the

diffraction, or *elastic scatter*, peak. One of the primary requirements for detectors for inelastic scattering instruments is that they should have exceptional gamma rejection for optimal measurement of these weak signals above the non-neutron background. Helium-3 gas detectors exhibit the lowest gamma sensitivities of the available detector technologies and were an obvious choice based on this criterion alone.

Inelastic scattering instruments can be subdivided into three types based on instrument geometry, which the following sections will discuss.

2.3.3.1 Triple Axis Spectrometers

Triple axis spectrometry (TAX, alternately TAS) was invented by Brockhouse (NRX, Chalk River, Canada) in the 1950s and is still used today in essentially its original form. TAX instruments represent the workhorse inelastic instrument at reactor-based sources. In TAX, crystal monochromators placed before and after the sample define the initial and final wavelengths, respectively. (These represent two of three rotational axes; the third is the sample itself.) The detector does not need to be position sensitive. Thus, single output ^{3}He gas-proportional tubes are an acceptable choice for the TAX instruments, such as FIE-TAX (Fixed-Incident-Energy Triple-Axis Spectrometer; recently renamed VERITAS, Versatile Intense Triple-Axis Spectrometer), PTAX (Polarized Triple-Axis Spectrometer), TAX (Triple-Axis Spectrometer), and CTAX (Cold Neutron Triple-Axis Spectrometer), all at HFIR. Helium-3–filled single-output gas-proportional detectors are discussed in Sect. 3.3.

2.3.3.2 Direct Geometry Spectrometers

Direct geometry spectrometers use neutron beam choppers to select the initial neutron energy, and neutron TOF to determine the final energy. Hence, they are also referred to as *chopper spectrometers*. The derivation of the expression for the final neutron energy based on TOF is given in Appendix C. Tens of square meters of position-sensitive detector panels surround the sample in a cylindrical geometry with the angular range in some instances spanning $>160°$ horizontally and 50° vertically. The secondary flight path (between the sample and the detector) is either in vacuum or argon atmosphere to minimize neutron scattering from air. Resolution and rate requirements are modest owing to the large areal coverage and relatively long secondary flight path (3–6 m). Low gamma ray background is essential here as well.

Based on the instrument design criteria above, vacuum-capable ^{3}He gas–filled LPSDs were selected for the direct-geometry spectroscopy instruments: CNCS (Cold Neutron Chopper Spectrometer), SEQUOIA (Fine-Resolution Fermi Chopper Spectrometer), and ARCS (Wide Angular-Range Chopper Spectrometer), all at SNS. HYSPEC is also classified as a direct geometry spectrometer, although it is a hybrid instrument (hence the name, HYbrid SPECtrometer), utilizing a combination of choppers and focusing monochromators. Although HYSPEC is in air, ^{3}He LPSDs

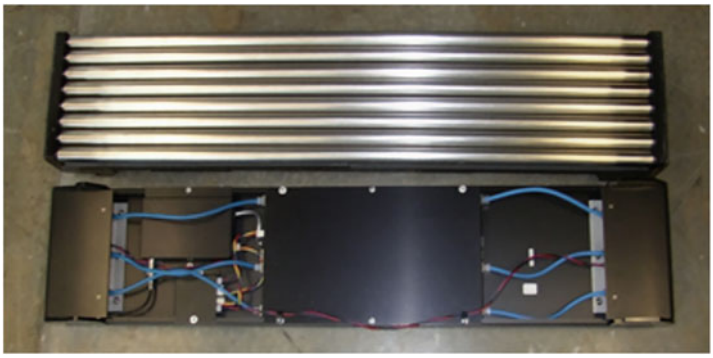

Fig. 2.20 Photo showing front and rear views of a typical ^{3}He eight-pack detector. (*top*) Front view of the eight ^{3}He-filled tubes. (*bottom*) Rear view; preamplifiers are located inside the enclosures at each end (black anodized to facilitate radiant heat transfer for vacuum operation). The enclosure in the center (rear view), also black anodized, contains additional signal processing electronics. ARCS contains 115 of these eight-packs, arranged in three horizontal rows

were chosen for this instrument as well to satisfy the moderate resolution, rate, and the low gamma background requirements.

A modular detector approach was adopted early on at SNS for ease of handling, installation, and maintenance. The so-called *detector eight-pack module*, an assembly of eight gas-proportional tubes with integrated preamplifiers and signal processing electronics, represents the repeating unit for these types of installations. Fig. 2.20 is a photo of eight-packs for the ARCS instrument. A detailed description of the ^{3}He LPSD is provided in Sect. 3.2.

CORELLI (Elastic Diffuse Scattering Spectrometer at SNS) is a chopper spectrometer that has much in common with the design of the direct-geometry spectrometry instruments. CORELLI, however, is unique in that it also employs a statistical chopper to distinguish diffuse scatter from Bragg peaks. Bragg peaks provide information on atomic positions; diffuse scattering gives information on a larger length scale (e.g., magnetic short-range order). The CORELLI detectors are also in vacuum with horizontal and vertical angular coverage comparable to ARCS. Vacuum-capable ^{3}He LPSDs were selected for CORELLI.

2.3.3.3 Indirect Geometry Spectrometers

While a direct geometry spectrometer generally uses a known incoming neutron energy and measures the outgoing neutron energy modified by the inelastic scattering on sample, indirect geometry spectrometers use a broad range of incoming energies and only measure a fixed outgoing energy. Both types of instruments use TOF to reconstruct the unknown energy and calculate the energy transfer to or from the sample. Indirect geometry spectrometers typically use crystal monochromators in backscattering configuration to define a fixed final neutron wavelength. The initial

wavelength is determined through TOF. Two instruments at SNS, BASIS (Backscattering Spectrometer) and VISION (Vibrational Spectrometer), employ backscattering monochromator crystals. BASIS is a vacuum instrument; VISION operates in air. Helium-3 LPSDs were selected for these instruments for many of the same reasons given for detector requirements for inelastic spectrometers. Appendix D presents the derivation of initial and final neutron energies in indirect geometry.

2.3.4 Small-Angle Neutron Scattering

Small angle neutron scattering (SANS) is a technique to study relatively large-scale features or structures from a few angstroms up to a few thousand angstroms. Use of the small-angle technique can be understood by a rearrangement of Bragg's law (Eq. [1.8]) to give Eq. (2.19):

$$d = \frac{n\lambda}{2\sin\theta} \tag{2.19}$$

where d is the distance between crystal lattice planes, n is an integer, λ is neutron wavelength, and θ is the incident angle of the beam. From Eq. (2.19), large d (typically the distance between scattering centers, but in this case, representative lengths of features under study) implies a long wavelength λ and/or small angle θ.

The elastic scattering diagram is shown in Fig. 2.21. Wavevector $\boldsymbol{k} = |\boldsymbol{k}| = 2\pi/\lambda$, where λ is the neutron wavelength. Common units for k are inverse Angstroms [$Å^{-1}$]. The scattered wavevector $\boldsymbol{Q}$ is the vector difference between the final and the incident wavevectors, $\boldsymbol{k_f}$ and $\boldsymbol{k_i}$, respectively. Since SANS is an elastic technique, the magnitudes $|\boldsymbol{k_f}|$ and $|\boldsymbol{k_i}|$ are equal. Small scattering angles imply a small value for $\boldsymbol{Q}$, and in fact SANS is referred to as a low $\boldsymbol{Q}$ technique.

There are two SANS instruments at HFIR (the General Purpose, or GP-SANS, and the Biological, or Bio-SANS) and one at the SNS (Extended Q-Range, or EQ-SANS). The two HFIR SANS instruments are located in the Cold Guide Hall, and both use velocity selectors to define the relatively long (> 4 Å) incident wavelengths. The EQ-SANS instrument employs neutron choppers for wavelength determination.

SANS is by definition a low angle technique, thus the detector must be positioned to collect data at small scattering angles. Typically, this requires a 2-D detector placed normal to the neutron beam. [Neutron absorbing beam stops prevent the extremely high event rates from the direct beam from saturating the detector]. The requirements on resolution, rate, low gamma ray sensitivity, and vacuum operation have led to the selection of 2D ^{3}He detectors as the optimal choice for current SANS instruments. The main detector for all three SANS instruments is a 1×1 m arrangement of ^{3}He LPSDs in vacuum. (Bio-SANS has an additional LPSD bank located off-angle to provide somewhat higher Q-range capability.)

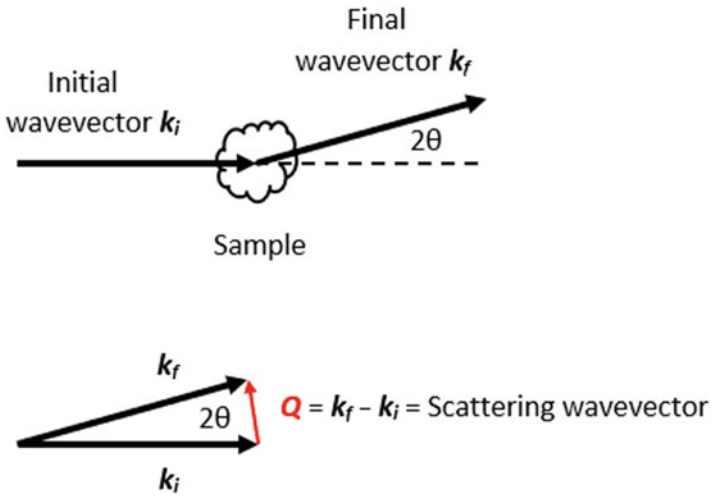

Fig. 2.21 Elastic scattering triangle. Initial wavevector $\boldsymbol{k_i}$ scatters from sample into angle 2θ. Final wavevector $\boldsymbol{k_f}$ is the vector sum $\boldsymbol{k_i} + \boldsymbol{Q}$, where $\boldsymbol{Q}$ is the scattered wavevector. For elastic scattering, the magnitudes $|\boldsymbol{k_f}|$ and $|\boldsymbol{k_i}|$ are equal ($\boldsymbol{k_f} = \boldsymbol{k_i}$). $\boldsymbol{Q}$ decreases with scattering angle 2θ. SANS is referred to as a low $\boldsymbol{Q}$ technique

The Ultra-Small Angle Neutron Scattering instrument (USANS) uses a combination of monochromator crystals and the TOF technique to provide discrete Bragg reflections that are separated in time. The primary requirement for this instrument is an extremely low background. Two ^{3}He LPSD eight-packs were chosen for USANS. Even though position sensitivity was not essential (data from the eight individual ^{3}He tubes are added to a give total counts), LPSDs were used to provide spatial discrimination capability—that is, the rejection of background events located outside the area of the primary signal.

2.3.5 *Reflectometers*

Neutron reflectometry provides a technique for 1D probing of thin films, surfaces, and interfaces. Since incident and reflected angles are typically very small, neutron reflectometry is also a low $\boldsymbol{Q}$ technique (refer to the scattering triangle in Fig. 2.21). As with SANS, a 2D detector is placed normal to the beam to record the reflections from the sample. Though not technically the direct beam, reflected beams still have a very high neutron flux. Detector requirements for reflectometers include high-rate capability, low gamma ray sensitivity, and very good (1–2 mm FWHM) spatial resolution. There are two reflectometer instruments at Oak Ridge National Laboratory, and both are at the SNS. The LIQREF (Liquids Reflectometer) is designed to accommodate a variety of horizontal surfaces and interfaces (air–liquid, liquid–

liquid, liquid–solid). MAGREF (Magnetism Reflectometer) is designed for vertically oriented surfaces and is particularly intended to study magnetic structure. Thus, an additional detector requirement for that instrument is insensitivity to stray magnetic fields.

Helium-3–filled multiwire proportional detectors, designed and constructed at Brookhaven National Laboratory, were chosen for the two reflectometers at SNS. Minor modifications were made to the original design, including compatibility with the SNS data acquisition format. Although these detectors were selected for day one operation, it was recognized from the start that they exhibit insufficient rate capability, which limits instrument performance. Unfortunately, suitable alternatives have not yet been deployed on the SNS reflectometer instruments. These detectors are described in Sect. 3.4.

2.3.6 Neutron Imaging

Each of the instrument types described in previous sections relies on the detection of neutrons that have been scattered or reflected from a sample in the beam. Neutron imaging, however, is instead a transmission technique, whereby images in the detector result from the transmission or attenuation of neutrons as they pass through the sample. This process is illustrated in Fig. 2.22. A 2D detector is required in the direct beam and downstream from the sample. Neutron imaging detectors must have extremely high-rate capability and preferably extremely high spatial resolution (<100 μm). Event mode or fast frame data acquisition is an essential capability for many applications that rely on energy-dispersive neutron detection.

Existing detector technologies include neutron-sensitive scintillators combined with charge-coupled device (CCD) or scientific complementary metal–oxide–semiconductor readout technologies, or with microchannel plates coupled with Timepix chips. MARS (Multimodal Advanced Radiography Station) at HFIR and VENUS (Versatile Neutron Imaging Instrument) at SNS (currently under construction) are

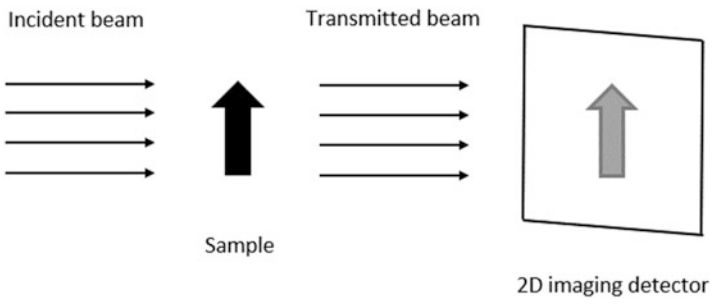

Fig. 2.22 Diagram illustrating the layout of a neutron imaging experiment. A high-resolution, 2D neutron detector records the neutrons that are transmitted through a sample in the beam

Table 2.4 SNS instruments, instrument types, and detector types

Beamline	Name	Long description	Instrument type	Detector type
BL-1A	USANS	Ultra-small angle neutron scattering	Sans	LPSD
BL-1B	NOMAD	Nanoscale ordered materials diffractometer	Diffractometer	LPSD
BL-2	BASIS	Backscattering spectrometer	Spectrometer	LPSD
BL-3	SNAP	Spallation neutrons and pressure	Diffractometer	Anger
BL-4A	MAG REF	Magnetism reflectometer	Reflectometer	MWPC
BL-4B	LIQ REF	Liquids reflectometer	Reflectometer	MWPC
BL-5	CNCS	Cold neutron chopper spectrometer	Spectrometer	LPSD
BL-6	EQ-SANS	Extended Q-range small angle neutron scattering	Sans	LPSD
BL-7	VULCAN	Engineering materials diffractometer	Diffractometer	LPSD
BL-9	CORELLI	Elastic diffuse Scattering spectrometer	Spectrometer	LPSD
BL-10	VENUS	Versatile neutron Imaging instrument	Imaging	Multiple
BL-11A	POWGEN	Powder diffractometer	Diffractometer	WLSF
BL-11B	MANDI	Macromolecular neutron diffractometer	Diffractometer	Anger
BL-12	TOPAZ	Single crystal diffractometer	Diffractometer	Anger
BL-14B	HYSPEC	Hybrid spectrometer	Spectrometer	LPSD
BL-15	NSE	Neutron spin Echo spectrometer	Spectrometer	MWPC
BL-16B	VISION	Vibrational spectrometer	Spectrometer	LPSD
BL-17	SEQUOIA	Fine-resolution Fermi chopper spectrometer	Spectrometer	LPSD
BL-18	ARCS	Wide angular-range chopper spectrometer	Spectrometer	LPSD

MWPC multiwire proportional chamber

dedicated to neutron imaging. Neutron imaging can greatly benefit from advancements in detector performance, and a significant development effort is underway to provide the next generation of high-rate, high–spatial resolution detector technologies to improve the science that neutron imaging can deliver.

Table 2.4 lists the instruments at SNS, instrument type, and detector. BL stands for SNS beamline location. Table 2.5 shows the same information for HFIR. HB stands for Horizontal beamline location in the Thermal Beam Room, and CG stands for Cold Guide Hall beamline location.

Table 2.5 HFIR instruments, instrument types, and detector types

Beamline	Name	Long description	Instrument type	Detector type
Thermal beam room				
HB-1A	FIE-TAX	Fixed-incident-energy triple-Axis spectrometer	Spectrometer	^{3}He single
HB-1	PTAX	Polarized triple-Axis spectrometer	Spectrometer	^{3}He single
HB-2A	POWDER	Neutron powder diffractometer	Diffractometer	^{3}He single
HB-2B	HIDRA	High intensity Diffractometer for residual stress analysis	Diffractometer	MWPC
HB-2C	WAND^2	Wide-angle neutron diffractometer	Diffractometer	MWPC
HB-3	TAX	Triple-Axis spectrometer	Spectrometer	^{3}He single
HB-3A	DEMAND	Dimensional extreme magnetic neutron diffractometer	Diffractometer	Anger (SiPM)
Cold guide hall				
CG-1D	Imaging	Neutron Imaging facility	Imaging	Multiple
CG-2	GP-SANS	General-purpose small-angle neutron scattering	Sans	LPSD
CG-3	BIO-SANS	Biological small-angle neutron scattering	Sans	LPSD
CG-4C	CTAX	Cold neutron triple-Axis spectrometer	Spectrometer	^{3}He single
CG-4D	IMAGINE	Quasi-Laue diffractometer	Diffractometer	Image plate

MWPC multiwire proportional chamber

References

1. A.-J. Dianoux, G. Lander (eds.), *Neutron Data Booklet*, 2nd edn. (Institut Laue–Langevin and OCP Science, Grenoble, 2003)
2. D.L. Garber, R.R. Kinsey, *Neutron Cross Sections. Volume II. Curves.*; BNL-325(Ed. 3) (Vol. 2), EANDC(US)-183, INDC(USA)-58; US Department of Energy (Brookhaven National Laboratory: Upton, New York, 1976)
3. Nuclear Wallet Cards Search. https://www.nndc.bnl.gov/nudat3/indx_sigma.jsp
4. C.W.E. van Eijk, A. Bessière, P. Dorenbos, Inorganic thermal-neutron scintillators. Nucl Instrum Methods Phys Res **529**(1–3), 260–267 (2004). https://doi.org/10.1016/j.nima.2004.04.163
5. Scintacor. *Glass Scintillators: Lithium glass scintillators for neutron detection*. Scintacor (2022). https://scintacor.com/wp-content/uploads/2022/06/GlassScintillators-rev-3-June-22.pdf

6. R.A. Serway, C.J. Moses, C.A. Moyer, *Modern Physics*, 3rd edn. (Thomson Brooks/Cole, Boston, 2005)
7. M. Boronat et al., *Physical Limitations to the Spatial Resolution of Solid-State Detectors.* arXiv (2014). http://cds.cern.ch/record/2002654/files/arXiv:1404.4535.pdf
8. Design and performance of a large area neutron sensitive anger camera. R.Riedel et. al. NIMA 792 (2015) pp 224–233.
9. R.T. Kouzes, J.H. Ely, A.T. Lintereur, D.L. Stephens, Neutron Detector Gamma Insensitivity Criteria (PNNL-18903; US Department of Energy, Pacific Northwest National Laboratory, Richland, 2009)
10. Berger, Coursey, Zucker, Chang, Stopping-Power & Range Tables for Electrons, Protons, and Helium Ions, *NIST*, 124 (2017).

Chapter 3
Gas-Based Detectors

Justin Beal, Kevin D. Berry, and Loren Funk

Abstract This chapter is devoted to thermal neutron detectors which rely on gas proportional detection technology, and in particular, detectors which use helium-3 as the proportional gas. The physics of neutron capture and charge creation and drift in helium-3 detectors is discussed. The construction and operation of position sensitive detectors, both linear PSD and 2-D, or area detectors, is described in detail. Materials of construction, detector signal processing electronics, and noise sources and noise analysis are among the topics covered. The chapter concludes with a section on neutron beam monitors, a specialized type of detector which is typically placed in the direct beam to provide neutron beam flux and timing information relevant to the neutron scattering experiment.

3.1 Neutron Detection in Helium-3

The ^{3}He-based gas-proportional counters are by far the most common type of detector installed in the neutron scatteringinstruments at the Spallation Neutron Source (SNS) and the High Flux Isotope Reactor (HFIR), comprising around 80% of the combined instrument suite. The three basic configurations are (1) the single-output gas-proportional detector tube, (2) the dual-output linear position-sensitive detector (LPSD) tube, and (3) the 2D multiwire proportional chamber. Most of the gas detectors are installed as arrangements of adjacent LPSD tubes, effectively providing relatively large areas (tens of square meters in some instances) of 2D detector coverage. LPSDs provide the flexibility of many different detector configuration options, as shown in Fig. 3.1. Planar, curved, or radial arrangements may be realized. The single-output tubes are installed either individually or side by side to construct a 1D detector array. In the multiwire proportional chambers, horizontal and vertical readout grids provide continuous neutron detection coverage over modest

J. Beal · K. D. Berry (✉) · L. Funk
Neutron Sciences Directorate, Oak Ridge National Laboratory, Oak Ridge, TN, USA
e-mail: bealjd@ornl.gov; berrykd@ornl.gov; funkll@ornl.gov

Y. Diawara (ed.), *Neutron Detectors for Scattering Applications*, Particle Acceleration and Detection, https://doi.org/10.1007/978-3-031-36546-1_3

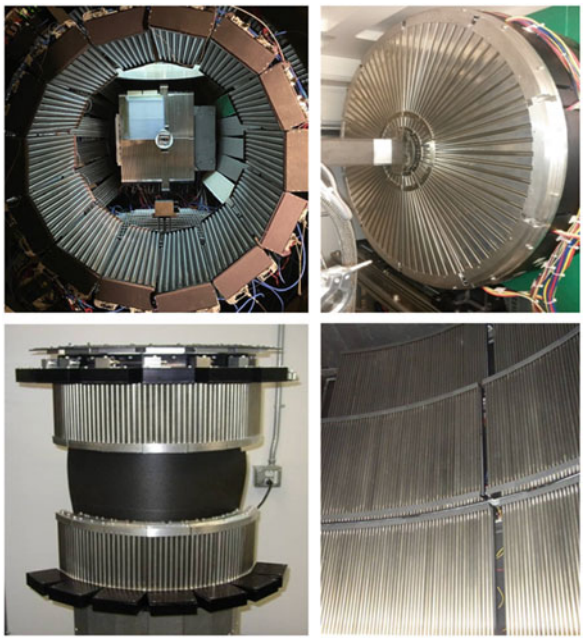

Fig. 3.1 Variety of detector configurations possible with arrangements of linear position–sensitive detectors (LPSDs). Clockwise from upper left: concave, radial, large area curved, and convex geometries

(60–250 cm^2) areas and good spatial resolution (1–3 mm) in 2D. Each of these detector types are discussed in more detail later in this chapter.

This section describes the process of neutron absorption in ^{3}He, the creation and distribution of the resulting ionization charge, and the operating principles of ^{3}He gas-proportional detectors.

3.1.1 Ionization Charge

Equation 3.1 describes the neutron conversion reaction with the ^{3}He nucleus, previously discussed in Chap. 2.

$$^1\mathrm{n} + {}^3\mathrm{He} \rightarrow {}^3\mathrm{H} + {}^1\mathrm{H} + 0.764\ \mathrm{MeV} \tag{3.1}$$

This reaction is exothermic, so the Q value energy of 0.764 MeV is imparted to the two reaction products—a tritium atom (triton) and a proton—as kinetic energy. This reaction has exactly two products, so the principle of conservation of linear momentum states that they must be emitted in antiparallel trajectories. Following the derivation in Chap. 2, the kinetic energies are distributed between the two reaction products according to their relative masses, thus the triton energy (E_T) is 191 keV, and the proton energy (E_P) is 573 keV.

Gas	First Ionization Potential (eV)	W-Value (eV/ ion pair)	
		Fast Electrons	Alpha Particles
H_2	15.6	36.5	36.4
He	24.5	41.3	42.7
N_2	15.5	34.8	36.4
Ne	21.6	35.4	36.8
Ar	15.7	26.4	26.3
Kr	14.0	24.4	24.1
Xe	12.1	22.1	21.9
CH_4	14.5	27.3	29.1
CO_2	13.8	33.0	34.2

Fig. 3.2 Table of ionization potentials and *W* values for several gases commonly used in proportional counters [1]

As these particles travel through the gas, they undergo scattering collisions with the ^{3}He gas atoms, losing kinetic energy with each interaction. Some scattering collisions result in ionization of the ^{3}He atom (with first ionization potential 24.5 eV), whereas others promote ground-state electrons to higher excitation states with no ionization. The W *value*, defined as the average energy required to produce one electron–ion pair, ranges from about 41–43 eV for ^{3}He. Because some fraction of the collisions results in electronic excitation rather than ionization, the *W* value average is always greater than the ionization potential. Comparing the average *W* value of 42 eV with the *Q* value of 764 keV suggests that 764,000/42, or approximately 18,000 electron–ion pairs are created within the ^{3}He gas following a single neutron-capture reaction (Fig. 3.2). Figure 3.2 tabulates the first ionization potentials and W-values for several gases commonly used in proportional counters.

The range of a 573 keV proton in 1 atm of ^{3}He is about 6 cm [2], much too long for a practical neutron detector that is expected to measure and record neutron interaction locations with centimeter or better precision. Proton range is inversely proportional to pressure, but even for common ^{3}He pressures of 10–20 atm, they are still too long for many applications. It is common practice to combine additional gases with the ^{3}He with the goal of reducing particle ranges to acceptable distances based on the detector's spatial resolution requirements. These so-called *stopping gases* typically have lower ionization and excitation energies and hence a greater potential for inelastic scattering collisions per unit track length than for ^{3}He alone. Commonly used stopping gases include Ar/CO_2 and CF_4.

Figure 3.3 shows the range of 573 keV protons and 191 keV tritons in several common stopping gases as a function of gas pressure, ranging from 0.1 to 10 atm [3]. Depending on the specific requirements of the detector, the stopping gas can vary from a fraction of a percent, to as much as 50% of the overall gas pressure in extreme cases.

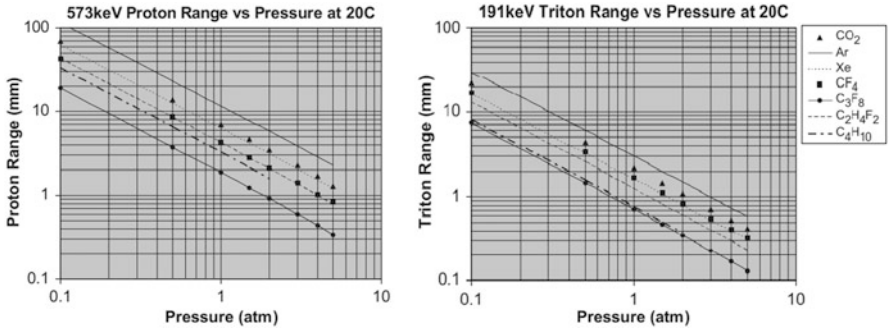

Fig. 3.3 Range of 573 keV protons (*left*) and 191 keV tritons (*right*) in various stopping gases as a function of pressure. (All data are from Stopping and Range of Ions in Matter simulations [3])

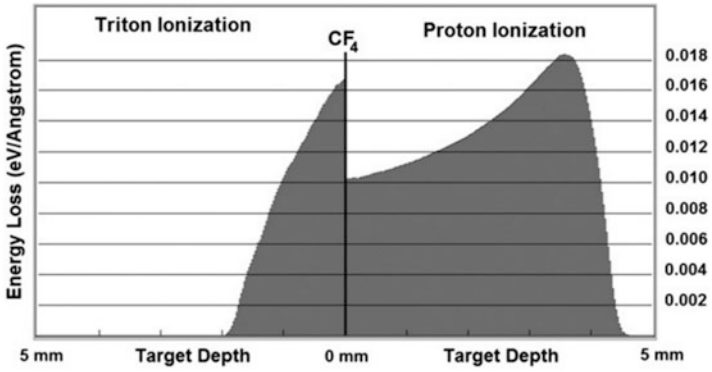

Fig. 3.4 Ionization distribution for 573 keV protons and 191 keV tritons as a function of distance traveled from the conversion site in 1 atm of CF_4 [3]

Because the proton carries three times as much kinetic energy as the triton, its range is generally larger. The resulting charge distribution is neither uniformly distributed nor centered about the interaction location. The centroid of the charge distribution is skewed closer to the proton endpoint, displaced from the interaction by about 0.4 times the proton range R_p [4]. To the extent that protons (and tritons) are emitted isotropically, the overall distribution of charge centroids for many detection events is about $0.8R_p$. Figure 3.4 is a plot of energy loss of the proton and the triton in 1 atm of CF_4. The ranges are determined by the endpoints in the energy-loss curves, roughly 4.5 mm for the proton and 2 mm for the triton. This is consistent with the values seen in Fig. 3.3 for CF_4.

Scattering collisions resulting in electron excitation are problematic for gas detectors. Visible and ultraviolet photons emitted during de-excitation can be absorbed in the detector (either in the gas or the detector wall) at points far removed from the original neutron interaction location, generating secondary electron emission that could falsely be recorded as a neutron event. To prevent this problem,

so-called *quench gases* are added to absorb this unwanted photon emission. Quench gases must be able to absorb the radiant energy and then undergo nonradiative (e.g., rotational, vibrational) de-excitations. Therefore, monatomic gas atoms are not suitable: a quench gas must be polyatomic to provide a mechanism for rotational or vibrational modes of de-excitation. Polyatomic stopping gases can however also act as quench gases (e.g., CO_2, C_3H_8, CF_4, CH_4, and C_2H_6). If a noble gas such as argon or xenon is used as the stopping gas, then a polyatomic gas must be added for photon quenching.

Strongly electronegative gases are detrimental to detector performance. *Electronegative gases* are gases that are likely to capture free electrons. Examples include oxygen, fluorine, chlorine, and water vapor. Electronegative gases within the detector gas volume act to decrease the signal charge amplitude, possibly degrading the signal-to-noise and spatial resolution. Therefore, electronegative gases are generally avoided as much as possible. Some detector manufacturers provide active filtering to remove electronegative gas species from the detection gas volume.

Selection of stopping and quench gases plays a role in the gamma sensitivity of ^{3}He neutron detectors. Gamma rays interact with matter via three main mechanisms: the photoelectric effect (PE), Compton scattering, or pair-production (PP). PP dominates at the highest gamma energies ($E_\gamma > 1.022$ MeV), the PE dominates in the lower energy regime. Both have a strong dependence on atomic number Z (PP is proportional to Z^2; PE is proportional to Z^n, with $4 < n < 5$). Figure 3.5 shows a graph of the cross section for gamma absorption for various gases commonly used in

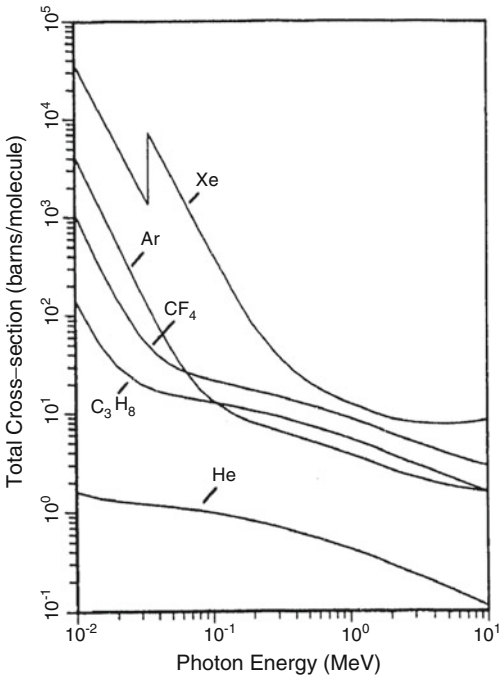

Fig. 3.5 Gamma-ray cross sections for materials commonly used in gas-proportional detectors [5]

gas detectors. The general trend of cross-section dependence on atomic number is apparent from the graph.

With the addition of different gases (stopping and quench) of typically lower W value, the resultant average energy per electron–ion pair also decreases, and therefore the number of electron–ion pairs generated by the overall process increases. Most of the ^{3}He gas detectors in use at SNS and HFIR have an ionization charge of about 4–5 fC. Considering the electron charge of 1.6×10^{-19} C, this corresponds to about 25,000–30,000 electron–ion pairs per neutron event.

Neutron capture efficiency is defined as the fraction of neutrons incident on a detector that undergo a nuclear conversion reaction. The most common expression for efficiency is derived from the Lambert law for beam attenuation in matter, given in Eq. (3.2):

$$I(x) = I_0 \exp\{-\mu x\} \tag{3.2}$$

Here, $I(x)$ is the transmitted beam intensity, I_0 is the incident beam intensity, μ is the linear attenuation coefficient (a material property of the absorbing medium), and x is the depth into the absorber where $I(x)$ is to be evaluated. Strictly speaking, this expression only applies for a narrow beam at normal incidence into a material of uniform attenuation coefficient. Because $I(x)$ is the transmitted intensity, it follows that $I_0 - I(x)$ is the absorbed intensity. Thus, the expression for beam absorption as a function of depth x is given by Eq. (3.3):

$$A = I_0 - I(x) = I_0 - I_0 \exp\{-\mu x\} = I_0(1 - \exp\{-\mu x\}) \tag{3.3}$$

Replacing x with the neutron conversion layer depth d gives the overall capture efficiency of a planar detector. Expressed as a fraction of incident beam intensity I_0, Eq. (3.3) becomes

$$Eff = \frac{I_0 - I(d)}{I_0} = 1 - \exp\{-\mu d\} \tag{3.4}$$

The absorption cross section σ from Chap. 2 is contained within the linear attenuation coefficient μ, along with the number density n of absorbing atoms. Recalling that σ is wavelength-dependent, Eq. (3.4) can be written as

$$Eff = 1 - \exp\{-n\sigma(\lambda)d\} \tag{3.5}$$

Applying dimensional analysis to the argument in the exponential confirms that n (cm^{-3}) × σ (cm^2) × d (cm) is dimensionless, as it must be.

Figure 3.6 is a plot of the neutron capture efficiency of a 1 cm thick planar gas detector containing 10 atm of ^{3}He. In this case, n is evaluated by multiplying the number density of atoms in a gas (2.69×10^{19} atoms/[cm^3·atm]) by 10 atm gas pressure to give 2.69×10^{20} atoms/cm^3. Neutron absorption in the detector window has been neglected.

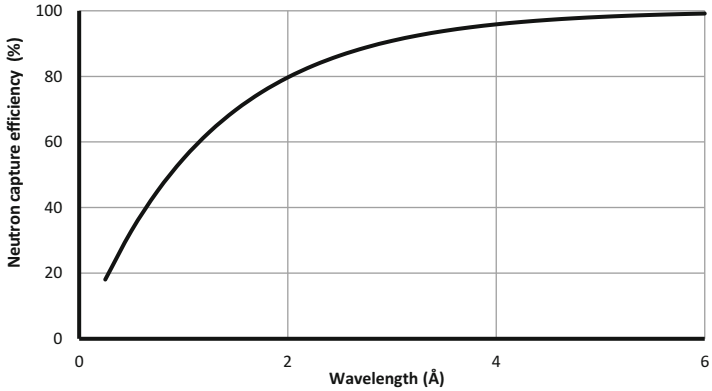

Fig. 3.6 Plot of neutron capture efficiency for a 1 cm thick gas detector containing 10 atm of ^{3}He. The capture efficiency is a function of the neutron wavelength

3.1.2 Ionization Mode vs. Proportional Mode

The previous section describes the formation of electron–ion pairs resulting from neutron capture in ^{3}He gas. No net electrical signal can be induced because the charges are created in essentially equal numbers. If there were no externally applied electric field to separate the positive and negative charges, then electron–ion recombination would occur, and the ^{3}He gas would return to its previous state. This process corresponds to the recombination region shown in the far left of Fig. 3.7.

Constructing a functioning detector requires creating an electric field within the gas volume to separate the positive and negative charge and employing some form of readout electrode or electrodes to collect the induced signal charge. Either planar or coaxial configurations can be used, and the resulting electric field is a function of the specific geometry and the strength of the applied potential.

Regardless of geometry, if the electric field strength is just sufficient to separate the initial electron–ion pairs, then the charge collected would be that of the primary ionization. This operating mode is in the ionization chamber region (the second region from the left in Fig. 3.7). Although the signal charge is rather small (typically ~ 4–5 fC), practical neutron detectors have been constructed which operate exceptionally well in ionization mode [7, 8].

In the proportional region (the center region in Fig. 3.7), the electric field strength is increased to the point at which additional ionizing collisions occur, resulting in a signal charge greater than, and proportional to, that of the primary ionization. Proportional mode is the operating regime of all ^{3}He gas-based neutron detectors at SNS and HFIR; therefore, it will be the focus of the remainder of this chapter.

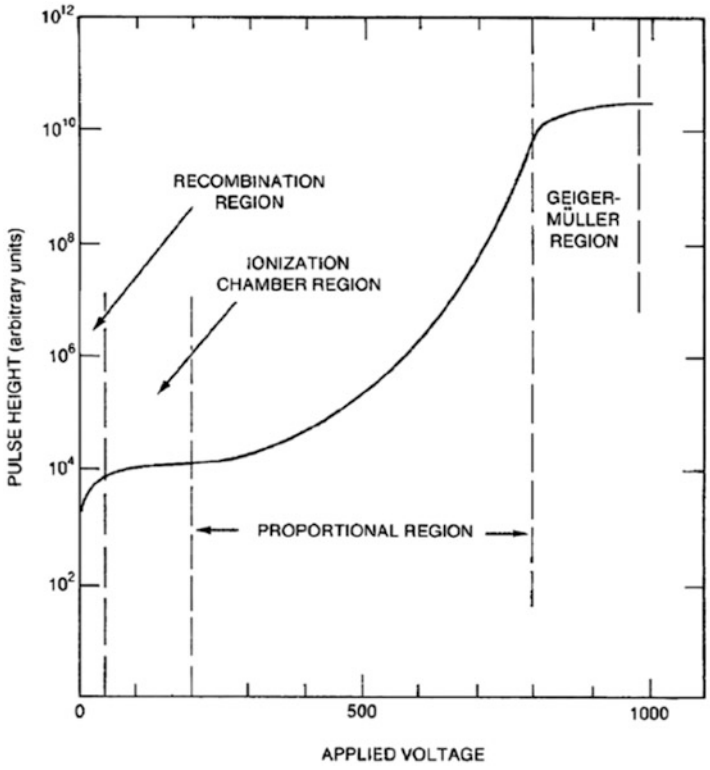

Fig. 3.7 Regions of operation for gas detectors [6]

3.1.3 Gas-Proportional Detectors

In ionization mode, an electric field is applied across the gas volume to separate the electrons from the ions in the primary ionization cloud. The signal charge is equal to that of the primary ionization.

In proportional mode, the electric field is increased to a level at which the primary ionization charges attain sufficient kinetic energy between scattering collisions to further ionize additional gas atoms as they drift toward the biased electrodes. This has the effect of increasing the signal charge beyond that of the primary ionization. This process is referred to as *impact ionization*, or *gas multiplication*. *Proportional mode* refers to the regime in which the multiplication charge remains proportional to the primary ionization charge.

Proportional detectors can have either planar or cylindrical geometry. In planar geometry, the electrodes form a parallel plate configuration, with constant electric field $E = V/d$ between the two electrodes, where V is the applied voltage, and d is the distance between electrodes. The typical configuration for cylindrical geometry is

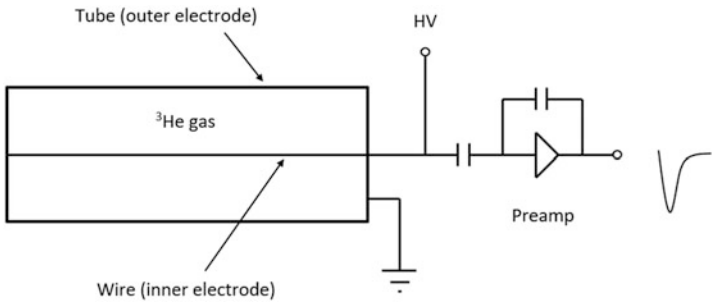

Fig. 3.8 Diagram of typical cylindrical gas-proportional tube

shown in Fig. 3.8. A cylindrical tube forms the outer electrode, and a coaxial wire along the tube center is the inner electrode.

The electric field in cylindrical (coaxial) geometry takes the form

$$E(r) = \frac{V}{r} \ln\left(\frac{b}{a}\right) \tag{3.6}$$

where V is the applied voltage across the electrodes, r is the radial distance from the center of the tube, and b and a are the distances to the outer and inner electrode surfaces, respectively. Specifically, b is the radial distance to the inside surface of the tube, and a is the radius of the wire.

The voltage to produce a given electric field is significantly higher for planar geometry than for cylindrical geometry. To give a realistic example for cylindrical geometry, let voltage $V = 1800$ V, $b = 1.25$ cm, and $a = 100$ μm. The electric field (plotted in Fig. 3.9) has a value just over 37,000 V/cm at the surface of the wire. To achieve the same field in a 2.5 cm thick (to give an equivalent gas depth) planar detector would require detector operation around 92,000 V, quite an unreasonable specification for a practical detector. For this reason, proportional detectors most often use cylindrical geometry.

Either the wire or the tube wall (or both) can be biased, but in practice, high voltage is usually applied to the central wire only while the tube wall is held at ground potential. The detectors at SNS and HFIR have this configuration, which is illustrated in Fig. 3.8. Electrons are much easier to accelerate than positive ions because of their smaller mass (proton-to-electron mass ratio is ~1836); therefore, most proportional detectors are designed to have the electrons drift into the higher electric field regions (i.e., toward the tube center). This design requires the central (anode) wire to be at positive high voltage.

The process of gas multiplication is illustrated in Fig. 3.10. A single electron drifting through a high electric field attains sufficient kinetic energy to ionize a neutral gas atom, resulting in a positively charged ion and two free electrons. The process repeats, yielding a final signal charge much larger than the initial ionization

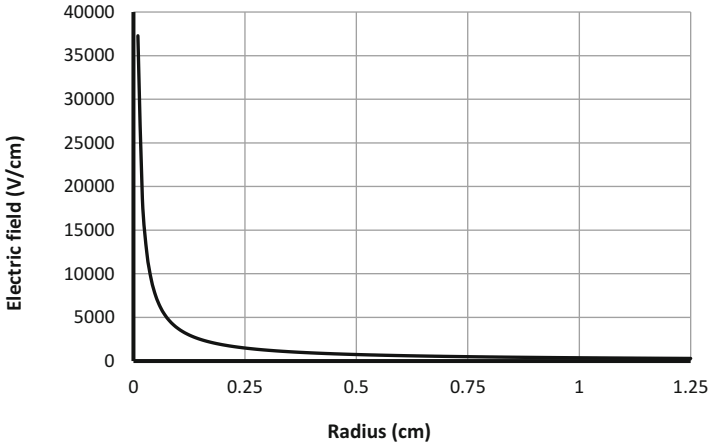

Fig. 3.9 Plot of electric field from Eq. (3.6), using the realistic example of $V = 1800$ V, $b = 1.25$ cm, and $a = 0.01$ cm. The $1/r$ dependence from Eq. (3.6) is clearly shown

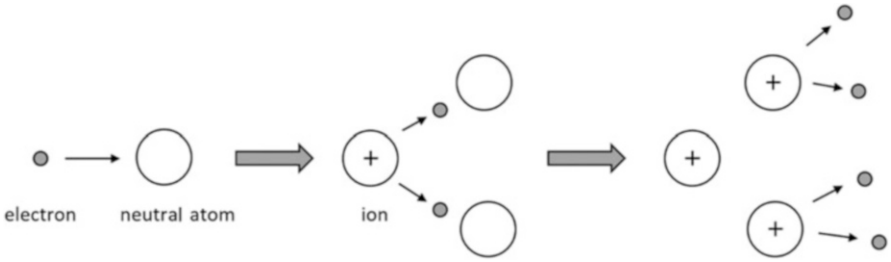

Fig. 3.10 Illustration of the process of charge multiplication in a gas. (*left*) A single electron impacts a neutral gas atom with sufficient energy to ionize it. (*center*) Both electrons (the original and the newly emitted one) are now available to ionize additional neutral gas atoms. (*right*) This process continues as long as the electric field is large enough to support impact ionization

charge. Gas multiplication factors on the order of 200-300 are common for the LPSDs.

The following presents a derivation for gas gain in coaxial geometry [9].

For electric fields above a critical value E_c (corresponding to critical radius r_c), electrons gain enough kinetic energy between scattering collisions to ionize additional gas atoms upon impact.

The fractional increase in the number of electrons created dn/n per unit path length dr is given by

$$\frac{dn}{n} = \alpha(r)dr \tag{3.7}$$

where $\alpha(r)$ is the first Townsend coefficient (number of electron–ion pairs created per unit length).

Integrating Eq. (3.7) from the anode wire radius a to the critical radius r_c (where the electric field no longer supports gas multiplication) yields Eq. (3.8):

$$\int \frac{dn}{n} = \ln\left|\frac{n}{n_0}\right| = \int_a^{r_c} \alpha(r)dr \tag{3.8}$$

where n_0 is the initial ionization charge, and n/n_0 is the gas multiplication factor, or gas gain M.

Because $(\partial r/\partial E) = [V/\ln|b/a|]\,(-1/E^2)$, changing the variable of integration from radius r to electric field E and using Eq. (3.6) for $E(r)$ gives Eq. (3.9):

$$\ln\left|\frac{n}{n_0}\right| = \ln|M| = \int \alpha(E)[\partial r/\partial E]dE = \frac{V}{\ln\left|\frac{b}{a}\right|}\int_{E(a)}^{E(r_c)} -\frac{\alpha(E)}{E^2}dE \tag{3.9}$$

The critical electric field where gas multiplication begins is given by Eq. (3.10):

$$E(r_c) = \frac{V}{r_c\ \ln\left|\frac{b}{a}\right|} \tag{3.10}$$

The electric field at the surface of the wire is given by Eq. (3.11):

$$E(a) = \frac{V}{a\ \ln\left|\frac{b}{a}\right|} \tag{3.11}$$

Removing the negative sign by changing the order of integration limits yields Eq. (3.12):

$$\ln|M| = \frac{V}{\ln\left|\frac{b}{a}\right|}\int_{E(r_c)}^{E(a)} \frac{\alpha(E)}{E^2}dE \tag{3.12}$$

At this point, the explicit form of $\alpha(E)$ must be determined as function of E.

If one assumes a linear proportionality $\alpha(E) = kE$ (first derived by Diethorn 1956 [10]) gives Eq. (3.13):

$$\ln|M| = \frac{Vk}{\ln\left|\frac{b}{a}\right|}\ln\left|\frac{E(a)}{E(r_c)}\right| \tag{3.13}$$

In this expression, $k = \ln 2/\Delta V$, where ΔV is the change in potential between two ionizing events.

Substituting Eqs. (3.10) and (3.11) into Eq. (3.13) gives Eq. (3.14):

$$\ln|M| = \frac{Vk}{\ln\left|\frac{b}{a}\right|}\ln\left|\frac{r_c}{a}\right| \tag{3.14}$$

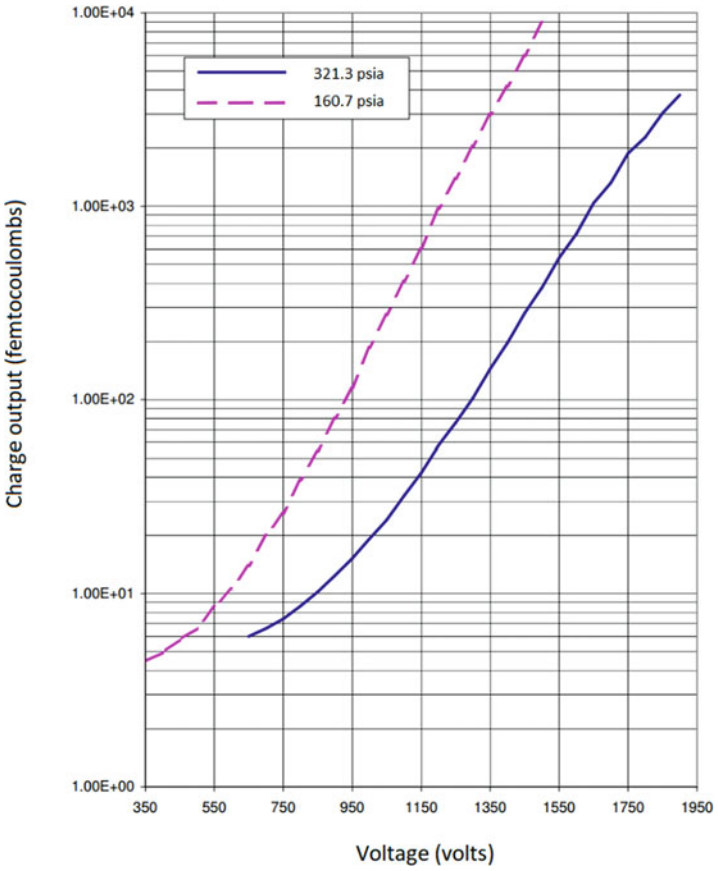

Fig. 3.11 Gas gain for two otherwise identical ^{3}He gas-proportional tubes at different gas pressures (The pressure corresponding to the dashed curve is 160.7 psia, and the pressure for the solid curve is 321.3 psia [11])

Solving for M gives Eq. (3.15):

$$M = \exp\left\{\frac{Vk}{\ln\left|\frac{b}{a}\right|}\ln\left|\frac{r_c}{a}\right|\right\} \tag{3.15}$$

Equation (3.15) suggests that gas gain M increases approximately exponentially with applied voltage. It is a function of the number of ionizing collisions and thus mean free path. Therefore, proportional tubes at higher gas pressures would be expected to require higher voltages to achieve a given gas gain, and this is found to be the case. Figure 3.11 is a plot of the gas gain for two tubes with the same dimensions and gas composition but at two different gas pressures. The gas pressure for the tube

represented by the solid curve is twice that for the tube represented by the dashed curve. A higher voltage is required for the higher-pressure tube to achieve the same charge output as the lower pressure tube.

From the Shockley–Ramo theorem [12, 13], the induced charge and induced current on a conductor (e.g., anode wire) owing to a charge carrier can be determined by postulating a weighting potential V_{W} and weighting field $\boldsymbol{E}_{\mathbf{W}}$ based on the following three criteria. (1) The charge carrier is assumed to be absent. (2) The potential on the conductor of interest is defined to be 1. (3) The potential on all other conductors is zero. The induced charge q_{ind} is a product of the actual charge of the charge carrier and the value of the weighting potential at the location of the charge carrier. The induced current i_{ind} is the product of the actual charge of the charge carrier, and the inner (or dot) product of the vector velocity of the charge carrier and the vector value of the weighting field at the charge carrier location. The expressions for induced charge and induced current are given by Eqs. (3.16) and (3.17), respectively.

$$q_{\mathrm{ind}} = qV_{\mathrm{W}} \tag{3.16}$$

$$i_{\mathrm{ind}} = q\boldsymbol{v} \cdot \boldsymbol{E}_{\mathbf{W}} \tag{3.17}$$

The weighting potential in cylindrical geometry is given by Eq. (3.18) [14]:

$$V_{\mathrm{W}}(r) = \frac{\ln\left|\frac{r}{r_2}\right|}{\ln\left|\frac{r_1}{r_2}\right|} \tag{3.18}$$

where r is once again the radial distance from the tube center, r_1 is the inner electrode radius (previously a), and r_2 the outer electrode radius (previously b).

Weighting potential $V_{\mathrm{W}}(r)$ is plotted in Fig. 3.12 for various values of the expression $(r - r_1)/(r_2 - r_1)$, which ranges from the anode wire radius r_1 (0 in the plot) to the tube radius r_2 (1 in the plot).

Inspecting Fig. 3.12 reveals that the weighting potential is largest at $r = r_1$, thus most of the induced signal charge results from charges moving very near the surface of the anode wire.

Neutron pulses from cylindrical ^{3}He gas proportional detectors can take on a variety of shapes. Figure 3.13 shows three representative examples of preamplifier output pulses, all from the same detector tube and the same operating conditions. In addition to the more familiar unipolar pulse shape (leftmost image in the figure), pulses can also have a two-lobed form (middle and right images), with the amplitude of the first lobe either greater or less than that of the second lobe. Leading edge risetimes can also vary somewhat between different pulses. It is conceivable, though entirely unsubstantiated, that these pulse shape variations reflect the difference in arrival times of the charge clouds due to the proton and triton, depending on the orientation of their trajectories relative to the anode wire.

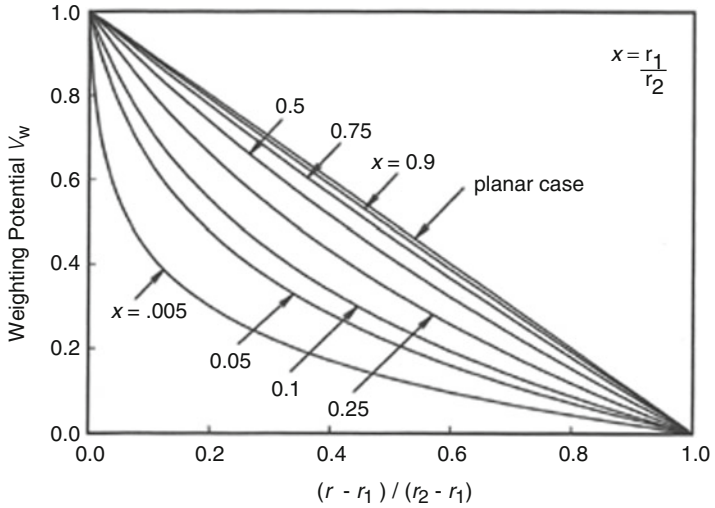

Fig. 3.12 Weighting potentials for various values of r_1/r_2 versus the normalized distance from r_1 to r_2 for a cylindrical detector [14]

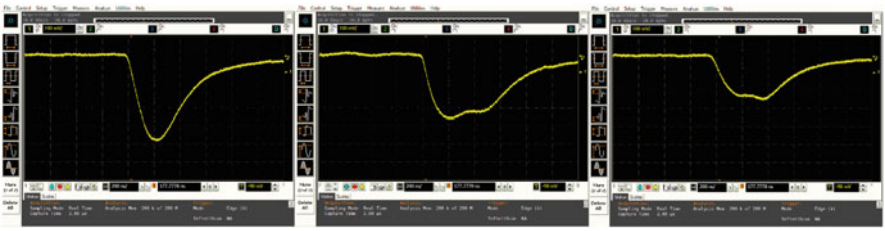

Fig. 3.13 Oscilloscope traces of typical neutron pulses from a ^{3}He proportional tube. The vertical scale is 100 mV per division and the horizontal scale is 200 ns per division for all

3.2 Linear Position–Sensitive Detectors

3.2.1 General Description

3.2.1.1 Introduction

A LPSD is a gas-filled tube with a resistive central wire stretched along its axis. It is biased to operate in proportional mode—the charge introduced to the gas by radiation absorption causes a several-fold larger charge pulse to travel from the tube wall to the central wire. The charge in the pulse is measured at both sides of the wire. Because of the resistance of the wire, the charge fraction that appears at each end varies depending on the position along the wire where the charge deposition occurs.

A detector's sensitivity to neutrons requires introduction of an isotope that can absorb a neutron (n) and then emit energetic charged particles. The most common choice is ^{3}He, which undergoes the reaction n + ^{3}He → ^{3}H + p + 0.764 MeV. Helium-3 can exist in the detector as the primary component of the fill gas. An alternative is ^{10}B, which could be introduced as a gas such as BF_3 or as a thin film of boron inside the detector.

The detector tube operates with the central wire positively charged with respect to the tube wall. The energetic charged particles emitted by the neutron absorption are emitted in opposite directions, creating ionization trails in the detector gas. The released electrons are attracted to the central wire, and the ions are attracted to the tube wall. The electrons gain energy from the electric field between collisions with the detector gas, and, for a high enough field, this energy is enough to cause additional ionization of the detector gas. The electric field increases near the central wire, and it eventually becomes high enough for this additional ionization to occur, creating a region of charge multiplication near the wire, which increases the number of electrons reaching the wire by some factor. Positive ions are left behind, and they drift to the tube wall at a slower rate. These reactions are illustrated in Fig. 3.14.

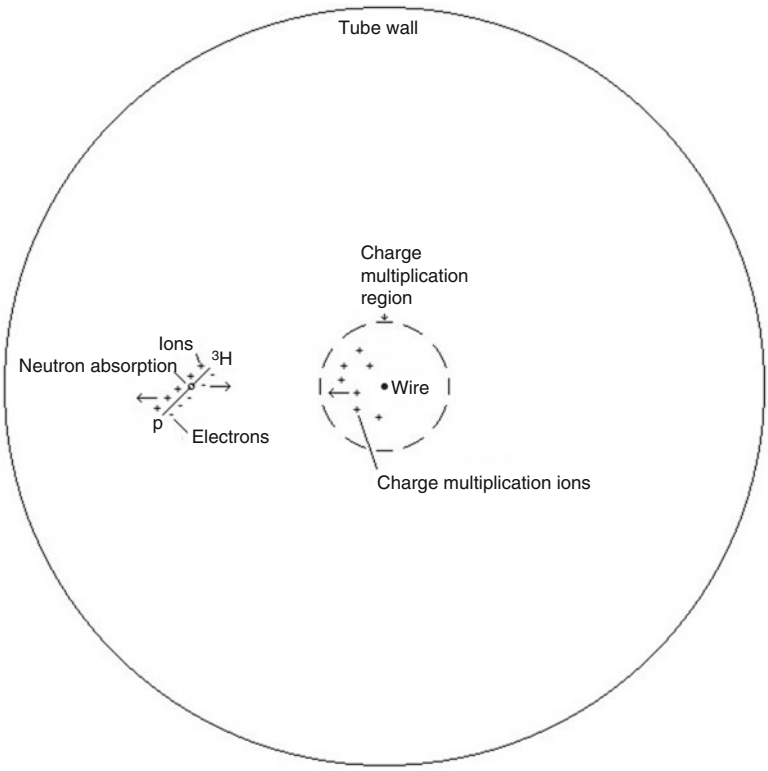

Fig. 3.14 Events associated with neutron detection

There is a space charge from the positive ions, which limits the extent to which the electrons deposited on the wire can exit along the wire. As discussed in Sect. 3.1.2, this effect is strongest when the ions are near the wire, and it diminishes as the ions drift away from the wire. The ions influence the rate at which the charge from an event is released along the wire, but most of the charge will be released before the ions drift all the way to the tube wall.

3.2.1.2 Detector Tube Construction

Because of the detector tube's cylindrical geometry, the electric field inside the tube is inversely proportional to the distance from the center of the central wire. The rate of secondary ionization is highly sensitive to the electric field strength. Therefore, secondary ionization primarily occurs near the central wire. For a given bias, a small-diameter wire has a higher electric field at its surface than a large-diameter wire. This higher electric field allows for a higher amount of charge multiplication, which allows the small-diameter wire to achieve a desired rate of charge multiplication at a smaller bias voltage. The smaller-diameter wire also has more margin between its operating point and the bias at which electrical breakdowns occur. For these reasons, a very small diameter is chosen for the central wire, typically approximately 50 μm.

Figure 3.15 shows some details of how an end of an LPSD tube is constructed. A central electrode passes through and is sealed to a surrounding length of insulating material, which is typically alumina. Near the center of this insulator's length, its outer surface is sealed to some form of metallic ring, upon which the feedthrough is mounted. Because this feedthrough must hold off high voltages, the insulator extends beyond the outer mounting ring on both sides by approximately a centimeter, typically. The feedthrough is mounted to a machined metallic mounting piece, which also connects to the tube that forms the detector's outer wall. Typically, the tube forming the outer wall is welded to the mounting piece. In many cases, this mounting piece includes additional features to create attachment points between the detector tube and the detector module.

A metallic shielding tube is attached to the feedthrough electrode on the end that is inside the detector. One end of a tiny coil spring inside the shielding tube is attached to the shielding tube and suspended near the center line. The other end is attached to the center wire that runs along the length of the detector tube. The spring

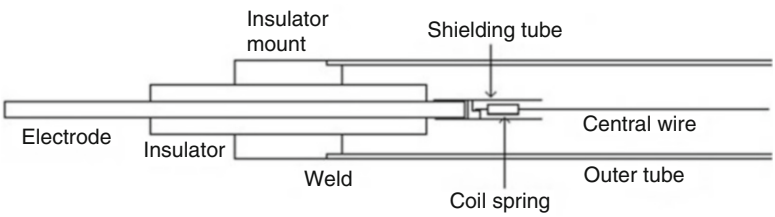

Fig. 3.15 Structure of an LPSD tube

maintains the tension on the central wire. The shielding tube is also used to create a well-defined distance, along which the central wire is exposed to the full biasing electric field of the detector. At this distance, the wire becomes active for neutron detection.

At least one of the central electrodes of the feedthroughs is a tube, which creates a passage for evacuating the detector tube and backfilling it with the detector gas. After the filling is complete, this tube is pinched off to create a seal.

Aluminum and stainless steel are the most common material choices for the tube that forms the detector's outer wall. The choice of aluminum is motivated by its low tendency to absorb or scatter neutrons. Aluminum tubes bend under modest loads. They can easily be strained beyond their elastic limit, beyond which the bend does not spring back. Aluminum also tends to form a poorly conductive surface layer, which can hinder achieving solid ground connections. Stainless steel tubes have a greater resistance to bending than aluminum tubes. Stainless steel's threshold for inelastic bending is also much higher that aluminum's, so most deflections that occur tend to spring back. Stainless steel is less likely than aluminum to form a resistive surface layer. It absorbs neutrons somewhat more strongly than aluminum. Stainless steel's better mechanical properties allow tubes to be built with a thinner wall than is needed for aluminum, thereby compensating for the higher absorption.

The fill gas pressure is often dictated by the range of neutron wavelengths the detector must manage. Helium-3 has a 5330 barn neutron absorption cross section for thermal neutrons. It is a $1/v$ absorber, which makes its cross section proportional to the wavelength. Thermal neutrons have a 1.8 Å average wavelength, so the cross section for wavelength λ is $\sigma = \lambda\sigma_0$, where $\sigma_0 = 5330$ barn/1.8 Å $= 2.961 \times 10^{-24}$ cm^2/Å. A neutron beam of intensity I and wavelength λ traveling through a region with ^{3}He atom density N will have a loss of intensity over a travel distance dL of $dI = -\sigma_0\lambda N dL$. After traversing a total distance L, a beam of original intensity I_0 will have intensity $I = I_0\exp\{-\sigma\lambda NL\}$. The fraction of the beam that is absorbed into the gas, causing potentially detectable reactions, is given by Eq. (3.19).

$$f = \frac{I_0 - I}{I_0} = 1 - \exp\{-\sigma_0\lambda NL\} \tag{3.19}$$

The value of f decreases as $\sigma_0\lambda NL$ increases, with $f = 0.63$ for $\sigma_0\lambda NL = 1$. If that is taken as the minimum acceptable efficiency, the efficiency is acceptable for all $\lambda > 1/(\sigma_0 NL)$. The maximum value of L is the inner diameter of the detector tube—even less for neutrons that enter the tube offset from the central axis. The value of N is proportional to the gas pressure given by the gas law $N = P/(k_B T)$, where P is the ^{3}He partial pressure, T is the temperature, and k_B is the Boltzmann constant (1.38×10^{-23} J/K). Typically, the chosen fill gas pressure is a few atmospheres. The mean free path for electrons in the gas decreases as the pressure increases, which increases the bias voltage required to obtain a desired gas gain.

If a neutron that has a high wavelength (compared with the wavelength at which the efficiency drops off) enters the detector, then that neutron is likely to interact very soon after it enters the detector. A neutron whose wavelength is comparable to the

drop off wavelength is likely to penetrate more deeply. This effect may result in some wavelength dependence on the amount of charge collected. If the neutron's trajectory is not perpendicular to the tube, the penetration depth may also influence the position determination.

3.2.1.3 Pulse-Height Spectrum

Figure 3.16 is a pulse-height spectrum from a ^{3}He-filled LPSD. The horizontal axis is the amount of charge collected from the central wire of the LPSD owing to a detection event. The charge range for which the detector is configured is divided into 1024 bins. The vertical axis is the number of events that are detected in each bin during an acquisition. For the acquisition in Fig. 3.16, the maximum charge observed in the pulse height spectrum is approximately 1 pC. This maximum charge is sensitive to the bias, gas pressure, and geometry of an LPSD tube. Under conditions in which the detector works well, it is often in the 1–2 pC range. The nuclear reaction by which a neutron is detected always occurs with the same energy, independent of the neutron wavelength. The pulse-height spectrum reveals a considerable variation in the amount of charge collected from such events. In the 0.8–1.0 pC region in the figure, the intensity drops off to zero moderately rapidly after the primary peak.

In the 0.2–0.8 pC region, a more gradual intensity drop-off occurs before the central peak. Two secondary peaks appear in this region. These secondary peaks are caused by the wall effect, in which one of the charged particles emitted from the

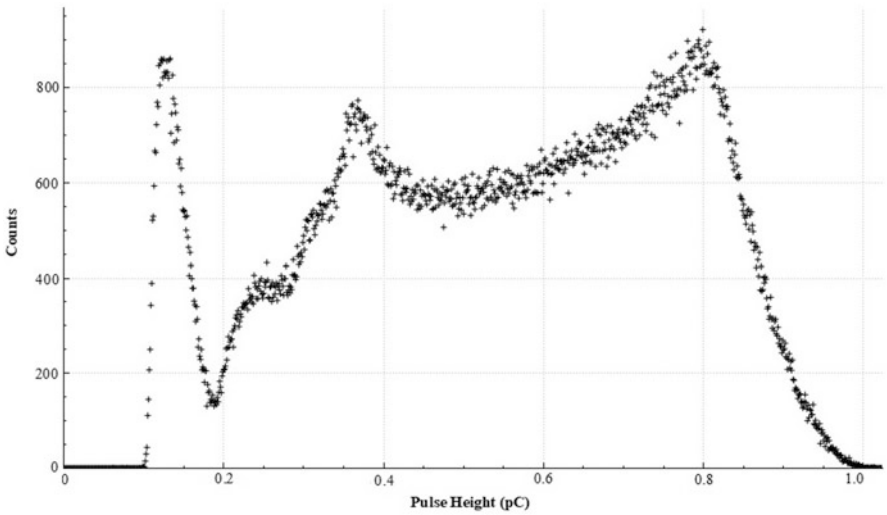

Fig. 3.16 Pulse-height spectrum. The horizontal axis is the charge collected during a detection event. The charge range for which the detector is configured is divided into 1024 bins. The vertical axis is the number of events detected within each bin

reaction strikes the tube wall and is absorbed before its kinetic energy is fully used to ionize the gas. The gradual drop-off is partly caused by the tube geometry. An event near the tube wall is in a region where the electric field is low, the ion drift distance is low, and the electron drift distance is high. An event near the wire is in a region where the electric field is high, the ion drift distance is high, and the electron drift distance is low. These differences because of the position of an event can influence the probability that electrons and ions will recombine before being collected. They might influence the amount of charge multiplication that occurs. They will influence the drift time required for the ions to reach the tube wall and for the electrons to reach the tube wire. In some cases, the drift time may exceed the integration time for the detector pulse. This excess time can cause pulse height spectrums obtained using short integration times to have less clearly defined peaks than pulse-height spectrums obtained with long integration times. The spectrum in Fig. 3.16 used a short 750 ns integration time, chosen to optimize other aspects of detector performance.

In the 0.12–0.20 pC region, the intensity increases. Gamma ray detections occur in this region. The lack of counts in the 0.0–0.1 pC region is an artifact of the discriminator settings. Otherwise, gamma rays and electronic noise would also appear in this region. The energy released from the nuclear reaction is high enough that the charge released from a neutron absorption is considerably higher than the charge released from a gamma ray interaction with the detector. Therefore, it is straightforward to establish discriminator settings that strongly reject gamma ray events while still accepting most of the neutron events. A small portion of the pulse-height spectrum from neutrons does extend into the region where gamma ray rejection is required, so a few percent of neutrons that have a reaction in the tube will still be rejected.

The charge multiplication in the detector tube is sensitive to the bias voltage. Typically, the range of the pulse-height spectrum doubles after a 100 V increase in the bias voltage. Both gamma ray– and neutron-sensitive fractions of the pulse-height spectrum range tend to increase when a higher bias voltage is used.

3.2.1.4 Count-Rate Effects

Count-rate limitations for LPSDs can be difficult to characterize because the performance does not decline abruptly. A dead time of approximately a microsecond occurs while the charge from an event is being integrated. High rates increase the probability that the charge from a second event will arrive while the charge from the first event is being integrated, resulting in an incorrect position determination. A small amount of the charge from an event arrives after the end of the integration interval. If a second event is integrated while this residual charge is arriving, then the position determination is skewed. The increased levels of ionization in the tube at high rates can reduce the amount of charge multiplication. The decreased amount of charge collected degrades the position resolution and increases the fraction of events that are vetoed. These effects are of minimal importance at rates of 10,000 counts per second, but these effects increase gradually at higher rates.

3.2.1.5 Circuitry for Position Determination

First, the charge-division principle for determining the position of a neutron detection along a detector tube is derived for an idealized case that ignores error sources. Figure 3.17 shows a simplified diagram of the circuitry used for position determination. Here, the detector tube is assumed to have a central wire of resistance R and length L. At some time t after a detection event, a current I_0 is deposited on the wire at a distance D from side one. The portion of the wire on side one from the deposition location has resistance $R_1 = RD/L$, whereas the portion on side 2 has resistance $R_2 = R(L - D)/L$. A current-to-voltage amplifier that—in the ideal case—maintains its negative input at ground potential is located on each side of the tube. Therefore, the current I_0 conducts to ground through resistances R_1 and R_2 in parallel, raising the voltage at the deposition location by $V_0 = (I_0R_1R_2)/(R_1 + R_2)$. Therefore, currents

$$I_1 = \frac{I_0R_2}{R_1 + R_2} = \frac{I_0(L-D)}{L} \tag{3.20}$$

and

$$I_2 = \frac{I_0R_1}{R_1 + R_2} = \frac{I_0D}{L} \tag{3.21}$$

go to the amplifiers, creating voltages

$$V_{A1} = \frac{I_0R_{f1}(L-D)}{L} \tag{3.22}$$

and

$$V_{A2} = \frac{I_0R_{f2}D}{L} \tag{3.23}$$

at their outputs. These voltages go to integrators, which have time constants τ_1 and τ_2 such that $(dV_{I1}/dt) = (V_{A1}/\tau_1)$ and $(dV_{I2}/dt) = (V_{A2}/\tau_2)$. If the total charge Q from the detection event is assumed to be delivered between times $t = 0$ and $t = t_m$, $Q = \int_0^{t_m} I_0 dt$. If $V_{I1} = V_{I2} = 0$ at $t = 0$, then at $t = t_m$,

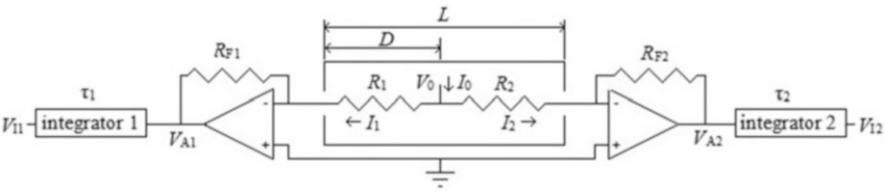

Fig. 3.17 Simplified diagram of position-measuring circuit

$$V_{I1} = \frac{R_{f1}(L-D)}{\tau_1 L}\int_0^{t_m} I_0 dt = \frac{R_{f1}(L-D)Q}{\tau_1 L} \tag{3.24}$$

and

$$V_{I2} = \frac{R_{f2}D}{\tau_2 L}\int_0^{t_m} I_0 dt = \frac{R_{f2}DQ}{\tau_2 L} \tag{3.25}$$

For matched gains where $(R_{f1}/\tau_1) = (R_{f2}/\tau_2)$,

$$D = \frac{LV_{I2}}{V_{I1} + V_{I2}} \tag{3.26}$$

and

$$Q = \frac{\tau_1(V_{I1} + V_{I2})}{R_{f1}} \tag{3.27}$$

A complete circuit for handling LPSD detection events must handle many details not included in the simplified diagram of Fig. 3.17. A more complete but still simplified diagram is shown in Figs. 3.18 and 3.19. These figures are based on a design used for LPSDs at SNS. Figure 3.18 has circuits for the preamplifier boards, along with their connection to the detector tube. These amplify the weak high-impedance signal from the detector tube to a larger, low-impedance signal. These boards are mounted to the detector within shielded enclosures with short, shielded connections to the tube ends. The preamplifier output is transmitted as a low-voltage differential signal (LVDS) over a cable to the rest of the signal processing circuits located on a board called the readout circuit (ROC). These circuits are diagrammed in Fig. 3.19.

One feature shown in Fig. 3.18 is the means for applying bias to the detector wire. Components R_{fill1}, C_{F1}, R_{fill2}, and C_{F2} form a pair of cascaded low pass filters, which are intended to reduce ripple in the voltage V_{bias} coming from the high-voltage power supply. The ripple can be a significant source of noise introduced to the detector. R_B is the resistor that restores the charge lost from the wire when a detection event occurs. These features are only needed for one side of the wire. Both sides need the capacitors C_{S1} and C_{S2}, which block the steady bias voltage on the tube wire while passing the rapid fluctuations caused by a detection event. Typical values used are $R_{\text{fil1}} = R_{\text{fil2}} = R_B = 2$ MΩ, $C_{F1} = C_{F2} = 8.5$ nF, and $C_{S1} = C_{S2} = 15$ nF.

Additional resistances, R_{P1} and R_{P2}, are often in the path from the detector wire to the current to voltage amplifier. These resistances are part of transient protection circuits for the amplifier with values in the 10–100 Ω range. The current pulses from neutron detections tend to have durations in the 500 ns to 1 μs range, so the impedance of capacitors C_{S1} and C_{S2} at 1 MHz should be a reasonable estimate of their influence on such pulses. At 15 nF, this influence is approximately10 Ω. A real-world current-to-voltage amplifier also exhibits some impedance between its

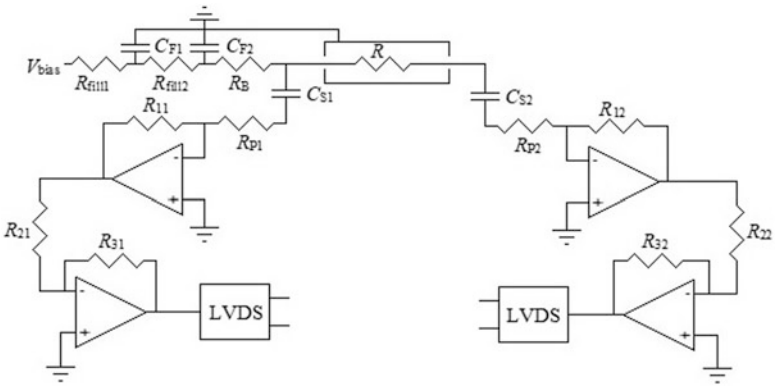

Fig. 3.18 Bias circuit for the detector wire and preamplifier stages

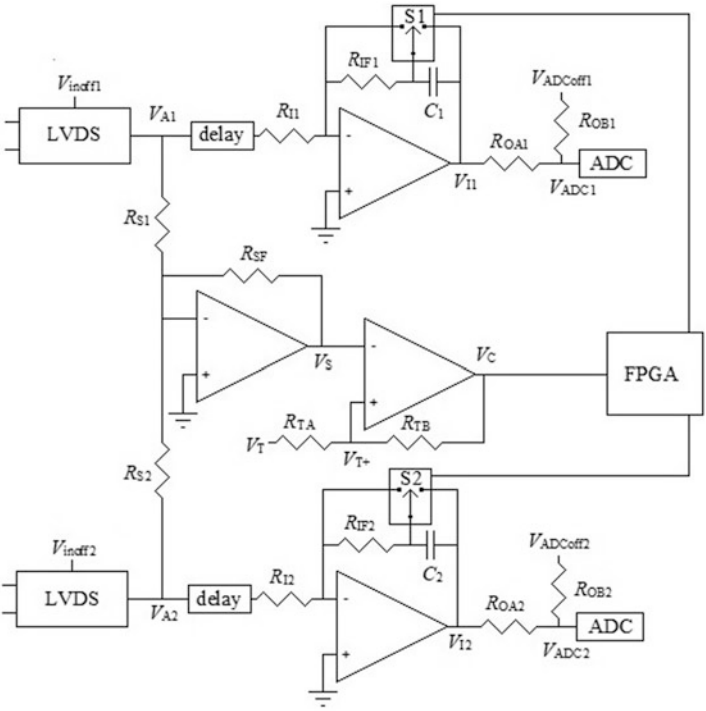

Fig. 3.19 ROC board components of position-measuring circuit

negative input and its ground. All these effects influence the charge-division position calculations, causing the calculated position along the wire to be displaced toward the tube center away from the actual position. Because uncertainties exist both in the magnitude of some of these impedances and in the mounting details of the detector

wire, correcting for this error empirically is best. Neutrons can be supplied to the detector at several known positions along the tube, and the ratio between the known and the calculated displacements can be used to determine a correction factor.

Figure 3.18 also has a more complete depiction of the preamplifier stages. Two stages of amplification are seen. These stages are followed by a conversion of the single-ended signal to LVDS for transmission to the next board. As far as gain is concerned, R_{F1} and R_{F2} in Fig. 3.17 actually mean $R_{F1} = (R_{11}R_{31}G_{L1})/R_{21}$ and $R_{F2} = (R_{12}R_{32}G_{L2})/R_{22}$. G_{L1} and G_{L2} are the gains associated with the conversion to LVDS. R_F should be high enough to use as much of the voltage range of the preamplifier second stage as possible without causing preamplifier saturation for the strongest pulses. The desired value can vary owing to detector characteristics and operating conditions, but common values of R_F are in the 70–150 kΩ range.

The ROC board signal processing in Fig. 3.19 begins with two convertors from LVDS to single-ended signals, one for each side of the tube. These convertors also have a provision for applying offset voltages V_{inoff1} and V_{inoff2} to compensate for any offset voltages that may be present in the preamplifier. The output of these convertors corresponds to the voltages V_{A1} and V_{A2} in Fig. 3.17. For these voltages to be integrated at the correct time, some form of discriminator circuit must exist to determine if an event is occurring. One scheme is to look for times when the current to the tube wire exceeds some threshold. Owing to the charge division, this scheme is equivalent to determining when $V_{A1} + V_{A2}$ exceeds some threshold. From Fig. 3.19, if $R_{S1} = R_{S2} = R_S$, then

$$V_S = R_{SF}\left(\frac{V_{A1}}{R_{S1}} + \frac{V_{A2}}{R_{S2}}\right) = \frac{R_{SF}}{R_S}(V_{A1} + V_{A2}) \tag{3.28}$$

The circuit after V_S is a comparator, for which $V_C = V_{CH}$ when it is saturated high, and $V_C = V_{CL}$ when it is saturated low. Initially, $V_C = V_{CH}$, yielding Eq. (3.29):

$$V_{T+} = V_T + (V_{CH} - V_T)\frac{R_{TA}}{R_{TA} + R_{TB}} = \frac{V_T R_{TB}}{R_{TA} + R_{TB}} + \frac{V_{CH} R_{TA}}{R_{TA} + R_{TB}} \tag{3.29}$$

When V_S is greater than V_{T+}, V_C decreases from V_{CH} to V_{CL}, causing V_{T+} to decrease to V_{T-}, as calculated using Eq. (3.30):

$$V_{T-} = \frac{V_T R_{TB}}{R_{TA} + R_{TB}} + \frac{V_{CL} R_{TA}}{R_{TA} + R_{TB}} \tag{3.30}$$

The change in V_T is given by Eq. (3.31):

$$V_{T+} - V_{T-} = (V_{CH} - V_{CL})\frac{R_{TA}}{R_{TA} + R_{TB}} \tag{3.31}$$

This decrease in V_{T+} creates a hysteresis, which reduces the chance that the comparator will fire multiple times on a single pulse. For typical values of $V_{CH} = 3.3$ V, $V_{CL} = 0$ V, $R_{TA} = 1000\ \Omega$, and $R_{TB} = 330$ KΩ, the hysteresis is 0.01 V.

By the time the comparator responds, a large portion of the pulse from the detector has already occurred. For the entire pulse to be integrated, its arrival to the integrator must be delayed. This delay is the purpose of the delay lines shown in Fig. 3.19. The delay time is set at 200 ns.

The integrators are gated by the complementary metal–oxide–semiconductor (CMOS) switches, which appear as components S1 and S2 in Fig. 3.19. When the integrators are off, the capacitors C_1 and C_2 are shorted to have zero charge, and resistors R_{IF1} and R_{IF2} provide feedback. Thus, the integrator behaves as an amplifier with gain less than 1. When the integrators are on, resistors R_{IF1} and R_{IF2} are shorted, and capacitors C_1 and C_2 provide feedback. The integrators integrate the delayed voltages V_{A1} and V_{A2} with time constants $\tau_1 = R_{I1}C_1$ and $\tau_2 = R_{I2}C_2$, generating outputs V_{I1} and V_{I2}, which correspond to the voltages of the same name in Fig. 3.17. The outputs are read by analog to digital convertors (ADCs), which cover a range from 0 V on the low end to a high end that ranges from 1 to 2 V depending on the configuration. The time constant should be chosen so that it is high enough for the integrated pulses to use most of the ADC range but not so high that the strongest integrated pulses exceed the ADC range. On the SNS ROC boards, $\tau = 2.2 \times 10^{-7}$ s is used.

When integrating with no signal, which is sometimes required for calibrations, noise can sometimes cause V_{I1} to be negative, which is outside of the ADC range, forcing the reading to be inaccurately reported or vetoed. In either case, the result is an inaccurate determination of the average value of V_{I1}. To avoid this issue, resistors R_{OA1} and R_{OB1} are added to provide a voltage offset, as shown in Eq. (3.32).

$$V_{\mathrm{ADC1}} = V_{I1} + (V_{\mathrm{ADCoff1}} - V_{I1})\frac{R_{OA1}}{R_{OA1} + R_{OB1}} = \frac{V_{I1}R_{OB1}}{R_{OA1} + R_{OB1}} + \frac{V_{\mathrm{ADCoff1}}R_{OA1}}{R_{OA1} + R_{OB1}} \tag{3.32}$$

For typical values of $R_{OA1} = 50\ \Omega$ and $R_{OB1} = 1000\ \Omega$, 95% of V_{I1} is passed to V_{ADC1}, and the offset is 5% of V_{ADCoff1}. The offset circuit for the second integrator works the same way.

A field-programmable gate array (FPGA) on the board handles all digital logic activities. It monitors the comparator output and times the gating of the integrators. The FPGA captures the ADC outputs at the desired times during the integration, and it loads values into digital to analog converters (DACs), which supply voltages such as V_{inoff1}, V_{inoff2}, V_{ADCoff1}, V_{ADCoff2}, and V_T. It controls communications with other components of the data acquisition system, and it can read the time from the last synchronizing trigger for a detected event. Depending on the acquisition mode, the FPGA either returns the raw ADC readings and time for an event, or it can calculate the position and return a position and time.

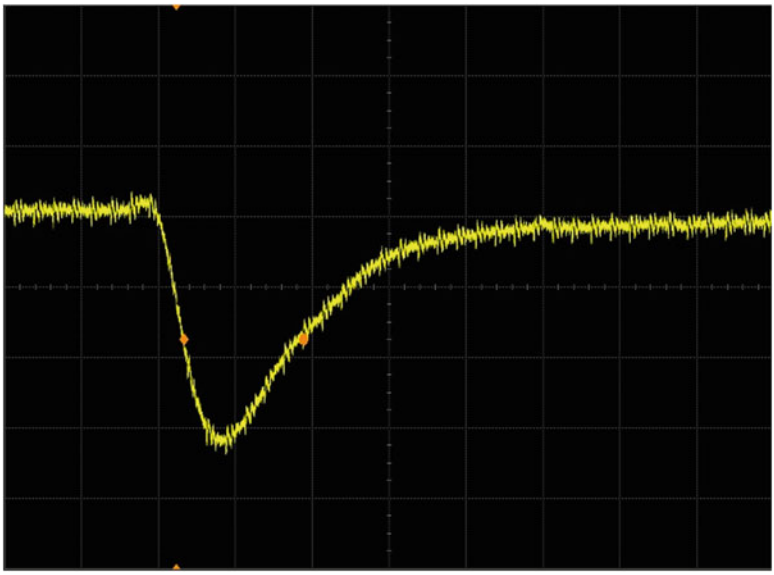

Fig. 3.20 Typical pulse shape from neutron detection by an LPSD tube, measured at point corresponding to V_{A1} in Fig. 3.19. 200 mV/division with 200 ns/division sweep rate

Figure 3.20 shows an oscilloscope trace for a typical pulse from an LPSD tube for a neutron detection. It was measured at the point corresponding to V_{A1} in Fig. 3.19 after being amplified by the preamplifier. Figure 3.21 shows an oscilloscope trace for a typical gated integrator output from a neutron detection. It was measured at a point corresponding to V_{I1} in Fig. 3.19.

The shape of the pulse from the detector tube can vary between detection events. Therefore, a range in the amount of delivered charge Q corresponds to the discriminator cutoff. If Q is the basis for discrimination, then the discriminator settings must be low enough to admit most events with the minimum desired Q. The ADC readings after the integration can then be examined to veto events with less than the desired Q. Notably, the vetoed events still contribute to the dead time of the detector.

3.2.1.6 Correction for Voltage Offset Errors in Position Determination

One source of error in the position determination is a voltage offset in an amplifier. Referring to Fig. 3.17, assume the following in Eq. 3.33:

$$V_{A1} = V_{A1\text{off}} + \frac{I_0 R_f (L - D)}{L} \tag{3.33}$$

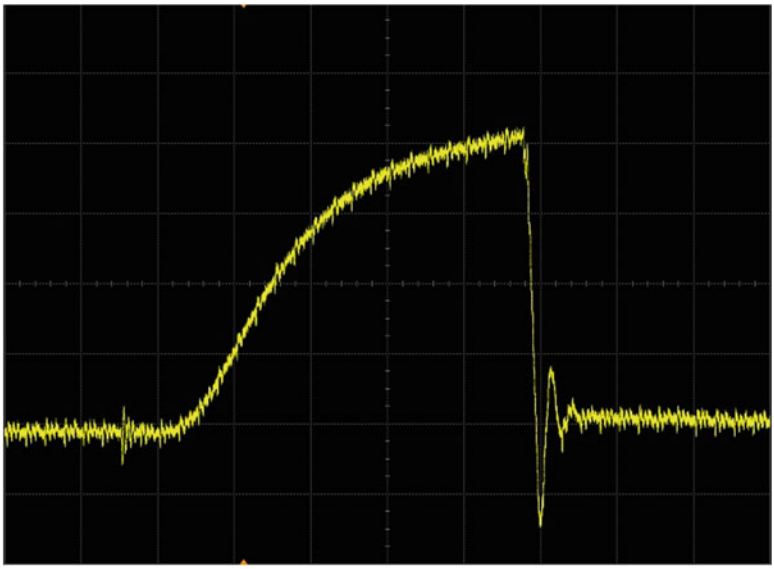

Fig. 3.21 Typical gated integrator output from a neutron detection, measured at a point corresponding to V_{I1} in Fig. 3.19. 200 mV/division with 200 ns/division sweep rate

For this calculation, assume that $\tau_1 = \tau_2 = \tau$ and $R_{F1} = R_{F2} = R_F$, ignoring gain differences. After integrating a detection event, the output of integrator 1 is given by Eq. (3.34):

$$V_{I1\text{off}} = \int_0^{t_m} \frac{V_{A1\text{off}}}{\tau} dt + \frac{R_f(L-D)}{\tau L} \int_0^{t_m} I_0 dt = \frac{t_m V_{A1\text{off}}}{\tau} + \frac{R_f(L-D)Q}{\tau L} \tag{3.34}$$

A position calculation using this value gives Eq. (3.35):

$$\begin{aligned} D_{\text{off}} &= \frac{LV_{I2}}{V_{I1\text{off}} + V_{I2}} \\ &= \frac{L\dfrac{R_f DQ}{\tau L}}{\dfrac{t_m V_{A1\text{off}}}{\tau} + \dfrac{R_f(L-D)Q}{\tau L} + \dfrac{R_f DQ}{\tau L}} \\ &= \frac{R_f DQ}{t_m V_{A1\text{off}} + R_f Q} \\ &= \frac{D}{B+1} \end{aligned} \tag{3.35}$$

where $B = (t_m V_{A1\text{off}})/(R_f Q)$.

B can be interpreted as the error in determining the delivered charge on side 1 because of the offset voltage divided by the total charge from the event. The error in the position determination is determined by Eq. (3.36):

$$\Delta D = D_{\text{off}} - D = \frac{-BD}{B+1} \tag{3.36}$$

The error is seen to be position-dependent, rising linearly from 0 on the side with the voltage offset to the maximum value on the other side. ΔD is also inversely proportional to the delivered charge Q from the event.

The position-measuring circuit contains adjustment provisions for canceling out voltage offsets. The value of the offset correction can be measured by integrations at times when no current owing to detection events is present. If the offset correction has the correct value, the output from the integrator at the end of an integration will be the same as it was at the start of the integration. Because of noise that is present in the detector, the results from many integrations must be averaged to measure the change reliably. In practice, a series of stepwise changes to the offset correction are tried until a value is found that minimizes the difference between the starting and ending integrator outputs, but a small difference will remain owing to the finite size of the DAC steps. This difference can be canceled out by using an alternate correction technique. The offset dependent term in Eq. (3.34), $(t_m V_{A1\text{off}})/\tau$, is independent of the size of the pulse being detected. If $V_{I1\text{off}0}$ is the measured value of $V_{I1\text{off}}$ for integrations when no current owing to detection events is present, then a measurement of a pulse, which has an integrator 1 output of $V_{I1\text{off}}$, will have an offset corrected value of $V_{I1} = V_{I1\text{off}} - V_{I1\text{off}0}$. This correction can be included as part of the position calculation.

The type of coupling between amplifier stages has implications for offset corrections. Although direct coupling between stages can minimize frequency-dependent effects in signal transmission, it has the drawback that temperature -dependent drifts in the offset of the first stage of the amplifier are multiplied by the full amplifier gain. This multiplication causes the offset correction to be strongly temperature -dependent, so a calibration to update the offset corrections must be repeated after a change in the detector temperature of only a few degrees. Capacitive coupling between stages creates high-pass filters, which block offsets from earlier stages. This blocking greatly reduces the temperature sensitivity. Pulse widths for detection events are typically a microsecond or less. Care must be taken to ensure that the time constant of the filter formed by a coupling capacitor interacting with the input impedance of the next stage is substantially longer than a microsecond.

3.2.1.7 Correction for Mismatched Gain Errors in Position Determination

Another source of error in the position determination is mismatched gains between the amplifiers or integrators on each side of the tube. In this case, $(R_{f1}/\tau_1) \neq (R_{f2}/\tau_2)$.

Given a gain mismatch A such that $(R_{f1}/\tau_1) = A(R_{f2}/\tau_2)$, then a position calculation, which is not corrected for the gain mismatch, gives the result in Eq. (3.37):

$$\begin{aligned} D_A &= \frac{LV_{I2}}{V_{I1}+V_{I2}} \\ &= \frac{\dfrac{LR_{f2}DQ}{\tau_2 L}}{\dfrac{R_{f1}(L-D)Q}{\tau_1 L}+\dfrac{R_{f2}DQ}{\tau_2 L}} \\ &= \frac{LD}{\dfrac{R_{f1}\tau_2}{R_{f2}\tau_1}(L-D)+D} \\ &= \frac{LD}{A(L-D)+D} \\ &= \frac{LD}{AL+(1-A)D} \end{aligned} \tag{3.37}$$

D_A differs from the actual position by Eq. (3.38):

$$\begin{aligned} \Delta D &= D_A - D = D\left(\frac{L}{AL+(1-A)D}-1\right) \\ &= D\left(\frac{(1-A)L-(1-A)D}{AL+(1-A)D}\right) \\ &= \frac{(1-A)D(L-D)}{LA+(1-A)D} \end{aligned} \tag{3.38}$$

The numerator is a parabola with a maximum value of $([1-A]L^2)/4$ at the center of the tube and 0 at the tube ends. The denominator varies linearly from AL at side 1 of the tube to L at side 2. Most cases of interest have small differences in gain where A is close to 1, so to a good approximation, the denominator can be assigned the value L everywhere. This approximation gives $\Delta D = ([1-A]L)/4$ near the center of the tube, or Eq. (3.39):

$$A = 1 - \frac{4\Delta D}{L} \tag{3.39}$$

If the value of A is known, then the position can be correctly calculated using Eq. (3.40):

$$D = \frac{ALV_{I2}}{V_{I1}+AV_{I2}} \tag{3.40}$$

An experimental determination of ΔD can be used to determine a value for A. This determination can be done by placing a neutron absorber in front of the detector tube

at a known position near its center. The detector is put in a state where voltage offset corrections are handled. The detector is illuminated by a neutron source, and a position histogram of counts vs. position along the tube is collected. If the absorber is a slit, a peak will appear in the position histogram, whose shape will be nearly Gaussian if the detector is working well. A least squares fit of a Gaussian curve to the peak is performed, allowing the peak position to be deduced from the fit coefficients. Then, ΔD is the difference between the peak position and the absorber position. If the absorber is not a slit, its edge will cast a shadow, which will appear in the position histogram. The shadow edge often declines gradually over a span of several pixels. A hyperbolic tangent function is used as a model of such an unsharp edge. The coefficients from a least squares fit of the hyperbolic function to the shadow edge are used to deduce its position. These fits are restricted to a small range of pixels spanning the feature to avoid distortion from other features that may exist elsewhere in the histogram. Adequate statistics for curve fitting are required, which usually requires at least 50 counts per pixel in the histograms.

Data acquisition systems will generally split up the length of a detector tube into some number N of pixels and only report the pixel number in which an event is calculated to lie. Position calculations often take place within an FPGA, in which it is awkward to carry out floating point multiplications. The gain correction is therefore accomplished by multiplying V_{I1} by some integer K_1, and V_{I2} is multiplied by the integer closest to $K_2 = AK_1$. If the feature in the position histogram is determined to be ΔN pixels displaced from the absorber position, the gain mismatch is $A = 1 - (4\Delta D/L) = 1 - (4\Delta N)/N$, and the multiplier for V_{I2} becomes Eq. (3.41):

$$K_2 = K_1 - \frac{4K_1}{N}\Delta N \tag{3.41}$$

For the common case where $K_1 = 2048$ and $N = 256$, $(4K_1)/N = 32$.

3.2.1.8 Position Resolution and Noise Sources

Another parameter of interest for an LPSD is its position resolution. If many neutrons hit the detector at the same location along its length, the measured positions will scatter around that location. If an acquisition is performed where neutrons are only allowed to reach the detector tube at one position along its length, a peak will appear in the position histogram. The resolution can be measured as the full width at half maximum (FWHM) of the peak in the position histogram from such a measurement, with small values for the FWHM being desirable. For a detector that is working well, the peak shape is often well-approximated by a Gaussian curve. In such cases, the resolution can be measured by a least squares fit of a Gaussian curve to the peak. The FWHM can then be deduced from the fit parameters. The achievable resolution is dependent on many factors, which will be discussed in this section. FWHM values in the 5–20 mm range are often observed.

The position resolution is primarily determined by noise in the electronics used to measure the position. An important contribution to this noise is the intrinsic noise in the resistors and operational amplifiers, which are used in the detector circuits. A detailed analysis of the influence of these noise sources on the resolution is the subject of Sect. 3.2.2. One significant result is that noise from the central wire of the detector tube is often dominant. Under such conditions (with other factors being equal), the FWHM will be inversely proportional to the square root of the central wire resistance. Another result is that the FWHM is inversely proportional to the charge Q delivered by a detection event. Actions to increase Q, such as raising the detector bias or restricting attention to events high on the pulse height spectrum, will make the FWHM smaller. The S/N in the detector tends to be proportional to the FWHM, expressed as a fraction of the tube length. For a constant S/N, the FWHM in distance units will be proportional to the tube length. If the central wire resistance is the dominant noise source and that resistance is proportional to the tube length, the S/N will be inversely proportional to the square root of the tube length, making the FWHM in distance units proportional to the square root of the tube length.

This dependence of resolution on the delivered charge creates a tradeoff in the choice of discriminator settings. As can be seen in Fig. 3.16, considerable variation exists in the amplitude of pulses from an LPSD tube. As the discriminator threshold is increased, the fraction of low amplitude events that get rejected will increase. Because the eliminated events have the poorest position resolution, the overall position resolution of the detector will improve. This comes at the cost of a decreased fraction of accepted events.

Noise pickup can add to the intrinsic noise. One source can be the preamplifier power cables. The need to supply power forces some current to flow along the ground wires in these cables, which tries to create an offset between the preamplifier ground and the power supply ground, which may differ between the preamplifiers. The preamplifiers also need to be grounded to the detector frame to be referenced to the detector tube ground. The competing ground references can cause a ground loop current to flow through the detector frame and along the power cable ground wires. Magnetic pickup in the loop formed by the power cables and the detector frame can also generate similar ground loop currents. If resistance along the path of the ground loop current exists between the preamplifiers along the detector frame, offset voltages will be generated, which the preamplifiers pick up as noise. To minimize this effect, it is important to have a low-resistance connection of the preamplifier ground to the detector frame. There must also be low resistance for the ground current along the detector frame. For detector geometries where most of the ground loop current passes along the detector tubes, a solid grounding of the tube to the frame on both sides is important. Magnetic pickup can be minimized by routing the power supply cables close to the detector frame.

The currents in the tube to preamplifier wires are small. The lowest resistance path for pickup voltages on these wires to create noise currents is along the central wire of the tube between the preamplifiers. This path has a few thousand ohms of resistance, low enough for such currents to be significant compared with the currents from a detection event. The tube to preamplifier wires need to be mounted within a

grounded enclosure to minimize noise pickup. Crosstalk between traces on a circuit board can be significant. One observed example of this crosstalk was a trace carrying a 10 MHz timing signal that ran too close to the trace from an integrator output to the ADC. The ADC saw the integrator output with crosstalk from the 10 MHz signal added, increasing the noise in the measurement. Noise pickup can come from differences and fluctuations in ground references between the power supplies, the communication connections, the bias connections, and the mounting points of a detector module. Such problems are solved by isolating some grounds and tying together other grounds, with judgement and compromises required.

During a measurement, the ADC converts the continuous analog signal from the integrator to a digital output, making the uncertainty in the reading at least as large as the ADC step size. The length of the detector tube is partitioned into some number of bins. When a position calculation is performed, the result is used to determine the bin in which it fits. The bin number gets turned into a pixel ID, which is what gets transmitted as data. This process makes the uncertainty in the position reading at least as large as the bin length.

The ADC step size is represented by ΔV_{ADC}. Assume that a detector pulse delivers a charge Q at a distance D from side 1 along a tube of length L. If this pulse delivers voltage V_{ADC1} to ADC 1, this amounts to $(N_{\mathrm{ADC1}} + E_1) = (V_{\mathrm{ADC1}}/\Delta V_{\mathrm{ADC}})$ ADC steps, where N_{ADC1} is the nearest integer, and E_1 is the error from digitization. Rounding is assumed to be carried out so that $-1/2 < E_1 < 1/2$. Figure 3.22 illustrates the definition of these quantities.

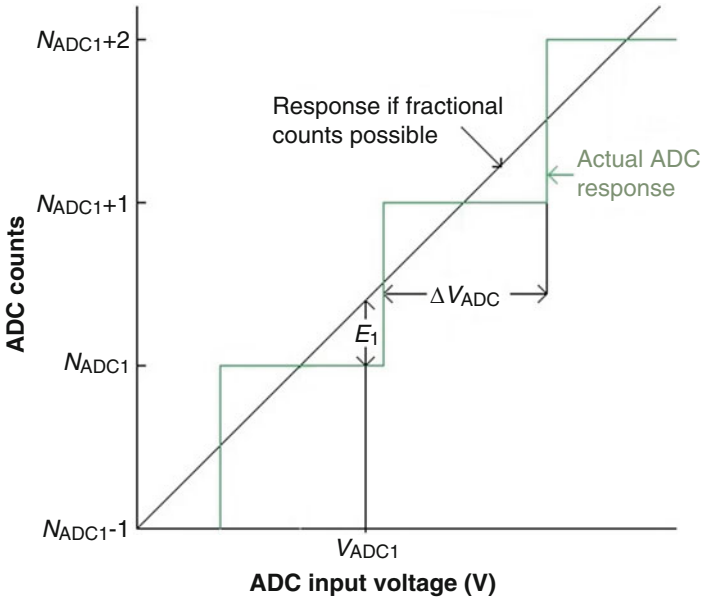

Fig. 3.22 Plot of ADC counts as a function of the input voltage, illustrating the definition of quantities used in digitization error calculations

An error E_2 can similarly be defined as the error from digitization on side 2. When $N = Q/\Delta V_{\mathrm{ADC}}$, a calculation analogous to the derivation of Eq. (3.36) yields a position offset $\Delta D_1 = (-E_1 D)/(E_1 + N)$ owing to E_1 and a position offset $\Delta D_2 = (E_2[L - D])/(E_2 + N)$ owing to E_2. The combined offset is $\Delta D = \Delta D_1 + \Delta D_2$. Defining $R = D/L$ and assuming $N \gg 1$ gives Eq. (3.42):

$$\begin{aligned} \Delta R &= \frac{\Delta D_1 + \Delta D_2}{L} \\ &= \frac{E_2(1-R)}{E_2 + N} - \frac{E_1 R}{E_1 + N} \\ &\approx \frac{E_2(1-R) - E_1 R}{N} \end{aligned} \tag{3.42}$$

Assuming E_1 and E_2 vary independently and are equally likely to have any value in their range, the average value of $(\Delta R)^2$ is given by Eq. (3.43):

$$\int_{E_1=-\frac{1}{2}}^{\frac{1}{2}} \int_{E_2=-\frac{1}{2}}^{\frac{1}{2}} (\Delta R)^2 dE_2 dE_1 = \frac{1}{12N^2}\left((R-1)^2 + R^2\right) \tag{3.43}$$

Because the average value of ΔR is 0, the root mean square (RMS or rms) value of ΔR is given by Eq. (3.44):

$$\Delta R_{\mathrm{rms}} = \frac{1}{2N}\sqrt{\frac{(R-1)^2 + R^2}{3}} \tag{3.44}$$

ΔR_{rms} weakly depends on the position along the tube: $\Delta R_{\mathrm{rms}} = 0.2886/N$ at the tube ends, and $\Delta R_{\mathrm{rms}} = 0.2041/N$ at the center. The factor for converting an RMS deviation to FWHM for a Gaussian distribution is $2\sqrt{2\ln 2} = 2.354$. To the extent that ΔR matches this distribution, $\Delta R_{\mathrm{FWHM}} = 0.6795/N$ at the tube ends, and $\Delta R_{\mathrm{FWHM}} = 0.4805/N$ at the center. Large values of N are desired for minimizing this deviation. An upper limit on its value is set by the number of bins on the ADC, which is 1024 for the version used on the ROC board. Gains should be set up to make the pulse height spectrum come as close to spanning the full range of the ADC without saturating as is feasible.

Assume that the length of the detector tube is partitioned into K bins. An event calculated to lie at distance D along the tube is at $(DK/L) = N_{\mathrm{bin}} + E$ bins, where N_{bin} is the nearest integer, and $-½ < \mathrm{E} < ½$. The position offset as a fraction of the tube length is $\Delta R = E/K$. The average value of $(\Delta R)^2$ is given by Eq. (3.45):

$$\int_{-\frac{1}{2}}^{\frac{1}{2}} \frac{E^2 dE}{K^2} = \frac{1}{12K^2} \tag{3.45}$$

The RMS deviation is given by Eq. (3.46):

$$\Delta R_{\text{rms}} = \frac{1}{\sqrt{12}K} = \frac{0.2886}{K} \tag{3.46}$$

which is independent of the position. Converting ΔR_{rms} to ΔR_{FWHM} yields $\Delta R_{\text{FWHM}} = 0.6795/K$.

The contributions to the resolution must be added in quadrature, as shown in Eq. (3.47):

$$\Delta R_{\text{FWHM total}} = \sqrt{\Delta R^2_{\text{FWHM tube bins}} + \Delta R^2_{\text{FWHM ADC bins}} + \Delta R^2_{\text{FWHM noise}}} \tag{3.47}$$

3.2.1.9 Detector Module Construction

The position determinations reveal the location of a neutron along the axis of the tube. Perpendicular to that axis, the neutron is only determined to have arrived within the inner diameter of the tube. Arrays of tubes must be used to locate a neutron in two dimensions. Several LPSD tubes are usually mounted together to form a detector module, which usually comprise eight tubes each. The modules are often designed to be installed beside each other so that an array of modules can cover a greater distance perpendicular to the tubes. Several geometries are possible, as indicated in Fig. 3.23. The two-sided geometry has two preamplifier boxes—one for each side of the tube. The tubes mount to these boxes, which hold them in the correct positions relative to the module. This mounting is also a place where the tubes connect to the module ground. The preamplifier is mounted in the box, which forms a shielded enclosure for it and for the wires from the tube end to the preamplifier. The preamplifier must

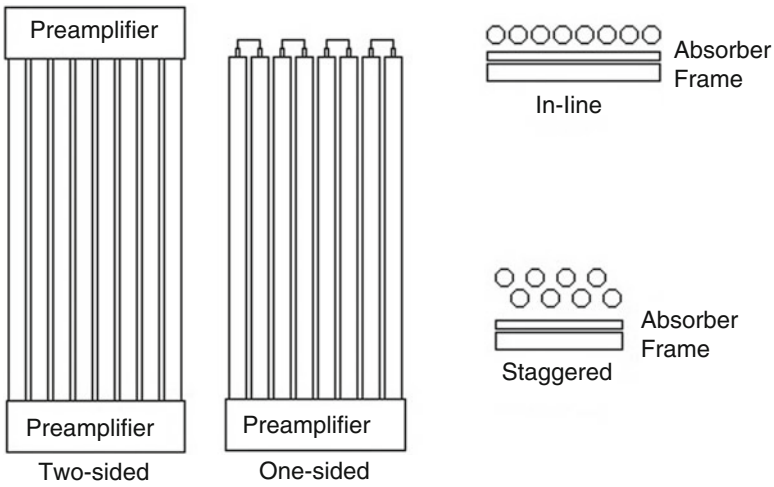

Fig. 3.23 Detector geometries

be mounted to the box in a manner that creates a good ground connection to the module. In some cases, the tubes are attached to the detector frame instead of the preamplifier box. Details of the shape and mounting of the preamplifier boards and their boxes can vary greatly. They often depend on the geometric constraints of the instrument for which the module is designed.

Sometimes, the instrument geometry may be such that no room is available to install a preamplifier on one of the detector sides. A one-sided geometry is then used—the preamplifier and its box are installed on only one side of the module. The tubes of the module are grouped into adjacent pairs. A jumper is installed between the center wire feedthroughs of a pair on the other side of the tubes. As far as resolution and position determination are concerned, the two tubes of length L behave as if they form a single tube of length $2L$.

The most straightforward way to arrange the tubes on the detector module is in-line; that is, the tubes are in the same plane, parallel to each other, and near each other. This arrangement helps maintain uniform illumination conditions between tubes. It also minimizes differences in neutron flight distance from tube to tube. The primary drawback is the gaps between the tubes, which are regions in which an arriving neutron will fail to be detected. The staggered arrangement is sometimes used to eliminate these gaps. The tubes are mounted in two rows—one slightly more than a tube's diameter behind the other. Traversing sideways across the module, the tubes alternate between being in the front or back row. The spacing between tubes is such that the inner diameters of the front-row tubes overlap the inner diameters of the back-row tubes. This overlap eliminates the gaps in coverage and causes the back-row of tubes to be partially shadowed by the front-row tubes. The amount of shadowing depends on the direction of an arriving neutron. An arriving neutron must travel farther to reach a back-row tube than to reach a front-row tube. This discrepancy must be accounted for when interpreting time-of-flight (TOF) measurements.

Figure 3.23 shows an absorber mounted between the tubes and the detector frame. It is possible for neutrons that have traveled past the detector tubes to be scattered off the frame and back into the tubes. Neutrons backscattered by other means may also approach the detector tubes from the rear. In either case, the neutrons create a neutron background with a poorly defined trajectory that should be eliminated. To absorb the backscattered neutrons, an absorber—a sheet of neutron-absorbing material—is often attached to the frame.

The frame's importance as a structural component varies. In some cases, the detector tubes are the main source of structural support between the preamplifier boxes at the ends, and the frame is only a thin sheet of metal to support the absorber plates and some circuit boards. In other cases, the frame is the primary source of structural support for the module and therefore must have more rigid construction. The frame should provide a low-resistance ground path between the preamplifiers to minimize the sensitivity of detector noise to the quality of the tube-to-ground connections.

The position resolution of an LPSD perpendicular to the detector tube is limited by the inner diameter of the tube. This relation creates a desire to use small diameter

tubes, which can lead to tubes with a high length-to-diameter ratio. These tubes are susceptible to a form of catastrophic failure in which the central wire of a biased tube is electrostatically attracted to the tube wall. When the wire approaches the wall, an electrical discharge occurs, which is powerful enough sever the wire. A theoretical analysis of this mechanism is the subject of Sect. 3.2.3. This analysis predicts that the danger of such a failure occurring depends on the value of a parameter K, which will be derived as Eq. (3.107) and is reproduced here as Eq. (3.48):

$$K = \frac{V_0^2 L^2}{W_0 R^2 (\ln[w])^2} \tag{3.48}$$

where V_0 is the bias voltage, L is the tube length, W_0 is the tension on the central wire, R is the inner radius of the tube, and w is the ratio of the wire diameter to the inner diameter of the tube. The mechanism begins to be a concern for $K > 9 \times 10^{10}$ V^2/N, where N refers to newtons. Failure is likely regardless of the tube straightness at $K = 18 \times 10^{10}$ V^2/N. The value of K that can be tolerated improves if the tube is kept very straight. When operating close to the upper limit, the tolerance for deviations from straightness can be as low as 0.1 mm. To give some sense of conditions for which these effects matter, a 1 m long detector tube with an 8 mm outer diameter and 7.1 mm inner diameter can be successfully operated at an 1800 V bias, but attention to straightness is important at these conditions.

Tubes with a high length-to-diameter ratio are not very stiff with respect to sideways deflections. Therefore, additional supports along the length of the tube are needed to maintain the required straightness. Typically, three additional supports are used at approximately one-fourth, one-half, and three-fourths of the way along the length of the tube. These supports can be a source of additional neutron absorption and scattering behind the detector tubes, and they create gaps in the absorber plates. Such effects can cause minor variations in the counts at the positions where a support is present.

3.2.1.10 Detector Calibration and Characterization

One objective of detector calibration is to have a known relationship between the bin number where a neutron detection is reported and the physical location along the detector tube where the neutron was absorbed. This objective involves three lower levels of calibration. One level is correction for voltage offsets in the detector electronics. Section 3.2.1.6 discussed the influence of such offsets on position determinations and calibration techniques for canceling them out. The second level is to ensure that a linear relationship exists between the bin number and the corresponding position along the detector tube. Section 3.2.1.7 discussed the influence of gain mismatches on this type of error and outlined techniques for determining the required corrections. The third level is to determine the distance along the detector tube that a bin occupies. As mentioned in Sect. 3.2.1.5, end effects make this

more complex than dividing the tube length by the number of bins. It is perhaps best determined by illuminating the detector with neutrons emerging from a slit at several known distances along the detector tube and then determining the shift in the position of the peaks in the measured position histograms.

Another position-related characterization of a detector is its position resolution. Section 3.2.1.8 discusses what this means, how it is measured, and the factors that influence it.

Two related characterizations of detector performance are the counting efficiency and gamma rejection. Counting efficiency is the fraction of neutrons arriving at the detector that are detected, which requires two steps to occur. The first step is for the neutron to have an interaction with the detection gas, which has a probability discussed in Sect. 3.2.1.2. The second step is for the detector pulse generated by the reaction to be strong enough to trigger the discriminator. The efficiency of this step can be improved by lowering the discriminator setting. However, as discussed in Sect. 3.2.3, too low of a discriminator setting will allow some unwanted gamma ray detections to also occur, resulting in poor gamma ray rejection. Although LPSD detectors have better gamma ray rejection than many alternative detector types, a trade-off still exists between counting efficiency and gamma ray rejection, which must be considered. Examination of the pulse-height spectrum from a detector can provide some guidance in the selection of the best discriminator setting. The pulse-height spectrum can also be used to estimate how the fraction of neutron rejections varies with the discriminator setting. The counting efficiency and gamma ray rejection of a detector can be determined by measuring its count rate when exposed to neutron and gamma ray sources of known intensity. The accuracy of this technique is usually limited by uncertainties in the intensity of the sources. Although a reference detector can be used to measure the source intensities, the results are still no better than the uncertainties in the counting efficiency of the reference detector.

Similar to other types of detectors for neutrons in thermal energy ranges, LPSD detectors have no intrinsic ability to measure the kinetic energy of the neutrons they detect. This lack of ability is because the kinetic energy of a thermal neutron is approximately 0.025 eV, which is swamped by the 765 keV released when the neutron reacts with ^{3}He. The kinetic energy determination is dependent on other features of the instrument in which they operate. For continuous neutron sources, the energy is typically set using either a velocity selector or diffraction of the neutrons by a crystal. For pulsed neutron sources, TOF can be used to determine the kinetic energy of a neutron. This use of TOF requires every neutron detection to be associated with a time stamp measuring the time interval between the creation and the detection of the neutron. The time resolution needed for this time stamp can be estimated by noting that a typical thermal energy neutron moves at 2200 m/s, but there is an uncertainty of a millimeter or more in the distance within the detector tube in which the neutron interacts with the detector gas. This uncertainty creates an uncertainty of at least 0.5 μs in the time in which the neutron will be detected. A time stamp resolution of 100 ns, as is used at SNS, is short enough to be a negligible contribution to the TOF uncertainty.

3.2.2 LPSD Intrinsic Noise

The influence of intrinsic noise in amplifier first-stage components on the resolution of an LPSD is examined in this section. Noise contributions from external sources are not considered, nor is additional noise owing to later amplification or integration stages. The simplified representation of the input circuit shown in Fig. 3.24 is analyzed in this section. All arrows next to current labels in this figure show the direction of current flow for positive values of the parameter. All arrows next to voltage symbols show the direction of increasing voltage for positive values of the parameter. Here, I_P is current injected by a detection event at some point along the wire of a detector tube. This wire is represented by resistors R_{W1} and R_{W2}. The total wire resistance is $R_W = R_{W1} + R_{W2}$. The gain of first-stage amplifiers 1 and 2 is set by resistors R_{F1} and R_{F2}. Each of these resistors has an intrinsic noise, which is represented by V_{nF1}, V_{nF2}, V_{nW1}, and V_{nW2}. Furthermore, intrinsic noise is associated with the operational amplifiers for the first stage, which occurs in two distinct ways. First, voltage noise can be thought of as fluctuating inaccuracies in an operational amplifier's determination of the voltage presented to its input. This quantity is represented by V_{n1} and V_{n2}. Second, current noise is caused by fluctuations in the current draw of the operational amplifier input. This quantity is represented by i_{n1} and i_{n2}. The first-stage outputs, V_{O1} and V_{O2}, are integrated over a time interval t_m to create the outputs V_{I1} and V_{I2}, which are used for the position calculation.

3.2.2.1 Solution Using Instantaneous Values of Noise Voltages

In the circuit in Fig. 3.24, voltages should add up to 0 around the loop from the positive input of amplifier 1, through the ground to the positive input of amplifier 2, across to the negative input of amplifier 2, through the tube wire to the negative input of amplifier 1, and back to the positive input. This path gives $0 = -V_{n1} - V_{nW1} + R_{W1}I_{W1} - R_{W2}I_{W2} + V_{nW2} + V_{n2}$. Because $I_{W1} = I_p - I_{W2}$, $0 = -V_{n1} - V_{nW1} + V_{nW2} + V_{n2} + R_{W1}I_P - R_WI_{W2}$. Solving for I_{W2} gives Eq. (3.49):

$$I_{W2} = \frac{R_{W1}I_p - V_{n1} - V_{nW1} + V_{nW2} + V_{n2}}{R_W} \tag{3.49}$$

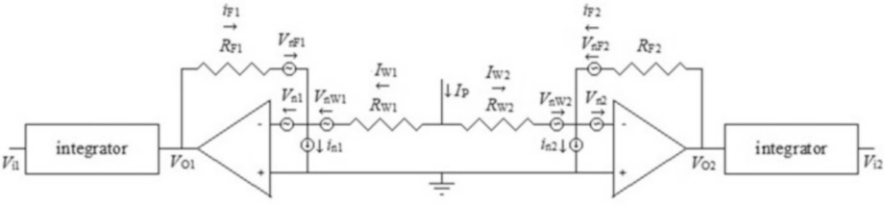

Fig. 3.24 Simplified first-stage input circuit for an LPSD

Substituting Eq. (3.49) into $I_{W1} = I_p - I_{W2}$ gives Eq. (3.50):

$$I_{W1} = \frac{R_{W2}I_p + V_{n1} + V_{nW1} - V_{nW2} - V_{n2}}{R_W} \tag{3.50}$$

The feedback connection from the amplifier 1 output to its input yields $V_{O1} = R_{F1}i_{F1} - V_{nF1} - V_{n1}$.

Because $i_{F1} = i_{n1} - I_{W1}$, V_{O1} is given by Eq. (3.51):

$$V_{O1} = -V_{nF1} - V_{n1} + R_{F1}i_{n1} - \frac{R_{F1}}{R_W}\left(R_{W2}I_p + V_{n1} + V_{nW1} - V_{nW2} - V_{n2}\right) \tag{3.51}$$

Similarly, V_{O2} is given by Eq. (3.52):

$$V_{O2} = -V_{nF2} - V_{n2} + R_{F2}i_{n2} - \frac{R_{F2}}{R_W}\left(R_{W1}I_p - V_{n1} - V_{nW1} + V_{nW2} + V_{n2}\right) \tag{3.52}$$

The integrator output is the integral of the input voltage over a fixed time interval t_m. If an integrator time constant τ is defined such that the output voltage of the integrator is $\frac{1}{\tau}\int_0^{t_m} V dt$, then the integration function can be defined by Eq. (3.53):

$$\mathrm{INT}(V) = \frac{1}{\tau}\int_0^{t_m} V dt \tag{3.53}$$

The action of this function is illustrated in Fig. 3.25.

Note that $\mathrm{INT}(I_P) = Q/\tau$, where Q is the charge delivered by I_P over the time interval t_m. It is convenient to define the following values in Eqs. (3.54), (3.55), and (3.56):

$$D = \mathrm{INT}(V_{n1} + V_{nW1} - V_{nW2} - V_{n2}) \tag{3.54}$$

$$E = \mathrm{INT}(-V_{nF2} - V_{n2} + R_{F2}i_{n2}) \tag{3.55}$$

$$F = \mathrm{INT}(-V_{nF1} - V_{n1} + R_{F1}i_{n1}) \tag{3.56}$$

Then, V_{I1} and V_{I2} are given by Eqs. (3.57) and (3.58), respectively:

$$V_{I1} = \mathrm{INT}(V_{O1}) = F - \frac{R_{F1}R_{W2}Q}{\tau R_W} - \frac{R_{F1}D}{R_W} \tag{3.57}$$

$$V_{I2} = \mathrm{INT}(V_{O1}) = E - \frac{R_{F2}R_{W1}Q}{\tau R_W} + \frac{R_{F2}D}{R_W} \tag{3.58}$$

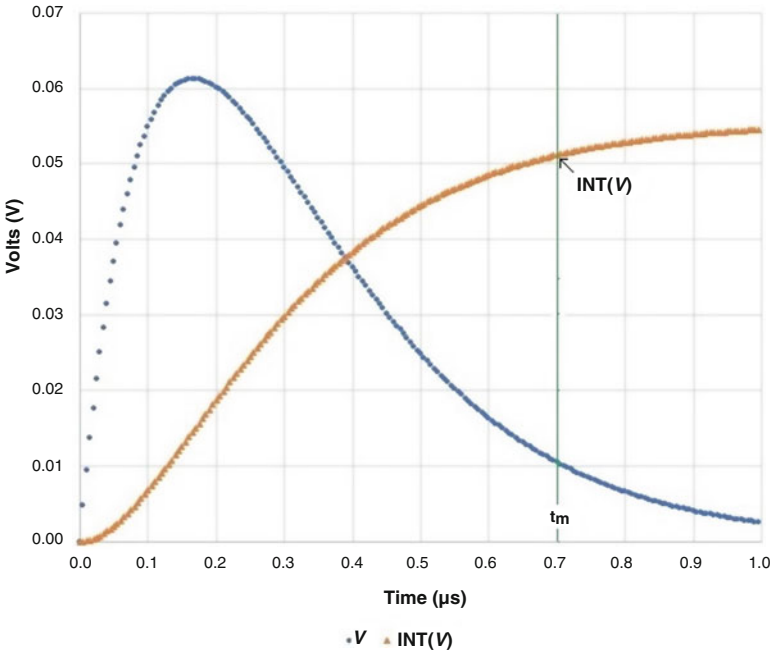

Fig. 3.25 Illustration of the integrator function acting on a voltage input that resembles a pulse from a detector. For this illustration, $\tau = 0.5$ μs, and $t_m = 0.7$ μs. The arrow points to the voltage, which would be the output value of INT(V)

The amplifier gains must be matched for this circuit to yield accurate position measurements, so $R_{F1} = R_{F2} = R_F$ is expected. The position P along the wire can be calculated using Eq. (3.59):

$$P = \frac{V_{I2}}{V_{I1} + V_{I2}} = \frac{E - \frac{R_F R_{W1} Q}{\tau R_W} + \frac{R_F D}{R_W}}{E + F - \frac{R_F Q}{\tau}} = \frac{\frac{R_{W1}}{R_W} - \frac{\tau E}{Q R_F} - \frac{\tau D}{Q R_W}}{1 - \frac{\tau}{Q R_F}(E + F)} \tag{3.59}$$

If Q is large enough that $(\tau/QR_W)(E + F) \ll 1$, then a good approximation is obtained by multiplying the numerator and denominator by $1 + (\tau/QR_F)(E + F)$ and then discarding any terms that are a product of noise voltages. This process results in Eq. (3.60):

$$P = \frac{R_{W1}}{R_W} - \frac{\tau E}{Q R_F} - \frac{\tau D}{Q R_W} + \frac{\tau R_{W1}}{M Q R_F R_W}(E + F) = \frac{R_{W1}}{R_W} - \frac{\tau D}{Q R_W} - \frac{\tau R_{W2} E}{Q R_F R_W} + \frac{\tau R_{W1} F}{Q R_F R_W} \tag{3.60}$$

This calculation gives the expected P based on whatever values the various noise voltages and currents happened to be during a particular acquisition. The next goal is

to determine the expected variation in the measured P values over many acquisitions. The noise voltages present at the amplifier outputs are filtered through the integrators before being applied to the calculation of P, so calculating the influence of this filtering is necessary.

3.2.2.2 Filtering of Noise by the Integrator

A noise source with spectral density N_f is assumed to be processed through an integrator, which outputs $1/\tau$ times the integral of its instantaneous values over time t_m. If it can be assumed that N_f is significant over a frequency range from f_1 to f_2, then a frequency interval Δf can be chosen such that $\Delta f \ll 1/t_m$. The resultant waveform, selecting all noise in the range f to $f + \Delta f$, will have an average RMS amplitude of A_f, which is determined by Eq. (3.61):

$$A_f^2 = \int_f^{f+\Delta f} N_f^2 df = N_f^2 \Delta f \tag{3.61}$$

The frequency dispersion will be small enough that within the integration time t_m, the dispersion can be approximated as $V_f = \sqrt{2} A_f \exp\{iB\} \exp\{i2\pi ft\}$, where t is the time since the integration began, and B is a phase factor, which varies randomly between frequency intervals and between successive integrations. The noise from the frequency interval Δf will emerge from the integrator as a contribution V_{If} calculated by Eq. (3.62):

$$\begin{aligned} V_{If} &= \frac{1}{\tau} \int_0^{t_m} V_f dt \\ &= \sqrt{2\Delta f} \frac{N_f}{\tau} \exp\{iB\} \int_0^{t_m} \exp\{i2\pi ft\} dt \\ &= \sqrt{2\Delta f} \frac{N_f}{2\pi f \tau} \frac{\exp\{iB\}}{i} (\exp\{i2\pi f t_m\} - 1) \end{aligned} \tag{3.62}$$

Euler's formula yields Eq. (3.63):

$$\exp\{i2\pi f t_m\} - 1 = \cos 2\pi f t_m - 1 + i \sin 2\pi f t_m \tag{3.63}$$

which has amplitude given by Eq. (3.64):

$$\| \exp\{i2\pi f t_m\} - 1 \| = \sqrt{2 - 2\cos 2\pi f t_m} \tag{3.64}$$

Because $(\exp\{iB\})/i$ remains a random phase, V_{If} is a vector with amplitude given by Eq. (3.65):

$$\| V_{If} \| = \sqrt{2\Delta f}\frac{N_f}{2\pi f\tau}\sqrt{2-2\cos 2\pi f t_m} \tag{3.65}$$

The amplitude in Eq. (3.65) is random phase, yielding an RMS amplitude given by Eq. (3.66):

$$V_{If\text{rms}} = \frac{N_f\sqrt{\Delta f}}{2\pi f\tau}\sqrt{2-2\cos 2\pi f t_m} \tag{3.66}$$

To calculate the RMS amplitude over the frequency range from f_1 to f_2, the sum of squares must first be formed, given by Eq. (3.67):

$$S = \sum V_{If\text{rms}}^2 = \sum_{j=0}^{(f_2-f_1)/\Delta f}\frac{N_f^2\Delta f(2-2\cos 2\pi f t_m)}{4\pi^2 f^2\tau^2} \tag{3.67}$$

where $f = f_1 + j\Delta f$. Going to the limit $\Delta f = 0$ gives the integral in Eq. (3.68):

$$S = \frac{1}{4\pi^2\tau^2}\int_{f_1}^{f_2}\frac{N_f^2}{f^2}(2-2\cos 2\pi f t_m)df = \frac{t_m}{\tau^2}G\left(N_f^2\right) \tag{3.68}$$

where $G\left(N_{\text{f}}^2\right)$ is given by Eq. (3.69):

$$G\left(N_f^2\right) = \frac{1}{\pi}\int_{\omega_1}^{\omega_2}\frac{N_f^2}{\omega^2}(1-\cos\omega)d\omega \tag{3.69}$$

where $\omega_1 = 2\pi f_1 t_m$, and $\omega_2 = 2\pi f_2 t_m$.

The RMS value for the noise over the full frequency range is then given by Eq. (3.70):

$$V_{I\text{rms}} = \sqrt{S} \tag{3.70}$$

For cases in which N_f is not frequency-dependent, $G\left(N_f^2\right) = G_1 N_f^2$, where G_1 is given by Eq. (3.71):

$$G_1 = \frac{1}{\pi}\int_{\omega_1}^{\omega_2}\frac{(1-\cos\omega)d\omega}{\omega^2} \tag{3.71}$$

$G_1 = 0.5$ when all frequencies are included. For a low-frequency cutoff $\omega_1 = 2\pi f_1 t_m \ll 1$, subtract $(\omega_1/2\pi)\left(1-\omega_1^2/18\right)$ from G_1. For a high-frequency cutoff $\omega_2 = 2\pi f_2 t_m \gg 1$, subtract $1/(\pi\omega_2)$ from G_1.

3.2.2.3 Calculation of RMS Noise Amplitudes

A resistor of size R will at best have noise with a spectral density $N_f = \sqrt{4\pi k_B T R}$, where $k_B = 1.38 \times 10^{-23}$ J/K is the Boltzmann constant, and T is the temperature. In upcoming equations, $C_r = 4\pi k_B T$ is used as the noise multiplier for resistors, and $S\left(N_f^2\right)$ is used as an operator that calculates the integral of Eq. (3.68) for N_f^2. Also, V_{n1}, V_{n2}, and i_n are interpreted as the spectral density of these noise sources. Let D_n, E_n, and F_n be the squared noise sums associated with the values D, E, and F, which were defined in Eqs. (3.54), (3.55), and (3.56).

$$D_n = S\left(V_{n1}^2 + V_{n2}^2 + C_r R_{W1} + C_r R_{W2}\right) = S\left(V_{n1}^2 + V_{n2}^2 + C_r R_w\right) \tag{3.72}$$

$$E_n = S\left(C_r R_{F2} + V_{n2}^2 + R_{F2}^2 i_{n2}^2\right) \tag{3.73}$$

$$F_n = S\left(C_r R_{F1} + V_{n1}^2 + R_{F1}^2 i_{n1}^2\right) \tag{3.74}$$

H is defined as the sum of the squares of all noise sources in the position calculation in Eq. (3.60). Then, H is given by Eq. (3.75):

$$H = \frac{\tau^2}{Q^2}\left(\frac{D_n}{R_W^2} + \frac{R_{W2}^2 E_n}{R_W^2 R_F^2} + \frac{R_{W1}^2 F_n}{R_W^2 R_F^2}\right) \tag{3.75}$$

If a good match in amplifier properties exists between the two sides, then $V_{n1} = V_{n2} = V_n$, $i_{n1} = i_{n2} = i_n$, and $R_{F1} = R_{F2} = R_F$. Therefore, $E_n = F_n$, and Eq. (3.75) can be rewritten as Eq. (3.76):

$$\begin{aligned} H &= \frac{\tau^2}{Q^2}\left(\frac{D_n}{R_W^2} + \frac{R_{W1}^2 + R_{W2}^2}{R_W^2 R_F^2} E_n\right) \\ &= \frac{\tau^2}{Q^2} S\left(\frac{2V_n^2}{R_W^2} + \frac{C_r}{R_w} + \frac{R_{W1}^2 + R_{W2}^2}{R_W^2}\left(\frac{C_r}{R_F} + i_n^2 + \frac{V_n^2}{R_F^2}\right)\right) \end{aligned} \tag{3.76}$$

The RMS amplitude of the noise in the position determination, as a fraction of the wire length, is given by Eq. (3.77):

$$\begin{aligned} P_n = \sqrt{H} &= \frac{\tau}{Q}\sqrt{S\left(\frac{2V_n^2}{R_w^2} + \frac{C_r}{R_W} + \frac{R_{W1}^2 + R_{W2}^2}{R_W^2}\left(\frac{C_r}{R_F} + i_n^2 + \frac{V_n^2}{R_F^2}\right)\right)} \\ &= \frac{\sqrt{t_m}}{Q}\sqrt{G\left(\frac{2V_n^2}{R_W^2} + \frac{C_r}{R_W} + \frac{R_{W1}^2 + R_{W2}^2}{R_W^2}\left(\frac{C_r}{R_F} + i_n^2 + \frac{V_n^2}{R_F^2}\right)\right)} \end{aligned} \tag{3.77}$$

For a Gaussian distribution, conversion from an RMS amplitude to FHWM requires multiplication by a factor of $2\sqrt{2\ln 2} = 2.354$.

P_n would need to be multiplied by the wire length to obtain the noise in terms of a distance. The only term in H that depends on the position along the wire is $\left(R_{W1}^2 + R_{W2}^2\right)/R_W^2$, which varies from 0.5 at the center of the wire to 1 at the ends of the wire.

J is defined as the sum of the squares of all noise sources in the determination of V_{I1} in Eq. (3.78):

$$J = F_n + \frac{R_{F1}^2}{R_W^2} D_n = S\left(CR_{F1} + V_{n1}^2 + R_{F1}^2 i_{n1}^2 + \frac{R_{F1}^2}{R_w^2}\left(V_{n1}^2 + V_{n2}^2\right) + \frac{CR_{F1}^2}{R_W}\right) \quad (3.78)$$

The RMS noise at the integrator output V_{I1} is given by Eq. (3.79):

$$\begin{aligned} V_{I1\text{rms}} &= \sqrt{J} \\ &= \sqrt{S\left(C_r R_{F1} + V_{n1}^2 + R_{F1}^2 i_{n1}^2 + \frac{R_{F1}^2}{R_W^2}\left(V_{n1}^2 + V_{n2}^2\right) + \frac{C_r R_{F1}^2}{R_W}\right)} \\ &= \frac{\sqrt{t_m}}{\tau}\sqrt{G\left(C_r R_{F1} + V_{n1}^2 + R_{F1}^2 i_{n1}^2 + \frac{R_{F1}^2}{R_W^2}\left(V_{n1}^2 + V_{n2}^2\right) + \frac{C_r R_{F1}^2}{R_W}\right)} \end{aligned} \quad (3.79)$$

3.2.2.4 Noise Calculations for a Specific Detector

In this section, values for noise parameters are calculated for an actual detector with 654 mm long tubes whose wire resistance is measured to be 3380 Ω. The feedback resistance is $R_F = 24{,}000\ \Omega$. AD8022 operational amplifiers are used, for which the data sheet [15] quotes $i_n = 1.2 \times 10^{-12}$ A/√Hz and $V_n = 2.5 \times 10^{-9}$ V/√Hz. The integrators use an integration time of $t_m = 7 \times 10^{-7}$ s.

Bandwidth limitations on the noise sources vary with the nature of the source. For the thermal noise from the tube wire resistance, a low-frequency roll-off is created because the currents from this source must travel along a path between the preamplifier inputs on each side of the tube. As can be seen in Fig. 3.18, this path includes capacitors C_{s1} and C_{s2}. These are 15 nF bias isolation capacitors, which, for this path, are connected in series, giving a combined capacitance of 7.5 nF. At low frequencies, the impedance of these capacitors limits the current that the wire noise can induce along this path, which limits the gain of the preamplifiers. A roll-off frequency for this mechanism can be estimated by calculating the frequency for which the amplitude of the capacitor impedance is equal to the tube wire resistance, as shown in Eq. (3.80):

$$f_1 = \frac{1}{2\pi\left(3{,}830\ \Omega \times \left(7.5 \times 10^{-9}\ \text{F}\right)\right)} = 5{,}540\ \text{Hz} \quad (3.80)$$

For the correction to G_1, $\omega_1 = 2\pi f_1 t_m = 0.0243$, $\Delta G_1 \approx \omega_1/2\pi = 0.0038$.

Table 3.1 Equation terms

Term	Value (A^2/s)	S (A^2)	$R_F^2 S$ (V^2)
$\frac{2V_n^2}{R_W^2}$	1.094×10^{-24}	1.01×10^{-15}	5.81×10^{-7}
$\frac{C_r}{R_W}$	1.538×10^{-23}	1.419×10^{-14}	8.176×10^{-6}
$\frac{C_r}{R_F}$	2.166×10^{-24}	1.999×10^{-15}	1.151×10^{-6}
i_n^2	1.44×10^{-24}	1.329×10^{-15}	7.655×10^{-7}
$\frac{V_n^2}{R_F^2}$	1.08×10^{-26}	9.96×10^{-18}	5.74×10^{-9}

Although they are not depicted in Fig. 3.18, 5 pF capacitors are installed in parallel with feedback resistors R_{11} and R_{12} to suppress feedback oscillations. These capacitors decrease the preamplifier gain at high frequencies because they reduce the feedback impedance. This creates a high-frequency roll-off for many of the noise sources. A roll-off frequency can be estimated by calculating the frequency for which the amplitude of the capacitor impedance equals the resistance of R_{11} or R_{12}, as shown in Eq. (3.81):

$$f_2 = \frac{1}{2\pi\left(24{,}000\ \Omega \times \left[2 \times 10^{-12}\ \mathrm{F}\right]\right)} = 1.32 \times 10^6\ \mathrm{Hz} \tag{3.81}$$

For the correction to G_1, $\omega_2 = 2\pi f_2 t_m = 5.833$, and $\Delta G_1 = 1/\pi\omega_2 = 0.0545$. Combining both corrections, $G_1 = 0.5 - 0.0038 - 0.0545 = 0.4417$. An additional gain of 12 occurs between the first-stage output and the integrator input, which then integrates with a time constant of 2.2×10^{-7} s. Therefore, $\tau = (2.2 \times 10^{-7}\ \mathrm{s})/12 = 1.83 \times 10^{-8}$ s. For noise sources whose spectral density is not frequency-dependent, the effect of applying the operator S (Eq. [3.68]) is to multiply by an effective bandwidth of $(t_m G_1)/\tau^2 = 9.23 \times 10^8$ Hz. The charge delivered by a pulse is $Q = ([V_{I1} + V_{I2}]\tau)/R_F$. To get $V_{I1} + V_{I2} = 1$ V requires $Q = 7.62 \times 10^{-13}$ C for an average current over the integration period of $Q/T = 1.09 \times 10^{-6}$ A. If operation at 300 K is assumed, then the noise multiplier for resistors $C_r = 4\pi(1.38 \times 10^{-23})(300) = 5.20 \times 10^{-20}$ (V^2s)/Ω.

The terms that appear in the formulas for H and J are listed in Table 3.1.

The term C_r/R_W, which is the thermal noise current from the tube wire, dominates. At the center of the wire, using Eq. (3.77), the uncertainty in the position determination evaluates to $P_n = (1/Q) \times (2.381 \times 10^{-15})$ C. For $Q = 7.62 \times 10^{-13}$ C, $P_n = 0.00312$, and Eq. (3.79) yields $V_{I1n} = 0.00327$ V.

3.2.2.5 Experimental Test of Noise from Wire Resistance

A test of some of the predictions about the influence of the tube wire resistance on noise was done, using the detector which was the basis for the previous calculations. For these tests, the tube wire connections to the preamplifiers for channel 1 were altered in various ways. After each alteration, a calibration was performed. During

Table 3.2 Standard deviations

Test	σ_1 (ADC)	σ_2 (ADC)
1	2.35	2.27
2	1.27	1.21
3	2.63	1.25
4	2.09	0.84
5	2.46	2.10
6	1.27	1.65
7	0.71	1.73

this calibration, the values of V_{I1} and V_{I2} were measured approximately 300 times with no pulse present, and the standard deviation of these values was one of the calculations performed. Calling these standard deviations σ_1 and σ_2, the results are shown in Table 3.2. The standard deviations are in units of ADC steps, in which one ADC step is approximately 0.1 V.

For test 1, the tube wire was connected normally. For test 2, the wire was disconnected on side 2 and left floating. This disconnection decreased the noise by nearly a factor of 2. For test 3, the wire was connected directly to the detector ground on side 2. This connection caused the higher noise on side 1 to reappear. For test 4, the power to the preamplifier for side 2 was disconnected. This disconnection was a check to determine if the return currents along the preamplifier power supply ground wires could be driving a ground loop current between the preamplifiers, which is a potential noise source. The noise for side 2 decreased but did not go all the way to 0 owing to noise in the integrator and later preamplifier stages. The noise on side 1 decreased slightly but remained high. For test 5, the side 2 preamplifier power was restored. A 3300 Ω resistor was attached between the side 2 preamplifier input and the preamplifier ground. The tube wire was connected to ground. The noise levels on both sides were close to the levels observed during test 1. Test 5 suggests that the thermal noise current owing to the tube wire resistance dominates over any currents induced by external sources. For test 6, the resistor was increased to 6600 Ω, and the tube wire connection to ground was removed. The noise levels at side 2 decreased, showing that an increased resistance reduces the noise. The side 1 noise was the same as that for test 2, and it had a low value because the tube wire lacked a path through which noise currents could travel. For test 7, the side 1 preamplifier power was disconnected, and the rest of the setup remained the same. The noise on side 2 was very close to the level seen on test 6. Test 7 was performed as a further verification that crosstalk between preamplifiers was not contributing to the noise.

3.2.3 The Attraction of the Central Wire to the Tube Wall for LPSD Tubes

LPSD tubes are constructed as circular tubes with an electrical feedthrough on each end. A small-diameter central wire is suspended under tension between these feedthroughs. This wire must be electrically biased with respect to the tube wall

for the detector to function. For tubes with a high length-to-diameter ratio, a significant failure mechanism is the electrostatic attraction of the wire to the tube wall. If the wire reaches the wall, then a spark will be created, which can be strong enough sever the central wire, ruining the detector. This attraction can be theoretically modeled to gain some insight into the conditions under which it occurs.

3.2.3.1 Electrostatic Attraction of an Off-Center Wire to a Cylindrical Tube

The electrostatic attraction of an off-center wire to a cylindrical tube is calculated using the following simplifying assumptions. Variations in the off-center distance of the wire with the position along the axis of the tube are ignored. Variations in the potential along the axis of the tube are ignored, and the second derivative of any such variations is assumed to equal zero. For these assumptions to be reasonable, any such variations must occur over distances that are large compared with the tube radius. Variations in the angular distribution of charge on the surface of the wire are ignored. For this assumption to be reasonable, the wire diameter must be small compared with the tube diameter.

A straight, infinitely long conducting cylindrical tube of inside radius R_T is assumed to be held at ground potential. Inside this cylinder is a straight, infinitely long wire of radius R_W held at voltage V_B. This wire is displaced by a distance R_D from the center of the tube. A cylindrical coordinate system is defined such that R is the distance from the central axis of the tube, Z is the distance along the axis of the tube, θ is the angle around the axis, and the origin is chosen so that $\theta = 0$ is in the direction of the wire displacement. It is convenient for the analysis to express the wire radius and wire displacement as fractions of the tube radius, so set $w = R_W/R_T$ and $D = R_D/R_T$. Figure 3.26 illustrates the definition of these quantities.

If the wire is at the center of the cylinder, then no charge redistribution is on the tube surface, and the potential distribution around the wire follows the free-space result $V = V_S \ln(R/R_T)$. The ratio R/R_T is chosen for the logarithm so that $V = 0$ when $R = R_T$. V_S must be chosen so that $V = V_B$ when $R = R_W$, implying that $V_B = V_S \ln(R_W/R_T) = V_S \ln(w)$. This creates an electric field $E = -\partial V/\partial R = -V_S/R$. The charge density at the wire surface is $\epsilon_0 E = -(\epsilon_0 V_S)/R_W$, where $\epsilon_0 = 8.854 \times 10^{-12}$ F/m is the electric permittivity. Given the wire circumference $2\pi R_W$, this charge density yields a charge per length given by Eq. (3.82):

$$Q = -\frac{2\pi\epsilon_0 V_B}{\ln w} \tag{3.82}$$

When the wire is offset from the center, its distance R_A to the tube wall varies with θ, as given by Eq. (3.83):

$$R_A(\theta) = R_T\sqrt{1 - 2D\cos\theta + D^2} \tag{3.83}$$

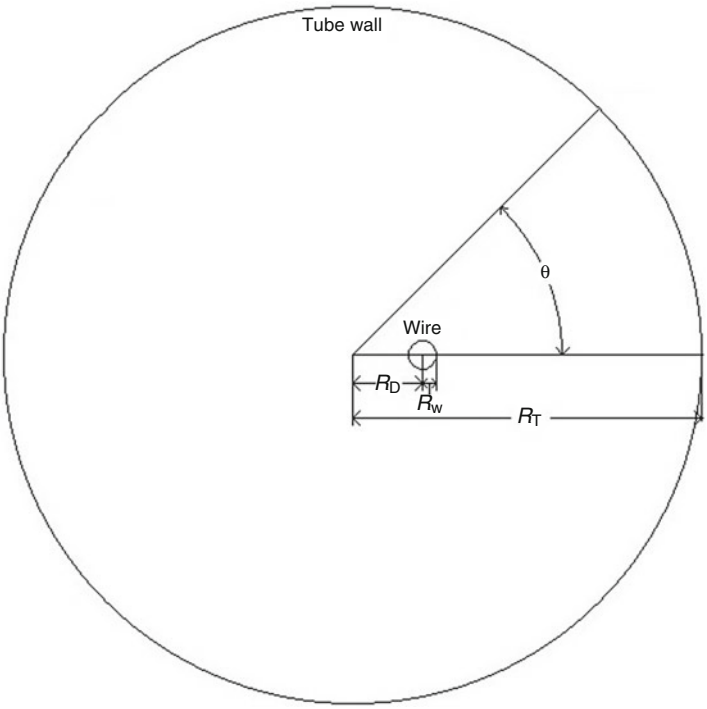

Fig. 3.26 Diagram of a cross section of an LPSD tube, illustrating the definition of several quantities used in the calculations. The z-axis is along the length of the detector tube, rising out of the page. The radius of the central wire is exaggerated in the diagram

If the redistribution of charge at the tube wall was suppressed, then the potential at the tube wall varies with θ, as given by Eq. (3.84):

$$V_1(\theta) = V_S \ln\left(\frac{R_A}{R_T}\right) = V_S \ln\left(\sqrt{1 - 2D\cos\theta + D^2}\right) \tag{3.84}$$

Because the tube is conductive, the surface charge at the tube wall redistributes to create an additional potential of $-V_I(\theta)$, restoring the sum of the potentials to zero. Inside the tube, the potential owing to the redistributed charge is source-free, yielding Eq. (3.85):

$$\nabla^2 V = 0 = \frac{\partial^2 V}{\partial R^2} + \frac{1}{R}\frac{\partial V}{\partial R} + \frac{1}{R^2}\frac{\partial^2 V}{\partial \theta^2} + \frac{\partial^2 V}{\partial Z^2} \tag{3.85}$$

Assuming that $(\partial^2 V)/(\partial Z^2) \approx 0$, voltage can be calculated using Eq. (3.86):

$$V = V_0 + \sum_{n=1}^{\infty} A_n R^n \cos(n\theta) + \sum_{n=1}^{\infty} B_n R^n \sin(n\theta) \tag{3.86}$$

The symmetries of this problem are such that $B_n = 0$ for all n. At the tube radius R_T, Eq. (3.86) must evaluate to the required potential $-V_I(\theta)$, as shown in Eq. (3.87):

$$-V_S \ln\left(\sqrt{1 - 2D\cos\theta + D^2}\right) = V_0 + \sum_{n=1}^{\infty} A_n R_T^n \cos(n\theta) \tag{3.87}$$

Defining coefficients C_n such that $V_0 = V_S C_0$ and $V_S C_n = A_n R_T^n$ forms Eq. (3.88):

$$-\ln\left(\sqrt{1 - 2D\cos\theta + D^2}\right) = C_0 + \sum_{n=1}^{\infty} C_n \cos(n\theta) \tag{3.88}$$

The coefficients C_n are dimensionless, depend only on D, and can be determined by Fourier fitting to this formula.

For $\theta = 0$, electric field is given by Eq. (3.89):

$$E = -\frac{\partial V}{\partial R} = -\sum_{n=1}^{\infty} n A_n R^{n-1} = -V_S \sum_{n=1}^{\infty} n C_n R_T^{-n} R^{n-1} \tag{3.89}$$

For $R = R_D$, Eq. (3.89) evaluates to a field E_D at the wire position given by Eq. (3.90):

$$E_D = \frac{-V_S}{R_T} G(D) \tag{3.90}$$

where $G(D)$ is given by Eq. (3.91):

$$G(D) = \sum_{n=1}^{\infty} n C_n D^{n-1} \tag{3.91}$$

E_D acts on the charge on the wire to create a force per length, given by Eq. (3.92):

$$F = QE_D = \frac{2\pi\epsilon_0 V_B^2}{R_T \ln(w)^2} G(D) \tag{3.92}$$

The remaining evaluation is of function $G(D)$, which is calculated numerically. For a chosen value of D and for $n < 10$, the expression $-\ln\left(\sqrt{1 - 2D\cos\theta + D^2}\right)\cos(n\theta)$ was evaluated at 0.5° intervals. The results were summed to generate the integral needed to evaluate C_n. Then, $G(D)$ can be

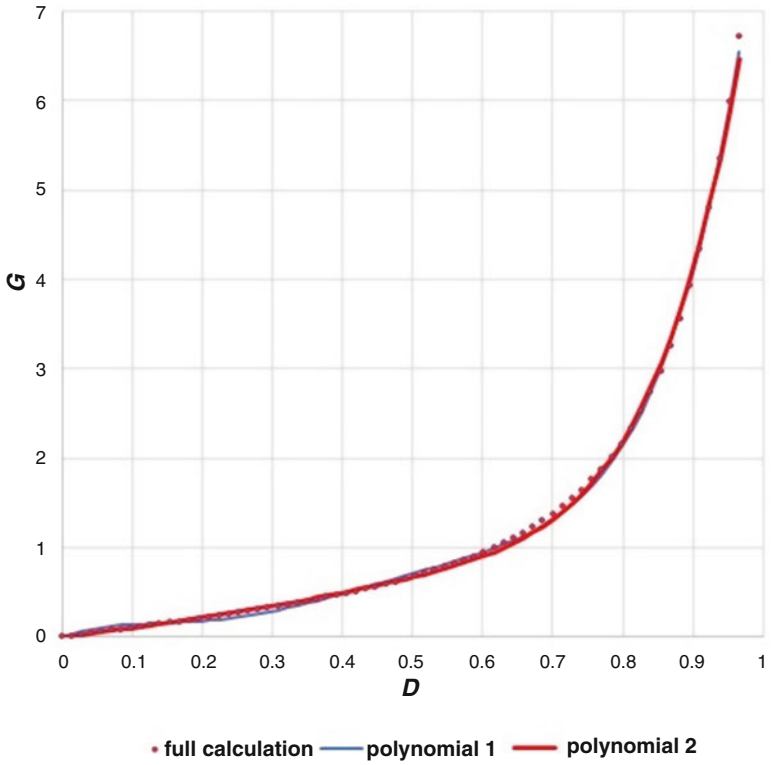

Fig. 3.27 Full-scale plot of $G(D)$

calculated for terms in which $n < 10$. For 70 values of D, $G(D)$ was calculated at intervals of 0.014, covering the range $0 \leq D \leq 0.966$. The results are plotted over the full range in Fig. 3.27 and with an expanded view of the low-amplitude portion in Fig. 3.28. The results were fitted to polynomials to create a less computationally intensive representation. The first polynomial tried was $G(D) = \sum_{n=1}^{5} H_n D^n$, which had fit results $H_1 = 3.0649$, $H_2 = -24.748$, $H_3 = 9.5873$, $H_4 = -14.586$ and $H_5 = 79.954$ and is plotted as polynomial 1 in Figs. 3.27 and 3.28. Although polynomial fitting works well for tracking the behavior at large values of D, the polynomial oscillates around the true values when D is small and is therefore a poor model of the behavior for small values of D. The second polynomial tried is given in Eq. (3.93):

$$G(D) = D + \sum_{n=1}^{3} H_n D^{2n+1} \tag{3.93}$$

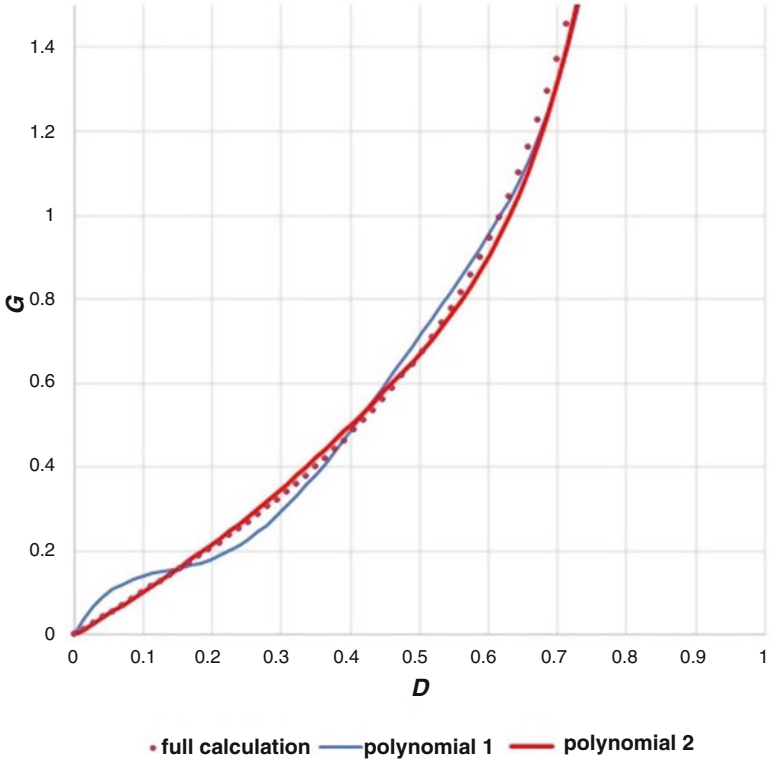

Fig. 3.28 Expanded-scale plot of $G(D)$

which had fit results $H_1 = 2.334$, $H_2 = -6.770$, and $H_3 = 11.564$ and is plotted as polynomial 2 in Figs. 3.27 and 3.28. Polynomial 2 tracks the function well for large values of D and is much better behaved for small values of D compared with polynomial 1.

G(D) is defined in Eq. (3.91). D is a normalized measure of the offset of the wire from the tube center, and G is a normalized measure of the strength of the electrostatic attraction.

3.2.3.2 Wire Deflection in Response to Side Forces

This section's analysis assumes that all side forces remain within a single plane. The z-axis is the line between the feedthroughs of the detector tube, and $z = 0$ is one of the attachment points of the wire to the feedthrough. Then the y-axis is the direction perpendicular to the z-axis that lies in the plane where the side forces are being exerted. The function $Y(z)$ describes the y coordinate of the deflected wire's position. The function $\theta(z)$ describes the angle between the wire and the z-axis direction at

position z. The function $W(z)$ describes the tension in the wire at position z. The function $F_y(z)$ describes the force on the wire from sources other than tension in the y direction per unit length in the z direction at position z, and $F_z(z)$ describes the force on the wire from sources other than tension in the z direction per unit length in the z direction at position z.

A section of the wire between $z = z_0$ and $z = z_0 + \Delta z$ experiences a force in the z direction of $-W(z_0)\cos(\theta[z_0])$ at one side, a force of $W(z_0 + \Delta z)\cos(\theta[z_0 + \Delta z])$ at the other side, and a distributed force of $F_z\Delta z$. For the wire to remain stationary, these forces must add up to zero: $0 = F_z\Delta z + W(z_0 + \Delta z)\cos(\theta[z_0 + \Delta z]) - W(z_0)\cos(z_0)$. For small Δz, $W(z_0 + \Delta z)\cos(\theta[z_0 + \Delta z])$ expands to $W(z_0 + \Delta z)\cos(\theta[z_0 + \Delta z]) = W(z_0)\cos(\theta[z_0]) + (dW/dz)\cos(\theta[z_0])\Delta z - W(z_0)\sin(\theta[z_0])(d\theta/dz)\Delta z$. Using this expansion and dividing by Δz gives Eq. (3.94):

$$0 = F_z + \frac{dW}{dz}\cos\theta - W\sin\theta\frac{d\theta}{dz} \tag{3.94}$$

A similar analysis for forces in the y direction yields Eq. (3.95):

$$0 = F_y + \frac{dW}{dz}\sin\theta + W\cos\theta\frac{d\theta}{dz} \tag{3.95}$$

Adding Eq. (3.94) multiplied by $\cos\theta$ to Eq. (3.95) multiplied by $\sin\theta$ yields Eq. (3.96):

$$0 = F_z\cos\theta + F_y\sin\theta + \frac{dW}{dz} \tag{3.96}$$

Substituting dW/dz from Eq. (3.96) into Eq. (3.94), applying some trigonometric identities, and dividing out a common $\sin\theta$ term yields Eq. (3.97):

$$0 = F_z\sin\theta - F_y\cos\theta - W\frac{d\theta}{dz} \tag{3.97}$$

Because $\tan\theta = dY/dz$, $d^2Y/dz^2 = (1 + \tan^2\theta)(d\theta/dz)$. Therefore, Eq. (3.97) can be rewritten as Eq. (3.98):

$$\frac{d^2Y}{dz^2} = \left(1 + \tan^2\theta\right)\frac{F_z\sin\theta - F_y\cos\theta}{W} \tag{3.98}$$

$E_z(z)$ is defined as the component of the electric field in the z direction at the wire for$z$ coordinate z, and $E_y(z)$ is the component of the electric field in the y direction. $V(z)$ is defined as the voltage present on the wire at z coordinate z. Between a point on the wire (y_0, z_0) and a nearby point on the wire $(y_0 + \Delta y, z_0 + \Delta z)$, $\Delta V = E_y\Delta y + E_z\Delta z = (E_y(dY/dz) + E_z)\Delta z$. Therefore, Eq. (3.99) is written as

$$\frac{dV}{dz} = E_y \frac{dY}{dz} + E_z \tag{3.99}$$

The electrostatic attraction analysis provides an expression for evaluating E_y. Although some E_z component to the field may be present, it is difficult to characterize. The value of E_z is not likely to be large because any charge redistributions driving it will be spread out over the length of the tube; therefore, the approximation $E_z = 0$ can be made. Because E_z is the only source for F_z, F_z can also be set equal to zero. Therefore, for small θ, Eq. (3.100) is written as

$$\frac{d^2Y}{dz^2} = \left(1 + \tan^2\theta\right)\frac{-F_y \cos\theta}{W} = \frac{-F_y}{W\cos\theta} \approx \frac{-F_y}{W} \tag{3.100}$$

To relate this equation to the wire deflection in a detector tube, the y-axis will be associated with the $\theta = 0$ direction in Fig. 3.26. The wire offset from the tube center R_D comes from two sources. One source is the deviation of the wire from straightness, described by the function $Y(z)$. The other source is the deviation of the tube from straightness. Attention will be limited to deviations of the tube in the y-axis direction, with $C(z)$ defined as the deviation of the center of the tube from a straight line between the feedthroughs to which the wire is mounted. The sign convention for $C(z)$ is chosen such that $R_D = Y + C$. Therefore, $D = (Y + C)/R_T$. The source for F_y is the electrostatic attraction of the wire to the tube wall given by Eq. (3.92). Thus, Eqs. (3.101), (3.102), and (3.103) are obtained:

$$\frac{d^2Y}{dz^2} = \frac{-2\pi\epsilon_0 V^2}{WR_T(\ln w)^2} G\left(\frac{Y + C}{R_T}\right) \tag{3.101}$$

$$\frac{dW}{dz} = -F_Y \sin\theta \approx \frac{-2\pi\epsilon_0 V^2}{R_T(\ln w)^2}\frac{dY}{dz} G\left(\frac{Y + C}{R_T}\right) \tag{3.102}$$

$$\frac{dV}{dz} = \frac{-V}{R_T \ln w}\frac{dY}{dz} G\left(\frac{Y + C}{R_T}\right) \tag{3.103}$$

3.2.3.3 Scaling Rule

It is desirable to determine rules for how the deflection of the wire in a detector tube scales with tube construction and operation parameters such as length, diameter, wire tension, straightness, and bias voltage. This determination helps to identify combinations of parameters that pose a risk for catastrophic wire deflection. It also allows results from numerical simulations of wire deflection to be applied to a wider variety of cases.

Parameter $A = 0$ at one side of the tube and 1 at the other side. Parameter $B = 0$ when $Y = 0$ and equals 1 when Y equals the tube radius R_T. Then, $z = LA$ for a tube of length L, and $Y = R_T B$ with

$$\frac{d^2Y}{dz^2} = \frac{R_T}{L^2}\frac{d^2B}{dA^2} \text{ and}$$

$$\frac{dY}{dz} = \frac{R_T}{L}\frac{dB}{dA}.$$

If functions $C_B(A)$ and $V_m(A)$ are defined as

$$C_B(A) = \frac{C(LA)}{R_T} \text{ and}$$

$$V_m(A) = \frac{V(LA)}{V_0}$$

where V_0 is the bias at $z = 0$, then Eq. (3.103) becomes Eq. (3.104):

$$\frac{dV_m}{dA} = \frac{-V_m}{\ln(w)}\frac{dB}{dA}G(B + C_\mathrm{B}) \tag{3.104}$$

Define function $W_m(A)$ as

$$W_m(A) = \frac{W(LA)}{W_0},$$

where W_0 is the wire tension at the feedthrough. Equations (3.101) and (3.102) can be combined to yield

$$\frac{dW}{dz} = W\frac{dY}{dz}\frac{d^2Y}{dz^2},$$

which becomes Eq. (3.105):

$$\frac{dW_m}{dA} = W_m\frac{R_T^2}{L^2}\frac{dB}{dA}\frac{d^2B}{dA^2} \tag{3.105}$$

Then, Eq. (3.101) can be rewritten as Eq. (3.106):

$$\frac{d^2B}{dA^2} = \frac{-2\pi\varepsilon_0 V_0^2 L^2}{W_0 R_T^2(\ln[w])^2}\frac{V_\mathrm{m}^2}{W_\mathrm{m}}G(B + C_\mathrm{B}) = -2\pi\varepsilon_0 K\frac{V_m^2}{W_m}G(B + C_B) \tag{3.106}$$

where

$$K = \frac{V_0^2 L^2}{W_0 R_T^2 (\ln(w))^2} \tag{3.107}$$

which is independent of the distance along the tube and the position of the wire.

Some path is assumed to exist for the wire $B = P(A)$, which satisfies Eq. (3.106) for some choice of V_0, T_0, L, R, w, and $C(z)$. A different set of choices for V_0, T_0, L, R, and w can yield the same value for K, and $C(z)$ can be altered as required to leave C_B unchanged. To within the accuracy that V_m^2/W_m remains unchanged, $P(A)$ still satisfies Eq. (3.106). As long as changes in voltage along the wire are small compared with the applied bias V_0, the value of V_m should remain near 1. As seen in Eq. (3.104), the only tube parameter that affects the determination of V_m is w, and that dependence is weak. W_m is a small correction to the tension on the wire, whose value should remain near 1. As seen in Eq. (3.105), its determination depends on the tube parameter dependent value R_T/L. Although w and R_T/L are terms that appear in Eq. (3.107) for K, their values are not uniquely determined by K. Within the approximation that K independent variations in V_m^2/W_m can be ignored, the wire path B is determined by K and C_B.

3.2.3.4 Numerical Simulation

The length of the wire was divided into 200 equal segments, and arrays were created to list the values of Y, dY/dz, d^2Y/dz^2, C, V, and T at each segment boundary. An iteration cycle used a set of known estimates for d^2Y/dz^2, initially from calculations for an undeflected wire and later from the results of the previous iteration. Starting with $z = 0$, $y = 0$, and an estimate of the slope at $z = 0$ from the previous iteration, the second derivatives were used to extrapolate values for Y and dY/dz to the other end of the wire. This extrapolation was not guaranteed to end up at $Y = 0$ for $z = L$, so a slope correction was then added to all the Y and dY/dz values to force $Y = 0$ at $z = L$. Integrating from $z = 0$, Eqs. (3.102) and (3.103) can be used to determine values of V and T at each segment boundary. Equation (3.101) can then be used to calculate a new set of estimates for d^2Y/dz^2, completing the iteration cycle. Values for $G(D)$ were calculated using polynomial 2 in Figs. 3.27 and 3.28.

Values for the deviation from straightness C were generated from three parameters: the deviation depth D_D, the deviation position P_D, and the deviation length L_D. Equation (3.108) was used in regions where C is positive; $C = 0$ was used elsewhere.

$$C = D_D - \frac{4D_D}{L_D^2}(z - P_D)^2 \tag{3.108}$$

The iterations are not guaranteed to converge on a stable deflection of the wire. If all other parameters are kept the same and only the voltage is varied, then a threshold

voltage is observed. Below the threshold, the wire deviation settles to a stable value. Above the threshold, the deviation increases with each iteration until it encounters the tube wall. For voltages far below the threshold, a small number of iterations is sufficient to converge on a stable deflection. For voltages far above the threshold, the wire reaches the tube wall after a small number of iterations. The number of iterations required becomes large when the voltage is close to the threshold. This threshold likely represents a genuine instability in the wire's behavior, and it can be interpreted as the voltage at which the tube will fail.

3.2.3.5 Simulation Results

The simulation calculations used $L = 1.0$ m, $R = 0.0035$ m, and $R_W = 0.00005$ m (giving $w = 0.01428$). These are typical dimensions for LPSD tubes used in small-angle neutron scattering arrays. A wire tension of 0.115 N was selected to yield threshold voltages consistent with known failures.

A simulation using 100 iterations with an indent position of 0.5 m, an indent length of 0.25 m, an indent depth of 0.00025 m, and bias equal to 1925 V was examined for the variation of the voltage and the tension along the wire. The bias was 1 V under the threshold voltage. The maximum tension observed was 0.115000478 N, a fractional increase of only 4.21×10^{-6}. The maximum voltage observed was 1936.24 V, an increase of 11.24 V, or 0.583%. Changes in wire tension were negligible, and changes in the wire voltage could be considered a small correction, improving the justification for using Eq. (3.48) as a measure of a tube's susceptibility to wire deflections.

A series of threshold voltages for runaway wire deflection were determined while varying the deviation depth and the deviation position. The deviation length was kept at one-fourth of the tube length. Initially, the highest voltage V_{100}, for which the wire does not reach the tube wall after 100 iterations, was determined by varying the voltage in 1 V increments. A sampling of a few cases in which the number of iterations was increased to 1000 revealed that $V_{100} - V_{1000} \approx 4$ V, so $V_{100} - 4$ V was used as a better measure of the threshold voltage. The results are plotted in Fig. 3.29.

A series of threshold voltages for runaway wire deflection were determined while varying the deviation depth and the deviation length. The deviation position was kept at the center of the tube. The results are plotted in Figs. 3.30 and 3.31.

The depth of a deviation from straightness is not by itself sufficient to assess the risk for a tube failure. The position of the deviation along the tube and the length over which it is occurring also have a significant influence.

The threshold voltages are dependent on the detector dimensions and wire tension chosen for the simulation. A more universal way to state the thresholds is in terms of the value of K to which they correspond. Table 3.3 lists the value of K in units of 10^{10} V^2/N for several voltages in the range of interest. The dimensionless quantity $2\pi\epsilon_0 K$, which appears in Eq. (3.106), is also listed.

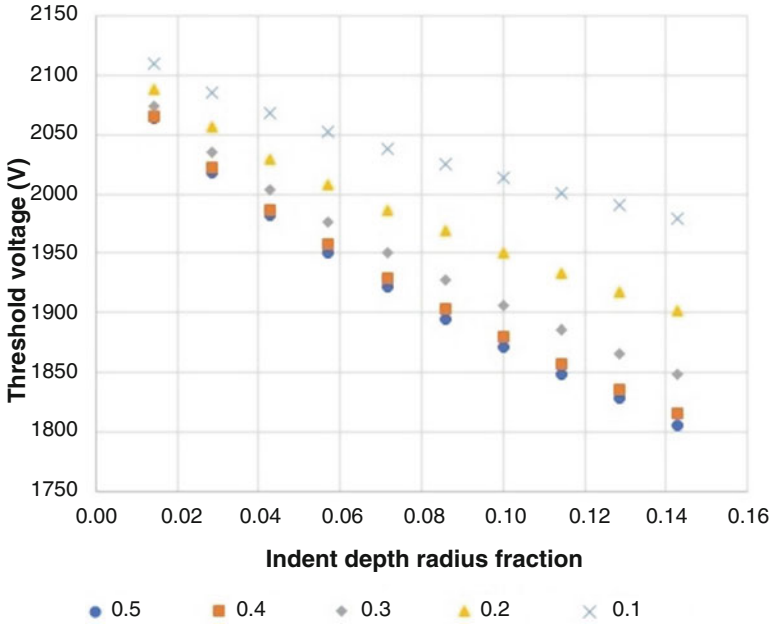

Fig. 3.29 Voltage threshold for runaway wire deflection using an indent length of one-fourth of the tube length. Entries in the legend are the location of the center of the indentation, expressed as the fraction of the tube length from a tube end

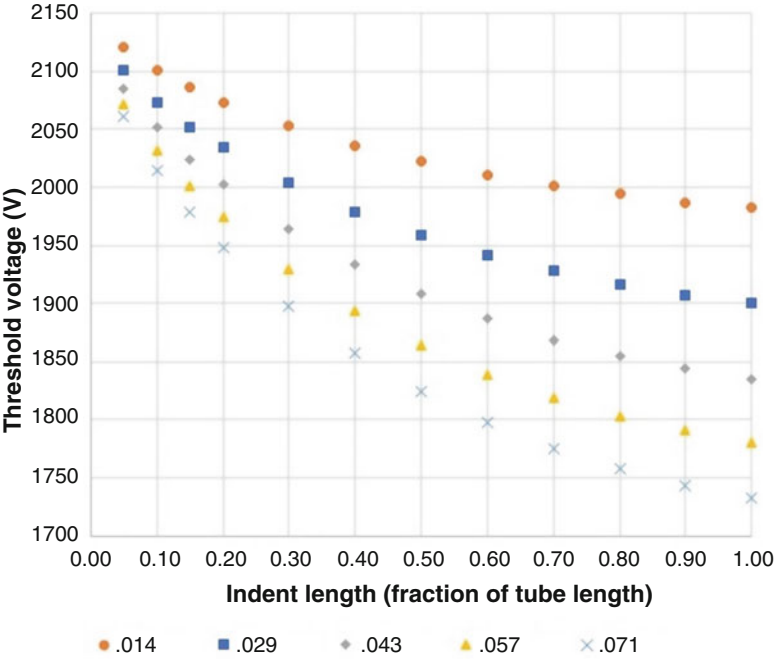

Fig. 3.30 Threshold voltage for runaway wire deflection using an indent position at the tube center. Entries in the legend are the depth of the indentation, expressed as a fraction of the tube radius

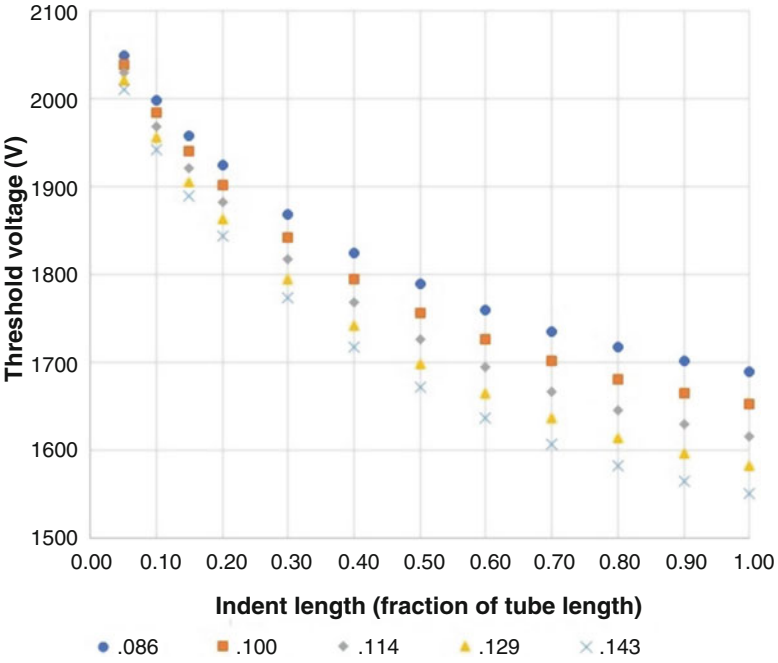

Fig. 3.31 Threshold voltage for runaway wire deflection using an indent position at the tube center. Entries in the legend are the depth of the indentation, expressed as a fraction of the tube radius

Table 3.3 Values of K

Volts (V)	K (10^{10} V^2/N)	$2\pi\epsilon_0 K$
1550	9.448	5.256
1600	10.068	5.601
1650	10.707	5.956
1700	11.366	6.323
1750	12.044	6.700
1800	12.742	7.088
1850	13.460	7.488
1900	14.197	7.898
1950	14.954	8.319
2000	15.731	8.751
2050	16.527	9.194
2100	17.343	9.648
2150	18.179	10.133

3.3 Single-Output Helium-3 Detector Tubes

Helium-3–filled gas-proportional detector tubes can be constructed as position-sensitive detectors or as simple neutron counters. In the first configuration, two outputs are required to provide a way to determine position along the central anode

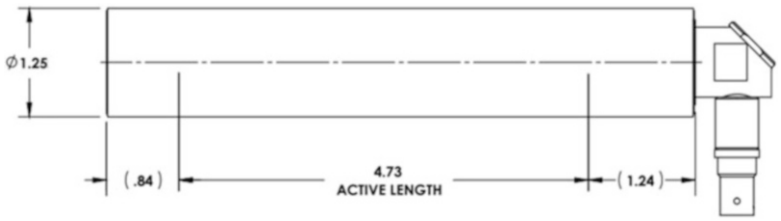

Fig. 3.32 Single-output gas-proportional neutron detector. The anode connector in this example is a right angle–type safe high voltage (SHV) adapter. All dimensions are in inches. (Drawing courtesy of Reuter–Stokes)

wire, either by using resistive charge division or some other method (e.g., time-based encoding using delay lines). If position determination is not required, then a single output suffices. In this instance, the anode wire exits the tube at only one end, and all signal charge is delivered to a single preamplifier. The only information available about the neutron interaction location is that it occurred somewhere within the gas volume.

This section describes the construction and operation of a single-ended ^{3}He detector tube, such as that shown in Fig. 3.32. For the detector in this example, the outer diameter of the tube shell is 3.175 cm (1.25 in.), and the tube length is 17.3 cm (6.8 in.). The enclosed gas is 4 atm of ^{3}He with a trace amount (<0.1 atm) of CO_2 as the quench gas.

An anode wire runs down the center of the tube. Alumina headers electrically isolate the anode wire from the 304 stainless steel outer shell. Two field tubes, one at either end of the anode wire, surround the anode but are of a somewhat larger radius. Referring to Eq. (3.6), a larger inner radius (a) yields a smaller electric field around the field tubes than around the anode wire. This larger inner radius affects a gradual rather than sharp transition region where the electric field decreases to zero, thus minimizing the effect of fringing fields near the ends of the detector active region. The active length, defined as the region between the field tubes, is 12.01 cm (4.73 in.).

The anode wire is accessible outside the tube via a standard right-angle safe high voltage (SHV) type high-voltage connector. Other connector types that can support high voltage, such as Type HN and MHV, may also be used. A biased preamplifier is connected to the anode wire via this connector. The anode is biased to positive high voltage (1350 V in this case) to produce the necessary gas gain. A transimpedance preamplifier with gain equal to 1.8×10^6 V/A provides the output pulses, which are then fed to a counter in the data acquisition system.

The neutron capture efficiency across the tube diameter (within the active region) is shown in Fig. 3.33. This plot shows the efficiency values calculated using Eq. (3.5) (for $\lambda = 2$ Å), scanned across the tube diameter. As expected, the efficiency is greatest at the center, where the diameter, hence the gas depth, is largest, and efficiency diminishes as the gas depth decreases to zero.

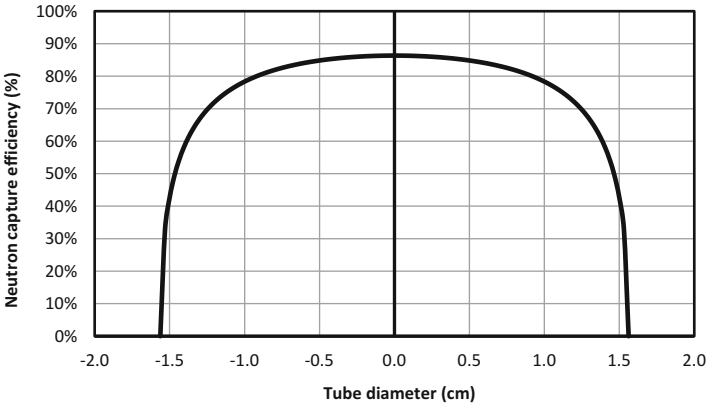

Fig. 3.33 Plot of neutron capture efficiency across the tube diameter. The gas depth, hence efficiency, is greatest at the full diameter (0.0 on the horizontal axis). This plot is for neutron wavelength $\lambda = 2$ Å

Neutrons are absorbed throughout the entire detector active volume. However, interactions that occur very near the inside surface of the tube wall have important ramifications on the distribution spectrum of pulse amplitudes.

For interactions near the wall that occur within the range of either of the reaction products (the proton or triton), the proton or the triton may reach the wall before converting their full kinetic energy into ionization charge. The subsequent signal charge is then reduced by an amount proportional to what was lost to the wall interaction. This reduction is referred to as the *wall effect*.

The wall effect is illustrated by the three examples in Fig. 3.34, corresponding to three different regimes of charge collection, indicated in the pulse amplitude spectrum. In the upper half of Fig. 3.34, the circles represent the cross section of a cylindrical proportional tube, and the anode wire is the dot in the center. The left example represents the case where the proton range exceeds the distance from the neutron interaction point to the wall. If the ^{3}He atom is just inside the surface, then the proton does not contribute to the ionization charge. The resulting signal charge is solely due to the kinetic energy associated with the triton (i.e., $764 - 573 = 191$ keV). As the interaction location moves farther away from the wall, the proton contributes more and more to the ionization charge. This contribution is indicated by the continuum represented by the dotted lines ranging from 191 keV to the full ionization charge of 764 keV. Full ionization charge collection occurs when the interaction location is sufficiently far from the wall that both particles (proton and triton) convert all their respective kinetic energies into ionization. This full ionization is represented by the full-energy peak at 764 keV and the right illustration above the peak.

The example in the center of Fig. 3.34 represents the case where the proton and triton swap roles (i.e., the triton is absorbed by the wall, and the resulting signal charge is reduced by the corresponding ionization deficit). The endpoint in this case,

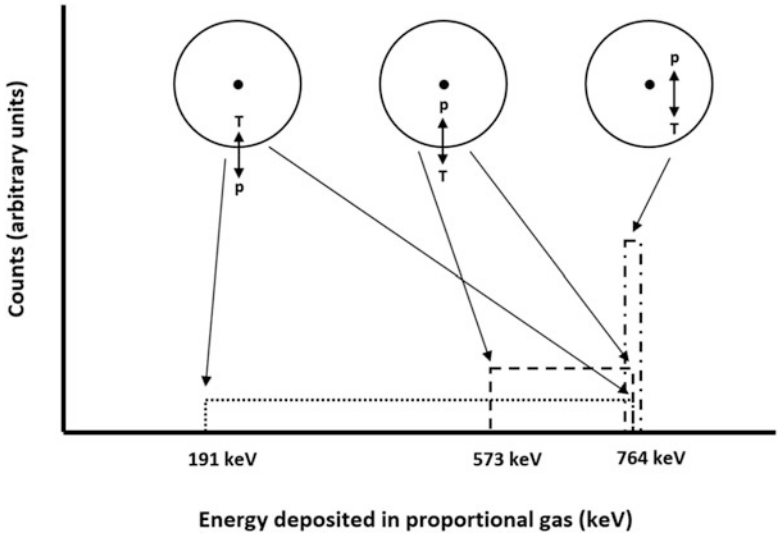

Fig. 3.34 Illustration of wall effect interactions for ^{3}He. T stands for triton, and p stands for proton

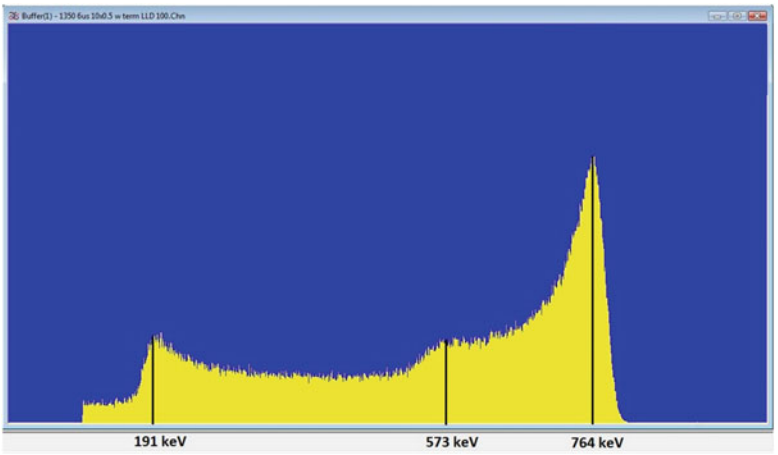

Fig. 3.35 Pulse height distribution for a ^{3}He proportional detector. A low-level discriminator was set to 100 keV (where the distribution abruptly decreases to 0) to reject electronic noise and other non-neutron events from the spectrum

764 keV − 191 keV = 573 keV, occurs when the triton contributes nothing to the ionization charge. The continuum, represented by the dashed lines, ranges from 573 keV to the full energy at 764 keV.

Factors that contribute to the wall effect include gas pressure and composition, tube diameter, and neutron energy (wavelength).

A typical pulse amplitude spectrum for the proportional tube described in this section is given in Fig. 3.35. In practice, electronic noise and other dispersion-

Fig. 3.36 Forty-four single-output tubes comprising a curved 1D detector array. (HB-2A Powder Diffractometer, HFIR)

broadening effects tend to smooth the sharp edges seen in Fig. 3.34, but the essential form is still observed.

Single-ended tubes are used individually (e.g., the triple-axis instruments), or they can be configured as a 1D detector array. The proportional tubes described in this section comprise the curved array at the Neutron Powder Diffractometer instrument at HFIR beamline HB2A. Figure 3.36 is a photo of this array. It consists of 44 single-output tubes, vertically oriented, forming an arc with a radius of 102 cm. Soller-type collimators, one per detector tube, are located just in front of the tubes, pointing toward the sample position to the left in the photo. The green structure is a radiation-shielding monolith, and the three pins support an upper shield plate that is installed during operation.

3.4 Brookhaven National Laboratory 20 cm Multi-Wire Proportional Chamber

An array of 1D position-sensitive detectors can be configured to effectively give 2D, or areal, coverage. One example of this is the ^{3}He-filled gas-proportional LPSD tube. A single tube has position sensitivity in one direction, but when the tubes are placed side by side, a 2D detector array is realized, as illustrated in Fig. 3.37*left*.

However, in this textbook, the terms 2D, or *area*, detectors will refer to a specific class of detector where position encoding exists in two orthogonal directions (e.g., horizontal and vertical). This detector is shown in Fig. 3.37*right*. Often, the two readouts are independent from each other but are combined to provide a 2D map of interaction locations, as determined from the intersection of coincident 1D neutron interactions. Many types of 2D or area detectors exist; in this chapter, the focus is only on those that utilize ^{3}He gas for the conversion medium.

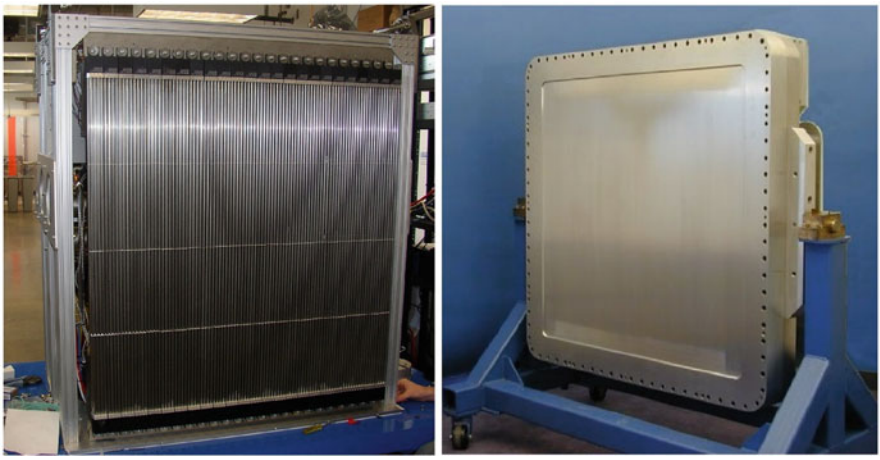

Fig. 3.37 Two methods of achieving 2D, or *areal*, detector coverage. (*left*) A vertical arrangement of individual 1D LPSDs (Reuter–Stokes). (*right*) A detector constructed with true 2D readout (ORDELA, Inc.)

The ^{3}He gas-based area detectors in use at SNS and HFIR can be classified into three types based on the position encoding electronics. The first type was designed and constructed at Brookhaven National Laboratory (BNL) and uses multi-node charge division. The second type was built by DENEX, GmbH and is based on delay line readout. The third type, from ORDELA, Inc., utilizes individual preamplifiers per wire. The BNL detector is described in this section, and the other two types will be described in subsequent sections.

For several decades beginning in the 1970s, the Instrumentation Division at BNL in Upton, NY had a robust program dedicated to research and development of high spatial resolution gas-based neutron detectors [16, 17]. This program was largely in support of the neutron scattering program at the High Flux Beam Reactor, formerly a research reactor on Long Island, NY. Following its shutdown in 1999, 3 of these detectors were made available for use at the SNS. These are multi-wire proportional counters with multi-node charge division and are identical in construction. They are generally referred to as the *Brookhaven detectors* and were among the earliest neutron detectors installed on SNS beamlines. Details of construction and principles of operation are summarized in the following sections.

3.4.1 Details of Construction: Pressure Vessel and Fill Gas

Figure 3.38 shows a photo of the three BNL detectors side by side. To give dimensional perspective, the square regions machined into the 6061-T6 aluminum entrance windows are 20 × 20 cm. This size corresponds with the active region of the detectors. The total enclosed gas pressure is 140 psia, necessitating a machined

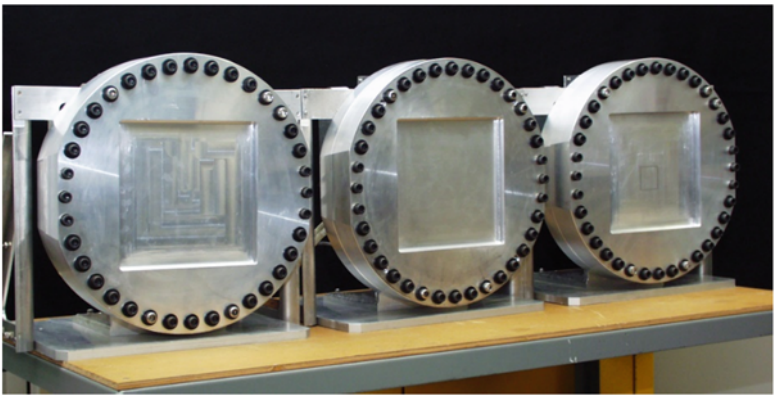

Fig. 3.38 Front view of three 20 cm BNL multi-wire proportional chambers. These detectors were designed and constructed at BNL and delivered to ORNL in 2003 for use in the SNS project

thickness of 9 mm for the aluminum entrance window for minimum deflection under gas load. The detector gas is a mixture of ^{3}He at 100 psia and propane at 40 psia. These partial pressures result from the detection efficiency and spatial resolution requirements. The rationale for these specific values is described in this section.

Helium-3 gas provides the medium for neutron conversion through the nuclear reaction discussed in Chap. 2. Neutron detection efficiency is a function of the total amount of ^{3}He the neutron must pass through; hence, it is related to the product of the gas pressure and gas depth. These detectors were designed to provide a detection efficiency of 80% at 2 Å. Figure 3.39 is a plot of neutron conversion efficiency versus wavelength for a range of ^{3}He gas pressures. This graph is for a gas thickness of 1.5 cm, which corresponds to the gas depth of these detectors. As shown in the figure, this efficiency specification requires a ^{3}He partial pressure just over 6 atm; the Brookhaven detectors contain 6.8 atm (100 psia) ^{3}He gas.

To achieve the desired spatial resolution (<1.5 mm FWHM), the size of the ionization cloud formed during the neutron conversion reaction must be minimized. In the BNL detectors, propane was selected as a stopping gas because of its relatively high stopping power for protons. It has the additional benefit of acting as a quench gas. According to the plot in Fig. 3.40 [19], a propane partial pressure greater than 2 atm provides the proton range necessary to meet the spatial resolution specification. For the BNL detectors, the propane partial pressure is 2.7 atm (40 psia).

The BNL detectors are also equipped with a gas purifier and a gas recirculating pump that operate as a closed-loop system. Electronegative gases, such as oxygen and water vapor, are known to act as electron traps and can degrade detector performance if they are present in large enough concentrations. The gas purifier consists of a stainless cylinder, which is half filled with Ridox (Fisher Scientific; Fair Lawn, New Jersey, USA) and half filled with a 3 Å zeolite molecular sieve. Ridox is an oxygen scavenger, and the molecular sieve adsorbs water vapor. The gas

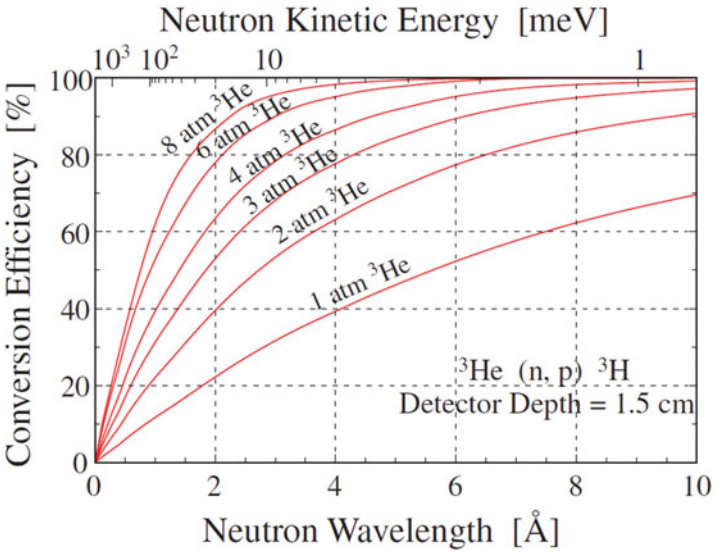

Fig. 3.39 Neutron conversion efficiency versus wavelength for a range of ^{3}He gas pressures. This plot is for a detector depth of 1.5 cm, which corresponds to the BNL 20 cm detectors [18]. Neutron is represented by n, and proton is represented by p

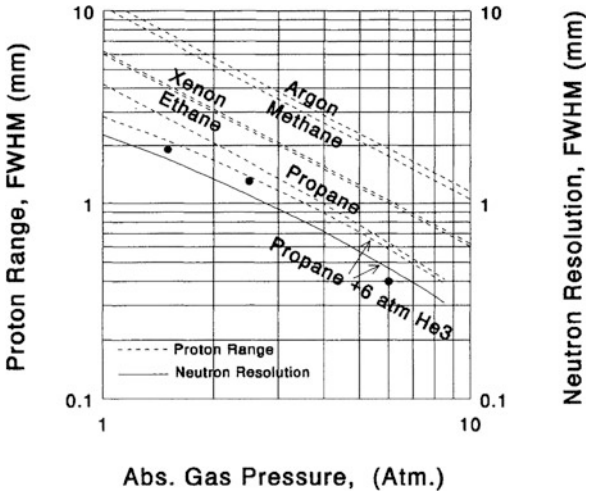

Fig. 3.40 Calculated range of 573 keV protons in various stopping gases as a function of gas pressure (dashed lines). The solid curved line in the middle of the figure represents the calculated neutron spatial resolution for propane combined with 6 atm ^{3}He. The dots are measured data for the spatial resolution with this gas composition [19]

recirculating pump operates continuously by forcing gas through the purifier at a rate of 1–2 L/min. The pump and purifier are identified in the photo in Fig. 3.41.

Two concentric elastomer O-ring seals contain the detector gas. However, these detectors lose gas pressure at an observed loss rate of approximately 3–4 psi/year. The loss of gas pressure results in a noticeable increase in gas gain, which requires a

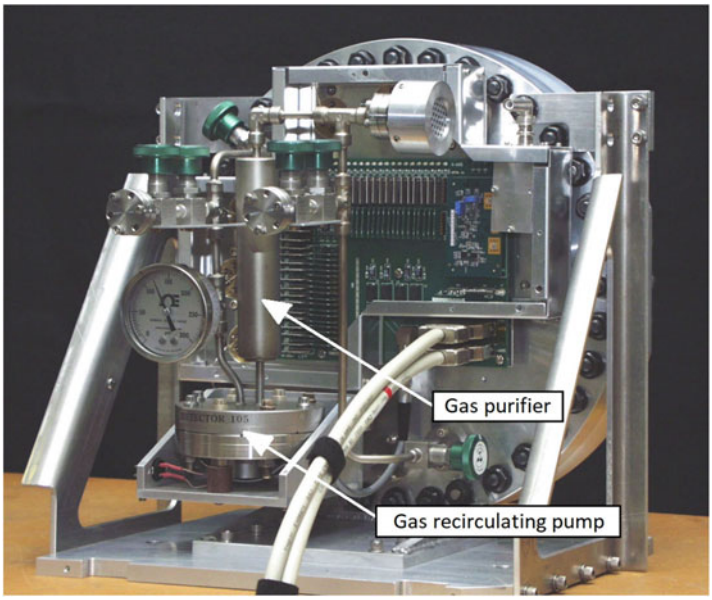

Fig. 3.41 Rear view of the Brookhaven 20 cm detector. The gas recirculating pump and gas purifier are labeled in the figure

periodic (roughly annual) adjustment of the anode voltage to maintain a reasonable anode signal amplitude (i.e., within the range of the sampling ADC). After a period of several years, the gas pressure decreases to the point at which the detector must be restored to original operating conditions. To date this restoration has been achieved by adding only ^{3}He gas under the assumption that the permeation rate of helium far exceeds that of propane.

3.4.2 Details of Construction: Wire Grids and Preamplifiers

Internal electrode construction consists of a single anode grid at positive high voltage sandwiched between two orthogonally oriented cathode grids at ground potential, which are referred to here as the x and y cathode grids. Traversing the detector gas volume from front to back, the first electrode encountered is the y cathode readout grid, then the anode grid, followed by the x cathode readout grid. The spacing between wire grid planes is 1.59 mm (1/16 in.). Figure 3.42 shows a section view of the three grid planes.

The y cathode grid comprises 226 wires, and each wire is 50 μm in diameter. The wires are electrically connected in pairs. The spacing between each wire pair is 1.59 mm (1/16 in.). These wires run horizontally relative to the orientation in Fig. 3.38. Thus, they provide information to determine the y, or *vertical*, coordinate.

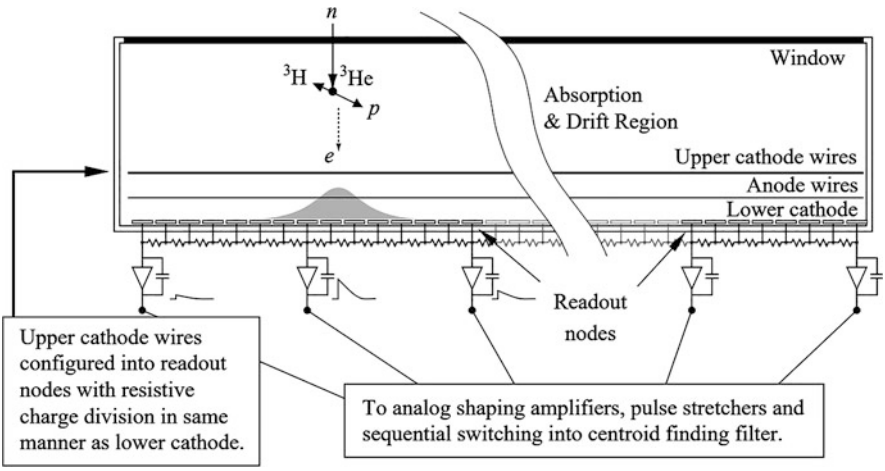

Fig. 3.42 Diagram showing the three grid planes inside the BNL 20 cm detector. The uppermost grid is the *y* cathode wire grid readout, and the bottom grid is the *x* cathode strip grid readout. The anode wire grid is sandwiched between the two cathode grids. Preamplifier readout nodes are connected to every seventh wire or strip. Chip resistors between each wire or strip create a resistive charge division network between preamplifier nodes [20]

At one end of the *y* cathode grid, 15 kΩ chip resistors are soldered between each wire pair to form a resistor chain. A series of charge-sensitive preamplifiers are attached to provide the output of every seventh cathode wire, forming a charge-division network between neighboring preamplifiers. The *y* cathode grid comprises 17 charge-sensitive preamplifiers. The distance between adjacent preamplifiers is 11.1 mm, and the width of the *y* cathode grid is 178 mm.

The anode grid comprises 112 gold-plated tungsten wires, each of a diameter of 12 μm. The wire spacing is 1.59 mm (1/16 in.). These wires run in the same direction (horizontally) and in registry with the wire pairs in the *y* cathode grid. Two guard wires of larger diameter are located on each side (four in total) to reduce electric field fringing at the edges.

The *x* cathode grid is farthest back on the detector, closest to the rear of the detector vessel, and is comprised of 134 vertically oriented copper strips vacuum deposited onto a glass plate. The strip width is 1.016 mm, and the pitch is 1.59 mm (1/16 in.). Like with the *y* cathode grid, 15 kΩ chip resistors are soldered between adjacent strips. A charge-sensitive preamplifier is connected to every seventh strip. Twenty preamplifiers are placed on the *x* cathode grid. The width of the *x* cathode grid is 211 mm.

In addition to these three grid electrodes, a copper coated Kapton drift electrode is attached to the inside of the front entrance window. It is electrically isolated from the detector housing and is negatively biased to provide an adjustable component to set the electric drift field within the detector gas volume.

3.4.3 Principle of Operation

Previously, this chapter described the process by which a neutron is captured in ^{3}He gas. The resulting ionization charge for these detectors is estimated to be approximately 25,000 electron–ion pairs, or 4 fC. The anode grid is positively biased, typically around 2 kV, and the drift electrode is negatively biased at around 1 kV. These two electrodes set the planar electric drift field to approximately 2 kV/cm. The primary ionization charge (electron–ion pairs) drifts through this constant electric field region, with electrons being pulled toward the anode grid and ions toward the drift electrode.

No gas gain occurs in this drift region. As the electrons approach within one wire spacing of the anode wire plane (1.6 mm), the field increases rapidly, approximating the coaxial $1/r$ form very near the wires. Here, the electric field values become sufficiently large that a charge avalanche can occur. These detectors are designed to operate with a relatively low gas gain of approximately 25 to minimize the known detrimental effects on detector longevity from extended high gas gain operation. Thus, the event charge collected at the anode is approximately 100 fC (25 × 4 fC). Less than half of this charge, approximately 40 fC, is induced onto the two orthogonal cathodes and provides the current signal used for position calculations.

An external motherboard contains 37 (20 for the x readout, 17 for y) sets of front-end electronics, namely charge-sensitive preamplifiers paired with signal buffer/driver boards. These boards convert the 40 fC signal charge to a voltage pulse of an amplitude of approximately 100 mV. The boards also provide a 50 Ω differential output to drive these analog signals along shielded, twisted pair cables to the signal-shaping and digitizing electronics. Figure 3.43 shows a picture of this motherboard. The preamplifiers and buffer/driver boards are identified in the photo. A detailed description of the detector front-end electronics is found in [21].

The charge signal from the anode grid is sent to a discriminator circuit. When the anode signal exceeds a programmed threshold, the anode trigger module initiates the data collection process, and the outputs from all 37 preamplifiers are individually digitized in 12-bit ADCs (1 per channel). The channel with the largest amplitude is identified, and the signal charge from it and its two adjacent neighbor channels are used in the calculation of the neutron interaction location, which is based on Eq. (3.109).

This operation is performed separately and independently for the x and y cathode grids. The individual x and y positions are combined in software to provide an (x, y) coordinate pair for each event and a time stamp coincident with the firing of the discriminator. The entire process occurs within an event processing time of just over 4 μs.

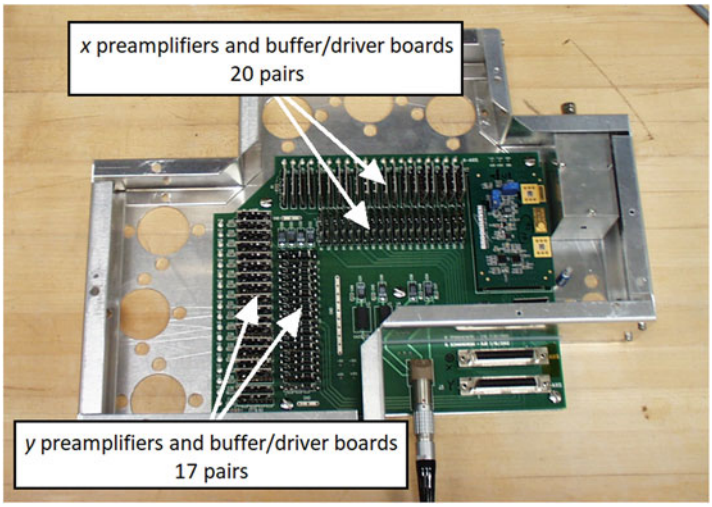

Fig. 3.43 Front-end electronics motherboard with rows of *x* and *y* preamplifiers and buffer/driver boards. In the lower right corner of the photo, two 50-pin signal connectors and the power input cable are also shown. The motherboard is installed on the rear of the gas detector, as seen in Fig. 3.41

The BNL detector is designed such that the signal charge is collected on two or (at most) three cathode wires (or strips). The mathematics of the position calculation is described in the following eqs.

B represents the measured charge in the channel with the largest charge signal. *A* and *C* represent the measured charge in the two channels adjacent to *B* (one on each side). The calculation is performed using Eq. (3.109):

$$P = \frac{C - A}{A + B + C} \tag{3.109}$$

The 210 kΩ resistance chain (15 kΩ × 14) between preamplifiers *C* and *A* is treated as a resistive charge-division network. The value of *P* ranges from −1 to +1, depending on the relative strengths of charges *A*, *B*, and *C*. A few examples are evaluated in the following three cases.

In case 1, if the neutron event is centered over *B*, then $A \approx C$, and $P = 0$.
In case 2, if the neutron event is midway between *B* and *C*, then $B \approx C$, $B \gg A$, and $C \gg A$. For this case, $P = C/(B + C) = +0.5$.
In case 3, if the neutron event is midway between *A* and *B*, then $P = -0.5$ (using the same argument as case 2).

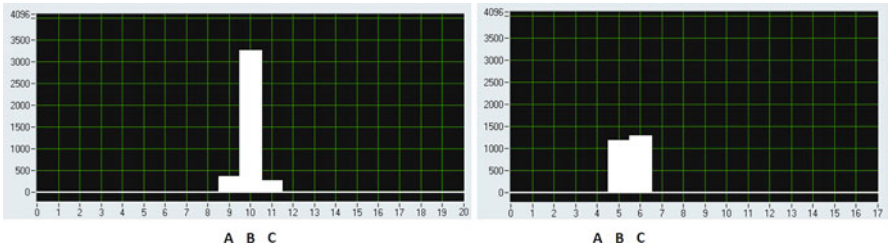

Fig. 3.44 Images illustrating the concept of position determination using two or three adjacent preamplifier outputs. The left figure shows the induced signal charge centered over preamplifier B ($A \approx C$, case 1 in the text), and the right figure shows induced signal charge midway between preamplifiers B and C ($B \approx C$, with $B \gg A$ and $C \gg A$, case 2 in the text) [22]

As Eq. (3.109) suggests, P can take on a continuum of values. When the neutron event location approaches A (or C), it then becomes the dominant charge output, and the wire assignments for A, B, and C all shift one wire over, but Eq. (3.109) is otherwise evaluated in the same way.

Once P is determined and assigned to its associated preamplifier channel (along either the x or y direction), the specific pixel is defined. The denominator is the summed charge from all three preamplifiers (A, B, and C) included in the expression to normalize the value to account for any variation in total signal charge. Representative examples of this calculation are illustrated in Fig. 3.44.

A neutron-absorbing pinhole and slit mask was constructed from 5 mm thick boron-doped aluminum. Figure 3.45 shows the hole and slit dimensions of this mask and the 2D neutron image through the mask. Figure 3.45 clearly shows the fine spatial resolution of this detector.

3.5 Brookhaven National Laboratory 120° Curved Multiwire Proportional Chamber

In 2002, BNL delivered a curved, 2D multiwire ^{3}He gas-proportional detector to Los Alamos National Laboratory to be installed on the new Protein Crystallography Station flight path FP15 at the Los Alamos Neutron Science Center. It utilized essentially the same internal design, construction, and operational parameters as the 20 cm multiwire proportional detectors but this time incorporating eight curved readout grids to create a seamless active area approximately 20 cm high and 150 cm wide, spanning a 120° arc with the radius of the curvature equal to 70 cm. This detector remained in operation at the Protein Crystallography Station from 2002 until the instrument was scheduled for decommissioning in 2015, and then it became available to the neutron scattering user program at ORNL. An instrument upgrade project was initiated and approved to (1) transport the detector to ORNL and (2) upgrade the data acquisition interface to be compatible with the standardized

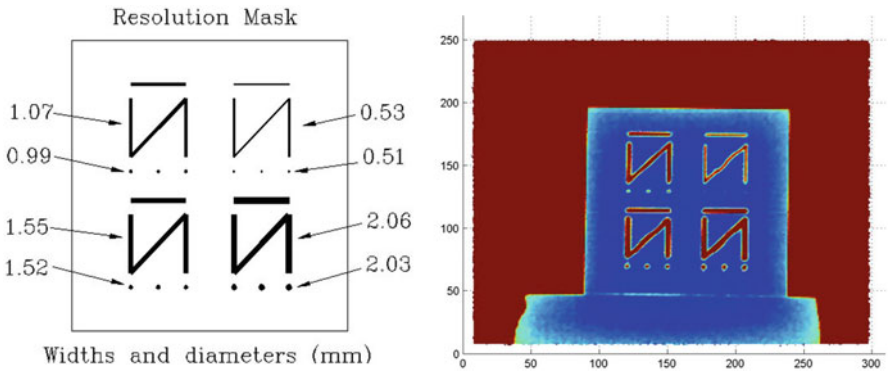

Fig. 3.45 The drawing on the left shows the dimensions of pinholes and slits in the neutron absorbing mask (5 mm thick borated aluminum) used to produce the image on the right

EPICS-based software platform used at SNS and HFIR. Staff from Los Alamos National Laboratory and BNL were integral to the success of this project. The 120° curved multiwire proportional chamber (MWPC) is one of two such BNL-built detectors in existence—the other one is currently in operation at the Wombat powder diffractometer at the Australian Nuclear Science and Technology Organisation.

3.5.1 Details of Construction: Pressure Vessel and Fill Gas

Owing to the much larger window area compared with the 20 cm detectors, the main detector housing was constructed from a higher strength aluminum alloy (7075-T6). The tensile strength of 7075-T6 is 73,000 psi compared with 40,000 psi for 6061-T6, which was used for the 20 cm detectors. The entrance window is 8 mm thick. The upper flange plate is made from 304 stainless steel and contains the feedthrough flanges for the preamplifiers and the high voltage inputs. Two gas recirculating pump and purifier assemblies are attached to the detector body (one at either end). These components are shown in Fig. 3.46. For the reasons outlined in Sect. 3.4.1, the gas composition and pressure are the same as for the BNL 20 cm detectors (i.e., ^{3}He at 100 psia and propane at 40 psia).

3.5.2 Details of Construction: Wire Grids and Preamplifiers

The readout grids are of essentially the same design as the 20 cm detectors (i.e., horizontal and vertical wires and strips). For ease of construction, the 120° readout grid structure was subdivided into eight identical segments, each subtending 15°

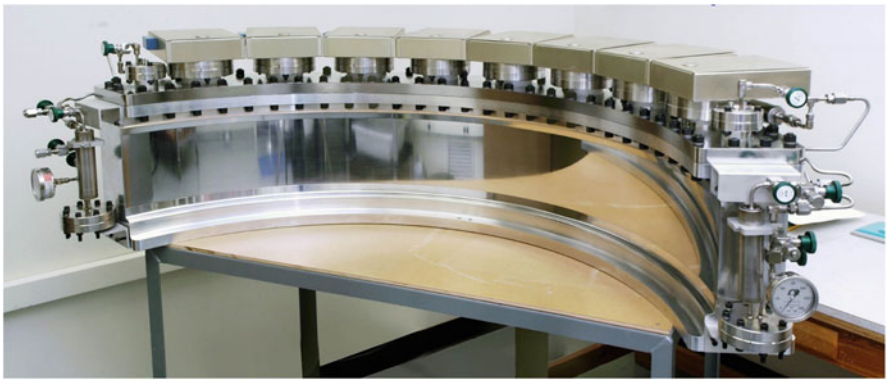

Fig. 3.46 The BNL 120° multiwire proportional detector [18]

horizontally and 15° vertically (relative to the 70 cm radius of curvature). Like the 20 cm detectors, each segment consists of an anode grid in between two orthogonal cathode grids.

However, the requirement for a curved, seamless readout led to a significant design change compared with the planar wire and grid construction used in the 20 cm detectors. Specifically, the curved wire and grid assembly required swapping the orientation of the cathode wires and strips. For the 20 cm detectors, the vertical copper strips defining the *x*-axis readout were furthest from the entrance window so as not to impede charge transport to the anode grid. The much-less-intrusive horizontal wires defining the *y*-axis were located closer to the front of the detector. Rather than attempt a horizontal curved wire design, the readout grid for the 120° detector consists of horizontal copper strips on a curved substrate for the vertical (*y*-axis) readout, which is located furthest from the entrance window, and the less-intrusive vertical wire grid for the *x*-axis readout is closer to the entrance window. The anode wires are vertically oriented and in registry with the *x*-axis cathode wire grid.

The front cathode grid comprises 120 wires, each 50 μm in diameter on a 1.59 mm (1/16 in.) wire pitch. These wires are vertically oriented, thus providing information to determine the *x*, or horizontal, coordinate. The chip resistors are 11 kΩ. Charge-sensitive preamplifiers are attached to provide the output of every eighth cathode wire. This setup forms an 88 kΩ charge-division network between adjacent preamplifiers. The *x* cathode grid comprises 15 charge-sensitive preamplifiers (per segment).

The anode grid consists of 120 gold-plated tungsten wires, each with a 15 μm diameter. The wire spacing is 1.59 mm (1/16 in.). These wires run in the same direction (vertically) and in registry with the *x* cathode grid.

The *y* cathode grid, which is closest to the rear of the detector vessel, comprises 129 horizontally oriented copper strips on a ceramic substrate. The strip width is 1.016 mm, and the pitch is 1.59 mm (1/16 in.). The *y* cathode grid uses 6.25 kΩ chip

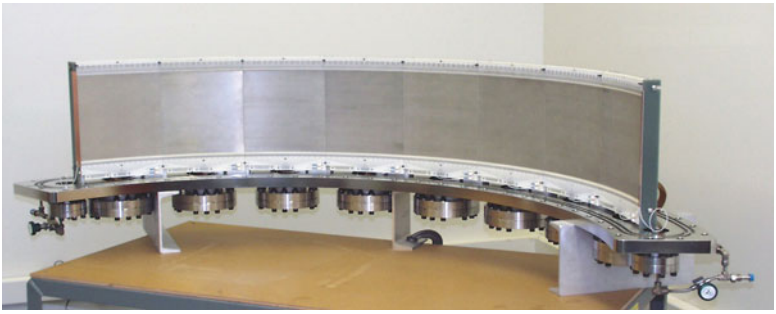

Fig. 3.47 Photo of the eight-segment wire and strip readout assembly [23]

resistors between adjacent strips. Charge-sensitive preamplifiers are present every eighth strip. Along the *y* cathode grid are 17 preamplifiers (per segment).

All eight segments abut to produce a continuous and seamless detection response over the entire 120° span. Figure 3.47 shows a photo of the eight-segment readout grid assembly.

3.5.3 Principle of Operation

Functionally, each of the eight segments has its own dedicated, parallel, and identical signal processing electronics such that the 120° detector operates like eight individual detectors. Thus, detector operation is largely the same as for the 20 cm detectors that are described in Sect. 3.4.3. The main difference is in how the boundaries between segments are treated. Figure 3.48 illustrates how the physical interface between two adjacent segments is realized. The distance between each vertical boundary wire and the substrate edge is half the wire pitch, so when two adjacent segments are abutted side by side, the interwire spacing is maintained across the boundary. Each boundary anode wire is bussed to its neighboring boundary anode wire in an adjacent detector segment and connected to a separate boundary anode preamplifier. When an event is triggered by the anode boundary preamplifier, the leftmost *x* boundary cathode (as viewed from the sample position) is disabled, and the rightmost *x* boundary cathode wire is used for the edge position calculation. Only enabling the rightmost *x* boundary cathode avoids double counting at the segment boundary. The principles of operation outlined in Sect. 3.4.3 Principle of Operation are otherwise applicable for the 120° detector as well.

Figure 3.49 shows a powder diffraction pattern from a silicon sample. The 120° coverage enables simultaneous data collection of the forward and backward scattered Debye–Scherrer cones.

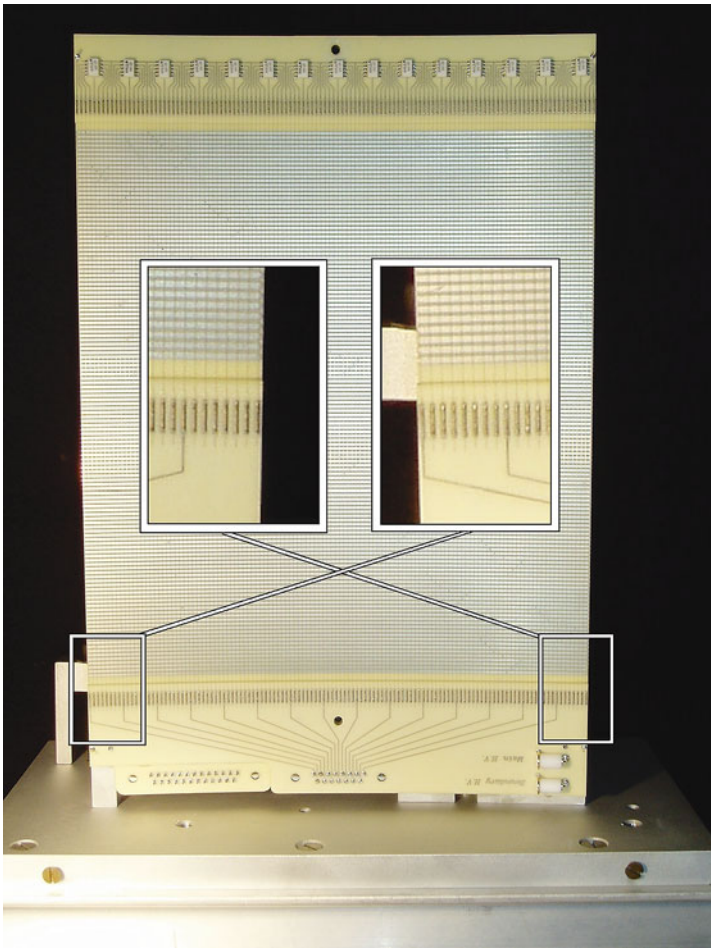

Fig. 3.48 Photo of one of the 8 readout segments seen in Fig. 3.47. In this view, the wires run vertical and the strips run horizontal. A portion of the left and right edges are seen in the two insets. When two of these segments are abutted side by side, both the vertical wire pattern and horizontal strip pattern are reproduced across the interface, generating a seamless readout [24]

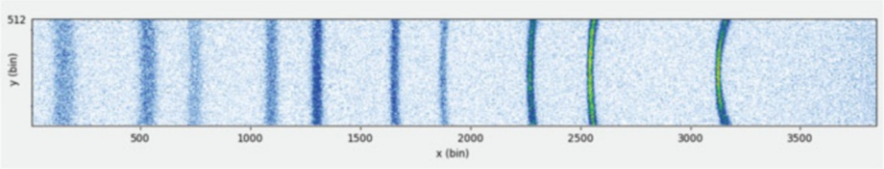

Fig. 3.49 Diffraction pattern from a powdered silicon sample [25]

3.6 Denex Delay Line Detector

The DENEX model DNX-300TN is a ^{3}He-filled neutron detector that utilizes delay line encoding for position determination. Unlike charge-division readout, delay line detectors rely on a comparison of the relative arrival times of the current signals along a 1D line. Combining the results from two orthogonal delay lines provides the (x, y) coordinate pair, which defines the neutron interaction location.

3.6.1 Details of Construction: Pressure Vessel and Fill Gas

Figure 3.50 shows the front view of the detector vessel. The aluminum front plate is machined thinner in the region defining the active area, consistent with the competing needs of containing the pressurized gas with minimal deflection in the entrance window and minimizing neutron scattering from the aluminum. The window thickness is 10 mm, and the machined recess is 30 × 30 cm.

The detector fill gas consists of ^{3}He at a pressure of 4 bar and CF_4 at 2 bar. US Department of Transportation regulations restrict the transportation of noncompliant pressurized gas vessels above a gauge pressure of 2 bar; therefore, the DENEX detector was shipped to ORNL with only the 2 bar (absolute) of CF_4 gas (99.99%

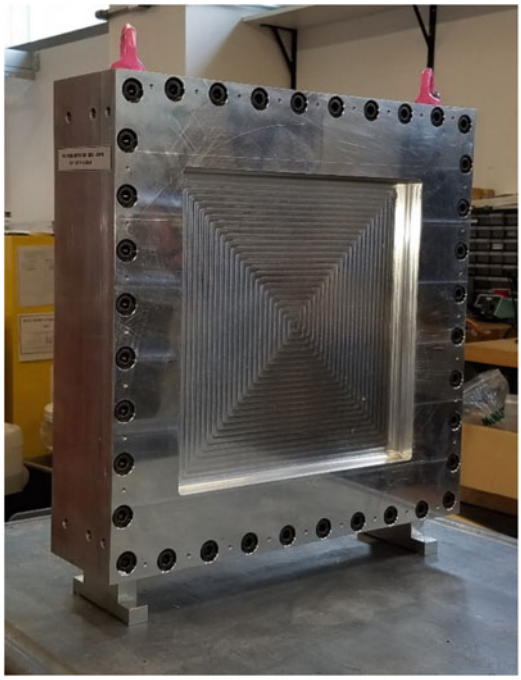

Fig. 3.50 Front view of the DENEX model DNX-300TN neutron detector. The active area is 30 × 30 cm, indicated by the machined recess in the aluminum entrance window

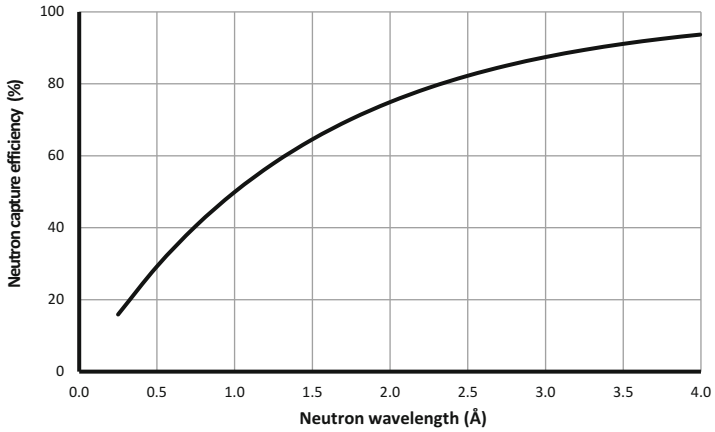

Fig. 3.51 Neutron conversion efficiency of the DENEX-300TN as a function of neutron wavelength

pure). The ^{3}He gas (99.999% pure) was added once it arrived on site. As previously discussed, ^{3}He gas is for neutron conversion, and CF_4 serves as both the quench and the stopping gas. The neutron efficiency versus wavelength curve for this ^{3}He gas pressure (4 bar) and gas depth (22 mm) is shown in Fig. 3.51.

The DENEX detector utilizes an all-metal seal (indium foil) to contain the pressurized gas; thus, loss of gas pressure is expected to be practically nonexistent. A pressure sensor is installed on the detector vessel to give a reading of detector fill gas pressure. This sensor is shown in the detector rear view in Fig. 3.52. The pressure sensor output drifts slightly with changes in room (and detector) temperature, but no decrease in pressure has been observed during the several years that the detector has been in operation.

3.6.2 Details of Construction: Wire Grids and Preamplifiers

The internal construction of the DENEX delay line detector consists of an anode grid at positive high voltage sandwiched between two orthogonally oriented cathode grids at ground potential. Delay line detectors rely on a comparison of the relative arrival times of the current signals at either end of a 1D (x or y) cathode. Signal propagation speeds in metallic wires are generally much too fast for any meaningful separation of these two signals in time, so they must be slowed for delay line detectors to operate effectively. In the case of the DNX-300TN, this propagation delay is achieved via a network of discrete LC (inductor/capacitor) elements along both the horizontal (x) and vertical (y) axes.

Preamplifiers are attached at the ends of each propagation delay line—two for x and two for y—to measure the relative arrival times of these current pulses. The neutron position is determined by examining the relative timing of these pulses.

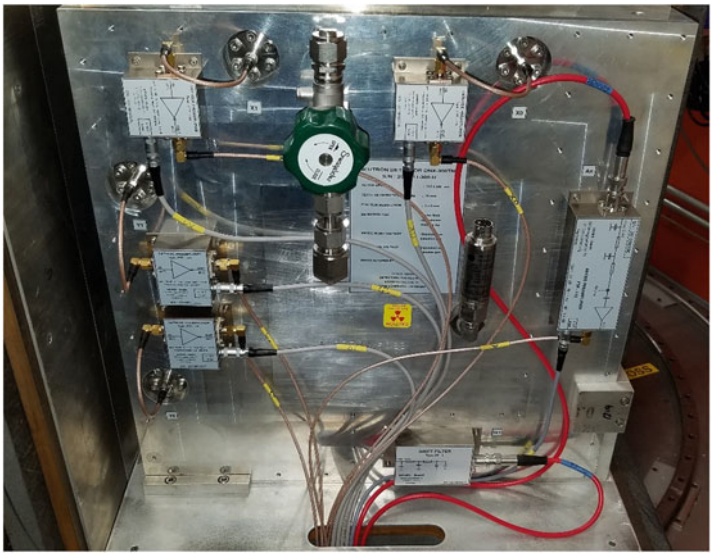

Fig. 3.52 Rear view of the DENEX model DNX-300TN neutron detector. The gas fill valve is just left of center, and the pressure sensor is just right of center. The anode and cathode preamplifiers and high-voltage filters are inside the white labeled boxes

Position determination is performed independently for x and y channels, and the intersection determines the coordinate. A fifth preamplifier records the output of the current signal on the anode grid and acts as the T_0 trigger on which to base the time measurements. These five preamplifiers (two for x, two for y, and the anode) are shown in the detector rear view in Fig. 3.52.

A drift electrode is epoxied to the inside of the front entrance window. It is a layered aluminum and Teflon assembly that is negatively biased (−1200 V) to help set the electric drift field. It is electrically isolated from the detector vessel housing.

The y cathode is located 5 mm from the inside surface of the entrance window. It consists of 300 horizontally oriented wires on a 1 mm pitch. The cathode wires are 30 μm diameter gold-plated tungsten/rhenium at ground potential. LC delay components connect each adjacent wire, yielding a roughly 1.7 ns delay between wires. This delay forms the vertical delay line. The summed propagation delay over the entire 299 mm length of the y cathode is 508 ns. Two preamplifiers are attached to the y delay line, one at either end. The y cathode acts as a 1D PSD.

The anode grid is located 5 mm behind the y cathode. It consists of 150 horizontal wires on a 2 mm pitch. The anode wires are also gold-plated tungsten/rhenium but with a 12 μm diameter. The anode wires are bussed together and connected to a single preamplifier output. The anode grid is positively biased (+4000 V) during operation.

The x cathode sits 5 mm behind the anode grid. It is identical in construction to the y cathode, but here, the wires run vertically. Like the y cathode, the x cathode has two preamplifiers, one at either end of the horizontally oriented delay line, which also act as 1D position-sensitive detectors independently from y.

3.6.3 *Principle of Operation*

Like the other detectors in this chapter, the process of neutron detection begins with neutron conversion in the ^{3}He gas, resulting in a primary ionization charge. The positively biased anode grid and the negatively biased window electrode create an electric drift field to separate the charges. The electrons drift toward the anode, where gas gain begins to occur at roughly 2 mm from the anode wire grid. Current signals are induced on the nearest *x* and *y* cathode wires.

These current signals travel to the ends of the delay lines, divided according to the line impedance between the interaction point and the nearest preamplifier. The line impedance is proportional to the length of delay line, which allows the position determination to be realized. These four cathode preamplifier signals, two each for *x* and *y*, are sent to the five-channel main amplifier along with a charge signal from the anode grid. The main amplifier provides voltage gain. An oscilloscope image of the four cathode preamplifier outputs is shown in Fig. 3.53.

The five signals from the main amplifier are individually fed into a constant fraction discriminator (CFD) for a more precise pulse time determination. Because pulses of different amplitude often have different rise times, threshold triggering is

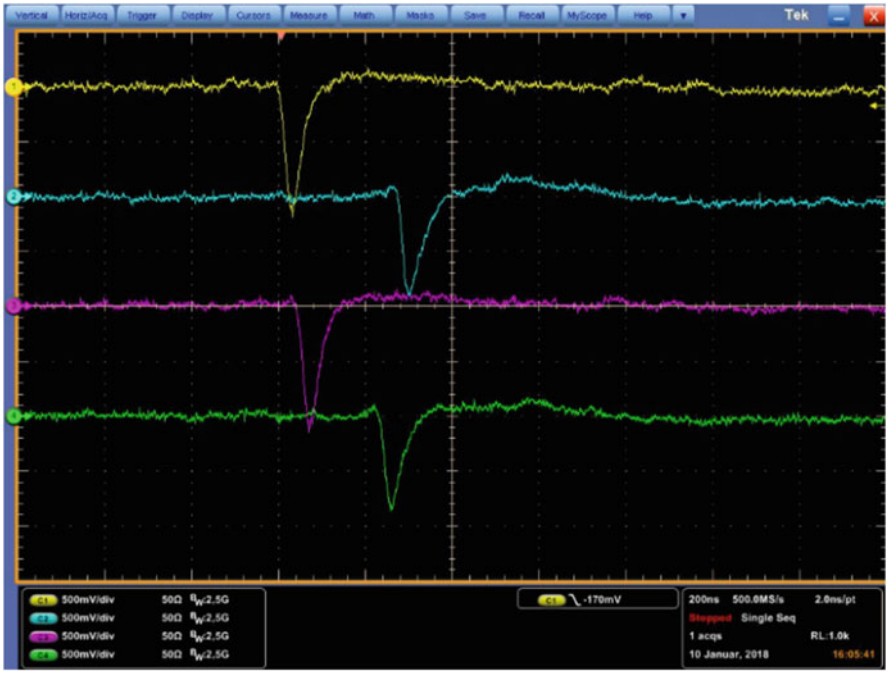

Fig. 3.53 Oscilloscope traces from the four preamplifier outputs (two for *x* and two for *y*) of the DENEX-300TN detector. The vertical scale is 500 mV/division, and the horizontal scale is 200 ns/division

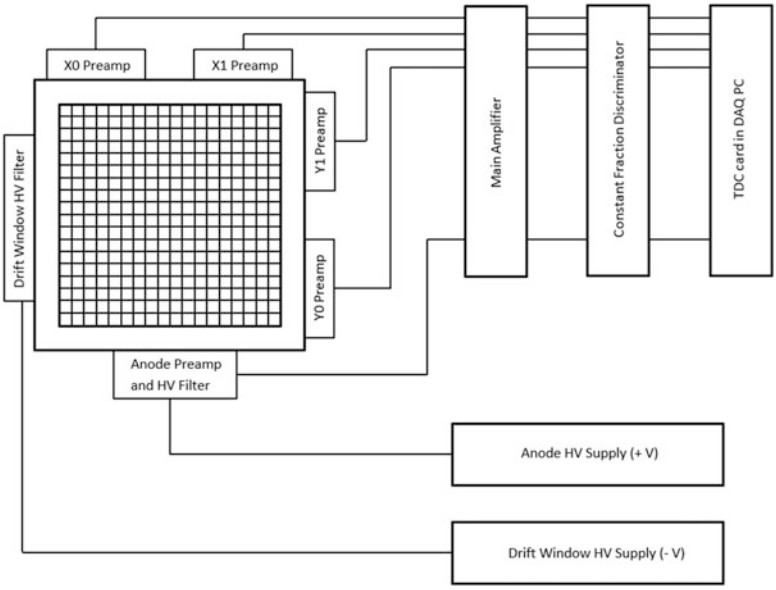

Fig. 3.54 Component and cabling diagram of the signal processing chain. Signals from the four cathode preamps (two for *x* and two for *y*) and the anode preamp are fed to a main amplifier, followed by a constant fraction discriminator, then to a time-to-digital convertor (TDC) card (installed in the data acquisition computer) for timing analysis, which allows for position determination

not a practical technique for applications in which precise timing is required. The role of the constant fraction discriminator is to identify a fixed fraction of the rise time for each pulse, independent of pulse amplitude.

A step-pulse timing signal is then delivered from the constant fraction discriminator to a time-to-digital convertor card (one for each preamplifier) to calculate the propagation time along each axis. From this propagation time, the location along both the *x* and the *y* axes is determined. The neutron interaction location is defined by the intersection of the independent *x* and *y* measurements. Figure 3.54 shows a layout of the main components in the signal processing chain.

As an illustration of the capabilities of this detector, the powder diffraction image from a sample of NAC ($Na_2Ca_3Al_2F_{14}$) is shown in Fig. 3.55. The detector is located at approximately $2\theta = 90$-degrees, hence both forward and backscattered Debye-Scherrer cones are visible in the image.

3.7 Ordela Preamplifier per Wire Detector

The ORDELA model 2410N detector is a ^{3}He-filled 2D position-sensitive proportional counter, which incorporates a preamplifier per cathode wire design. The detector active volume is a 40.6 × 40.6 × 2.5 cm gas depth. This detector was

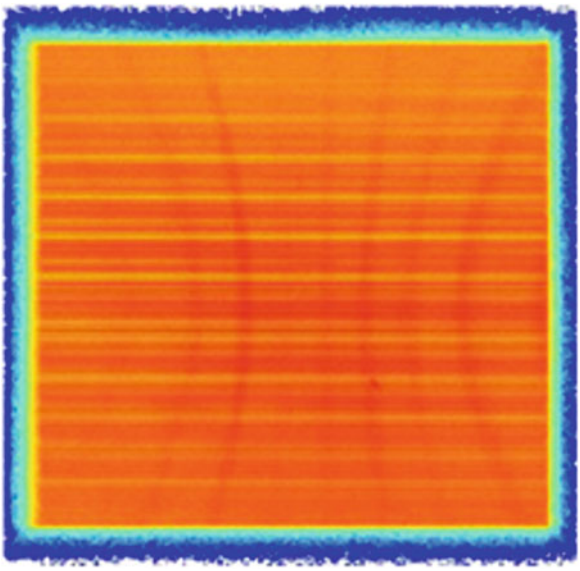

Fig. 3.55 Powder diffraction from NAC sample ($Na_2Ca_3Al_2F_{14}$)

originally built for the Intense Pulsed Neutron Source (IPNS) at Argonne National Laboratory, but it was brought to ORNL following the closure of the IPNS in 2008.

3.7.1 Details of Construction: Pressure Vessel and Fill Gas

The ORDELA 2410N is shown in Figs. 3.56 and 3.57. The pressure vessel is constructed from 6061-T6 aluminum, and the entrance window is machined to a thickness of 10 mm to define the active area of 40.6 × 40.6 cm. The detector gas composition is 1.78 atm ^{3}He plus 0.80 atm CF_4, which provides a nominal 50% detection efficiency at 2 Å. The signal processing electronics, power supplies, and cabling are in an electronics compartment located directly behind the detector, which can be sealed with an air-tight cover for vacuum operation.

3.7.2 Details of Construction: Wire Grids and Preamplifiers

The internal construction consists of three multiwire electrode grids: two orthogonal cathodes at ground potential and one anode grid at positive high voltage. Like the other multiwire designs, the anode grid is positioned between the two cathode grids. Traversing from front to back, the first grid is the *y* coordinate cathode, located 0.75 cm from the inside surface of the entrance window. The *y* cathode grid consists of 128 active wires and an additional 3 wires at each end of the grid (6 total), which

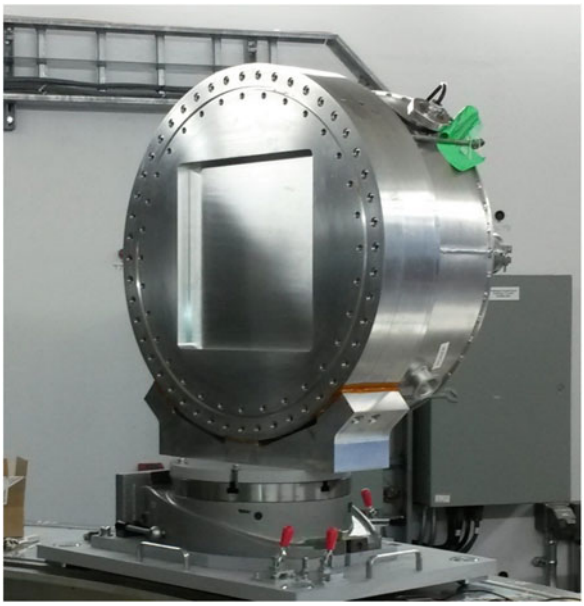

Fig. 3.56 Front view of the ORDELA 2410N detector. The 40.6 × 40.6 cm entrance window is machined to a thickness of 10 mm

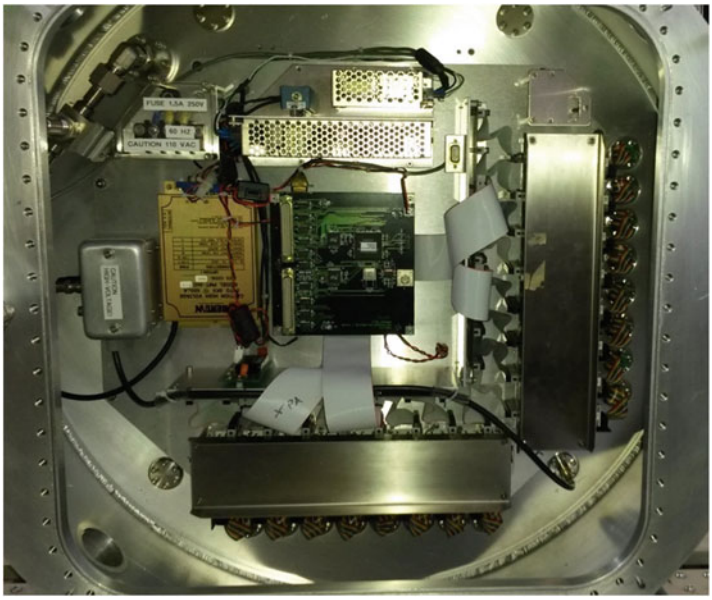

Fig. 3.57 Rear view of the ORDELA 2410N showing the electronics compartment. A cover plate can be installed if vacuum operation is desired

act as guard electrodes to maintain electric field uniformity near the edges. The cathode guard wires are connected to ground. The wires in the *y* cathode are 75 μm diameter stainless steel, oriented horizontally on a wire with a pitch of 0.313 cm.

The anode grid is located 0.5 cm behind the *y* cathode and is of identical construction. The wires in the anode grid are also oriented horizontally. The anode wires are bussed together to form a common electrode and held at positive high voltage (+3100 V) during operation.

The *x* cathode grid sits 0.5 cm behind the anode grid. The wires in this grid are oriented vertically, but otherwise its construction is identical to the *y* grid.

Each of the 256 cathode wires is connected to its own wide-bandwidth, low-noise, charge-sensitive preamplifier and discriminator. The 256 wires are combined into 16 groups of 16 (8 for *x* and 8 for *y*). These groups are shown in Fig. 3.57: the 16 groups of wires along the bottom feed into the horizontal preamplifier box, and the groups of wires along the right-side feed into the vertical preamplifier boxes.

3.7.3 Principle of Operation

The operating bias is determined by inspection of the counting curve, which is shown in Fig. 3.58. The counting curve is a measure of the detector count rate as a function of anode voltage. The operating bias occurs where the curve begins to level off (called the *knee* of the curve) because increasing bias further does not increase the count rate. For this detector, an operating bias of 3100 V was used.

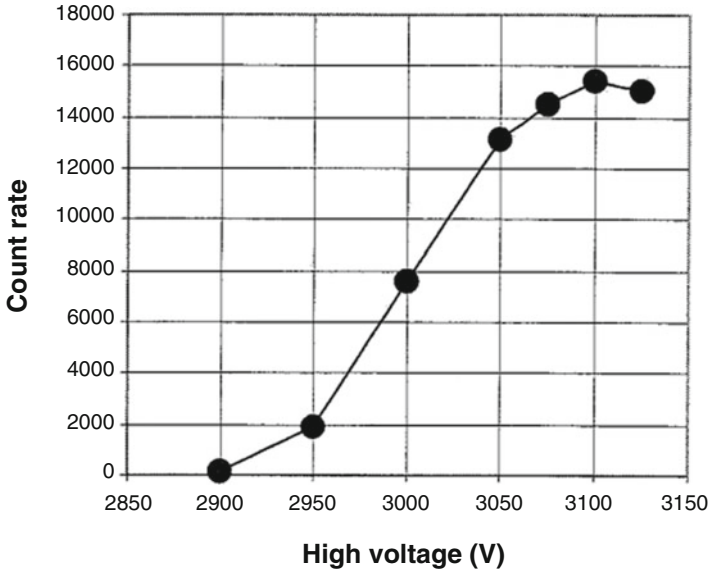

Fig. 3.58 Counting curve used to determine the operating voltage (3100 V) of the anode

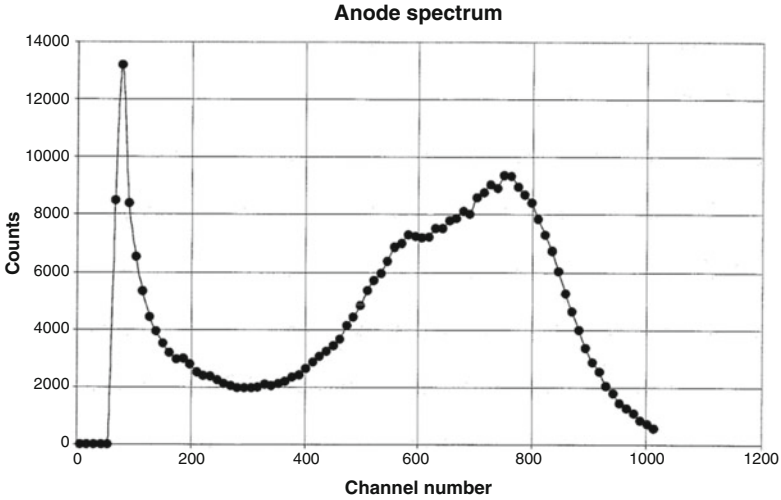

Fig. 3.59 Representative pulse amplitude spectrum illustrating the optimal choice for the discriminator setting to be around channel 300. This spectrum is for an anode voltage of 3075 V

An optimal setting for the discriminator was determined for each of the 256 cathode outputs. Figure 3.59 shows a typical pulse amplitude spectrum. The broad peak to the right (channels 400–1000) corresponds to detected neutron events, and the sharply rising peak to the left (below channel 200) results from lower amplitude events (typically electronic noise or gamma rays). The intervening valley represents the best discriminator setting, which rejects the unwanted low-amplitude events and retains events that result from neutron interactions in the detector.

The model 2410N position-sensitive proportional counter operates with a relatively low gas gain (~37) [26]. The ionization charge is estimated to be approximately 25,000 electron–ion pairs for the gas mix used, or approximately 4 fC per neutron. A gas gain of 37 produces an avalanche charge of approximately 150 fC on the anode grid, which induces current signals on the nearest *x* and *y* cathode wires as the ions drift from the anode toward the cathode wires. The combined proton–triton track length is approximately 0.66 cm (mostly resulting from the partial pressure of CF_4), which is about twice the anode and cathode wire pitch. Thus, up to three adjacent cathode wires can have an induced signal.

Position encoding consists of one preamplifier/discriminator per active wire, for independent amplification and discrimination of each of the 256 outputs (128 each for *x* and *y*). To avoid counting from multiple wires, each discriminator upon firing inhibits the triggering of its two adjacent neighbors, ensuring that only one discriminator from each cathode grid contributes to the position calculation. If two or more neutrons are detected simultaneously within a 100 ns time window, then they are flagged as pileup and rejected. All 256 cathode outputs are connected to an onboard processor for coincidence analysis. The neutron location is defined as the intersection of coincident events on the *x* and *y* cathode grids. Figure 3.60 shows an image of a 2D detector flood pattern under uniform illumination from a neutron source.

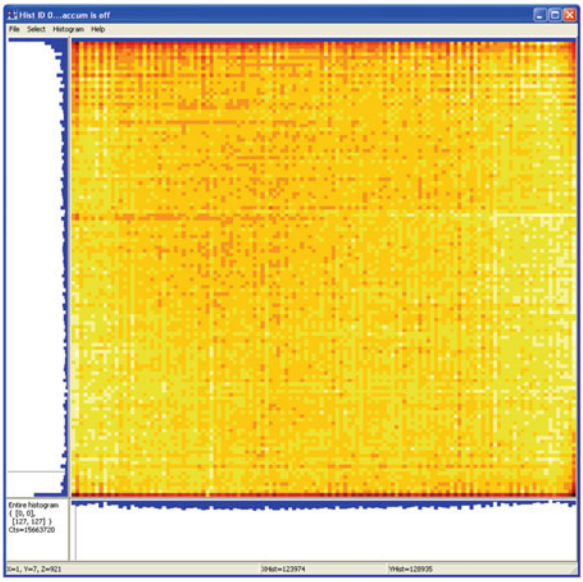

Fig. 3.60 2D detector flood pattern from the ORDELA 2410N detector. The horizontal and vertical integrated counts are shown along the bottom and the left edges

3.8 Beam Monitors

3.8.1 Introduction

Beam monitors are a critical component in neutron scattering experiments. They are used to characterize neutron beams, calibrate beamline equipment, and normalize data. For use in a neutron scattering environment, beam monitors are specifically designed neutron radiation detectors that monitor the neutron flux at various points along the beam path. They differ from typical neutron detectors in that their neutron detection efficiency is purposely low. Having a low enough collection efficiency so as to not distort too much of the neutron beam must be balanced with having a high enough count rate to obtain usable counting statistics.

Most of the neutron experiments at SNS and HFIR make use of cold and thermal neutrons, meaning that the neutrons are moderated or slowed to a range of approximately 0.12–12 meV (2.6–26.1 Å) for cold neutrons and 12–100 meV (0.9–2.6 Å) for thermal neutrons. Detectors and beam monitors designed for neutron scattering are built using isotopes that express a high probability that an incident neutron at these energies interacts to produce a measurable response. This reaction probability for a given isotope is called the *neutron cross section* and depends on the energy of the incident neutron. Table 3.4 lists the most-used isotopes for cold and thermal neutron detection and gives examples of typical detector topology in which they are used. The isotopes ^{3}He and ^{14}N are currently found in most beam monitors used at SNS and HFIR. In the following sections, beam monitor designs, theories of operation, acceptance criteria, and calibration techniques are examined.

Table 3.4 Commonly used isotopes for neutron detection

Isotope	Reaction	Q -value (MeV)	Neutron detection technology	Cross section at 1.8 Å (barns)
^{3}He	^{3}He + n → p (0.57 MeV) + ^{3}H (0.19 MeV)	0.764	Proportional gas counter Geiger–Muller tube	5330
^{14}N	^{14}N + n → p + ^{14}C	0.627	Low eff. proportional gas counter	1.91
^{10}B	^{10}B + n →		Gas electron multiplier Boron-lined ionization chamber	3840
	(6%) ^{7}Li (0.84 MeV) + ^{4}He (1.47 MeV)	2.792		
	(94%) ^{4}He + ^{7}Li + 0.48 MeV γ	2.310		
^{6}Li	^{6}Li + n → ^{4}He (2.05 MeV) + ^{3}H (2.73 MeV)	4.780	Scintillator detectors	940
^{235}U	^{235}U + n → fission fragments + n (5 MeV)	~200	Fission chambers	585

3.8.2 Neutron Beam Monitors

Neutron beam monitors are neutron detectors that are designed to have low absorption efficiencies to thermal and cold energy neutrons, permitting the maximum number of neutrons to reach the experiment sample and subsequent detector array. Beam monitors must also have a large dynamic range for thermal neutrons to provide sufficient counting statistics without saturation in high–neutron flux environments while also being able to discriminate neutron events from gamma ray and system noise in low-level background environments. Furthermore, beam monitors must have sufficient timing resolution to be used in TOF experiments, as well as a high level of radiation hardness, which is required for long-term operation in high-radiation environments. An ideal neutron beam monitor would allow for 100% transparency of the neutron beam, provide 2D position resolution to monitor the beam alignment, and be able to reproduce the complete incident beam energy profile to 100% accuracy independent of the impinging beam flux. However, this ideal monitor does not exist.

3.8.3 Beam Monitors Used in Neutron Science Experiments

Beam monitors perform instrument diagnostic checks, monitor neutron flux stability over an extended time period, normalize detector array data, correct chopper phasing, and calibrate other beamline equipment. At HFIR, monitors collect counting statistics to determine the number of neutrons that went into the sample and that scattered into the detector array. At SNS, the data collected from a beam monitor are

time stamped in reference to the accelerator pulses, and a TOF spectrum can be created for the intersecting neutron beam. This TOF spectrum can then be used to ensure that the instrument beam choppers are correctly phased to minimize the initial prompt pulse from the accelerator or to ensure that the chopped beam produces the correct energy band of neutrons required for a particular experiment. The beam monitor TOF spectrum can also be used to normalize the data collected by the main detector array because the beam presented to the instrument sample tends to have a variable distribution in the number of neutrons per energy bin. Additionally, the neutron flux and stability over time are vital for tracking overall facility health.

3.8.4 *Operation Physics of the Multiwire Proportional Chamber Beam Monitors*

The most widely used beam monitor type is based on an Multiwire Proportional Chamber (MWPC) design. This design includes a gas-filled proportional chamber that has multiple anode wires running through the active area. In the original design, each of these anode wires fed individual readout electronics to effectively create multiple radiation detectors within the same gas volume. To be used as a neutron flux beam monitor, these anode wires are connected to a common node to effectively create one continuous anode. The gas volume of the MWPC active area is filled with either ^{3}He or ^{14}N, depending on the intended efficiency range, as well as stopping and quenching gases. Stopping gases are added to limit the travel distance of the ionizing daughter particles created during a neutron absorption, thereby improving event localization. Quenching gases are polyatomic gas molecules, such as CF_4 or CO_2, that are added to absorb photons, which can be emitted during de-excitation of the energized molecules in the gas. If not captured, these photons can create their own avalanching effects and distort the data. Some gases, such as CF_4, have properties of stopping and quenching gases and can cover both necessities.

MWPC beam monitors work according to the following process. When a neutron is absorbed by the chosen isotope, the reaction creates ionizing daughter particles, as described in Table 3.4. These particles travel in opposite directions away from the interaction site. Electron–ion pairs are created by these daughter particles as they drift through the surrounding gas atoms and create ionization trails. The average number of primary electron–ion pairs created depends upon the type of fill gas in the MWPC. With the fill gas composition known, the total number of primary electron–ion pairs can be approximated using Eq. (3.110) and Table 3.5:

$$n_0 = \frac{\Delta E}{w_{\mathrm{i}}} \tag{3.110}$$

where ΔE represents the charged particle energy loss, and w_{i} is the average energy needed to create a pair dependent upon the used gas [27].

Table 3.5 Commonly used detector fill gases with calculated maximum number of electron–ion pairs created by a neutron absorption

Fill gas	w_i (eV)	n_0 for ^{3}He (all 764 keV are lost)	n_0 for ^{14}N (all 627 keV are lost)
H_2	37	20,649	16,946
He	41	18,634	15,293
N_2	35	21,829	17,914
O_2	31	24,645	20,226
Ne	36	21,222	17,417
Ar	26	29,385	24,115
CO_2	33	23,152	19,000
CH_4	28	27,286	22,393
CF_4	54	14,148	11,611
Xe	22	34,727	28,500

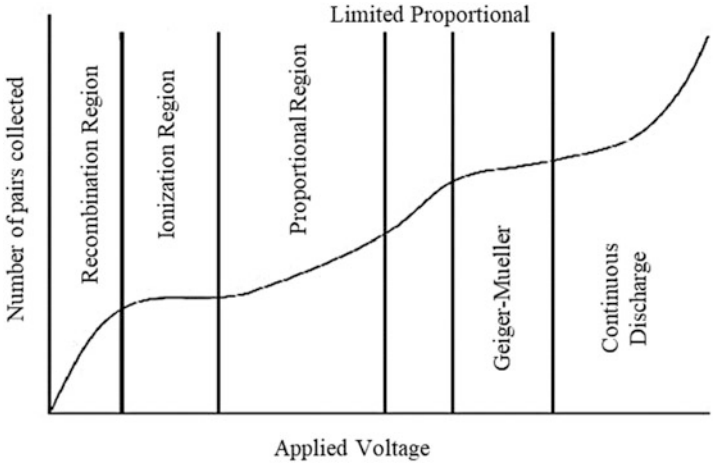

Fig. 3.61 Ionizing radiation detector operation range. Applied bias voltage depicts the number of electron–ion pairs collected [28]

The anode bias voltage is set such that the monitor operates in the proportional region, as described in Fig. 3.61. Within this operation region, the freed electrons begin to quickly drift toward the positively charged anode wire, and the positive ions drift toward the cathode walls. While the freed electrons drift in a small field, no additional charge is generated, corresponding to Fig. 3.65a. Unlike many other MWPC-type detectors, beam monitors often have a small number of anode wires at spacings that are large compared with the distance between the chamber walls. This design prohibits the monitor from forming a constant field drift region away from the anode wires. Instead, the potential distribution takes on the more complicated form shown in Fig. 3.62, which was obtained from a solution to the

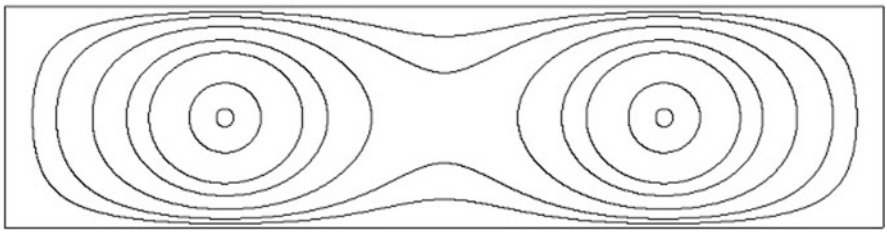

Fig. 3.62 Equipotential lines surrounding biased anode wires in a cross section of a typical beam monitor geometry. An active area 125 mm high by 500 mm wide is depicted with two anode wires centered vertically and 125 mm from the walls horizontally. The equipotential contours are for 10, 20, 40, 70, 100, and 200 V, assuming a 700 V bias

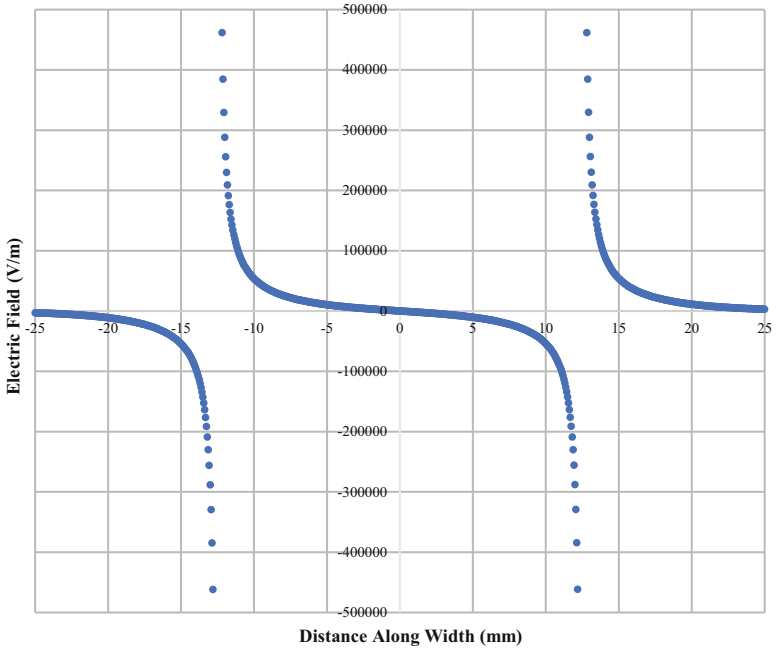

Fig. 3.63 Electric field along a line parallel to the long direction of the monitor shown in Fig. 3.62, passing through the anode wires. The horizontal field component is shown with positive values for the direction, which would drive a positive charge toward higher distance values

electrostatic boundary value problem. Figure 3.63 shows the electric field along an axis intersecting the anode wires from this solution. The high-field regions near the wires can be seen, but they are superimposed on a background field. The charged anode wires induce image charges on the chamber walls. The background field is generated mainly by these image charges, with a small additional contribution from the other anode wire.

As the electrons move closer to the anode wire, they enter the strong electric field surrounding the wire. Within this electric field, the freed electrons accumulate enough kinetic energy to produce secondary electron–ion pairs, as shown in Fig. 3.65b. This effect continues as the secondary electrons drift through the electric field and create tertiary (and more) electron–ion pairs, as shown in Figs. 3.65b and 3.66c, leading to a signal-multiplication effect called the *Townsend avalanche*. Equation (3.111), the Townsend avalanche equation, details the number of electrons created (dn) per path (ds), where α is the first Townsend coefficient of the gas. This coefficient depends on the electric field strength at a particular radial distance r from the center of the anode wire, as detailed in Fig. 3.64. Below the threshold for gas multiplication, the Townsend coefficient is zero, and it increases quickly above the threshold for gas multiplication [27].

$$dn = n\alpha ds \tag{3.111}$$

If n_0 electrons enter the avalanche region, then they will increase to n_f electrons passing through it, where Eq. (3.112) defines n_f as the following:

$$n_f = n_0 \exp\left\{\int \alpha ds\right\} \tag{3.112}$$

As described in Eq. (3.113), the total charge (Q_T) generated by the absorption of a neutron is dictated by the number of primary electron–ion pairs produced and the gas gain (M) of the monitor [9]. Gas gain is the average multiplication factor applied to the initial number of electron–ion pairs. Equation (3.114) shows that, in general, gas gain is dependent on the anode bias voltage and subsequent electric field, the first Townsend coefficient for the given electric field strength, the radius of the anode wire (a), the radial distance moving away from the center of the anode wire (r), and the critical radial distance (r_c) away from the anode wire beyond which there is not enough field strength to inhibit electron multiplication [9]. This Townsend avalanche effect eventually creates clouds of electrons and positive ions that surround the anode wire, as shown in Fig. 3.65d.

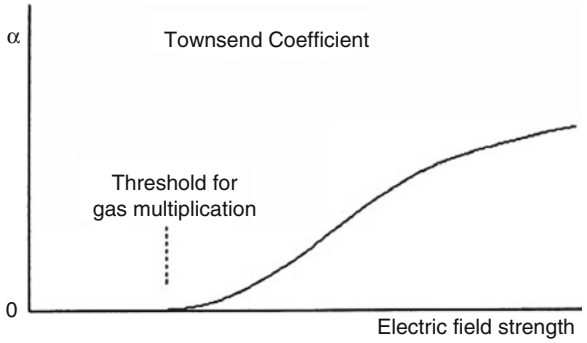

Fig. 3.64 Plot of the first Townsend coefficient vs. applied electric field strength [9]

$$Q_T = n_0 eM = en_f = en_0 \exp\left\{\int_a^{r_c} \alpha dr\right\} = en_0 \exp\left\{\int_{E(a)}^{E(r_c)} \alpha(E) \frac{\partial r}{\partial E} dE\right\} \quad (3.113)$$

$$\ln M = \int_{E(a)}^{E(r_c)} w(E) \frac{\partial r}{\partial E} dE \quad (3.114)$$

If only elastic collisions occur, then the electrons and ions drift through the gas at a rate proportional to the electric field (E) and the mean free path between collisions. This mean free path is inversely proportional to the gas pressure (p), so the drift velocity is proportional to E/p. If the charged particle accumulates enough energy from the electric field between collisions, then it can have an inelastic interaction with the atom or molecule that is struck, decreasing its velocity. The accumulated energy is proportional to the electric field multiplied by the mean free path between collisions and is thus proportional to E/p. The drift velocity remains a function of E/p, but the function is not linear. The ionization events within the Townsend avalanche region are examples of these inelastic collisions. Because the ions are several thousand times heavier than the electrons, they accelerate more slowly in the electric field, causing them to have much lower drift velocities.

The electrons released in the Townsend avalanche region are in a high–electric field region, have high mobility, and are near the anode wire. Therefore, they reach the anode wire and are absorbed by it within a few nanoseconds, as shown in Fig. 3.65e. The released ions do not move very far during this time. They are left behind to create a region with a positive space charge, which capacitively attracts electrons in the anode wire and in the beam monitor wall. Initially, this attraction keeps most of the electrons that were deposited on the wire confined to a region near where they were absorbed. At the wall, the attraction of electrons by the space charge is mostly canceled out by the repulsion from the extra electrons on the anode wire. As time passes, the ions drift away from the anode wire. The ions become less effective at confining the electrons that were deposited on the wire, allowing those electrons to disperse and create a current of electrons that are conducted through the anode wire and transfer into the external readout electronics. At the beam monitor

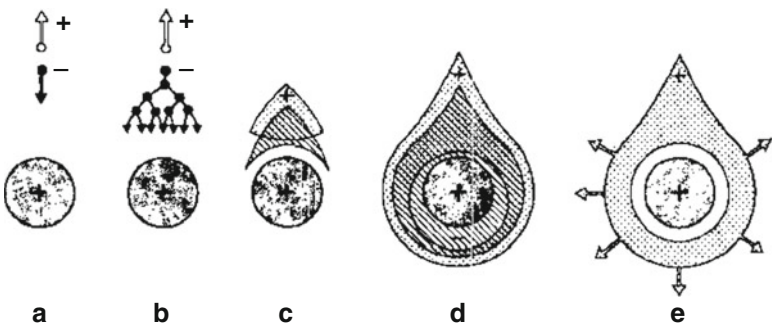

Fig. 3.65 Step-by-step development of charge clouds in general proportional counter [29]

wall, the attraction of electrons by the space charge is no longer fully canceled out by the repulsion from the extra electrons on the anode wire, allowing electrons to be pulled into the wall through an external connection. Eventually, over several microseconds, some of the ions drift all the way to the beam monitor wall. They pick up an electron from the wall and become neutral. This ion consumes one of the electrons that was attracted to the wall. However, it does not alter the electric field distribution within the beam monitor, and it does not cause more electrons to enter the wall from an external connection.

At the end of this process, all the charge that was deposited on the anode will have traveled through an external connection to the beam monitor wall. The motions of the positive ions influence the rate at which this external transfer occurs, but the bulk of the charge transfer may occur during a shorter time than it takes for the ions to reach the wall. The charge directly released by a neutron reaction is small compared with the charge generated near the anode wire by the Townsend avalanche. Each electron from the directly released charge that reaches the Townsend avalanche region near the anode wire creates a current pulse whose time evolution is set by the geometry of the wire relative to the beam monitor wall, not by the location of the initial release. This process occurs over a characteristic time (T_A), which could be defined as the FWHM. The arrival rate of electrons from the directly released charge to the anode wire also disperses by some characteristic time T_I. The position where the neutron absorption occurs should only influence the output pulse shape if T_I is a substantial fraction of T_A.

3.8.5 Beam Monitor Performance Characteristics

3.8.5.1 Count Rate Limitations

For a given neutron event, the resulting charge pulse has a current exceeding the discriminator setting for some time T. The value of T varies from pulse to pulse, but it has some average value T_d, which is often in the 1–2 μs range for the MWPC beam monitors. If a second event occurs in the same vicinity before a previous charge event has dissipated, then the second charge pulse will ride on top of the previous pulse, resulting in pulse pileup. If neutrons react within the beam monitor at a low rate (R_n), then some fraction of events (RT_d) is missed owing to the pulse pileup, resulting in a measured count rate (R_m) described by Eq. (3.115). Pulse pileup can cause the readout electronics to incorrectly measure the magnitude of both pulses, resulting in incorrect counting statistics. Figure 3.66 shows a graphic representation of the pulse pileup effect. At high rates, the chances of multiple pulse pileups within the time T_d becomes appreciable, and results in Eq. (3.115) taking on an exponential form, detailed in Eq. (3.116).

$$R_m = R(1 - RT_d) \tag{3.115}$$

$$R_m = R\exp\{-RT_d\} \tag{3.116}$$

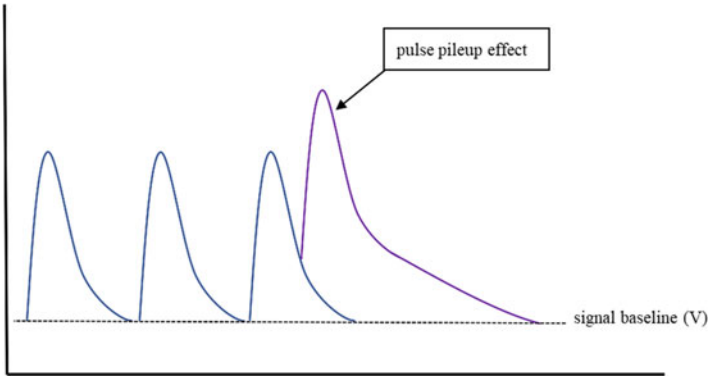

Fig. 3.66 Pulse pileup effect on pulse height measurement

As the impinging rate increases, the measured count rate first increases linearly until a maximum is reached at $R_m = 1/T_d$, then it decreases to zero. The rate at which an MWPC detector begins to experience degradation in counting linearity has been experimentally determined to be between 10,000 and 15,000 counts per second. At very high-count rates, the charge clouds that surround the anode wire begin to accumulate for a prolonged period without being able to fully dissipate. The charge clouds effectively saturate the anode and change the pulse shape from an event. The saturation is a more complex effect that is not easily modeled by a simple equation. In practice, it would be difficult to drive an MWPC beam monitor hard enough to progress beyond the reduced-linearity region. Figure 3.67 predicts the count rate linearity vs. impinging neutron flux based on the regimes governed by Eqs. (3.115) and (3.116).

3.8.5.2 Beam Monitor Neutron Absorption Probability

Two main probability factors determine the MWPC beam monitor neutron detection efficiency. The first factor is the probability (P_{eff}) that a neutron will be absorbed by a ^{3}He or ^{14}N nucleus and result in the emission of an energized charged particle. As shown in Eq. (3.117), this probability is influenced by the absorption cross section (σ), the number density of the nuclei (N), and the distance (D) that the neutron can travel through the gas medium. Many materials used for neutron absorption, including ^{3}He and ^{14}N, have an absorption cross section that is proportional to the incident neutron wavelength; therefore, the reaction probability is also proportional to the neutron wavelength. MWPC beam monitors are designed such that $\sigma ND \ll 1$, so $P_{eff} \approx \sigma ND$. For higher efficiencies, generally between 10^{-3} and 10^{-4}, ^{3}He is the preferred isotope, and for lower efficiencies, generally between 10^{-4} to 10^{-6}, ^{14}N is used.

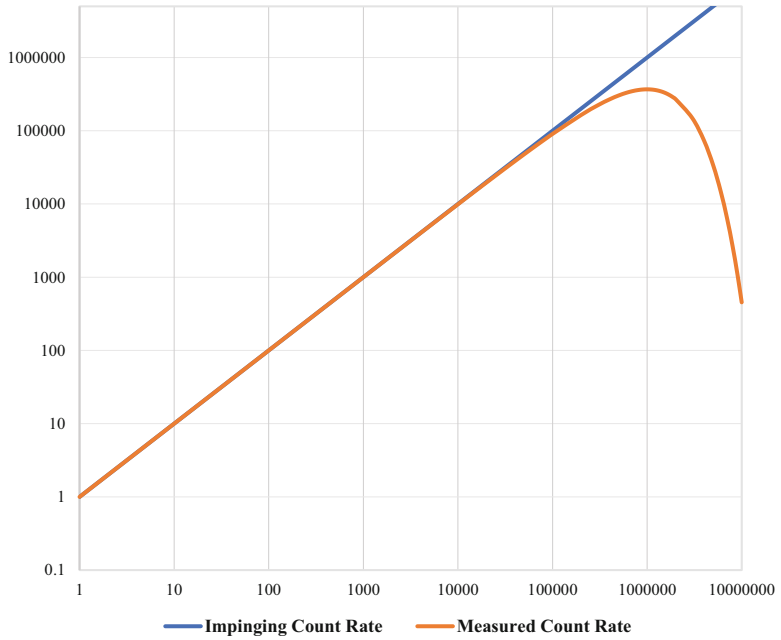

Fig. 3.67 Theorized flux rate vs. measured rate for an MWPC beam monitor

$$P_{\text{eff}} = 1 - \exp\{-\sigma ND\} \tag{3.117}$$

The cross sections of neutron absorbers are often quoted as their value σ_T for neutrons thermalized to 300 K, where they have an average wavelength $\lambda_T = 1.8$ Å. For wavelength λ, $P_{\text{eff}} = [(\sigma_T\lambda)/\lambda_T]ND$. A beam monitor's absorption probability is often quoted as $P_{\text{Thermal}} = \lambda_T ND$. This equation can be converted to $P_{\text{eff}} = P_{\text{Thermal}}(\lambda/\lambda_T)$ for other wavelengths.

For gaseous absorbers, the ideal gas law, $p = N_M k_B T$, can be used to calculate the desired partial pressure of the absorber. Here, N_M is the number density of molecules, k_B is the Boltzmann constant ($k_B = 1.38 \times 10^{-23}$ J/K), T is the temperature, and p is the gas pressure. If r_m is defined as the number of absorber atoms per molecule N/N_M, then $N_M = N/r_m = P_{\text{eff}}/(\sigma D r_m)$, and $p = (P_{\text{eff}} k_B T)/(\sigma D r_m)$. If a monitor operates at 300 K with $D = 1.2$ cm, and the desired efficiency using ^{3}He is 1×10^{-3} at $\lambda = 1.8$ Å, then $r_m = 1$, and $\sigma = 5330$ barn. These parameters yield a gas pressure of 647 Pa. This pressure is low enough that some carrier gas, such as argon, should be added when filling the monitor. If a 1×10^{-5}efficiency is desired using $^{14}N_2$ as the absorber, then $r_m = 2$, and $\sigma = 1.91$ barn. These parameters yield a gas pressure of 9031 Pa, which is still low enough that a carrier gas should be added. For a 1×10^{-4}efficiency monitor using $^{14}N_2$, the gas pressure is 90,310 Pa, which is nearly atmospheric pressure. In this case, the nitrogen might be the dominant component of the gas mixture.

3.8.5.3 Beam Monitor Neutron Event Detection Probability

The second factor is the probability that the current pulse created by a neutron absorption is large enough to activate the discriminator and generate an output pulse from the beam monitor system. Knowledge of the pulse-height spectrum is required to predict the influence of the discriminator setting on the fraction of neutron reactions that get discriminated. The pulse-height spectrum can be represented as a function (S) of the collected charge (Q) from a current pulse corresponding to a neutron reaction, where S is defined such that the probability that the collected charge from a current pulse is between Q, and $Q + \Delta Q$ is proportional to $S(Q)\Delta Q$. If a discrimination between accepted and rejected pulses could be based on some charge threshold Q_m, then Eq. (3.118) determines the probability that a neutron reaction passes the discriminator setting and triggers the output electronics (P_{Dis}). Here, Q_m represents the entire range of charge for which the function S has an appreciable value. Figure 3.68 shows an idealized depiction of a pulse-height spectrum from a neutron detector used to show appropriate choices for Q_{D} and Q_m, as used in Eq. (3.118). The discriminator level, Q_{D}, is carefully selected to just above the level of gamma ray detections and electronic noise to eliminate false counts in the system; both such events are shown on the far left of Fig. 3.68.

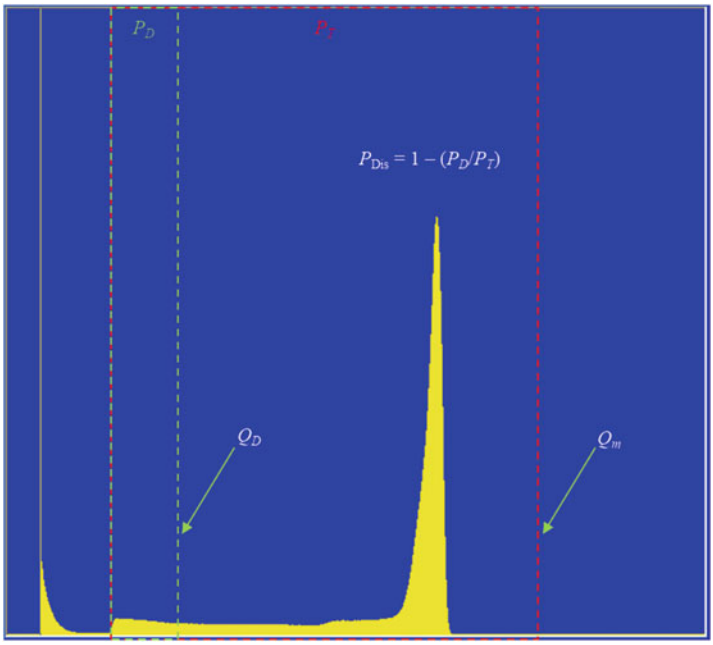

Fig. 3.68 The probability that an event triggers discriminator electronics [30]

$$P_T = \int_0^{Q_m} SdQ$$

$$P_D = \int_0^{Q_D} SdQ$$

$$P_{\text{Dis}} = 1 - \frac{P_D}{P_T} \tag{3.118}$$

Figure 3.69 shows a measured pulse-height spectrum from a 1×10^{-3}efficiency ^{3}He beam monitor operating at 580 V bias. The charge was determined by integrating the current from a pulse generated by a neutron event during a 3 μs period. The cutoff of the spectrum for charges less than 0.05 pC is an artifact of the measurement apparatus, which required a discriminator level to be set to trigger the integrations. The true spectrum would have some amplitude in this region. This spectrum's shape differs significantly from the idealized depiction shown in Fig. 3.68. The peak count rate corresponds to a charge that is approximately one-third of the maximum charge.

Figure 3.70 illustrates the dependence of the charge range of the pulse-height spectrum on the bias voltage. The data was collected using the same beam monitor and measurement apparatus as that for Fig. 3.69. The maximum charge is defined as

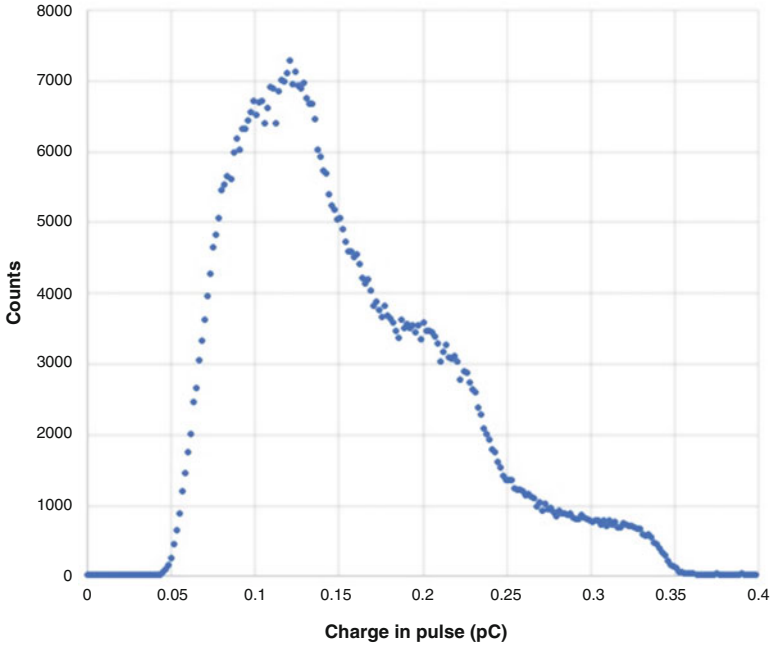

Fig. 3.69 Pulse-height histogram for a 1×10^{-3}efficiency beam monitor using ^{3}He as an absorber. A 580 V bias was used. The charge is measured by integrating the current from a pulse over a 3 μs period

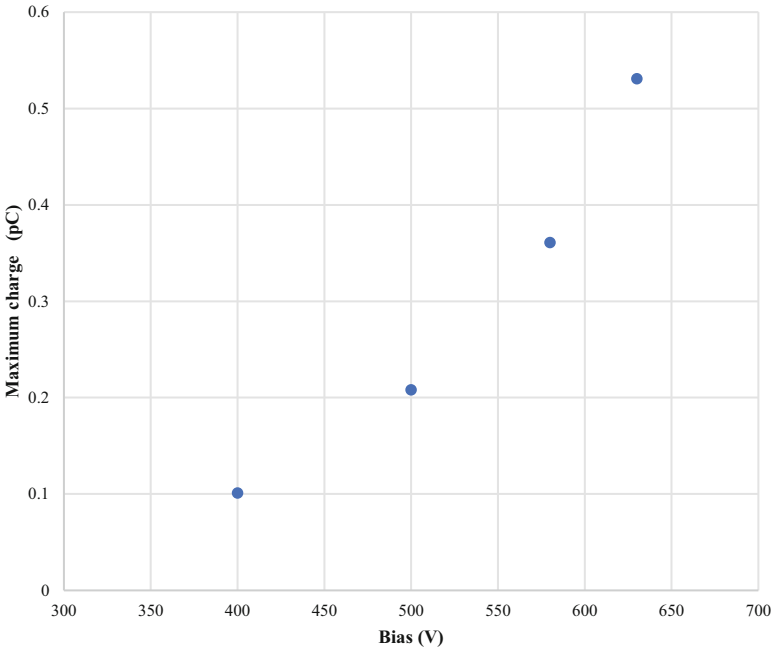

Fig. 3.70 Dependence of pulse-height spectrum range on the bias voltage. This used the same 1×10^{-3}efficiency^{3}He beam monitor and measurement setup that obtained the pulse height spectrum of Fig. 3.69. Maximum charge refers to the highest charge for which the pulse-height spectrum is observed to rise above the background level

the highest charge for which the pulse-height spectrum is observed to rise above the background level. The maximum charge depends strongly on the bias. The overall shape of the spectrum does not vary much as the bias changes. Higher bias voltages are more likely to trigger the discriminator, but they can also cause preamplifier saturation, raise the required discriminator level needed to reject gamma ray detections and noise, and reduce the recovery time between neutron events.

Figure 3.71 gives an example of a neutron pulse triggering the discriminator circuitry. This pulse reaches its maximum amplitude within 1 μs and maintains an appreciable amplitude over a time interval of approximately 3 μs. Significant variations in shape exist among the pulses. These variations include the time it takes for a pulse to reach maximum amplitude and the width of the of the pulse. Figure 3.72 shows an example of a gamma ray pulse from a ^{60}Co source that does not have the pulse height required to trigger the discriminator.

The decision to measure a detector pulse cannot initially be based on its charge because the charge is not known until after the pulse current has been integrated. Instead, most practical discrimination circuits rely on the pulse's peak amplitude to trigger the discrimination. If the pulse shape does not remain constant, then the ratio of the peak amplitude to the charge will not be constant. An amplitude-based

Fig. 3.71 Oscilloscope measurement of (*yellow trace*) neutron event triggering (*green trace*) discriminator circuitry. Discriminator level set to approximately 100 mV above baseline in this example

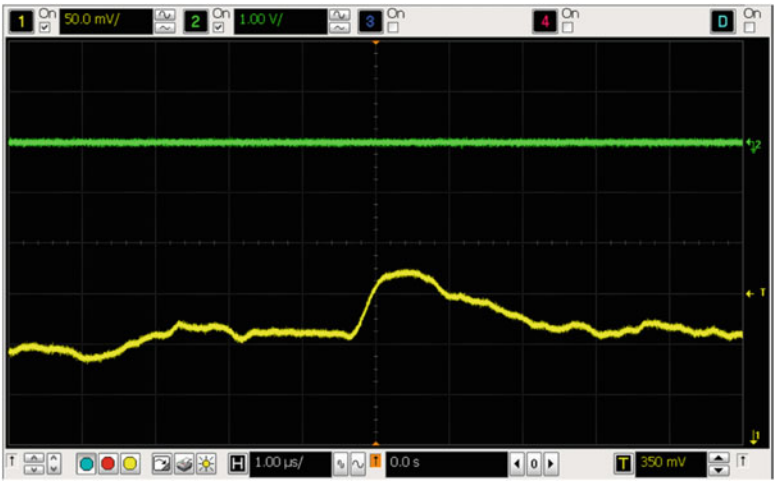

Fig. 3.72 Oscilloscope measurement of (*yellow trace*) gamma event using a ^{60}Co source that is too low in amplitude to trigger (*green trace*) discriminator circuitry. Discriminator level set to approximately 100 mV above baseline in this example

discrimination will cause some pulse-to-pulse variation in the charge Q_D from a pulse whose peak amplitude is just large enough to trigger the discriminator. Despite this variation, a peak amplitude-to-charge ratio for a typical pulse shape can be used to estimate the value of Q_D, which corresponds to a peak amplitude discriminator

voltage V_D. Dividing the total area under a time plot of a pulse by the peak amplitude of the pulse yields a time t_p. Multiplying the peak current I_p of the pulse by t_p gives the charge of the pulse. Between the beam monitor output and the discriminator is a preamplifier with some current-to-voltage gain R_A. For a pulse whose amplitude is just large enough to trigger the discriminator, $V_D = R_A I_p = R_A(Q_D/t_p)$, which means $Q_D = (t_p/R_A)V_D$. For the pulse in Fig. 3.71, t_p is approximately 2 μs. The preamplifier used at SNS has R_D = 5,600,000 V/A, giving $t_p/R_A = 3.57 \times 10^{-13}$ C/V.

The pulse-height spectrum is also influenced by the fill gas composition and pressure. Because the mean free path is reduced, increasing the pressure increases the bias voltage required to achieve a desired gas gain. The gas composition affects the energy required to form electron–ion pairs, influencing the number of such pairs produced by the detection event and the amount of charge multiplication. Therefore, a dependence exists between the fill gas composition and pressure and the required beam monitor bias voltage to obtain an adequate charge range in the pulse-height spectrum. This charge range is needed to keep discriminator cutoff of low-amplitude pulses from causing an unacceptably high loss of beam monitor efficiency. To obtain similar performance to a 1×10^{-3}efficiency ^{3}He monitor with 600 V bias, a 1×10^{-4}efficiency $^{14}N_2$ monitor needs 1250 V, and a 1×10^{-5}efficiency $^{14}N_2$ monitor needs 750 V.

As shown in Fig. 3.83, which appears later in Sect. 3.8.8, experiments have revealed that the detection efficiency of a beam monitor can be lower for neutrons arriving far from an anode wire than that of neutrons arriving near the wire. This effect is most pronounced when the monitor is operated at low bias voltages, possibly because the spread in arrival times for the electrons generated by a neutron detection far from the anode is larger than that for electrons from a neutron detection near the anode. This arrival time spread corresponds to the value T_I in the Townsend avalanche discussion. If the arrival time spread is large enough, then the pulse width increases, lowering the peak amplitude-to-charge ratio. This lower ratio increases the discriminated charge cutoff Q_D, causing a greater fraction of events to be rejected. The fraction of rejected events must be high for this effect to produce any significant distortion in the monitored count rate.

If the bias voltage is varied without making compensating changes to the discriminator setting, then the fraction of rejected events is highest at low bias voltages. This high fraction of rejected events may explain the bias dependence of the efficiency variations. Determining how much time the electrons need on average to drift to the anode helps to evaluate the importance of this effect. The drift velocity (v) depends on the electric field, the gas pressure, and the gas composition. Owing to the availability of published data on drift velocities [31], this velocity is calculated for nitrogen at a pressure of 1 atm and a temperature of 293 K. The calculated velocity is a reasonable approximation to conditions in a 1×10^{-4}efficiency monitor.

Figure 3.73 shows a log plot created using published data [31] for the dependence of drift velocity on E/p for nitrogen at a temperature of 293 K, where v is in units of centimeters per second, and E/p is in units of volts per torr-centimeters. The dependence seems nonlinear. A line of slope equal to one-half is also plotted on

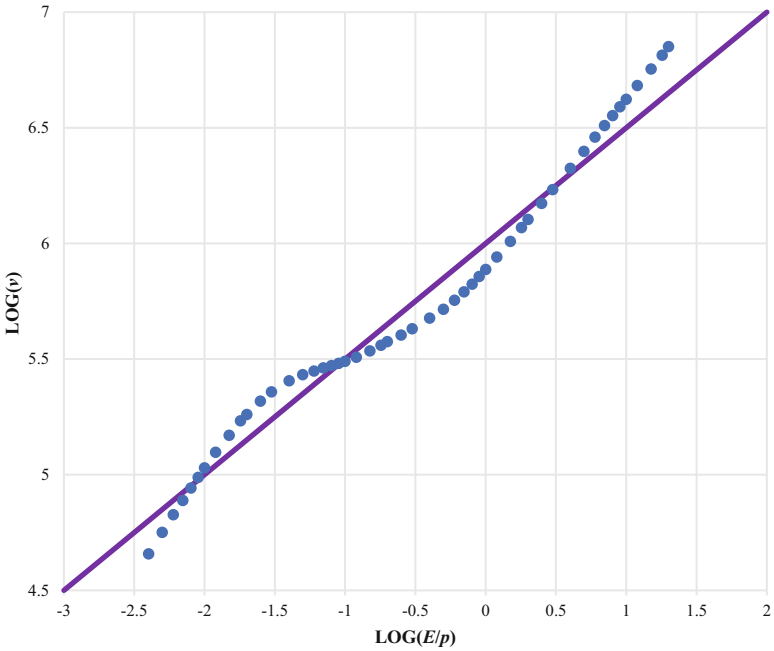

Fig. 3.73 Log plot to show dependence of v on E/p for nitrogen at 293 K

Fig. 3.73, corresponding to Eq. (3.119). Although the linear slope is not a perfect representation of the plotted data, it does remain within a factor of 2 of the plotted data's slope.

$$v = k\sqrt{\frac{E}{p}} \quad \text{where } k = 10^6 \left(\frac{\text{Torr} \cdot \text{cm}^3}{\text{s}^2\text{V}}\right)^{\frac{1}{2}} \tag{3.119}$$

Equation 3.120 calculates the time (t) that an electron released by an event that occurs at a distance (D) from the wire will take to drift to the anode wire. Equation 3.121 gives the formula for estimating the electric field that is present at a distance (r) from the wire, where V_{Bias} is the anode bias voltage, a is the radius of the anode wire, and r_{wall} is the distance from the anode wire to the beam monitor wall. Equation 3.121 should be accurate for distances that are short compared with r_{wall}. As shown in Fig. 3.63, Eq. (3.121) becomes more approximate at larger distances because of the noncylindrical wall and overlapping fields from other anode wires.

$$t = \int_0^D \frac{dr}{v} = \frac{\sqrt{p}}{k} \int_0^D \frac{dr}{\sqrt{E}} \tag{3.120}$$

$$E = \frac{V_{\text{Bias}}}{k_1 r} \quad \text{where } k_1 \approx \ln\left(\frac{r_{\text{wall}}}{a}\right) \tag{3.121}$$

Combining these equations leads to the estimate of the electron drift time in Eq. (3.122).

$$t = \frac{1}{k}\sqrt{\frac{pk_1}{V_{\text{Bias}}}}\int_0^D \sqrt{r}dr = \frac{2}{3k}\sqrt{\frac{pk_1 D^3}{V_{\text{Bias}}}} \tag{3.122}$$

For a beam monitor filled with nitrogen at 1 atm ($p = 760$ Torr) with a 25 μm anode wire radius and a 5 mm distance to the monitor wall operating at 700 V anode bias, Eq. (3.122) calculates that the electrons created from an event 2 cm from the wire will take approximately 4.5 μs to reach the wire. This time is a little longer than the duration of a typical output pulse from the beam monitor.

If all the electrons from the event were drifting at the same velocity, they would reach the anode with no spread in their arrival times, creating an output pulse that is delayed but whose width is not altered. The drift velocity refers to an average rate of travel, and the paths that the individual electrons take include some randomness. This randomness creates a spread in the electron arrival times, which might be a substantial fraction of the total drift time, in which case the spread widens the beam monitor output pulse, decreasing its peak amplitude-to-charge ratio. This ratio decrease increases the likelihood that the peak amplitude is below the discriminator threshold, causing the pulse to be rejected. Arrival time spreads of approximately a microsecond—one-fourth of the estimated drift time—are needed for this effect to become significant. Beam monitor output pulses have significant variations in duration, suggesting that significant variations in charge arrival times are occurring.

Charge recombination is another possible mechanism for position-dependent efficiency variations. The conjecture is that the low drift velocities and long travel times for charges generated far from the anode increase the fraction of the charges that recombine. This increase in charge recombination decreases the amount of charge reaching the anode, decreasing the amplitude of the output pulse. This pulse is more likely to be rejected by the discriminator. One possibility is that the charges recombine very soon after they form, before they have time to move apart. This fast recombination can be important in solids and liquids. The lower density of gases causes the generated charges to be more widely dispersed, which makes this form of recombination much less likely.

A second possibility is that the electrons are captured while they are on their way to the anode. The likelihood of this possibility depends on the presence of electronegative gases. An *electronegative material* is a substance whose atoms or molecules can form negatively charged ions. A free electron encountering such a material can be absorbed by it, creating a slowly drifting ion that does not contribute to the output pulse. The gases chosen to fill beam monitors are not electronegative, but the presence of an electronegative material as an impurity cannot be ruled out.

Although neither of the recombination mechanisms seems likely to account for substantial levels of charge recombination, the measured shape of the pulse-height spectrum must be considered. If all the charge from every event makes it to the anode, then a pulse-height spectrum that is strongly peaked near the maximum

charge cutoff is expected. However, this strong peak is not observed in the pulse-height spectrum.

3.8.6 *Mechanical Design of MWPC Beam Monitors*

Most of the beam monitors employed at SNS and HFIR are based on MWPC technology. As shown in Fig. 3.74, these monitors are made using a vacuum-sealed aluminum enclosure that presents a 1 mm thick window on either side of the active area. This active area (and, thus, the overall monitor size) is customizable depending on application requirements. The preamplifier enclosure is attached directly to the active area of the monitor and contains two feedthroughs, which access the monitor's active area, as shown in Fig. 3.75. One of the feedthroughs fills the enclosure with a volume of gas composed of a mixture of selected fill gas to ensure proportional mode operation, along with a finely controlled amount of either ^{3}He or ^{14}N as the neutron absorber. Depending on the length and width of the monitor's active area, two or four anode wires–on the order of 0.0005 in. in diameter (1.27 μm)–are routed through the active area. These wires are all connected at a central node to effectively make one continuous anode. The anode is positively biased by an external source using the second feedthrough. MWPC monitors are biased such that the monitor operates in the proportional mode to enable pulse height discrimination. Figure 3.76 shows the internal design of the active area for this type of monitor.

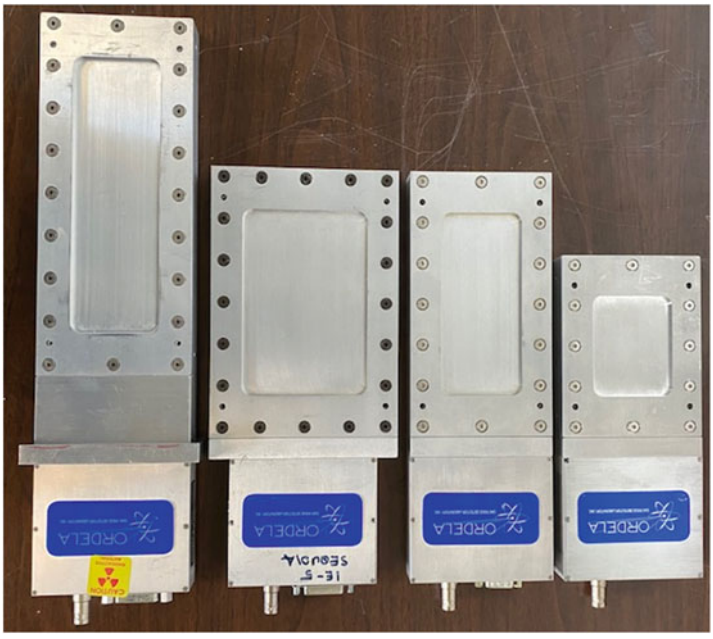

Fig. 3.74 MWPC beam monitors

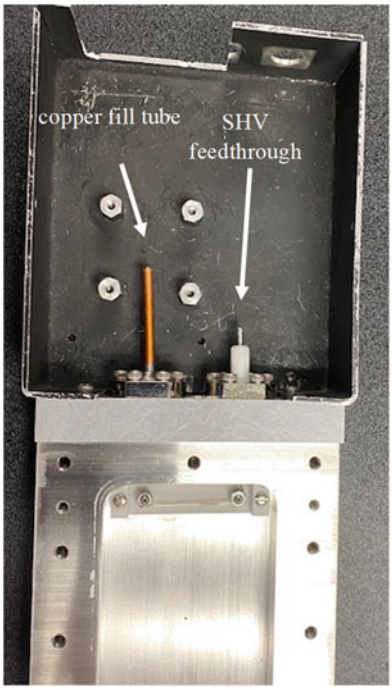

Fig. 3.75 MWPC active area feedthroughs

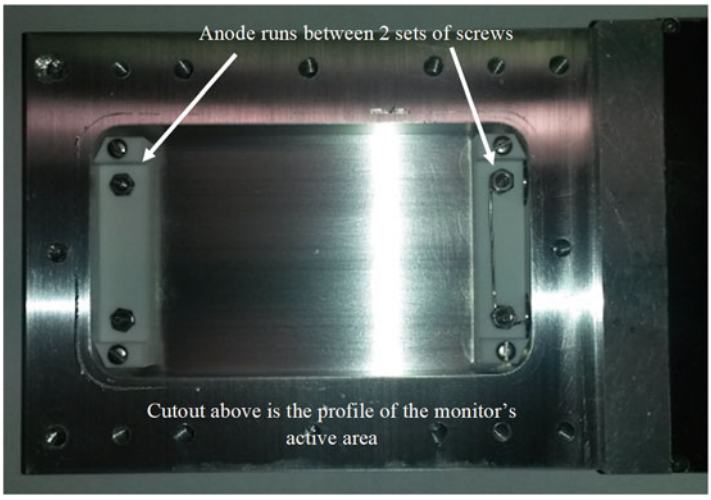

Fig. 3.76 Mechanical design of the MWPC beam monitor

3.8.7 Beam Monitor Readout Electronics Overview

3.8.7.1 Preamplifier

This section details the readout electronics of the SNS-style beam monitor system. The beam monitors used at HFIR employ an Ordela manufactured readout system, which will not be discussed here. The SNS beam monitor preamplifier housing, shown in Fig. 3.77, is attached directly to the beam monitor enclosure to limit potential noise pickup and signal attenuation of the charge pulse. Inside the housing sits the Beam Monitor Preamplifier Board; Fig. 3.78 shows an electrical schematic for the SNS-style beam monitor preamplifier. The preamplifier board consists of a low-pass filter and DC (direct current) blocking circuit, followed by four distinct stages of pulse shaping and amplification before a comparator circuit and single-ended to differential converter circuit. First, a low-pass filter consisting of a resistor and capacitor is connected in series with a 1 MΩ resistor to filter the anode bias

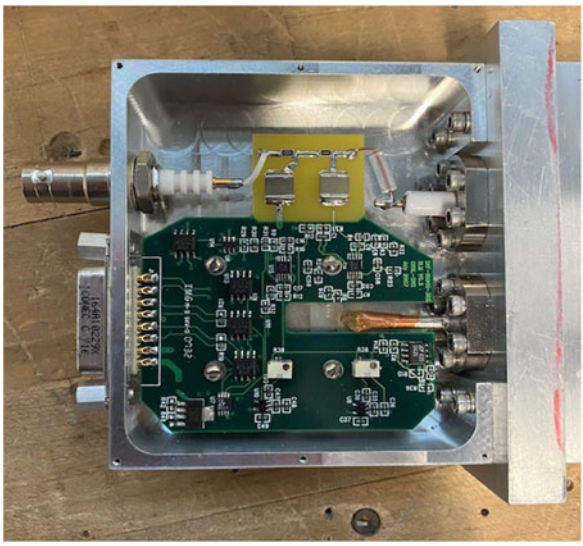

Fig. 3.77 Beam monitor preamplifier housing

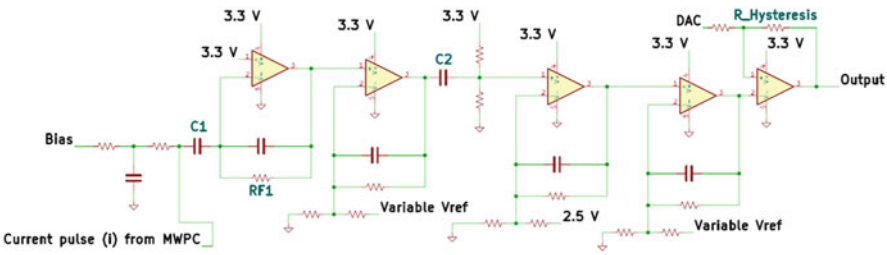

Fig. 3.78 MWPC SNS-style preamplifier schematic

voltage that is supplied from an external source through the safe high voltage bulkhead. A 15 nF capacitor, labeled C1 in Fig. 3.78, then blocks the DC bias voltage while allowing the detection current pulse to reach the subsequent amplification stages. The first amplification stage is a transimpedance amplifier, which transforms the current pulse (I) from the monitor to a voltage output through resistor *RF1* in Fig. 3.78, as detailed in Eq. (3.123).

$$V = I \times RF1 \tag{3.123}$$

Next, the voltage output of the first stage is shaped and amplified by three voltage amplification circuits. Stages one and three each have a potentiometer to manually adjust their respective voltage references, and the voltage reference used in stage two is set via a resistive voltage divider circuit. A series capacitor (C2) is used between the second and third stages of amplification to improve the preamplifier's thermal stability. Without this series capacitor, thermal drift in the voltage offset from the first stage would be amplified by the full gain of the remaining stages.

Finally, the last stage of the preamplifier board consists of an operational-amplifier comparator circuit, which acts as a discriminator for the amplified signal. An onboard DAC is used to set the discriminator threshold remotely. Another resistor (R_Hysteresis) is added between the DAC output and the positive input of the comparator. This resistor is part of a hysteresis circuit that prevents more than one triggered pulse per neutron event. The comparator output is then converted to a differential pair and sent to a beam monitor control box via a 15-pin data bus connector.

3.8.7.2 Control Box

The beam monitor data acquisition system consists of a beam monitor, beam monitor control box, and a data stream packetizer (DSP) board. The beam monitor control box, shown in Fig. 3.79, houses two main electronics boards: the beam monitor ethernet controller and the high-voltage module. Bias to the monitor anode is supplied by the high-voltage module. This module can receive an external interlock signal that quickly disrupts and lowers the bias voltage in the event of a vacuum leak or other undesired event. The FPGA on the controller configures the DAC settings for the preamplifier board and the high-voltage module. A network connection allows the ethernet controller to access these configurations and to remotely update the FPGA firmware.

Figure 3.80 shows an example of a beam monitor graphical user interface (operator interface [OPI]) used to control the beam monitor high voltage, control the comparator discriminator level, and display the TOF spectrum, among other features. The beam monitor ethernet controller receives the differential output signal from the beam monitor preamplifier and converts it to a logic-level, single-ended output. This signal is then passed to the onboard FPGA, where the signals can be locally acquired and used as diagnostic tools. The locally acquired histogram is

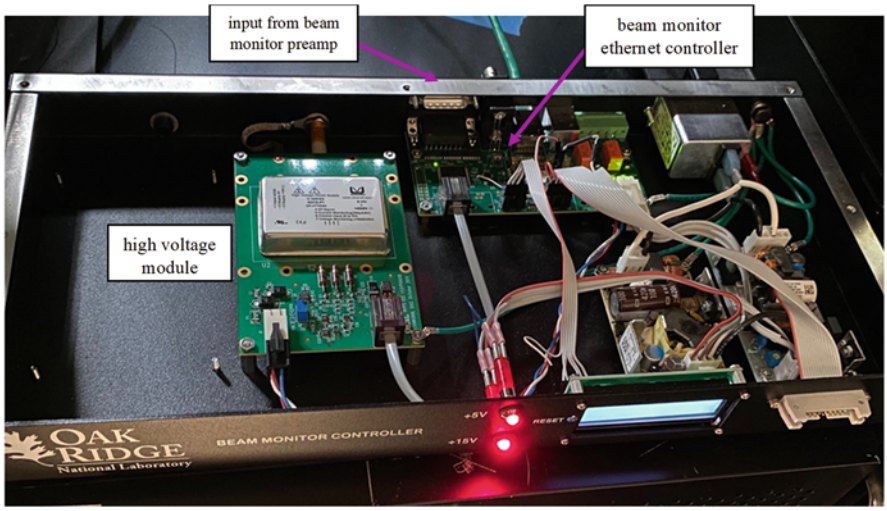

Fig. 3.79 Beam monitor control box

Fig. 3.80 Beam monitor OPI

transmitted to the instrument data acquisition system via the ethernet connection of the beam monitor ethernet controller. The beam monitor OPI reads this histogram and displays it as the blue bars shown in Fig. 3.80. The signal is also passed to a DSP

input. The DSP also receives signals from the accelerator, including a Tsync signal, which is synchronized to the times when the accelerator target generates bursts of neutrons. The DSP uses the difference in arrival times between the Tsync signal and the beam monitor signal to generate a time stamp. The DSP forwards this time stamp and the pixel ID associated with the beam monitor to the instrument data acquisition system. The data acquisition system reads this stream of beam monitor time stamps to create a TOF histogram. This histogram is displayed as the continuous red line overlapping the controller data in the TOF plot in Fig. 3.80.

3.8.8 Beam Monitor Characteristic Tests

Before any monitor is installed into a beamline at SNS or HFIR, it is first tested for overall performance characteristics to determine correct anode bias voltage and discriminator settings and to measure the monitor's efficiency for thermal neutrons. Typically, these tests are performed at the CG-1A experimental beamline located at the HFIR Cold Guide Hall. Here, a monochromatic neutron beam of approximately 4.2 Å is created via a pyrolytic carbon monochromator [32]. Figure 3.81 shows the CG-1A beamline layout. This beamline is allocated for the testing of new detector prototypes and configurations.

3.8.8.1 Beam Monitor Efficiency Test

Before installation, all beam monitors undergo a test to measure their efficiency for 1.8 Å neutrons, and this measured efficiency is compared with the manufacturer's designed efficiency for accuracy. To set up these tests, a control beam monitor with known efficiency is placed in the path of the neutron beam, and the monitor to be evaluated is placed closely behind it. A neutron absorber that is larger than the overall size of the largest beam monitor being tested is selected (usually borated aluminum), and an aperture roughly the size of the smallest monitor active area is

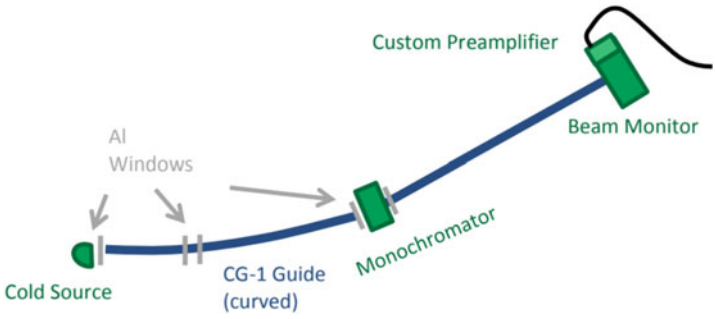

Fig. 3.81 Layout of beamline CG-1A located at the HFIR Cold Guide Hall [32]

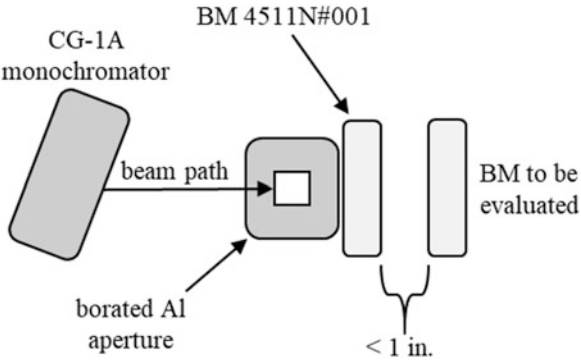

Fig. 3.82 Experimental setup for beam monitor (BM) efficiency test

created from it. This absorber is placed in front of the control beam monitor with the aperture aligned with the center of the active area of both monitors. An Ordela monitor designated as 4511N#001 is used as the control monitor for these tests because its known efficiency is 4.5×10^{-3} at 1.8 Å. Figure 3.82 illustrates this standard experimental setup.

Once set up, multiple acquisitions are collected at various bias voltages and discriminator threshold settings, and the count rates of the two monitors are compared to determine the new monitor's ideal operating condition. The efficiency for the new monitor is calculated using Eq. (3.124), where BM stands for beam monitor. This test only approximates the new beam monitor's efficiency as a ratio to that of the monitor with known efficiency characteristics. Some variables such as scatter or attenuation induced by the control monitor are not considered here.

$$\text{New BM eff.} = \frac{(\text{Control BM eff.}) \times (\text{New BM count rate})}{\text{Control BM count rate}} \tag{3.124}$$

In addition to the thermal efficiency measurement, tests have been conducted to determine the effects of inadequate anode bias and beam position within the beam monitor active area and the effects on efficiency for both. These tests were conducted on a ^{3}He monitor and a ^{14}N monitor at the CG-1A beamline with a similar setup to that shown in Fig. 3.82. For the first acquisition, the neutron beam was collimated using a 1 cm^2 aperture and positioned centered over one of the monitor's anode wires. Then, the acquisition was repeated, with the center of the collimated beam displaced 0.5 in. away from the anode wire toward the center of the monitor active area. The results for both monitors are shown in Fig. 3.83. The results show that adequate anode bias is a more critical parameter than the beam position on the monitor. With an inadequate anode bias, a substantial change in measured efficiency occurred when the neutron beam was not centered over the anode wire. This change makes sense considering that the electric field strength at low biases is not strong enough to create an output pulse with enough amplitude to trigger the discriminator electronics. As shown in Fig. 3.83, the on-anode and off-anode measurements agreed within approximately 4% at adequate anode biases.

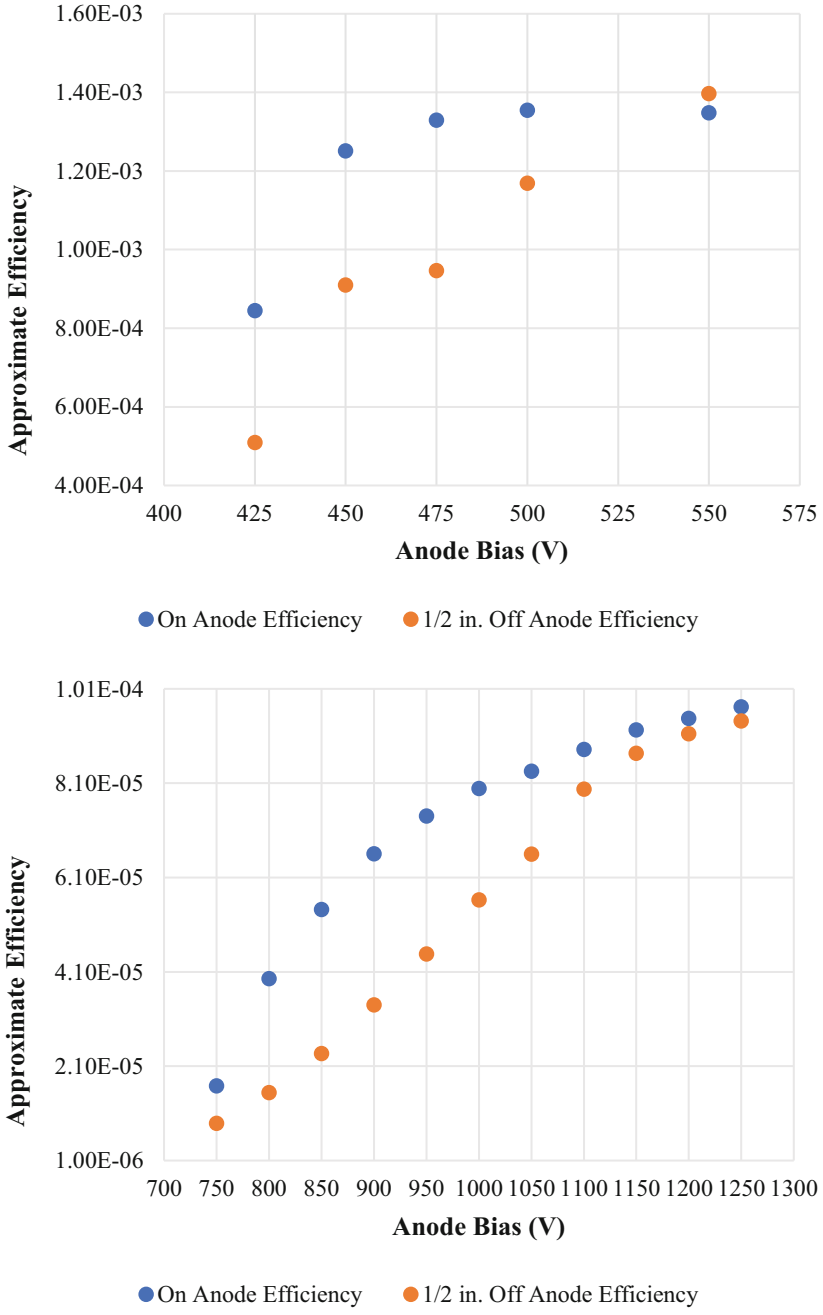

Fig. 3.83 Beam efficiency vs. anode bias voltage results for different beam positions. (*top*) ^{3}He monitor and (*bottom*) ^{14}N monitor

3.8.8.2 Beam Monitor Attenuation Test

Tests have been conducted at CG-1D in the HFIR Cold Guide Hall to determine the neutron wavelength-dependent transparency of a beam monitor. This beamline has a chopper at the beam port, which allows for neutron TOF calculations to measure the loss in count rate related to impinging neutron wavelength. Figure 3.84 illustrates the CG-1D beamline layout and the attenuation test setup.

The beam monitor in question is placed in the beam path with an aperture fixed in front of it to shield neutrons outside of the monitor's active area. Then, a high-efficiency (i.e., >95% at 1.8 Å) LPSD is placed behind it, and a TOF spectrum is taken on the high-efficiency detector. Next, the monitor is removed, and the measurement is taken again with only the LPSD. Finally, the count rate per wavelength for the two measurements can be compared to determine the percentage of rate lost per neutron wavelength. The results from this test are shown in Fig. 3.85. Using this method, the loss of beam intensity through Ordela monitor 4511N#001 was found to be approximately 5% over a wavelength spectrum from 1 to 10 Å.

3.8.8.3 Beam Monitor TOF Test

Neutron beam monitors at SNS can produce a TOF spectrum that can be used to determine the wavelength of the impinging neutron beam. The CG-1D beamline at HFIR has been used to test beam monitors for their accuracy in producing a reasonable time spectrum. The setup for this test was very similar to the attenuation test described previously except that no LPSD was required. The beamlines at HFIR

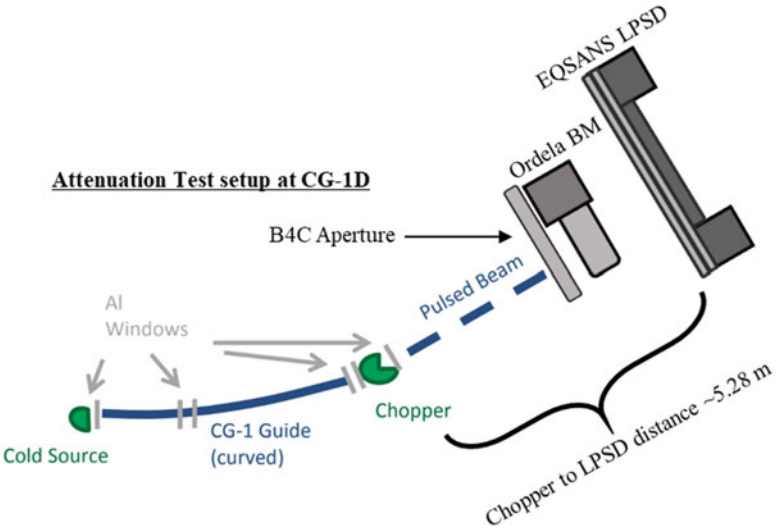

Fig. 3.84 CG-1D configuration and beam monitor attenuation test setup [32]

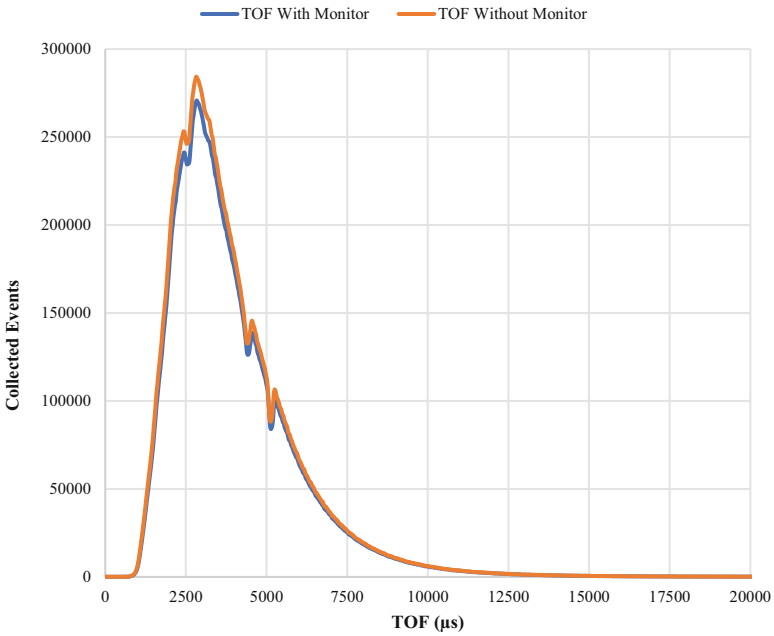

Fig. 3.85 Beam monitor wavelength-dependent attenuation test results

Table 3.6 Calculated results for aluminum attenuation based on Miller Indices using Eq. (3.125)

Al Miller Indices (h, k, l)	d_{hkl} (Å)	Wavelength (Å)	Calculated TOF (µs)	Delayed TOF (µs)
111	2.338	4.676	6242	7442
200	2.025	4.049	5405	6605
220	1.432	2.863	3822	5022
311	1.221	2.442	3259	4459
222	1.169	2.338	3121	4321

were built with aluminum windows, shown in Fig. 3.84, and they present a drop in transmitted neutrons at wavelengths parallel to the aluminum crystal lattice plane, at $\sin\theta = 1$ in Eq. (3.127), which is also known as Bragg's Law. Equation (3.125) details how the TOF is calculated. Table 3.6 gives the resulting calculations for the five aluminum crystal planes that can be seen in the 25 ms spectrum. The wavelength for the associated crystal lattice planes is calculated using Eq. (3.126) and Eq. (3.127), knowing that the lattice parameter (a) for aluminum is 4.05 Å, and n refers to the number of constructive harmonics of the given interatomic spacing (d_{hkl}) wavelength that fit within the timescale of the experiment—approximately 25 ms in this example. If the distance from the chopper to the beam monitor is known, then the TOF for these indices can be calculated and compared with the attenuation dips measured in the TOF spectrum to determine the monitor's TOF

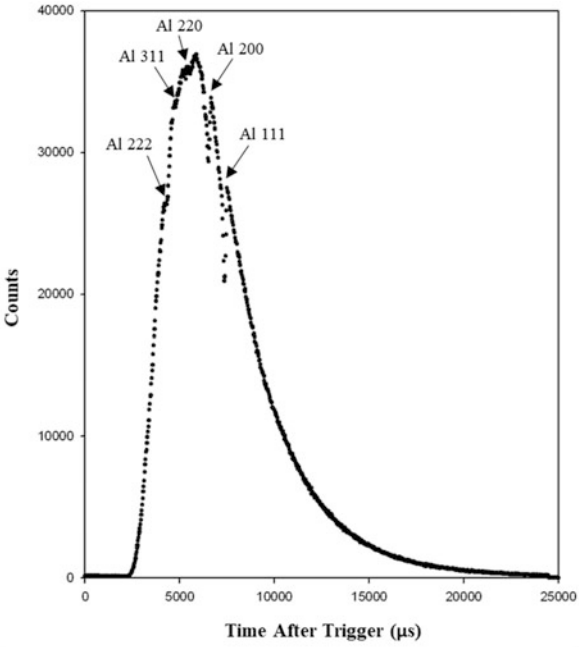

Fig. 3.86 TOF measurement results showing aluminum crystal lattice dips in transmission

capabilities. The arrival time of the timing signal is offset by 1200 μs from the chopper and the neutron pulse. This offset is captured in the measured waveform and is accounted for in the final column in Table 3.6. Comparing the calculated TOF for each of the indices and the measured results, as shown in Fig. 3.86, reveals that all the dips in neutron transmission measurement are close to the calculated time bin. Therefore, the monitor tested here is fully capable of producing an acceptable TOF spectrum.

$$\lambda = \frac{h}{mv} = \frac{3{,}956.0339 \times TOF}{D} \rightarrow TOF = \frac{D \times \lambda \mathrm{hkl}}{3{,}956.0339} + 1{,}200\ \mu\mathrm{s} \tag{3.125}$$

$$d_{hkl} = \frac{a}{\sqrt{h^2 + k^2 + l^2}} \tag{3.126}$$

$$\lambda = \frac{2\sin(\theta) d_{hkl}}{n} \tag{3.127}$$

3.8.9 Conclusion and Future Requirements

To conclude, a summary of some important performance characteristics for the MWPC beam monitor are shown in Table 3.7.

Table 3.7 Summary of performance characteristics for MWPC beam monitors

Performance characteristic	MWPC beam monitor
Thermal neutron efficiency	^{3}He: 10^{-3}–10^{-4}
	^{14}N: 10^{-4}–10^{-6}
Attenuation/scattering	4%–5%
Max count rate	~100,000 counts/s

The MWPC beam monitors are the default monitors employed at SNS and HFIR. The only real decisions made on a per-beamline basis are the number of beam monitors required, their location in the beamline, and their desired efficiencies. Because of this lack of attention, two surveys that asked how instrument beam monitors are used and what realistic improvements are desired were completed by SNS scientists in 2018 and HFIR scientists in 2021. These results were then compressed and tabulated to determine the beamline scientists' most pressing needs. The most-requested improvements are the following:

- Increased transparency of the neutron beam
- Position sensitivity
- Increased count rate
- Improved long-term stability

These findings have motivated efforts to identify and qualify commercially available monitors. Furthermore, research and development projects are focused on addressing one or more of the requested improvements.

One such commercially available monitor is a scintillator-based monitor manufactured by Quantum Detectors. This monitor was designed specifically for beamline diagnostics at the ISIS Neutron and Muon Source at the Rutherford Appleton Laboratory in the United Kingdom. The monitor was designed to provide a high level of neutron transparency, excellent neutron-to-gamma ray discrimination, and very high–count rate capabilities. Information pertaining to detailed performance characteristics for the ISIS beam monitor is contained in the literature [33, 34]. A sample monitor from Quantum Detectors was tested at BL-16B at SNS in December of 2014. The amplified detector signal was connected to a manufacturer-supplied discriminator card that was tuned to reject signals that fell below a 700 mV setting. This card produces a 200 ns width, −2 V amplitude pulse output per neutron absorption. Because each event produces the same output, the monitor is designed to be an event counter. These event pulses were fed to modified, SNS-style electronics to allow existing data acquisition software to be used for measurements and data logging.

To quantify the efficiency and count rate, the monitor was placed in front of an Ordela MWPC monitor with a known efficiency of 9.09×10^{-6} at 1.8 Å. A 1 mm thick borated aluminum plate with a 28 × 42 mm aperture was placed such that the aperture covered the quoted active area of the scintillating monitor while attenuating the beam elsewhere. The control monitor was placed 2 cm downstream of the scintillating monitor and had an 8 mm thick borated plate with a similar aperture cut into it to effectively mimic the same active area of the scintillating monitor. Once set up, the monitors sampled the neutron beam for approximately 20 min. The TOF

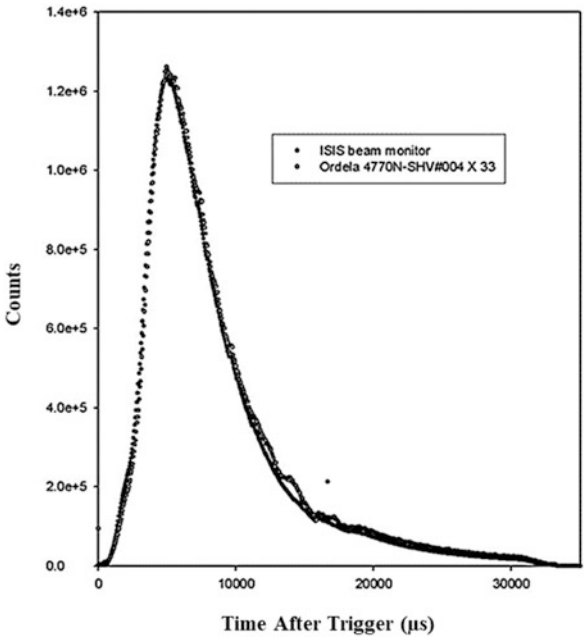

Fig. 3.87 TOF spectrum comparing ISIS beam monitor and MWPC monitor

spectrum results comparing the two monitors are shown in Fig. 3.87. The ISIS beam monitor was shown to track the TOF spectrum of the MWPC monitor extremely well. The efficiency of the Quantum Detectors scintillating bead monitor was calculated using Eq. (3.124) as approximately 2.9×10^{-4}. The ISIS monitor was tested up to 150,000 counts per second without saturation, which equates to approximately 1×10^{9} range beam flux. Upon completion of these tests, an ISIS monitor was purchased and commissioned for SNS BL-4A.

An R&D project was conducted to find a high–count rate and high–dynamic range beam monitor that ideally would not use ^{3}He as the conversion isotope. The monitor was based on a parallel-plate design inside a gas-filled enclosure. During project development, several different combinations of electrode materials, fill gas composition, and neutron conversion materials were used to determine a wide range of operating characteristics for this design. A particular combination yielded a count rate of 1×10^{6} counts per second at a thermal neutron efficiency of 10^{-3} without saturation. The data for this combination indicates that this specific monitor design can measure a neutron beam with a thermal flux rate of 1×10^{9} neutrons per second. All the information pertaining to the parallel-plate avalanche beam monitor was retrieved from a master's thesis, under which the project results were summarized [32]. Table 3.8 summarizes the results from this project and the different design methods that were tested.

In 2022, a research and development effort began that aimed to produce beam monitors based on semiconductor technology. Owing to their fast electron drift velocity, these devices provide superior high–count rate capabilities compared

Table 3.8 Parallel-plate beam monitor R&D summary of results and attempted designs

Beam monitor design A–C–isotope	Measured neutron efficiency	Expected beam flux that can be measured	Approximate flux used for measurement
Quartz–aluminum–^{3}He	$(4.0 \pm 0.5) \times 10^{-4}$	4.0×10^{10}	$(3.0 \pm 0.8) \times 10^{9}$
Alumina–aluminum–^{3}He	$(1.0 \pm 0.5) \times 10^{-5}$	1.0×10^{11}	$(1.4 \pm 0.2) \times 10^{8}$
Alumina–boron-doped silicon	$(1.1 \pm 0.3) \times 10^{-5}$	1.1×10^{11}	$(1.1 \pm 0.6) \times 10^{5}$
Silicon–boron-doped silicon–^{3}He	$(1.2 \pm 0.2) \times 10^{-3}$	1.2×10^{9}	$(1.4 \pm 0.2) \times 10^{8}$
Alumina–aluminum–LiF sample 1	$(2.2 \pm 0.5) \times 10^{-6}$	2.2×10^{12}	$(4.1 \pm 0.4) \times 10^{8}$
Alumina–aluminum–LiF sample 2	$(9.8 \pm 0.6) \times 10^{-7}$	9.8×10^{13}	$(4.1 \pm 0.4) \times 10^{8}$

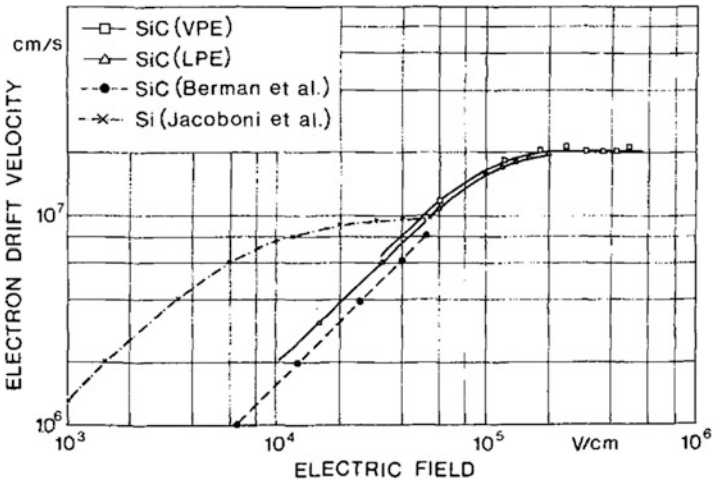

Fig. 3.88 Electron drift velocity vs. electric field potential for silicon [35]

with the MWPC beam monitors. As shown in Fig. 3.88, at very high electric fields (5×10^5 V/cm), the saturated electron drift velocity (v_s) approaches 2×10^{11} μm/s [35]. With this value, Eq. (3.128) calculates that the expected transit time (T_t) for electrons in the 300 μm thick ($Si_{\text{Thickness}}$) silicon semiconductor beam monitor is approximately 1.5 ns. By employing custom readout electronics that have 15 ns resolution time, the readout system for these monitors can track this electron drift alone. This ability allows for up to three orders of magnitude faster readout capabilities (theoretically, greater than 100×10^6 counts per second) than the MWPC, which is limited by the drift time of the heavier positive ions. For this project, two monitors are being constructed; one will provide a zero-dimensional counting mode

design that will be used as a high-rate flux monitor, and the second is being constructed as a 2D, position-sensitive design that can be used for beam profiling. Theoretically, by using semiconductors that have natural boron as the p-type doping material and the flexibility of adding either a ^{10}B or ^{6}Li layer on the entrance window, monitors of this design enable a controllable variation in thermal neutron absorption efficiencies.

$$T_t = \frac{Si_{\text{Thickness}}}{V_s} \approx 1.5 \text{ ns} \tag{3.128}$$

References

1. W-values from ICRU Report 31, "Average Energy Required to Produce an Ion Pair," International Commission on Radiation Units and Measurements, Washington D.C. 1979.
2. R.K. Crawford, Position Sensitive Detection of Slow Neutrons: Survey of Fundamental Principles. In *Proceedings of SPIE International Symposium on Optical Applied Science and Engineering*, San Diego, CA, July 19–24, 1992. https://www.osti.gov/servlets/purl/5095599
3. A. Doumas, G.C. Smith, Comparison of various stopping gases for ^{3}He-based position sensitive neutron detectors. Nucl. Instrum. Methods Phys. Res., Sect. A **675**, 8–14 (2012). https://doi.org/10.1016/j.nima.2012.01.035
4. V. Radeka, N.A. Schaknowski, G.C. Smith, B. Yu, High precision thermal neutron detectors, in*Neutrons in Biology*, Basic Life Sciences, ed. by B.P. Schoenborn, R.B. Knott, vol. 64, (Springer, Boston, 1996), pp. 57–67
5. E. Storm, H.I. Israel, Photon cross sections from 1 keV to 100 MeV for elements Z = 1 to Z = 100. Nucl. Data Tables **A7**, 565–688 (1970). https://doi.org/10.1016/S0092-640X(70)80017-1
6. X Ray Proportional Counter. *PhysicsOpenLab*. 23 July 2017. https://physicsopenlab.org/2017/07/23/x-ray-proportional-counter-2/
7. I. Dioszegi, B. Yu, G. Smith, N. Schaknowski, J. Fried, P.E. Vanier, C. Salwen, L. Forman, A new pad-based neutron detector for stereo coded-aperture thermal neutron imaging, in *Proceedings of 2013 IEEE Nuclear Science Symposium and Medical Imaging Conference*, Seoul, South Korea, October 27–November 2, 2013. https://doi.org/10.1109/NSSMIC.2013.6829416., https://ieeexplore.ieee.org/stamp/stamp.jsp?tp=&arnumber=6829416
8. N. Schaknowski, J. Fried, G. Smith, G. Mahler, B. Yu, Design and construction of a 1 m × 1 m thermal neutron imager operating in ionization mode with pad readout, in *Proceedings of 2018 IEEE Nuclear Science Symposium and Medical Imaging Conference*, Sydney, Australia, November 10–17, 2018. https://doi.org/10.1109/NSSMIC.2018.8824283., https://ieeexplore.ieee.org/stamp/stamp.jsp?tp=&arnumber=8824283
9. G.F. Knoll, *Radiation Detection and Measurement*, 4th edn. (Wiley, 2010)
10. W. Diethorn, A Methane Proportional Counter System for Natural Radiocarbon Measurements. Thesis, Carnegie Inst. of Tech., Pittsburgh, PA, 1956
11. K.D. Berry, et al., Characterization of the neutron detector upgrade to the GP-SANS and Bio-SANS instruments at HFIR. Nucl. Instrum. Methods Phys. Res., Sect. A **693**, 179–185 (2012). http://dx.doi.org/10.1016/j.nima.2012.06.052
12. W. Shockley, Currents to conductors induced by a moving point charge. J. Appl. Phys. **9**(10), 635 (1938). https://doi.org/10.1063/1.1710367
13. S. Ramo, Currents induced by electron motion. Proc. IRE **27**(9), 584–585 (1939). https://doi.org/10.1109/JRPROC.1939.228757

14. D. McGregor, J.K. Shultis, *Radiation Detection: Concepts, Methods, and Devices* (CRC Press, 2020)
15. Analog Devices, Inc *Data Sheet AD8022, Rev. C*, 2011
16. J. Alberi, J. Fischer, V. Radeka, L.C. Rogers, B. Schoenborn, A two-dimensional position-sensitive detector for thermal neutrons. Nucl. Instrum. Methods **127**(4), 507–523 (1975). https://doi.org/10.1016/0029-554X(75)90654-0
17. B. Yu, J.A. Harder, J.A. Mead, V. Radeka, N.A. Schaknowski, G.C. Smith, Neutron detector development at Brookhaven. Nucl. Instrum. Methods Phys. Res., Sect. A **513**(1–2), 362–366 (2003). https://doi.org/10.1016/j.nima.2003.08.063
18. J. Fried, J.A. Harder, G.J. Mahler, D.S. Makowiecki, J.A. Mead, V. Radeka, N.A. Schaknowski, G.C. Smith, B. Yu, A large, high performance, curved 2D position-sensitive neutron detector. Nucl. Instrum. Methods Phys. Res., Sect. A **478**(1–2), 415–419 (2002). https://doi.org/10.1016/S0168-9002(01)01787-9
19. V. Radeka, et al., in: B.P. Schoenborn, R.B. Knott (Eds.), Neutrons in Biology, Plenum Press, New York, 1996, pp. 57-67.
20. B. Yu, et al., Nucl. Instr. Meth. A **513**, 362-366 (2003).
21. B. Yu, Z. Zojceski, J.A. Harder, A. Hrisoho, V. Radeka, G.C. Smith, Front-end electronics for high rate, position sensitive neutron detectors. Nucl. Instrum. Methods Phys. Res., Sect. A **485**(3), 645–652 (2002). https://doi.org/10.1016/S0168-9002(01)02111-8
22. ORNL generated image.
23. J. Fried, et al., Advanced two-dimensional thermal neutron detectors for scattering studies Proc. SPIE 4785, Advances in Neutron Scattering Instrumentation, (18 November 2002); https://doi.org/10.1117/12.456300.
24. Photo courtesy Graham C. Smith, Brookhaven National Laboratory, Upton, New York
25. ORNL generated image courtesy Matthias Frontzek
26. *2410N Test and Calibration Report*; (ORDELA Inc., Oak Ridge, 2011)
27. G. Mauri, Development and Characterization of Detectors for Large Area Application in Neutron Scattering and Small Area Application in Neutron Reflectometry. PhD Thesis, Universita Degli Studi di Perugia, Perugia, Italy, 2019
28. Electric Power Research Institute. Portable Survey Instruments: RP0201 Approved Rev. SlideToDoc, retrieved August 19, 2022. https://slidetodoc.com/portable-survey-instruments-rp-02-01-approved-rev/
29. G. Charpak, F. Sauli, High-resolution electronic particle detectors. Ann. Rev. Nucl. Part. Sci. **34**, 285–349 (1984). https://doi.org/10.1146/annurev.ns.34.120184.001441
30. K.D. Berry, *Neutron Lifecycle Series: Helium-3 Gas Detectors at the SNS and HFIR*, The Neutron Lifecycle Lecture Series (Oak Ridge National Laboratory, 2016)
31. J. Lowke, The drift velocity of electrons in hydrogen and nitrogen. Australian J. Phys. **16**(1), 115–135 (1963). https://doi.org/10.1071/PH630115
32. A.K. Barnett, Investigation of Higher Count Rate and Helium-3 Alternative Beam Monitors for Neutron Scattering Facilities. MS Thesis, The University of Tennessee, Knoxville, TN (2013)
33. F. Issa, A. Khaplanov, R. Hall-Wilton, I. Llamas, M.D. Riktor, S.R. Brattheim, H. Perrey, Characterization of Thermal Neutron Beam Monitors. *arXiv* (*physics.ins-det*), February 3, 2017, 1702.01037v1. https://arxiv.org/pdf/1702.01037
34. Quantum Detectors, *Operational Guide for the ISIS Neutron Beam Monitor*. Retrieved April 7, 2022. ISIS-Neutron-Beam-Monitor (kosinc.co.kr)
35. W.V. Muench, E. Pettenpaul, Saturated electron drift velocity in 6H silicon carbide. J. Appl. Phys. **48**, 4823 (1977). https://doi.org/10.1063/1.323506

Chapter 4
Scintillator-Based Detectors

Matthew Loyd and Polad Shikhaliev

Abstract This chapter focuses on scintillation detectors for thermal neutron detection at neutron scattering facilities. The chapter includes two parts. The first part is on Anger camera-based thermal neutron detectors, and the second part is dedicated to thermal neutron detectors using Wavelength Shifting Fibers (WLSF).

Neutron sensitive Anger cameras offer many properties that are attractive for scattering applications such as single crystal diffraction. They can be tiled sufficiently in both planar and spherical geometries and offer a good spatial resolution and uniform active surface. This chapter describes the structure and operation of PMT-based Anger cameras in use at Oak Ridge National Laboratory neutron beamlines and discusses a new version that uses SiPMs for improved performance and capabilities.

The WLSF based detectors can provide effective alternative to other detectors, particularly He-3 tube based detectors. The WLSF can provide large area detectors with high detection efficiency, spatial resolution, timing resolution, and at substantially lower costs. This chapter describes physical principles of WLSF method, detector design concepts, and details of the position encoding methods. The current status, potential limitations, and possible solutions are also described. Finally, an example of the first results achieved with a new WLSF detector design is presented.

4.1 Anger Cameras for Neutron Detection

4.1.1 Anger Cameras

4.1.1.1 History

The 1940s and 1950s saw great interest in the medical industry for using radioisotopes to gain information about certain areas inside the body, such as cancerous

M. Loyd (✉) · P. Shikhaliev
Neutron Sciences Directorate, Oak Ridge National Lab, Oak Ridge, TN, USA
e-mail: loydms@ornl.gov; shikhalievpm@ornl.gov

Y. Diawara (ed.), *Neutron Detectors for Scattering Applications*, Particle Acceleration and Detection, https://doi.org/10.1007/978-3-031-36546-1_4

tumors. Because tumors have high metabolic activity, pinpointing certain molecules with radioactive isotopes can be used to determine the location of cancer. Therefore, developing a device that could not only detect high-energy radiation but also precisely determine its position on a 2D grid was imperative. One such attempt was made by Hal Anger, in which he used a pinhole aperture to focus gamma rays onto a single scintillation crystal mounted to multiple photomultiplier tubes (PMTs). Because scintillation light is isotopically emitted in a single crystal, multiple PMTs are struck by photons after a gamma ray is absorbed. By comparing the intensity of the signal from each PMT for any given event, he was able to calculate the position of the incident gamma ray to a finer precision than simply the number of PMTs used [1]. A schematic of the basic principle of Anger cameras is shown in Fig. 4.1.

Although the technology has improved since the 1950s, the basic principle of the Anger camera has stayed the same. The Anger camera has been used throughout the medical imaging field, as well as radiation detection in general. Current devices for single-photon emission computed tomography (SPECT) use a single scintillator coupled to a large array of PMTs [2, 52]. The incoming gamma rays are collimated to ensure that gamma rays that are not incident at normal angles are not detected, thus improving the resolution of the detector.

The Anger camera, although originally designed for gamma ray detection, has found use in the field of neutron detection for scattering experiments [3–8]. This chapter will cover the design and operation of neutron-sensitive Anger cameras currently in use at the Spallation Neutron Source (SNS) and High Flux Isotope Reactor (HFIR) at Oak Ridge National Laboratory (ORNL). Additionally, it will cover sources of error, paths for improvement, and future planned detectors.

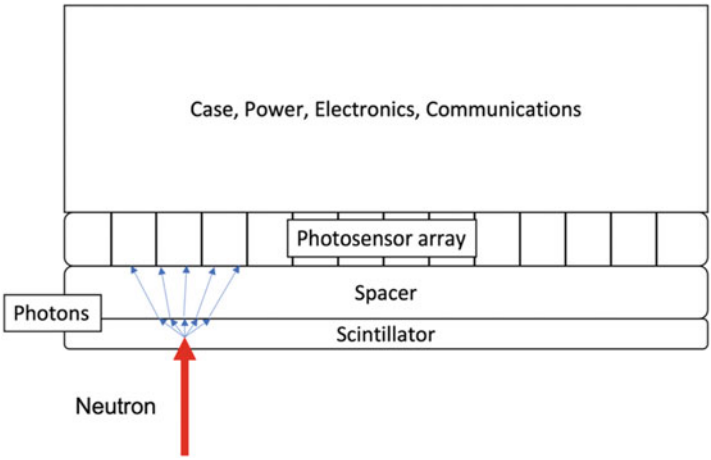

Fig. 4.1 The basic principle of an Anger camera. A neutron produces photons in a single scintillator, which spread over multiple photosensor pixels. The position of the neutron can be determined by looking at the signal on the pixel array

4.1.1.2 Principle of Operation

The basic process of Anger camera operation includes a neutron absorption in the scintillator, the chain that the generated signal follows, and the onboard software that processes the event. Each process and required components are described in detail in the following sections. Current-generation neutron Anger cameras have a front-end optics package that uses a ^{6}Li glass scintillator. To collect the maximum possible amount of light, this scintillator is coated with a reflector material on the beam side. A borosilicate glass spacer behind the scintillator allows the photons to spread out after leaving the scintillator and before striking the photosensor, which is either a PMT or a silicon photomultiplier (SiPM). The thickness of the scintillator and the spacer can be adjusted to change the shape of this so-called *light cone* of scintillation photons to optimize the spread of signal on the photosensors. A silicone gel component, called a *cookie*, between the spacer and photosensor and optical coupling between the scintillator and the diffuser improve light collection.

The entire process, from neutron absorption to data collection, begins with the scintillators. Scintillators for thermal neutron detection typically use an isotope with a high absorption cross section, such as ^{6}Li or ^{10}B. When a thermal neutron is absorbed by ^{6}Li, a ^{6}Li(n,α) reaction occurs (Eq. [4.1], n stands for neutron), and 4.78 MeV of energy is released as kinetic energy of daughter products [9].

$$^{6}_{3}\mathrm{Li} + {}^{1}_{0}\mathrm{n} \rightarrow {}^{3}_{1}\mathrm{H} + {}^{4}_{2}\alpha \tag{4.1}$$

These daughter particles rapidly deposit all their kinetic energy, and scintillation photons are produced. The scintillator emits photons in a time profile that is characteristic of the activator, as well as the scintillator compound. The photosensor converts detected photons into an electronic signal.

The signal from each array is summed in the x and y directions to reduce signal complexity. The summed x and y signals are then converted from analog to digital in the analog-to-digital boards and passed through a discriminator. If any of the signals exceed the discriminator, the integrators on the analog-to-digital board are run for a programable amount of time (approximately 600 ns). This integrated signal is then sent to the field-programable gate array (FPGA) board. On this board, the signal is corrected for dark current and electrical noise, and the x and y signals from each array are combined into a single x and y array of 24 (for PMT cameras) or 16 (for SiPM cameras) values. A Gaussian curve is then fit to the x and y signals to obtain an (x, y) position on the camera, and a geometric correction is added based on values from a lookup table. The event is then rejected if its total summed intensity is outside of a predetermined range for each position on the board to improve gamma ray discrimination. The final (x, y) position, as well as some additional information about the event, is then sent to the computer through a cable link. More details about the camera hardware and the specifics of each step in this process are discussed in the next sections.

4.1.2 Design

In this chapter, the specific designs—including the outer casing, front-end optics package, custom electronic circuit boards, FPGA board, firmware, software, and data-link protocol—of the Anger camera are discussed in detail. The two types of Anger cameras used at SNS and HFIR are shown in Fig. 4.2. Additionally, a schematic diagram of the Anger camera and its components is expanded in Fig. 4.3.

The outer casing of the Anger camera is custom-designed and depends on the geometry in which it is finally installed, but it serves three main purposes regardless. First, the casing protects and holds all the internal parts together and provides pressure to keep mounted boards in place. Second, the case ensures light tightness for the front-end optics. If the casing is not light tight, stray photons will strike the photosensor and increase noise in the detector. Finally, the housing serves as an electromagnetic shield for the electronics.

4.1.2.1 Front-End Optics

The three necessary components of the front-end optics package are the scintillator glass, the borosilicate spacer, and the photosensor. Additionally, all current Anger cameras have a few pieces of approximately 1 mm thick perfluoroalkoxy alkane Teflon that helps improve light collection and provides a springy back support to the scintillator to keep it coupled to the remaining optics. However, Teflon also scatters neutrons and should not be ignored as a possible source of error. A single piece of a

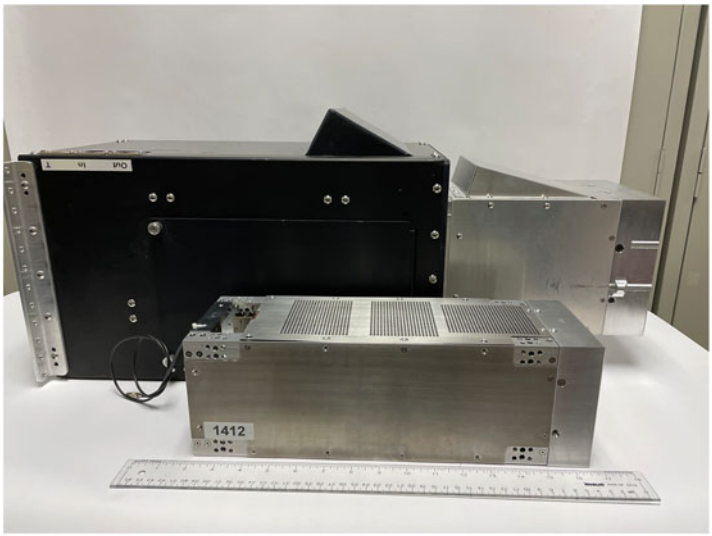

Fig. 4.2 (*back*) PMT-based Anger camera and (*front*) SiPM-based Anger camera

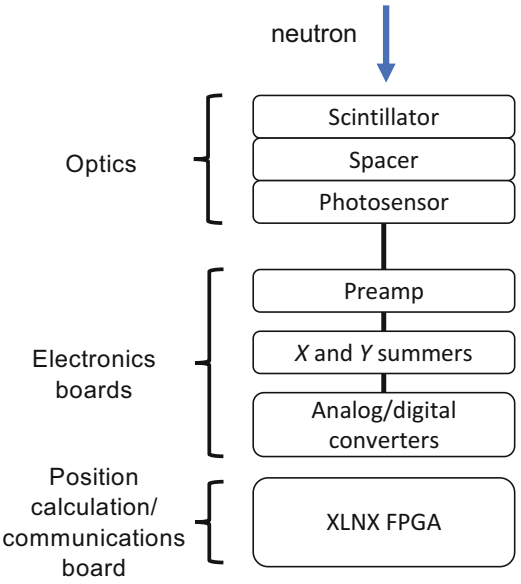

Fig. 4.3 Schematic block diagram of Anger camera components

Table 4.1 Properties of GS20 glass scintillator [10]

Property	Value
^{6}Li enrichment	95%
Total lithium (wt %)	6.6
Density (g/cm^3)	2.50
Photons per neutron	~6000
Decay times—neutron (ns)	18, 57, 98
Wavelength of maximum emission (nm)	395
Refractive index	1.55

^{6}Li-containing glass scintillator converts cold or thermal neutrons into visible light. Current-generation Anger cameras commonly use GS20, which is a commercially available aluminosilicate glass containing ^{6}Li that is doped with cerium. The properties of GS20 are listed in Table 4.1.

Each neutron absorbed in GS20 produces approximately 6000 photons within a few nanoseconds to 100 ns. This relatively prompt emission is required owing to the high flux available at beamlines. The decay time of the scintillator is a limiting factor of high–count rate applications. A single event of a GS20 scintillator coupled to an ET Enterprises 9124B PMT [11] under excitation from a ^{252}Cf source is plotted in Fig. 4.4a. The current from the photosensor is proportional to the number of photons absorbed by the sensor. Integrating many of these events (gamma ray and neutron) from the ^{252}Cf source and binning their intensities into a histogram produces a pulse-height spectrum, plotted in Fig. 4.4b. A neutron peak is resolved on this spectrum, with many gamma ray events also shown at lower energies.

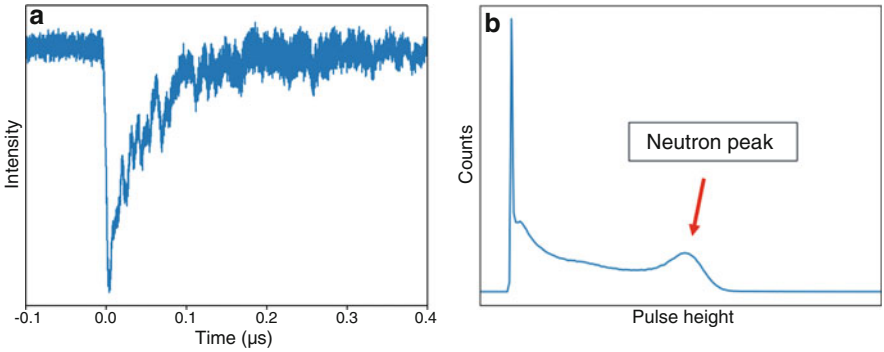

Fig. 4.4 (**a**) Single neutron event pulse collected on a PMT using a GS20 scintillator, (**b**) a pulse height spectrum of many neutron and gamma ray events

The backside of the scintillator glass is painted with a titanium oxide reflector. The scintillator glass is typically on the order of 1–2 mm thick. Based on the density of ^{6}Li in GS20, the thickness of the scintillator glass should result in a neutron detection efficiency of 75–90%. Although neutron detection efficiency increases with increasing thickness, positional resolution decreases. A thicker scintillator will have a greater variation in light spreading between neutron interactions at the front of the scintillator versus interactions that occur close to the photosensor.

The borosilicate spacer thickness can vary but is typically approximately 3 mm thick. This thickness allows for an adequate amount of light cone spreading, which affects the resolution and distortion of the detector. The scintillator and spacer are coupled together using optical grease. This optical grease should reduce diffuse scattering owing to the difference in index of refraction between the glasses and air. Additionally, an approximately 0.3 mm thick silicone piece with a gel-like consistency called a cookie is used to couple the spacer to the photosensor surfaces to help with light collection and even out any places where the PMT is surface is not level.

Beamlines at SNS currently are equipped with PMT-based Anger cameras, and DEMAND (Dimensional Extreme Magnetic Neutron Diffractometer, HB-3A) at HFIR uses the newer SiPM-based models. There are a few differences between the two. The PMT-based models use Hamamatsu H-8500 multianode PMT arrays. Each array has an 8 × 8 grid of pixels with a pixel width of approximately 6 mm. In the cameras at all SNS beamlines, 9 arrays are used in a 3 × 3 arrangement for a total of 576 pixels on each camera for an active area of 157 × 157 mm. There is a slight gap of approximately 4 mm between each array owing to the shape of the PMTs. The SiPM cameras have SensL ARRAYC-60035 arrays of 8 × 8 pixels with a width of 6.3 mm (pitch is 7.2 mm) in an arrangement of 2 × 2 arrays for a total of 256 pixels and an active area of 114.8 × 114.8 mm. Figure 4.5 shows the photosensor array for the PMT-based and the SiPM-based Anger cameras.

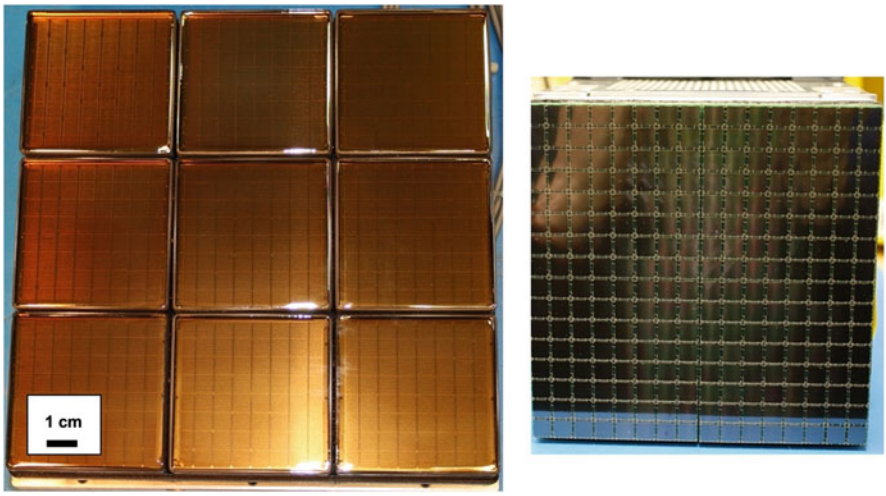

Fig. 4.5 Photosensor arrays for the (*left*) PMT and (*right*) SiPM Anger cameras. Both images are sized to the same scale

Light Cone

The position calculation of the Anger camera relies on Anger logic, which requires that photons activate at least two different pixels. If only a single pixel detects photons, then the greatest resolution that can be gleaned is the dimension of the photodetector pixels. However, if the light cone spreads too much, the position calculation has less accuracy owing to more spreading of the scintillation photons and lower statistics of photons detected on each individual photosensor. The error in position calculation decreases as the signal-to-noise ratio (S/N) of the photosensor increases. Therefore, the optimal light cone spread will distribute most of its light over three rows when centered on a pixel and two rows when centered on a gap.

To show this light cone spread, a simple model of light collection in one dimension was simulated. The dimensions of the photosensor array were assumed to be that of the ARRAYC 8 × 8 SiPM sensor, with 6.6 mm square pixels and a 0.6 mm gap between pixels. The light cone spread was modeled as a Gaussian curve with a standard deviation of 0.5, 1, and 1.5 pitch widths (pixel plus gap). The percent total light incident on each pixel is plotted in Fig. 4.6 for an event centered on a pixel and an event centered on the gap between pixels.

This model does not take into consideration the effect of incident photon angle on photosensor absorption, which can be significant depending on the spacing material, the photosensor face material, and any coupling materials. However, it does show how the light is mostly distributed on the photosensors. The most optimal standard deviation for events centered on a pixel is approximately 1 pitch width, and events centered on gaps have the best spread with a standard deviation of approximately half a pitch. Because the current design does not allow for a variation in light

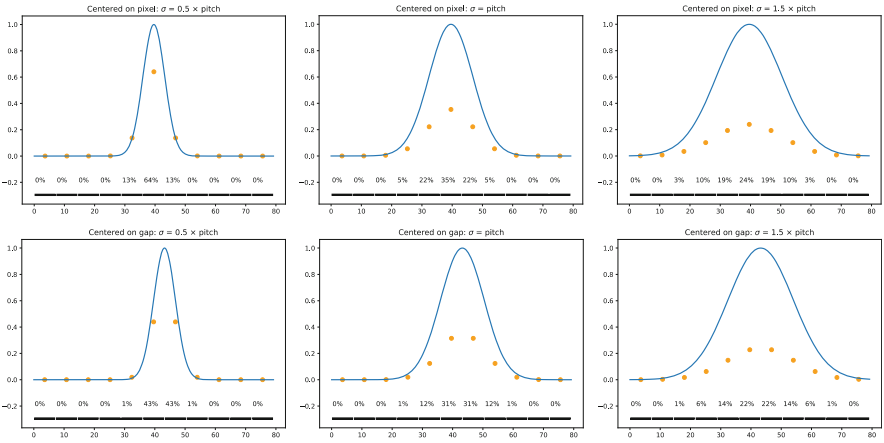

Fig. 4.6 Percent of total light incident on each photosensor pixel for (*top*) an event centered on a pixel and (*bottom*) the gap between pixels. The standard deviation of the light cone spread is (*left*) half of a pixel pitch, (*middle*) one pixel pitch, and (*right*) one and a half pixel pitches. The blue curves represent the distribution of photons, and the orange dotted curves are the intensity measured by each pixel

spreading across the camera face, a compromise was made: a final light cone was chosen with a standard deviation between 0.5 and 1 pitch widths.

The most direct way to control light cone spreading (and, consequentially, resolution) is by adjusting the thickness of the spacer glass. Light cones measured with different optic designs are plotted in Fig. 4.7.

In addition to resolution, position calculation distortion is a concern for Anger cameras. If a gap exists between pixels or arrays, or if the pixels are not uniformly sensitive to photons, then larger amounts of distortion on an image appear in these regions. For instance, imagine that an Anger camera is detecting a uniform radiation field, and that scintillation light is uniformly dispersed across the photosensor. Areas with higher sensitivity or less dead space (i.e., gaps between pixels) appear as if more photons struck the array in that location, and the location calculation skews in the direction of the error. A geometric position correction lookup table is generated to correct for this error and is discussed in a later section.

Gamma Ray Discrimination

Because of the nature of accelerator-driven and reactor sources, non-negligible gamma ray background signals often appear and are undesirable when detecting neutrons. The GS20-based Anger cameras use pulse height discrimination to differentiate between gamma ray and neutron events. The total light produced from a particle incident on the GS20 scintillator is approximately proportional to the energy of the particle and can be expressed in units of photons per megaelectron volts. However, this light yield is particle type–dependent. For GS20, the number of

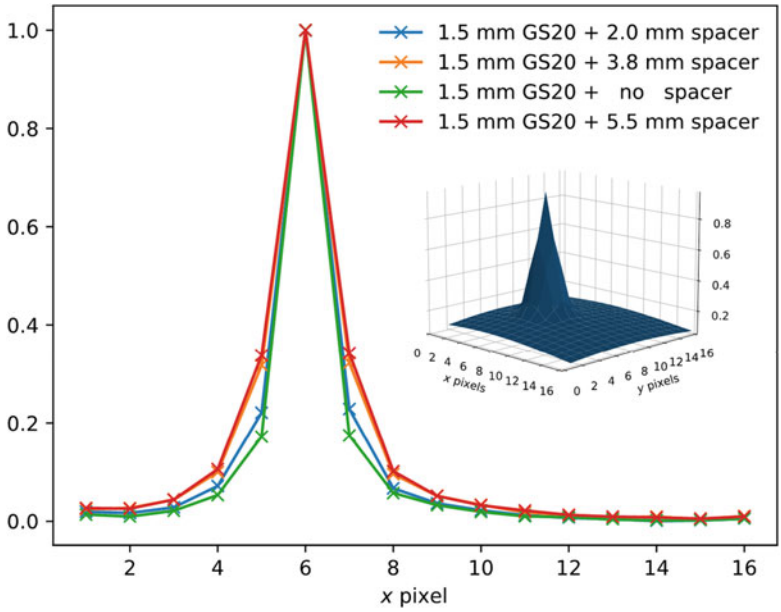

Fig. 4.7 *x*-direction light cones for various spacer thicknesses on a SiPM Anger camera with no optical grease or silicon gel. The light cones plotted are generated from neutron events that were determined to be centered on the sixth *x* pixel. The inset represents a typical 3D light cone shape

photons emitted per charged ion megaelectron volt is approximately one-third that of gamma rays. Fortunately, the total energy from a neutron reaction (4.78 MeV) is at least three times greater than typical background gamma ray energies.

The total light collected in an Anger camera from a single event is called the *photosum*. A typical distribution of photosums on a SiPM Anger camera measured with a ^{252}Cf source is plotted in Fig. 4.8. By fitting a Gaussian curve to the neutron peak in the photosum and only accepting events within approximately three standard deviations of the average, most gamma rays can be discriminated without significantly reducing neutron efficiency. However, this photosum distribution is also affected by light collection and is not the same across the active area of the Anger camera. For events that occur near the edge of the camera's face, less total light is collected, and the photosum is shifted to the left. To correct for this shift, a uniform flood pattern is measured, and a neutron photosum peak is fit for each position in a 512 × 512 array. Position-sensitive minimum and maximum value tables are produced that are used for rejecting non-neutron events (known as the sliding photosum method). The mean photosum values from a uniform flood on a 3 × 3 PMT detector are plotted in Fig. 4.9. The exact nature of the variation of the photosum strongly depends upon the size of the gap between sensor elements. In a multianode PMT, because of the glass envelope, this gap size can be quite large, leading to large variations in the photosum across the detector (Fig. 4.9). With the use of SiPMs, the

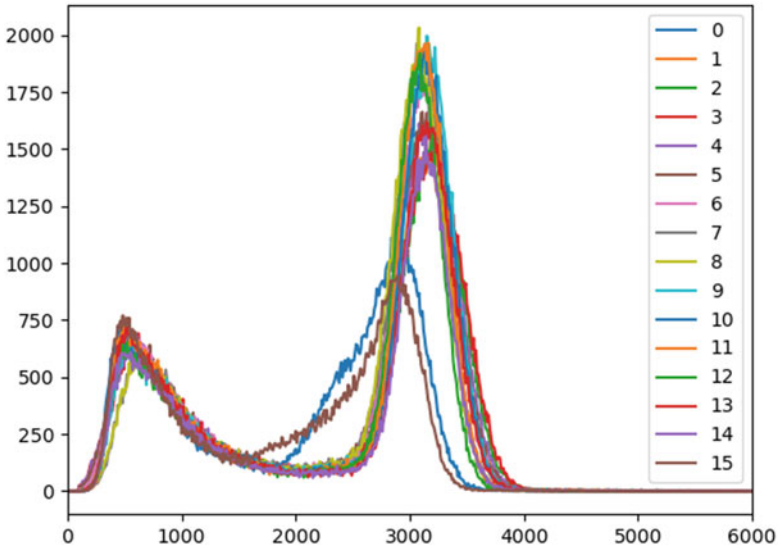

Fig. 4.8 Photosums for *x* columns of pixels on a SiPM Anger camera (1 mm GS20, 3.8 mm spacer *x* photosums). The two-peak shape is typical for GS20 and allows for effective gamma ray discrimination. The columns at the edge of the detector (labeled 0 and 15 in the chart) have worse light collection and reduced total photosum intensities

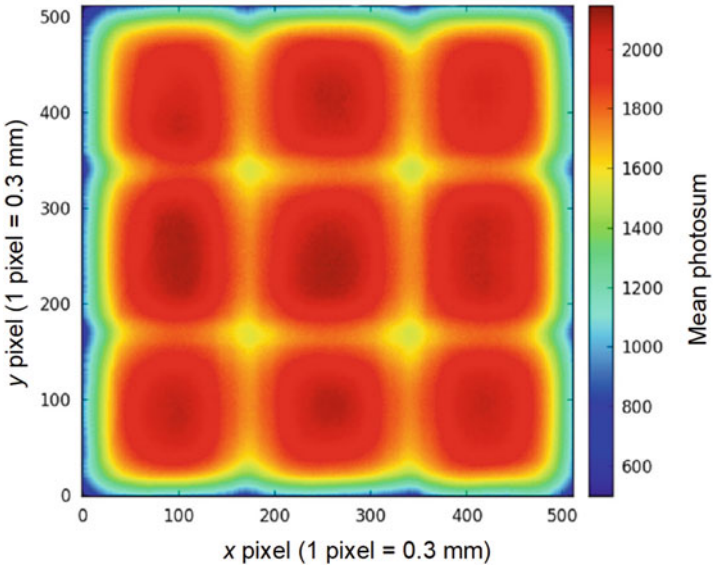

Fig. 4.9 Mean values of a neutron photosum peak measured from a uniform flood pattern on a 3 × 3 PMT detector. The variation across the detector is due to a combination of the light collection efficiency of the PMTs and light scattering effects at the edges of the detector (image reproduced from [12])

gap between elements can almost be eliminated, with strong variations occurring only near the edges of the detector.

When compared with fixed discriminator methods, reductions of 60% in gamma ray sensitivity can be achieved with the use of the sliding photosum method. Even with the use of this method, wide variations in gamma ray sensitivity still occur across the detector's sensitive area. Regions of comparatively poorer gamma ray rejection occur between sensor elements and at the edges, where the neutron photopeak is reduced in magnitude and broader. This variation is especially noticeable in weak scattering situations, where these regions of poorer gamma ray rejection appear brighter than average. Artifacts such as these can almost be removed with the use of localized curve fitting of the gamma ray spectra. To explain how this fitting can be accomplished, refer to Fig. 4.10. Figure 4.10 shows the photosum for all counted events (neutrons and gamma rays) in the region of a Bragg peak. The well-formed neutron photopeak is clearly shown, as well as the boron gamma ray peak, which is due to the prompt gamma rays from the absorption of neutrons in shielding that contains ^{6}B. The gamma ray tail is the part of the gamma ray spectra that is not discriminated by the sliding photosum method. However, by fitting the gamma ray tail (linear fit shown by the red line), this contribution to the Bragg Peak data can be substantively eliminated. This method can reduce gamma ray interference by close to an order of magnitude.

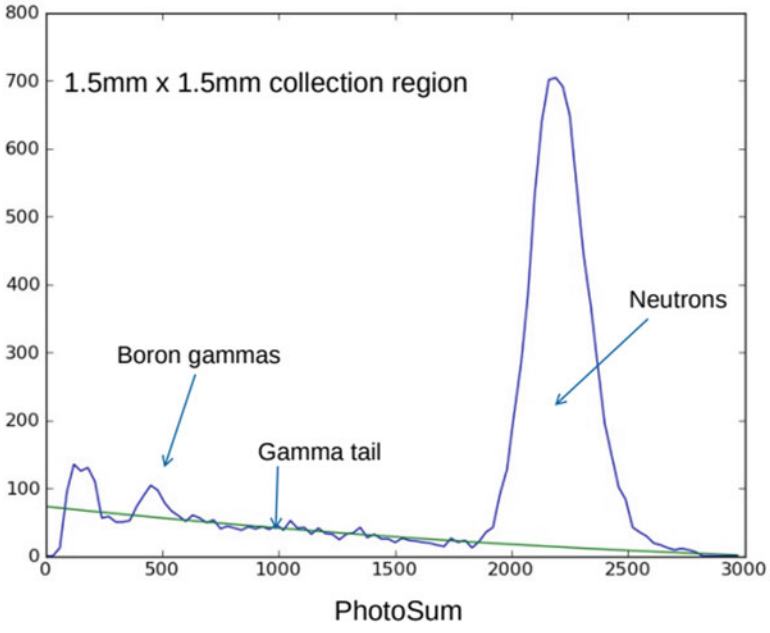

Fig. 4.10 The collected photosum spectra in a small region surrounding a Bragg peak

4.1.2.2 Electronic Boards

Although the exact layout depends on the number of arrays and varies between the SiPM and PMT, the basic components are the same for every Anger camera in use at SNS and HFIR. The PMT and SiPM arrays are mounted on printed circuit boards connected to preamplifier boards. For the PMT arrays, the gain of each pixel is adjusted by a hand-mounted resistor to ensure that the final gain of each pixel is within approximately 1% and that the array is set with a bias of 700–1000 V. Although the capability is available, the SiPM pixels currently do not have individually controlled gains. The bias for each SiPM camera is typically between 28 and 30 V (breakdown voltage of the ARRAYCs is ~24.5V, and an overvoltage of 3–5V is typical). The bias on each SiPM can be adjusted within a range to equalize gains across arrays. The preamplifier boards are connected to a summer board that sums up the signal in the *y* and *x* directions using summing amplifiers. This signal (eight *x* and eight *y* values per array) is then input into a gated integration stage [13].

The row and column signals are delayed via a 200 ns delay line and fed into a 12-bit pipeline analog to digital convertor (ADC). The time delay allows integration of the incoming signal to begin just before the rising edge of the signal. Each row and column signal is also fed into a simple threshold discriminator circuit (with hysteresis). The conversion electronics are handled by what is called an Anger camera readout control (AROC) board. The PMT cameras have an AROC board for each PMT tube (nine in total), and the SiPM cameras have two AROC boards, each handling the data from two SiPM arrays.

The signal from the AROC boards is combined on the Anger camera position calculation (ACPC) board, which also handles external communications and calibration configurations.

4.1.2.3 FPGA Board/Software

The position calculation, photosum discrimination, and communication streams are all handled on the ACPC board. Before the integration of the ACPC board, all raw data was sent to an operating computer, which carried out the position calculation. To improve counting capabilities, position calculation was implemented on an FPGA on the ACPC. On the FPGA, software written in C combines the signal from the separate AROC into two *x* and *y* arrays, each with either 24 or 16 values, depending on the number of photosensors.

Traditional Anger logic estimates position location using a simple, weighted sum. However, this method leads to distortions near boundaries and regions, where light collection is suboptimal. A more accurate method has been developed that involves fitting the collected *x* and *y* signals with a predetermined light cone shape [14]. During calibration, several light cones are collected. A reference curve is then determined by fitting a double Gaussian curve, seen in Eq. (4.2), to these light cones.

$$I_p(x) = A\left(a_1 \exp\left\{-b_1(x-\mu)^2\right\} + a_2 \exp\left\{-b_2(x-\mu)^2\right\}\right) \tag{4.2}$$

In Eq. (4.2), I_p is the intensity on a pixel at position x. The variance of these two Gaussian curves, as well as the intensity ratio between them, are saved as values a_1, a_2, b_1, and b_2. The FPGA then uses these values to fit the amplitude (A) and mean (μ) of light cones as they are collected using a Levenberg–Marquardt least squares fitting process with five iterations. Research has shown that reducing the number of iterations of this process can increase the maximum count rate but reduces the accuracy of the fit, and going above five iterations does not improve the accuracy. For the current applications of these detectors, count rate is not a limiting factor.

Once the position of the neutron event has been determined, the total photosum is compared with the photosum minimum and maximum lookup table described in Sect. 4.1.2.1. Finally, an x and y position correction value is added to the calculated position to correct for the geometric distortion discussed in Sect. 4.1.2.1. These values are determined by applying an algorithm to a uniform flood image collected on the detector without geometric corrections. Assuming that the neutron flux on the detector is uniform and neutron detection efficiency variance is minimal, then variations in intensity across the detector are because of errors in position fitting caused by gaps between arrays and variation in light collection efficiency on the photosensor. For instance, if a neutron event is centered on the edge of a PMT array, one side of the light cone will have a higher intensity, and the calculated position will be shifted away from the gap and toward the PMT array. This shift can be seen in Fig. 4.11, which includes a uniform flood collected on a 9 × 9 PMT detector without any geometric corrections. The regions with higher intensity in Fig. 4.11 are because of more events being binned into a region of constant area than should be in that region. The lookup table–generating algorithm, well-described in [15], effectively uses this increase in intensity profile in each direction to determine how much and in

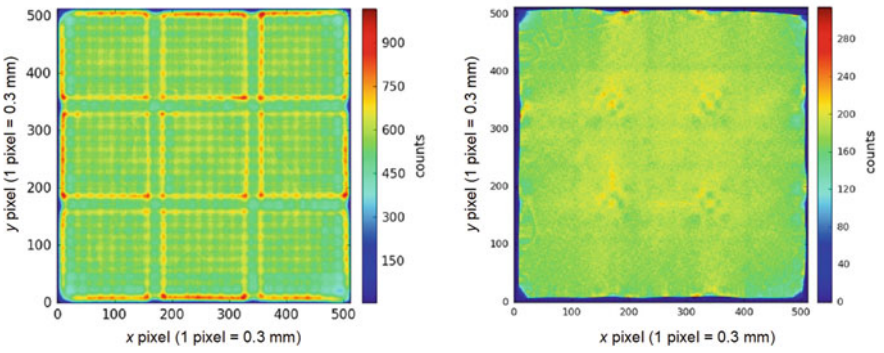

Fig. 4.11 (*left*) Uniform flood collected on a 9 × 9 PMT Anger camera and (*right*) a corrected uniform flood image. The areas with increased intensity are due to errors in the position calculation near the gaps between PMT arrays. Some minor, residual errors exist that are further improved on the SiPM Anger camera. (Image reproduced from [12])

which direction events at each pixel need to be shifted to be positioned correctly [15]. These x and y correction values are saved in a lookup table to be used by the FPGA code. A corrected flood image is also included in Fig. 4.11.

4.1.2.4 Communications

The PMT-based Anger cameras have been fully integrated into the SNS data collection software suit. Each AROC board has its own ip-address and can be communicated with independatly to set calibration values. However, the SiPM-based cameras have only a single point of communication. The SiPM detectors connect with a data acquisition computer using an ethernet or optic fiber cable and have two continuously running streams: a communication stream and a data stream. The communication stream is used to send commands to the detector, and the data stream sends events back to the computer. Both types of detectors can be operated in different modes. For calibrations, they run in raw mode and send all the x and y intensity values for each event. During normal operation, the x and y values are used for position calculation on the FPGA board. This position is then binned into a 512 × 512 array, and only the array indices, floating point x and y positions, and a time stamp are transmitted.

4.1.3 Performance

The performance of 2D detectors can be measured in two main ways: resolution and distortion. Resolution describes the size of features that can be resolved using the detector, and distortion describes how well the image is translated from the real 3D space onto a 2D image. For example, a detector with a slit mask might be able to fully resolve 10 mm slits but be unable to differentiate between separate 5 mm slits with a resolution between 5 and 10 mm. However, the slits could be exactly positioned without any residual distortion. Conversely, another detector fully capable of resolving 5 mm slits might produce an image in which the slits are distorted and bent. Because of the nature of Anger cameras and how they calculate position, an inherent trade-off exists between resolution and distortion. An Anger camera with no glass spacer and a thin scintillator might produce scintillation light that only activates one photosensor pixel. In that case, the resolution would be the size of the pixels, but there would be very little distortion because every event would be corrected and binned to the pixel it was directly above. A camera with larger light spreading would be able to resolve a position with finer accuracy than the size of the photosensor array, but it would do so with less signal per pixel, which decreases counting statistics and increases noise, especially near edges and gaps between pixels.

The spatial resolution of an Anger camera depends on many factors: the S/N of the photosensor, the number of photons produced per neutron event, the thickness of the scintillator, how well the scintillation photons are collected, statistical fluctuations in the distribution of photons, the width of the light spreading on the photosensors, the noise in the electronics chain, the number of background gamma

rays and the ability to discriminate them, and the position calculation method [2]. Additionally, any scattering of neutrons between the face of the detector and the scintillator can lead to events that are mislocated. Because of these factors, the spatial resolution is often calculated and optimized experimentally [16–19].

The resolution and distortion of both types of Anger cameras has been characterized. Resolution is determined by placing a borated aluminum slit mask on the face of the detector under a uniform neutron flux. The slit mask has a variety of slit widths, and the full width at half maximum of the slit profile describes the resolution. Results of the resolution measurements are plotted in Fig. 4.12. For distortion, a mask with evenly spaced 1 mm diameter pinholes is placed on the face of the detector. By measuring the difference between calculated position and actual position of the pinholes, a residual error as a function of location on the camera face is calculated. Images from these measurements are plotted in Fig. 4.13. In this figure, the resolution measured for the PMT Anger cameras is approximately 1 mm with a residual distortion approximately 0.5 mm in the worst locations and approximately 0.3 mm on average. The SiPM detectors show a better resolution of approximately

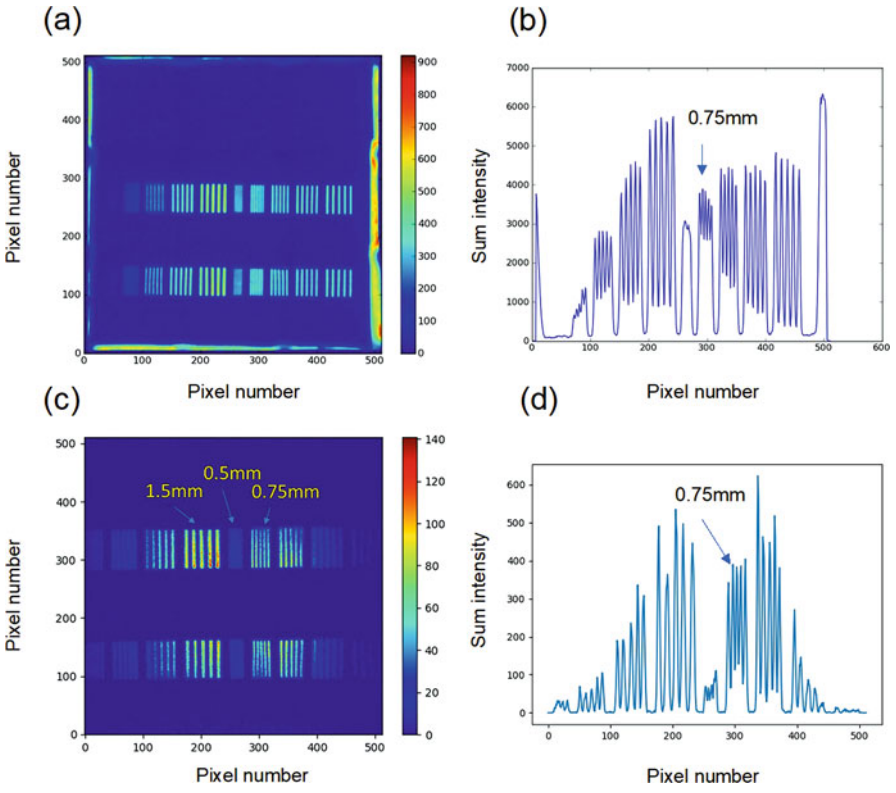

Fig. 4.12 Resolution comparison of (**a**) and (**b**) PMT Anger camera with (**c**) and (**d**) SiPM Anger camera. Resolution mask slit image for (**a**) PMT and (**c**) SiPM and intensity profile for (**b**) PMT and (**d**) SiPM. ((**a**) and (**b**) reproduced from [12])

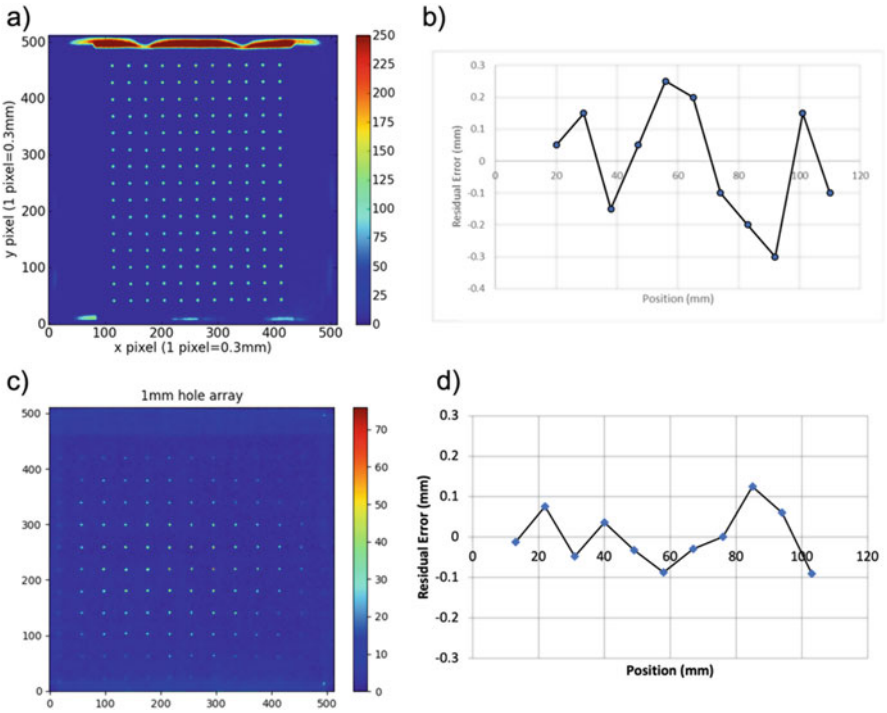

Fig. 4.13 Distortion comparison of (**a**) and (**b**) PMT Anger camera with (**c**) and (**d**) SiPM Anger camera. 1 mm pinhole mask image for (**a**) PMT and (**c**) SiPM and residual distortion profile for (**b**) PMT and (**d**) SiPM

0.6 mm and a residual distortion of approximately 0.2 mm. Resolution can be further improved by using a brighter scintillator to increase counting statistics and by using a smaller pixel size on the photosensor. Using an Onsemi ArrayJ series SiPM array with 3 mm pixels and a ZnS(Ag)/^{6}LiF scintillator, a spatial resolution of <200 μm has been observed. However, ZnS(Ag)/^{6}LiF is not used in Anger cameras because of its poor light collection efficiency. Finding a scintillator that is bright and transparent is necessary to further improve neutron Anger camera resolution. Distortion can be reduced by improving position correction algorithms and removing gaps between photosensor pixels.

The maximum count rate of Anger cameras is of interest because of the high flux of neutron beamlines. Although Anger cameras used in single-crystal diffraction beamlines do not experience full beam flux, they have potential for use in other instruments, such as small angle neutron scattering and imaging, both of which have much higher neutron fluxes. The current PMT Anger cameras have a maximum count rate of approximately 20 KHz, and the SiPM cameras with their newer FPGA hardware can process more than 100,000 events per second. This rate is currently limited by the position-fitting process. More-powerful FPGA hardware could improve this maximum count rate. If hardware were improved, then the next limiting

factor is the decay time of the scintillator. GS20 decay time allows for a maximum of approximately 1 MHz. Finding a faster replacement for GS20 would allow for an even higher maximum count rate.

4.1.4 Anger Cameras at Beamlines

Four beamlines at SNS and HFIR currently use Anger camera detectors to detect cold or thermal neutrons [20]. SNS beamline location (BL)-3 (SNAP, Spallation Neutrons and Pressure Diffractometer), BL-11B (MANDI, Macromolecular Neutron Diffractometer), and BL-12 (TOPAZ, Single-Crystal Diffractometer) all are equipped with PMT-based Anger cameras. HFIR Thermal Neutron Beam Guide Hall beamline location (HB)-3A (DEMAND) has SiPMs instead of PMTs. Properties of these beamlines are summarized in Table 4.2.

4.1.4.1 BL-3 SNAP

SNAP at BL-3 is a diffractometer for measuring samples under extreme pressure and temperature. Samples can be powder, single-crystal, or amorphous, and the sample environment can accommodate several sample sizes. Pressures of up to 20 GPa can be achieved from 80 to 1500 K and up to 6 GPa at higher temperatures [21]. Samples can also be tested at temperatures as low as 10 K. Typical applications for this beamline include hydrogen bonding in organic and inorganic materials, structural studies in functional oxides, structural signatures of pressure-induced phenomena in quantum systems, silicate melts, and studies of planetary ices under pressure.

To achieve a large angular coverage for this beamline while still leaving room for pressure and temperature sample environments, the front ends of the Anger cameras were detached from their typical configuration to allow for tight packing of the

Table 4.2 Specifications of Anger camera detectors at SNS and HFIR

Detector characteristic	BL-3 (SNAP)	BL-11B (MANDI)	BL-12 (TOPAZ)	HB-3A (DEMAND)
Photosensor	Multianode PMT	Multianode PMT	Multianode PMT	SiPM array
Number of detectors	18	42	25	3
Array size (pixels)	24 × 24	24 × 24	24 × 24	16 × 16
Pixel size (mm)	7.2 × 7.2	7.2 × 7.2	7.2 × 7.2	6.3 × 6.3
Scintillator thickness (mm)	2	1.5	1.5 and 2	1
Spacer thickness (mm)	3.3	3.3	3.3	2.8
Resolution (mm)	~1	~1	~1	0.6
Optical coupling (scintillator and spacer)	Silicone gel	Silicone gel	Silicone gel	Silicone gel
Cookie thickness (mm)	0.75	0.75	0.75	0.75

detector active areas. These front ends (optics, PMTs, and preamplifiers) were assembled in two 9 × 9 camera arrays that cover approximately 45 × 45 cm and sit facing one another, with the sample and beamline between them. Each detector array is 50 cm from the sample and can be rotated to cover a solid angle of at least 4 sr.

4.1.4.2 BL-11B MANDI and BL-12 TOPAZ

BL-11B (MANDI) and BL-12 (TOPAZ) are very similar instruments that both employ Anger cameras for Laue single-crystal diffraction. MANDI prioritizes the S/N by using TOF and a 30 m beam path to finely resolve neutron wavelength. It is typically used for measuring proteins and enzymes [22, 23]. TOPAZ has a shorter beam path (18 m) and is used to measure atomic positions and displacements. It is ideal for studying magnetic structures and phase transitions.

Both beamlines have the same basic detector structure of PMT Anger cameras arranged in a polyhedron around the sample. This arrangement allows for nearly total angular coverage, with each detector being approximately the same distance from the sample. Currently, MANDI operates with 42 detectors and has space for an additional 6, and TOPAZ has 25 detectors with space for an additional 9. The MANDI detector array is pictured in Fig. 4.14.

4.1.4.3 HB-3A DEMAND

DEMAND located at HB-3A at HFIR is a monochromatic diffractometer with wavelengths of 1.005, 1.546, and 2.541 Å available [24]. Because of the use of a

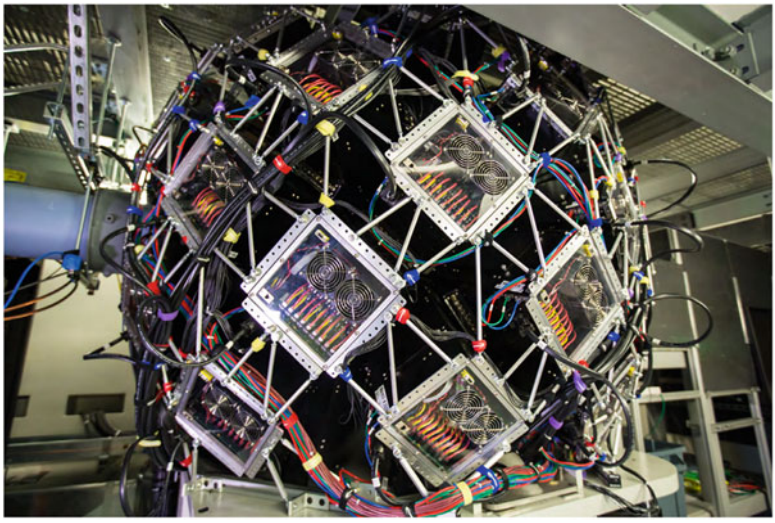

Fig. 4.14 Array of PMT Anger camera at BL-11B MANDI. The current configuration has 42 detectors, with room for a total of 48

magnetic field on the sample, PMT Anger cameras could not be used. Instead, three SiPM-based cameras are operated stacked on top of each other and can be rotated around the sample to achieve high angular coverage.

4.1.5 Improvements and Future Detectors

Although the current Anger cameras offer good performance, improvements can always be made. Future experiments may require better resolution, a higher maximum count rate, or reduced costs.

4.1.5.1 Resolution and Distortion

The fastest way to improve distortion on Anger cameras is to ensure the scintillator and photosensor are uniform over the active area and to reduce the size or space between photosensor pixels. The current SiPM-based Anger cameras have ArrayC SiPM arrays, but a prototype detector has been built with ArrayJ SiPM arrays. These ArrayJ arrays have the same number and size of pixels as the ArrayC arrays but with a very little gap (<0.25 mm) between pixels. The tighter packing factor of these pixels reduces the total active area per array, but it also decreases the dead area. Because no dead area exists, the array is more uniform, and a moving point source will produce a more standard response on the photosensors, therefore reducing distortion in the position-fitting process.

Improving resolution can be accomplished several ways. First, by improving the fitting algorithm, a more accurate position can be determined from the same photosensor response. However, the error in the photosensor response is driven mostly by the number of photons produced. Therefore, finding a suitable substitute to GS20 is a more likely method for improving resolution. A handful of brighter neutron-detecting scintillators are available, such as ZnS(Ag)/^{6}LiF and LiI:Eu. However, GS20's combination of transparency, efficiency, stability, and relative ease of manufacturing has proven difficult to replace.

4.1.5.2 Gamma Ray Discrimination

Two main methods can separate gamma ray pulses from neutron pulses: pulse height discrimination and pulse shape discrimination. Pulse shape discrimination relies on the fact that in certain scintillators, the decay time profile for scintillation light emission is different for gamma rays and neutrons. In systems with relatively low count rates or with a single channel, the pulses from the photosensor can be digitized and analyzed to determine the shape of each pulse and reject the characteristics of gamma rays. However, this method has not been implemented in the current design at SNS or HFIR [25]. The current photosum method of discrimination uses pulse

heights and simply rejects an event when the total signal from all the photodetectors is below a certain threshold. Reducing this threshold will reject more gamma rays, but it will also reduce neutron counting efficiency.

To improve this method of discrimination, the number of gamma rays that strike the scintillator or the number of photons produced from each gamma ray can be reduced. Current experiments focus on reducing the number of scintillation photons produced from incoming gamma rays by preventing the total absorption of energy from the gamma ray. Gamma rays can deposit energy via one of three ways: the photoelectric effect, Compton scattering, or pair production. All three of these ways result in an energetic electron that deposits its energy as it travels through the material. Conversely, neutrons deposit energy in GS20 by being absorbed by ^{6}Li ions, which results in an alpha particle and a ^{3}H. Both charged particles then deposit their energy. However, because the alpha particle and ^{3}H are much heavier than an electron, they have average path lengths in GS20 at least an order of magnitude shorter than that of electrons. The number of photons produced via scintillation is relatively proportional to the energy deposited by a charge particle. Reducing the cross section of a scintillator can allow higher-energy electrons to escape without drastically reducing the total energy collected from a neutron event. Better yet, the more energy an electron has—and, therefore, the more likely it is to produce a similar number of photons as a neutron—the more likely it is to escape.

The current experiment focuses on testing so-called *sandwich* scintillators made of GS20 separated by glass. Two pieces of 0.5 mm GS20 with a glass separator will have a nearly identical efficiency for neutron events as a single 1 mm piece. However, gamma rays absorbed near the glass separator may produce electrons that leave the scintillator and get absorbed in the glass, thereby reducing the number of photons produced per gamma ray. An improved gamma ray resolution using this method might hopefully allow for new applications of Anger cameras at SNS, such as reflectometry beamlines.

4.1.5.3 Large Angle Coverage Detector

A requirement for neutron scattering experiments is a large angular coverage, especially when looking for diffuse scattering information or fast phenomena that could not be captured by a scanning detector. When using Anger cameras, this large angle coverage is accomplished by having many cameras in an array, such as that used with MANDI and TOPAZ. However, the current cameras used at these beamlines cannot be arranged in such a way as to have zero space between each camera. The SiPM cameras are more compact and can be packed tighter, but they have less active area for each camera and still have spaces between SiPM faces.

A novel detector currently in testing solves these problems by having a continuous, curved scintillator face with optic fiber tapers directing scintillator light to Anger camera photosensors [26]. A schematic of this detector and initial beamline data collected with the detector are shown in Fig. 4.15. This detector was developed jointly with, and utilizes novel fiber optic tapers and scintillator surfaces developed

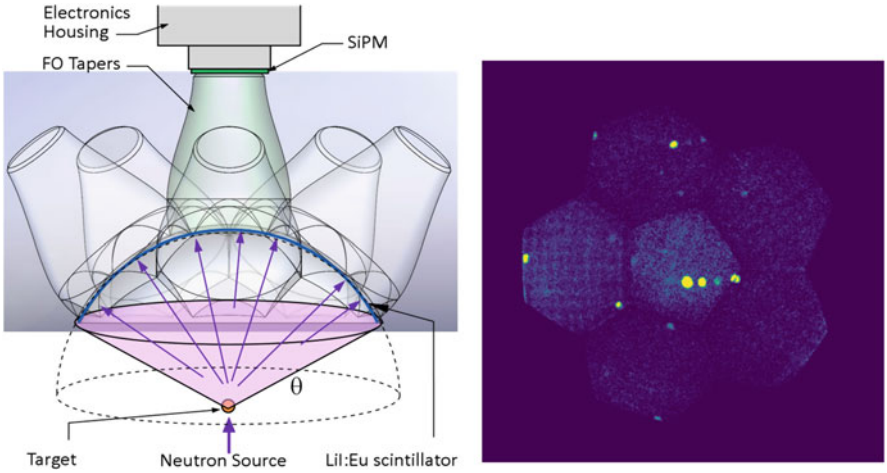

Fig. 4.15 (*left*) Schematic of spherical detector and (*right*) data taken at DEMAND with a triphylite single crystal using the ZnS(Ag)/^{6}LiF scintllator

by Radiation Monitoring Devices, Inc [27, 28]. Two newly designed, curved scintillator surfaces have been developed for this detector. The first is an aluminum dome with the outer (fiber optics–facing) surface coated in ZnS(Ag)/^{6}LiF. The fiber-optic tapers are mounted directly onto the scintillator surface. Because ZnS(Ag)/^{6}LiF is not transparent to its own light, the number of photons received on the SiPM depends on where the neutron interaction occurs in the ZnS(Ag)/^{6}LiF layer, leading to a lack of a clear photopeak on the photosum spectrum. The second scintillator is a quartz dome with the inside surface coated with LiI:Eu. LiI:Eu is hygroscopic, and it must be protected from the ambient atmosphere. The inside of the dome is coated and sealed to an aluminum surface while inside of a moisture- and oxygen-free environment.

Using a near-hemisphere LiI:Eu or ZnS(Ag)/^{6}LiF scintillator means that the distance from the sample to the scintillator is the same at all angles, which removes any parallax distortion. Powder diffraction cones will show up as vertical lines on this detector, making fitting data extremely easy. The fiber-optic light guides are mated to the scintillator in a soccer ball pattern without any gaps between tapers. This lack of gaps allows for detection of peaks between two SiPM detectors (such as in the data in Fig. 4.15) that would be lost on an array of cameras. The fiber-optic tapers are designed with a curved bottom face that matches the scintillator curvature and a flat top face that meets the face of a SiPM anger camera. The scintillator and tapers are held together using a light-tight mounting frame that can support the six SiPM anger cameras when fully assembled.

A flood pattern using the LiI:Eu dome is plotted in Fig. 4.16 to show how signal from the six fiber-optic tapers are combined into a single image.

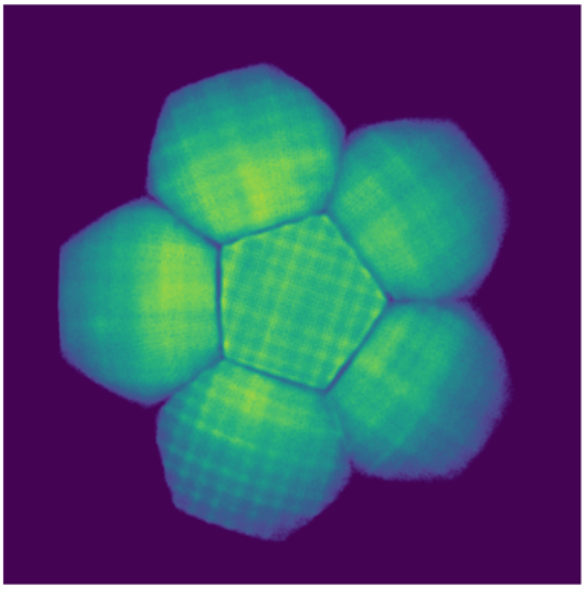

Fig. 4.16 Neutron flood pattern on the spherical detector with the LiI:Eu dome. The six images from the Anger cameras are combined into a single image

4.2 Neutron Imaging With Wavelength Shifting Fiber–Based Scintillation Detectors

4.2.1 Introduction

Neutron detectors have important applications in science, technology, security, and industry. Moderated neutron sources with increased intensities became available at pulsed spallationneutron sources, which opened new possibilities for neutron imaging using cold and thermal neutron beams [29–36]. It has been of particular interest to perform energy-resolved neutron imaging using a TOF neutron detection technique.

Generally, neutron detection can be performed using counting and integrating detectors. Neutron counting detectors based on gases, semiconductors, and scintillator sensors have been well-developed and used for neutron imaging and scatter applications. Alternatively, energy-integrating detectors, such as charge-coupled device (CCD) cameras and complementary metal–oxide–semiconductor (CMOS) cameras, have also been used for neutron imaging [37]. New CMOS cameras with frame rates of several tens of thousands of frames per second are now commercially available (https://photron.com/fastcam-nova-series/), and these cameras can be used for high-flux TOF neutron imaging.

Many neutron imaging and scattering applications require a combination of large detector areas, high detection efficiency, timing resolution, low sensitivity to gamma rays, and low cost. When these criteria are applied to existing detector technologies, scintillation detectors have advantages over gas-filled and semiconductor detectors.

Scintillation detectors can be developed with large areas at lower cost while providing sufficiently high neutron detection efficiency and timing resolution.

Using wavelength shifting fibers (WLSF) can help to read out scintillation light from large scintillators with different geometries, as well as from large arrays of isolated scintillator pixels, in efficient ways. WLSFs allow for a smaller number of readout channels at lower cost and flexible ways of interfacing scintillators and photosensors. The WLSF technique has found applications in high-energy physics, medical imaging, and neutron imaging, but further improvements can still be made.

4.2.2 Principles of WLSF

WLSFs are fabricated from plastic material doped with fluorescent dye that absorbs higher-energy photons and emits one or more lower-energy fluorescence photons. The key feature of this process is that the directions of the incident and emitted photons are not correlated, and fluorescent emission may occur isotropically at any angle. Because of that feature, some of the fluorescent photons emitted at smaller angles with respect to the fiber surface are internally reflected, captured in the WLSF, and transported along the fiber toward the photosensor (Fig. 4.17). The scintillation light from large scintillators with various shapes and sizes can be collected and transported to the photosensor using flexible and inexpensive WLSFs. Another advantage of the WLSF method is that it allows reading out of plastic scintillators and some useful inorganic scintillators with emissions in shorter wavelength ranges. The WLSF converts these photons to ones with a longer wavelength that better match to the photosensor sensitivity. WLSFs with different cross-sectional shapes,

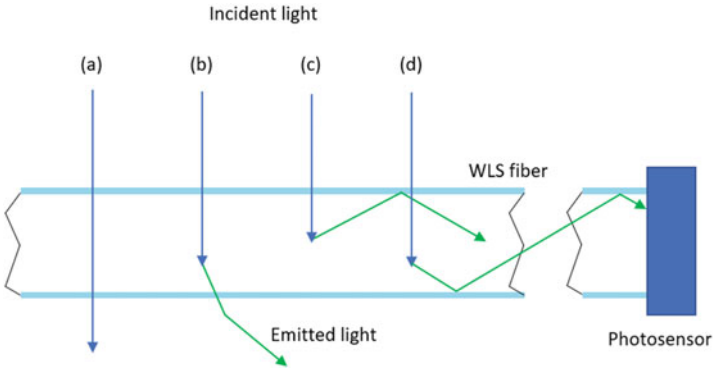

Fig. 4.17 Pathways of the incident scintillation light in WLSF. The incident light photon (**a**) may pass through WLSF without interaction; (**b**) may be absorbed in the WLSF, but the emitted fluorescence photon may leave the fiber; (**c**) the emitted fluorescence photon may be self-absorbed in the WLS fiber; and (**d**) the emitted fluorescence photon may reach the photosensor and be recorded

sizes, and lengths are commercially available. Depending on the application, they can also be fabricated as thin films, rods, slabs, and other forms.

WLSFs comprise a sensitive fiber core and the fiber cladding (Fig. 4.17). The internal reflection of the fluorescent light occurs at the interface of these two components when the incident angle (the angle between the photon incidence and normal to the surface) is larger than the critical angle. In turn, the critical angle θ_c depends on refractive indices n_1 and n_2 of the core and cladding materials, respectively, according to Eq. (4.3) [9]:

$$\theta_c = \sin^{-1}\left(\frac{n_2}{n_1}\right) \tag{4.3}$$

For a typical WLSF, the refractive index of the core material is 1.6, and the refractive index of the cladding material is 1.49 [38]. These values give a critical angle value of 69°, which determines the fraction of the fluorescence light that leaves the WLSF volume.

As shown in Fig. 4.17, the incident light photon arriving at the WLSF (a) may pass the fiber without any interaction; (b) may be absorbed in the fiber, but the fluorescent photon may leave the fiber volume; (c) the fluorescent photon may be self-absorbed in the fiber volume and not reach the photosensor; and finally, (d) the fluorescent photon may reach the photosensor. Each of these steps occurs with a certain probability depending on the chemical compositions of the WLSF, type and density of the fluorescent dye, and geometry of the fiber. Thus, in general, conversion of scintillation to fluorescence in the WLSF and its transport to the photosensor is not an efficient process.

The fraction of the fluorescence light self-absorbed in the WLSF can be determined experimentally. One end of the long WLSF is connected to the photosensor, which detects fluorescent light, and the other end is terminated. The excitation light is injected perpendicular to the fiber at different distances from the photosensor. The longer the distance from the sensor, the larger the fraction of the self-absorption of the fluorescent light. The signal from the photosensor is measured for different distances, and self-absorption of the fluorescent light vs. length of the WLSF is determined. Figure 4.18 shows a measured dependence of the fluorescent signal vs. fiber length for a particular WLSF (TROSIFOL, Kuraray Plastics Co., Ltd., Japan).

Self-absorption of the fluorescent light in the WLSF is multiexponential with respect to the fiber length. The attenuation is stronger for shorter lengths of fiber, and it slows down when the length is increased (see https://www.kuraray.com/products/psf). For example, the attenuation length (attenuates the light by a factor of e) of the WLSF equals 104 cm when the measured attenuation data points of 2 cm and 20 cm are used for calculations (see Fig. 4.18). However, the attenuation length is increased to 226 cm when the data points for 40 cm and 120 cm are used for calculations. A light-emitting diode (LED) light source with 450 nm (15 nm full width at half maximum) was used for this measurement. The different LED voltages represent

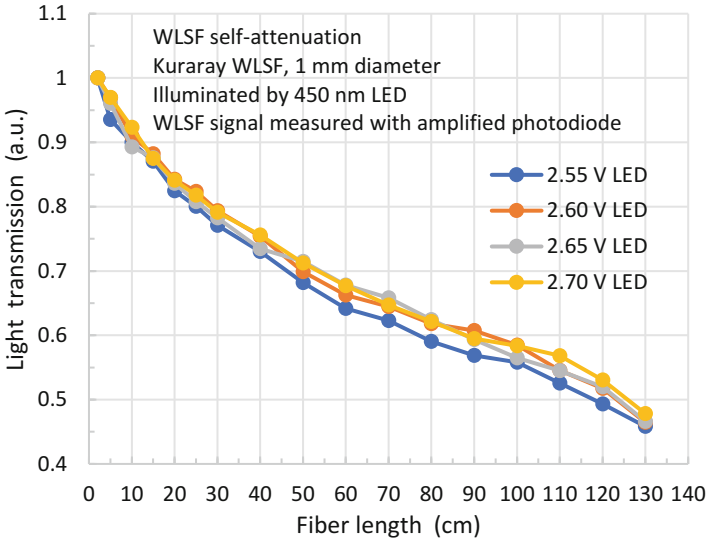

Fig. 4.18 Self-absorption curves of the fluorescence light in the WLSF. The blue light with a 450 nm wavelength was laterally injected to the WLSF, converted to the green fluorescence light with a 510 nm wavelength, and green light was measured at the end of the fiber by a photosensor. Transmitted intensity of the green light is plotted against the distance from the injection point. LED stands for light-emitting diode

different LED light intensities, which changes by a factor of 20 between 2.55 and 2.70 V. The measurement was performed for the WLSF with 1 mm diameter produced by Kuraray.

Absorption of the scintillation light by the WLSF is determined by the density of the fluorescence dye in the fiber [31]. According to [31], the absorption length of the 450 nm incident light in the WLSF BCF-91A (Saint-Gobain) is 400 μm, and the average absorption for a cylindrical fiber with the diameter of 1 mm is 85%.

4.2.3 Neutron Imaging Using WLSFs

4.2.3.1 Design Concepts

Figure 4.19 shows schematics of the two readout methods of the scintillation light in 2D position-sensitive detectors using WLSFs. In the first method, the scintillator includes a 2D array of individual pixels (Fig. 4.19a). Each pixel is optically isolated from neighboring pixels, but both of its ends are transparent to light. Each pixel is read out from two ends by a pair of two orthogonal WLSFs, and the x and y coordinates of the neutron event are determined from the numbers of these two fibers. The light photons from the WLSFs are fed to the photomultipliers, converted to charge, amplified, digitized, and sent to an encoding system. The neutron event is

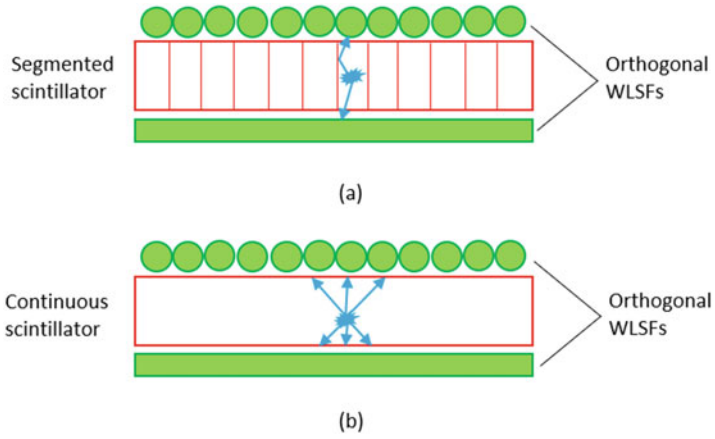

Fig. 4.19 Two design concepts of the scintillation detectors with WLSFs. (**a**) Pixelated scintillator array is used, and each fiber reads light from a single row of the pixels. Only two fibers are busy when a single event is read out. (**b**) A continuous scintillator is used, and light from a single event is spread over multiple fibers. The signal centroid is calculated to determine the coordinate of the event.In the second method, a continuous scintillator is used, and a light cone generated by the neutron event is spread over multiple WLSFs on both sides (Fig. 4.19b). As in the previous method, the signals from these fibers are fed to the photomultiplier, amplified, digitized, and sent to the encoding system. The light intensity distribution across the individual fibers has a Gaussian shape, and its center is determined numerically for the WLSFs on both sides of the scintillator, providing the x and y coordinates of the neutron events

identified based on the coincidence of the signals from the two orthogonal sets of the fibers. The signals from the background gamma rays are effectively discriminated using pulse height discrimination. In this method, the position resolution is determined by the pixel size. For this reason, increasing position resolution requires a corresponding increase in pixel numbers and numbers of the WLSFs.

Many practical applications of slow neutron detectors use thin layers of neutron-sensitive ZnS(Ag)/^{6}LiF scintillators with large areas. These scintillators require a mechanical support, and they are attached to a substrate, which also acts as a light reflector for better collection of the scintillation light. Schematics of the two such detectors are shown in Fig. 4.20.

In early detector designs [31, 39], the orthogonal WLSFs were arranged in a 2D mesh configuration and attached to a single layer of a scintillator (Fig. 4.20a). In later detector designs [30], the 2D mesh of the WLSFs were embedded between the two scintillator layers with smaller thicknesses (Fig. 4.20b). The reason for using two thinner scintillators instead of one thick scintillator is that the ZnS(Ag)/^{6}LiF scintillator used for neutron detection exhibits strong self-absorption of its emission, and two thinner scintillators provide more light output than the thick scintillator while the total neutron absorption remains the same. However, using two scintillators may introduce uncertainty in TOF measurements, and it is important to keep the distance between two scintillators as small as possible.

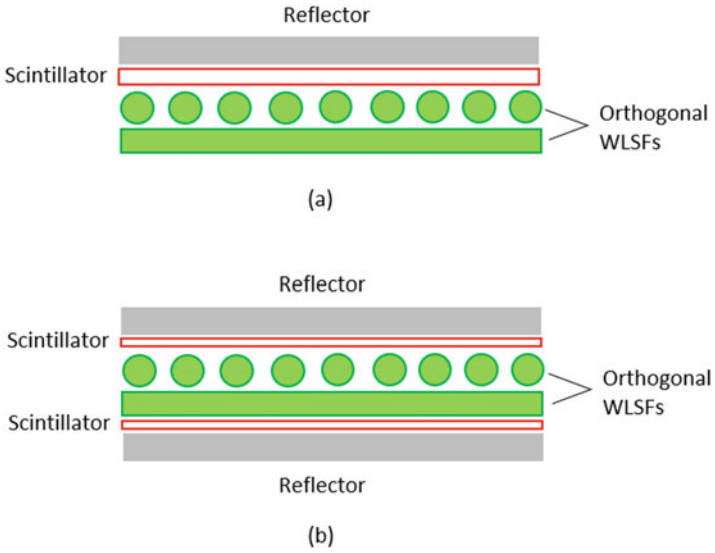

Fig. 4.20 Design concepts of the slow neutron detector based on ZnS(Ag)/^{6}LiF scintillator and WLSFs. (**a**) A thin ZnS(Ag)/^{6}LiF scintillator layer is built on a reflective substrate and matched to a mesh of the two orthogonal WLSFs. The first layer of fibers may have some gaps between them to allow part of the light to pass toward the second fiber layer. The scintillation light is shared by two sets of orthogonal fibers, from which *x* and *y* coordinates of the events are determined. (**b**) Upgraded version of the previous design, where two thin scintillators are used instead of one thick scintillator, allowing the collection of more light per absorbed neutron

As shown in Fig. 4.20a, the top WLSFs, as arranged, are separated with some gaps. This design allows for passing a sufficient fraction of the scintillation light to the second layer of the WLSFs. In the design shown in Fig. 4.20b, the first and second layers of the fibers have gaps so that the scintillation light can reach the top and bottom layers of the WLSFs. Alternatively, the gaps between the WLSFs can be set to zero, but the diameter of the fiber can be decreased such that some fraction of the scintillation light passes across one layer of the fiber and is absorbed by another layer [40]. Nevertheless, both methods require careful selection of the parameters of scintillators and WLSFs to provide the highest detection efficiency.

4.2.3.2 Position Encoding Methods

Analog Position Encoding

Anger logic is used for position encoding in WLSF-based slow neutron detectors. The method was introduced in 1958 [1] and was used in many areas, including medical gamma ray cameras, positron emission tomography, scientific imaging, security, and industry [2, 41].

The neutron detectors described in the previous section use two orthogonal, 1D arrays of WLSFs. Each of the 1D WLSF arrays is read out as a 1D Anger camera, determining the x and y coordinates of a single neutron event. Early applications of the Anger cameras used analog position encoding based on 1D or 2D resistive charge dividers [1, 2, 41]. The resistive charge dividing method was used also in a slow neutron imaging detector with WLSFs [33].

In the resistive charge dividing method, each fiber is read out by a photosensor output, which is connected to a resistive charge divider (Fig. 4.21). The charge from the neutron event is divided into two parts that are proportional to the resistance of the one side (q_1) and another side (q_2) of the resistive charge divider. These two charge signals are amplified, digitized, and saved in computer memory. The x coordinate of the event is determined from the two recorded charges q_1 and q_2 via Eq. (4.4):

$$x = L\frac{q_1}{q_1 + q_2} \tag{4.4}$$

where L is the total length of the fiber array. The y coordinate of the event is determined similarly. The other ends of the fibers are connected to a single photosensor that provides the sum of the charges, which is used as the coincidence signal to trigger event processing. The event coordinates determined using Eq. (4.4) may give some nonlinearities and distortions of the true event position. However, these nonlinearities can be addressed numerically using lookup tables. Thus, although the encoding method is analog, this method uses a digitized signal for

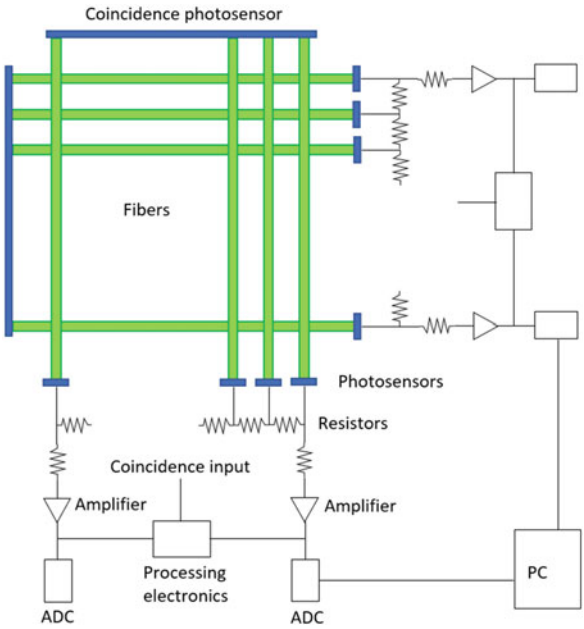

Fig. 4.21 Analog position encoding scheme using resistive charge divider. The light from each WLSF is converted to charge by the photosensors, and these charges are fed to the resistor chain. The total charge is divided into two parts, each proportional to the distance from the edge. The position of the event is determined from these two charges. PC stands for personal computer

position encoding and corrections, and the method can be considered a mixed analog and digital method.

Digital Position Encoding

Very early Anger cameras were fully analog because computers and ADCs were not readily available. The x and y coordinates of the events were derived using analog summing and division circuits. The derived analog signals' amplitudes were proportional to the x and y coordinates of the events. They were sent to the stroboscopic oscilloscope's x/y deflecting electrodes, and the event positions appeared on the scope screen as a bright spot. A photographic film was then attached to the scope's display, and a 2D intensity distribution of the events was recorded on the film. Further developments of computers and ADCs allowed for partial digitization of the method, as described in the previous section.

Approximately 20 years ago, the medical Anger cameras, primarily gamma ray cameras and positron emission tomography cameras, started using the fully digital position encoding method. This was possible because of the advancements of chip-level amplifiers and ADCs, as well as computational powers and memories. The more compact amplifiers and ADCs could be attached directly to the individual photosensors, signals could be amplified and digitized next to the sensors, and large amounts of data could be transferred to the computers and processed at high speeds. This method was called the *event-based acquisition* method [2]. All procedures associated with signal summing and thresholding and coincidence timing, as well as position encoding and distortion correction, were performed in the digital domain. Later, the fully digital data acquisition method was also used in neutron imaging applications [12, 34].

A simplified diagram of the neutron imaging detector with digital position encoding is shown in Fig. 4.22. In this detector, the light signals from each fiber are detected by an individual photosensor, amplified, digitized, and stored. The coordinate x of the event is determined by the weighting average method given by Eq. (4.5):

$$x = \frac{\sum x_i E_i}{\sum E_i} \tag{4.5}$$

where x_i is the coordinate and E_i is the signal of fiber i. The analog discrimination of the low-level signals is performed before the digitization step to remove noise pulses. The digital signal is further processed using a computer or FPGA. The coincidence condition is applied between the fiber arrays in x and y directions, where corresponding sums of the x and y digital signals are used. The gamma ray discrimination is performed by setting the threshold for the total number of recorded photoelectrons per event. Because the gamma rays yield substantially lower numbers of photoelectrons than neutrons, it is possible to discriminate the gamma ray events using pulse height discrimination.

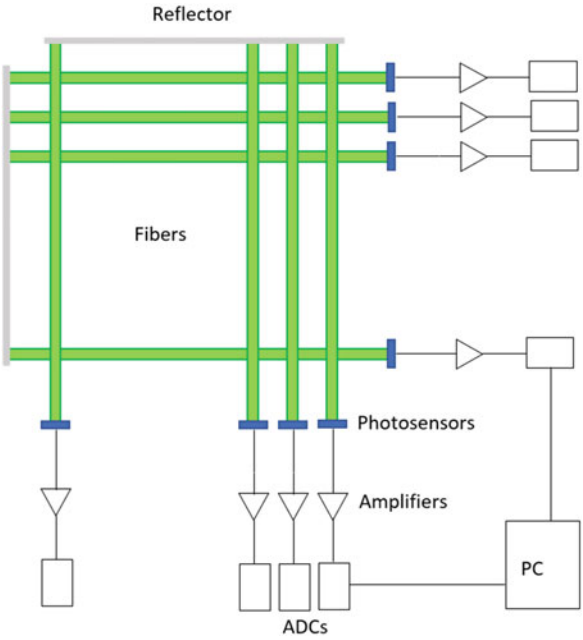

Fig. 4.22 Fully digital position encoding scheme. The light signals from the WLSFs are converted to charge by the photosensors, amplified, digitized, and used for signal coincidence, energy threshold, and event position calculation

4.2.3.3 Fiber Coding

In many imaging applications, WLSF-based scintillation detectors require large numbers of WLSFs in x and y directions. The total numbers of the used fibers can reach several hundred or more. Ideally, each of these fibers should be read out by an individual photosensor. Vacuum-based PMTs have been the only available photosensor for a long time. Owing to the relatively large size and high cost of the PMTs, it was difficult to populate the detectors with large numbers of these PMTs. The fiber coding method was used to enable reading out large numbers of fibers using smaller numbers of the PMTs.

The problem with large numbers of the readout channels mentioned previously also existed for other scintillation detectors, not just WLSFs. The fiber coding method described in this section was originally proposed for those other scintillation detectors [39] and later applied for WLSF-based detectors.

The general idea of fiber coding is that the light signal from each fiber (pixel) is split into m parts, and these parts are fed to m photosensors out of n available photosensors, where $m < n$, then detected in coincidence. The m fiber outputs can be connected to m out of the n photosensors using C_n^m different ways determined by combinatorial formula Eq. (4.6):

$$C_n^m = \frac{n!}{m!(n-m)!} \tag{4.6}$$

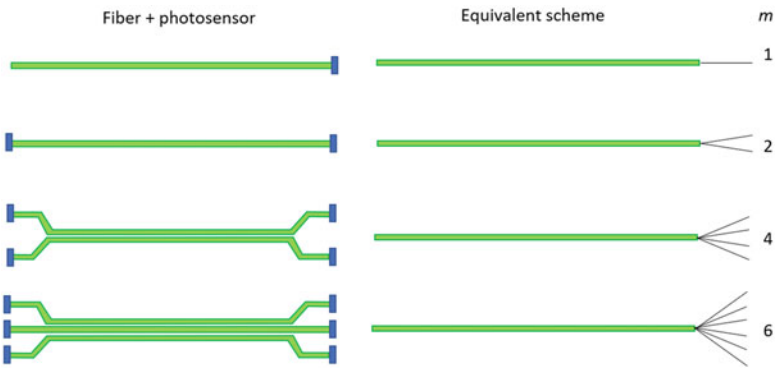

Fig. 4.23 Schematics of the fiber readout that allows splitting a fiber signal to several parts and using these parts for the fiber coding method

The ways of possible splitting fiber signals are shown in Fig. 4.23. Because each fiber has two open ends, the scintillation light is fundamentally split into two parts, and in that case, $m = 2$. If 16 PMTs are available, then Eq. (4.7) calculates the maximum number of fibers that can each be connected to the unique pair of PMTs.

$$C_{16}^{2} = \frac{16!}{2!(16-2)!} = 120 \tag{4.7}$$

For larger values of m, much larger numbers of the readable fibers can be used for the same number of PMTs. The correspondence of the fibers to a unique combination of the PMTs are saved in digital lookup tables and used for fiber encoding. Modified versions of the fiber coding algorithms have been used to resolve the cases when multiplicity effects may occur owing to the sensor crosstalk [35].

To increase m, the fibers are bundled into groups of two, three, or more, and both ends are connected to the photosensors. Because the diameter of the fibers is small (0.5–1 mm), the scintillation light cone can cover each bundle as whole. This bundle can act as a single resolution element (channel). Figure 4.23 shows two fibers bundled together providing $m = 4$ signal outputs per channel and three fibers bundled together providing $m = 6$ signal outputs per channel. In this case, using 16 PMTs would allow reading out 1820 fibers from the two-fiber bundle and 8008 fibers from the three-fiber bundle. Thus, the fiber coding method is particularly useful for reading out 2D scintillator pixel arrays with large numbers of pixels [39].

As can be seen from Table 4.3, the fiber coding method can allow reading out very large numbers of the detector channels using small numbers of photosensors. However, this method has a limitation in that it will have a decreased count rate because the entire detector is read out using a small number of readout channels.

New photosensors with small sizes, as well as 1D and 2D arrays of small SiPM, are now available. Examples include the 8 × 8 arrays of vacuum-based PMTs (Hamamatsu) and 8 × 8 and 1 × 16 arrays of SiPMs (Hamamatsu, Onsemi). These

Table 4.3 Fiber coding using C_n^m combinatorial formula for $n = 1–20$ and $m = 1–6$

n	C_n^1	C_n^2	C_n^3	C_n^4	C_n^5	C_n^6
1	1	–	–	–	–	–
2	2	1	–	–	–	–
3	3	3	1	–	–	–
4	4	6	4	1	–	–
5	5	10	10	5	1	–
6	6	15	20	15	6	1
7	7	21	35	35	21	7
8	8	28	56	70	56	28
9	9	36	84	126	126	84
10	10	45	120	210	252	210
11	11	55	165	330	462	462
12	12	66	220	495	792	924
13	13	78	286	715	1287	1716
14	14	91	364	1001	2002	3003
15	15	105	455	1365	3003	5005
16	16	120	560	1820	4368	8008
17	17	136	680	2380	6188	12,376
18	18	153	816	3060	8568	18,564
19	19	171	969	3876	11,628	27,132
20	20	190	1140	4845	15,504	38,760
21	21	210	1330	5985	20,349	54,264
22	22	231	1540	7315	26,334	74,613
23	23	253	1771	8855	33,649	100,947
24	24	276	2024	10,626	42,504	134,596
25	25	300	2300	12,650	53,130	177,100

new photosensors allow the packing of larger numbers of sensor elements in the small areas next to the scintillators and connecting each fiber to a separate sensor without fiber coding.

4.2.4 WLSF-Based Neutron Detectors at ORNL

Substantial developments have been made on WLSF-based neutron detectors at ORNL. Early prototypes of these detectors used ZnS(Ag)/^{6}LiF scintillators read out by WLSFs and were reported in 1996 [32]. These detectors used analog position encoding with resistive charge dividers [33] but later used the fiber coding method [31].

The first generation (Gen-1) of the ORNL WLSF detectors were developed for the POWGEN beamline, and these detectors are still in use (Fig. 4.24). The Gen-1 detector has 154 x × 7 y pixels, with a pixel size of 5.0 × 54.3 mm for horizontal (x) and vertical (y) directions, respectively; the active area is 77 × 38 cm^2. Each module

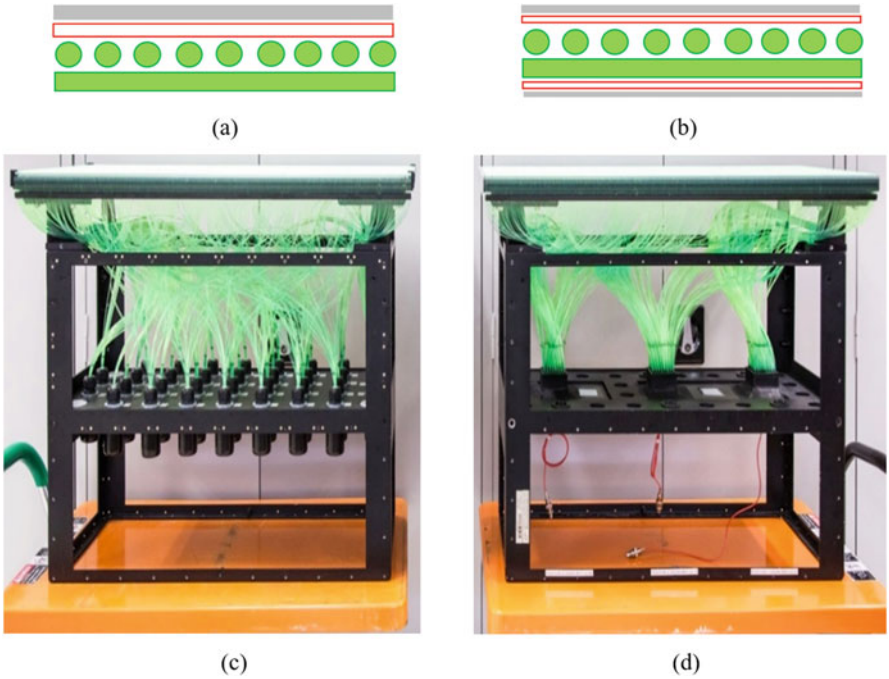

Fig. 4.24 First generation (Gen-1) and second generation (Gen-2) detectors developed for POWGEN beamline at ORNL. The (**a**) schematics and (**c**) picture of the Gen-1 detector that is currently used, and (b, d) the Gen-2 detector that is under initial testing and evaluations. The Gen-1 detector uses 32 individual PMTs and the fiber coding method. The Gen-2 detector uses 3 multichannel PMTs, each having 64 channels, and it does not use the fiber coding. Scintillator+ WLSF arrangements used in these systems are also shown

contains 308 of 1 mm diameter fibers oriented along the vertical direction and 152 of 1 mm diameter fibers oriented along the horizontal direction, from which the scintillation photons are detected by 25 (vertical direction) and 7 (horizontal direction) photomultipliers (PMTs). The *y* coordinates are read out from 7 PMTs without encoding. Two fibers with a center-to-center distance of 2.5 mm are combined to define an *x* column.

The Gen-2 detector has been developed to replace Gen-1 at the POWGEN beamline, but its preliminary evaluation has not yet been completed. The advantages of using Gen-2 over Gen-1 are that Gen-2 uses three multichannel PMTs, each having an 8 × 8 array of inputs, instead of using 32 single photomultipliers, and the total number of independent sensor inputs in the Gen-2 system is increased to 192 compared with 32 sensor inputs in the Gen-1 system. The increased number of sensor inputs allows direct readout of all 192 fiber channels without applying the fiber coding method. The increased number also allows decreasing the *y*-axis pixel size from 54.3 mm to 10 mm. Additionally, using three small multichannel PMTs requires less space than 32 large PMTs. Another potential advantage of the Gen-2

detector (yet to be tested experimentally) is that it uses two scintillator layers with the WLSF mesh sandwiched between them (see Sect. 4.2.3.1 and Fig. 4.20). This arrangement can improve light collection efficiency from the ZnS(Ag)/^{6}LiF scintillator as described in Sect. 4.2.3.1, which remains a major drawback of the neutron detectors based on ZnS(Ag)/^{6}LiF scintillators. The Gen-2 detector is being tested and optimized using different readout and position encoding methods. One method under consideration is using individual channel-by-channel readout and digitization, with further position encoding using digital centroiding. Another approach is using the resistive charge divider encoding method. This method is currently under development and initial testing and will be reported separately in future works.

Finally, the next generation of the detectors, Gen-3, is under design and development. This detector uses SiPMs instead of vacuum-based PMTs. The SiPMs have much smaller sizes on the millimeter scale, and they have immunity against external magnetic fields. Although the dark count rate of SiPMs is substantially higher than that of PMTs, preliminary studies show that this higher rate does not create a problem. Also, as SiPM technology improves, its dark count rate is steadily decreasing. Figure 4.25 shows the design concept of the Gen-3 system, which is essentially a fully digital flat panel detector that will be cost effective, compact, and immune to magnetic fields.

A small test detector has been developed to optimize parameters of the full-size systems such as Gen-2 and Gen-3 (Fig. 4.26). This setup includes a 1D array of 32 WLSFs with 1 mm diameter. The two ZnS(Ag)/^{6}LiF scintillators with 0.3 mm and 0.5 mm thicknesses are mounted on two sides of the fiber array to represent the

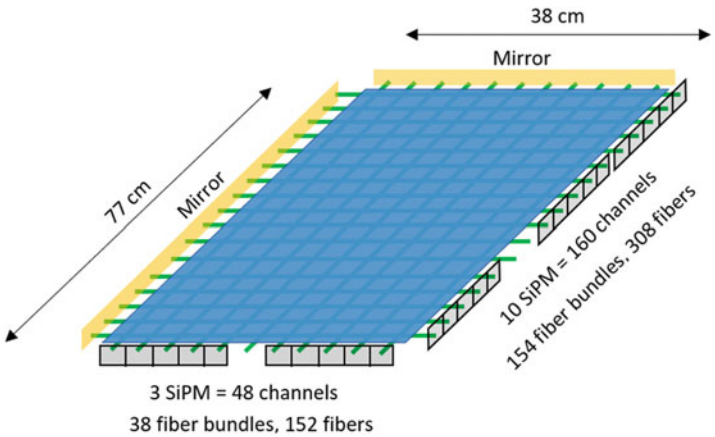

Fig. 4.25 Schematics of the full-size Gen-3 detector being developed for the POWGEN beamline. It uses linear arrays of SiPMs to read out the WLSFs. No fiber coding is used. Combination of analog and digital position encoding is considered. The effect of the dark count rate of the SiPM on the performance of the neutron detector was tested experimentally by the ORNL SNS Detector Group. The experiment demonstrated that the relatively high dark counts (90 kcounts/s for each pixel) of the SiPM does not represent a problem for the detector performance. The SiPM comprised individual pixels with a 1.3 × 1.3 mm^{2} sensitive pixel area

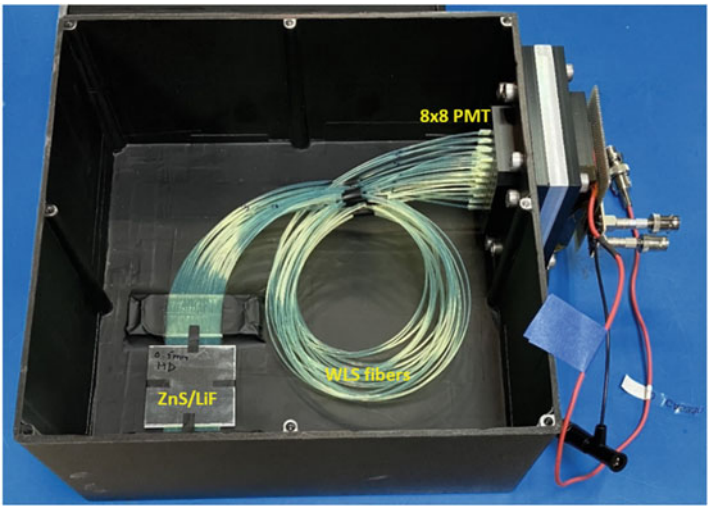

Fig. 4.26 A small test detector used for optimization of the parameters of full-size WLSF detectors to be developed

sandwich arrangement used in the Gen-2 system. The ends of the 32 fibers are connected to the 32 channels of the 64-channel Hamamatsu PMT. The 64 output signals from the PMT are led to the position encoding electronics. This setup allows for changing scintillators, fibers, gaps between them, and other factors so that these parameters could be optimized to achieve the highest possible light collection and neutron detection efficiencies, as well as the required spatial resolution.

4.2.5 Limitations and Potential Improvements

4.2.5.1 Scintillator Selection

Several scintillators are used for slow neutron detection [42]. These materials include ^{6}Li, ^{10}B, or neutron-sensitive isotopes of gadolinium. The two main scintillators used in large area neutron detectors are ZnS(Ag)/^{6}LiF and lithium glass (LG) scintillators such as GS20. The ZnS(Ag)/^{6}LiF scintillators have several advantages over LG. They are inexpensive, can be fabricated in large sizes (such as the 77×38 cm^2 size used in the Gen-1 detector of the POWGEN beamline at SNS), and have low sensitivity to gamma ray background. In combination with the WLSF readout, ZnS(Ag)/^{6}LiF scintillators offer a good combination of required specifications. The neutron converters ^{6}Li and ^{10}B are used in ZnS(Ag) scintillators, and ^{6}Li is used in LG scintillators. The ZnS(Ag)/^{6}LiF scintillator is prepared as a mixture of ZnS(Ag) powder, ^{6}LiF powder, and organic binder. The weight fractions of these three components are carefully selected to provide a required balance between

neutron absorption, scintillation light output, and mechanical stability of the mixture. The typical thickness of a ZnS(Ag)/^{6}LiF scintillator for slow neutron detection is in the range of 0.2–0.8 mm. The ZnS(Ag)/^{6}LiF layer is flexible and easy to handle and machine. It is typically deposited on pure aluminum foil, which serves as support material and as a light reflector. The LG scintillator is fabricated as glass plates with different thicknesses doped with ^{6}Li. It is difficult to fabricate LG scintillators with large sizes, and the typical size used for neutron detection is approximately 15 × 15 cm^{2}. The LG scintillators are about 10 times more expensive than the ZnS (Ag)/^{6}LiF scintillators. They are read out by multichannel PMTs or SiPMs, and Anger logic is used for position encoding.

The detectors based on ZnS(Ag)/^{6}LiF scintillators and WLSFs have two major limitations. First, the ZnS(Ag)/^{6}LiF scintillator is opaque to its own emission, and a large fraction of the scintillation light is self-absorbed in the scintillator volume. Second, conversion of the scintillation light by WLSFs and the light's transport to the PMT is inefficient. These factors have a dramatic effect on detector performance according to a simulation study [31], where out of 100,000 scintillation photons per absorbed neutron, only approximately 300 photons reached the photosensor. In practice, this number can be even smaller. Figure 4.27 shows the measured negative effect of the light loss during the conversion and transportation process. The scintillation light was first measured directly from the scintillator surface, and then it was measured from the end of the WLSFs using the same readout track. As can be

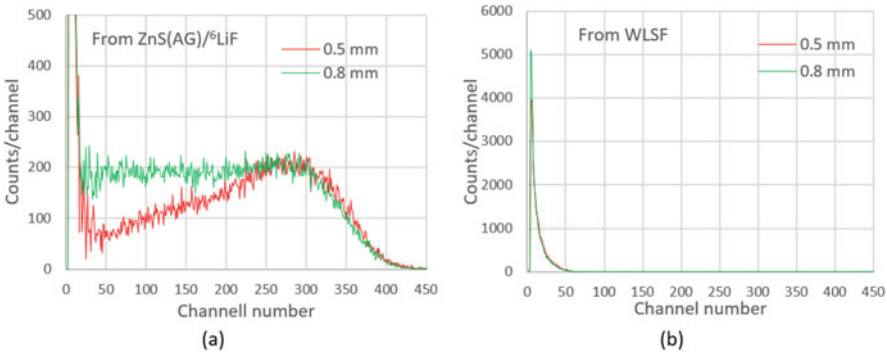

Fig. 4.27 The pulse-height spectra from thermal neutrons measured with ZnS(Ag)/^{6}LiF scintillators with 0.5 mm and 0.8 mm thicknesses. The scintillation lights were measured (**a**) directly from the scintillator surface and (**b**) from the end of the WLSFs. Scintillation light from ZnS(Ag)/6LiF is lost strongly when it is collected by WLSFs and converted to green light, part of which is captured by WLSFs and transported to the PMT. Because the absorption length of the scintillation light is very short in ZnS(Ag)/^{6}LiF layers, the neutrons absorbed in the deep regions of the scintillators are not detected. The neutron detection efficiency is decreased because of this parasitic absorption in the deep areas of the scintillator. Decreasing scintillator thickness should increase detection efficiency, but a too-thin scintillator will have less neutron absorption. Therefore, an optimal thickness of the scintillator should be found that will maximize the neutron detection efficiency via an optimal balance between the neutron absorption and scintillation light escape. This optimal thickness will depend on neutron energy and relative fractions of the ZnS(Ag), ^{6}LiF, and binder in the material and should be determined experimentally

seen in the figure, scintillation light from ZnS(Ag)/^{6}LiF is lost strongly (approximately 30 times in this case) when it is first collected by WLSFs and converted to the green light, part of which is then captured by WLSFs and transported to the PMT.

Another problem associated with ZnS(Ag)/^{6}LiF scintillator is the long tail of the slow emission component for the neutron events [43–45]. This effect is well-known, and many scintillators exhibit long decay components when densely ionizing particles such as protons, tritons, and alpha particles are detected. It is the result of the heavy excitation of triplet states of scintillators by dense ionization created by these particles. This heavy excitation is not possible when gamma rays are detected because the ionizing particle is Compton or a photoelectron, which do not create dense ionization. For the ZnS(Ag)/^{6}LiF scintillator, the decay time of the gamma ray–induced signal is approximately 5 ns, and it is 10 μs for the neutron signal (Fig. 4.28). The difference in the decay times and pulse shapes of gamma ray and neutron events helps with gamma ray discrimination. However, a too-long decay time in a ZnS(Ag)/^{6}LiF scintillator creates some problems [43–45]. First, it increases the detector dead time and limits the count rate. Secondly, the long signal tail extended after the 10 μs integration time can remain higher than the threshold level and trigger a new event. To mitigate this signal tail extension, the time window was extended to 20 μs, which further decreased the count rate, but the problem was not fully resolved [43, 44]. Some shortening of the decay time of the ZnS (Ag) scintillator was achieved by doping the scintillator with nickel [46], but further improvement is still needed.

Research and development efforts continue to shorten the decay time of the ZnS (Ag) scintillator and develop new scintillators with a similar set of advantages [47, 48]. Triton, which is the product of the neutron capture reaction on ^{6}Li, has a relatively long range in a ZnS(Ag)/^{6}LiF scintillator, reaching 30–70 μm depending on the composition and porosity of the material. Some of the tritons generated in shallow depths may escape the scintillator, decreasing the light output. These problems should also be mitigated to improve light collection efficiency.

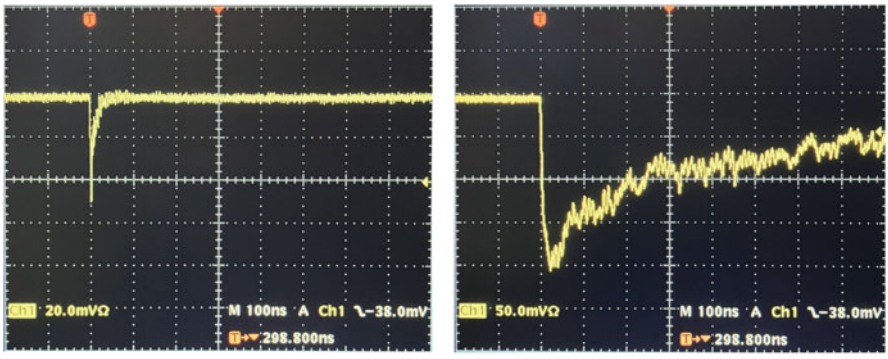

(a) (b)

Fig. 4.28 Two pulses, from (**a**) gamma ray quantum and (**b**) neutron, generated by ZnS(Ag)/^{6}LiF scintillator

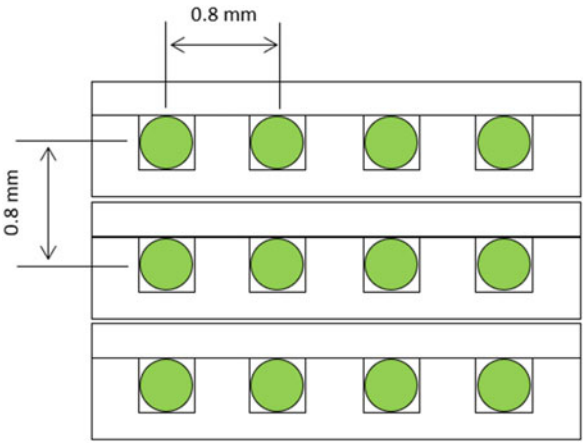

Fig. 4.29 Design of the neutron detector with 0.25 mm WLSFs embedded in the bulk of the ZnS (Ag)/^{6}LiF scintillator. This design should improve neutron absorption, light collection, and spatial resolution

The light output of the ZnS(Ag)/^{6}LiF scintillator also depends on the types of powder components used in the mixture (e.g., size and shapes of the powder granules and their relative fractions, type and amount of the binder affects the light output) [46]. To improve light collection, the WLSFs can be embedded into scintillator material [49]. This design concept is being explored to improve light collection in ZnS(Ag)/^{6}LiF [36], and one promising direction is using WLSFs with small diameters that are fully embedded into ZnS(Ag)/^{6}LiF material in a multilayer fashion (Fig. 4.29). This design uses four layers of the WLSFs with 0.25 mm diameters embedded in the bulk of the scintillator. The small diameter of the WLSFs together with small gaps between layers in the multilayer structure should simultaneously improve the neutron absorption and light collection efficiencies. A potential drawback of this design is that it may be expensive to extend it to the large areas needed by many applications. However, the high density of the WLSFs in the bulk of the detector may increase the parasitic absorption of the tritons in the fibers.

4.2.5.2 WLSF Selection

The WLSFs are commercially available with a large variety of absorption/emission wavelengths, circular and square cross sections with sizes of 0.1–2 mm, different lengths, flexibility, and more. The absorption and emission spectra of the particular fiber Y7 are shown in Fig. 4.30, and the list of the specifications of different fibers are shown in Table 4.4. These fibers are produced by Kuraray and can be fabricated with the previously-listed geometrical parameters.

Selection of the WLSF is determined by the design parameters of the detector (Fig. 4.20). The diameter and pitch of the fiber is selected such that enough light is absorbed in the upper layer of the mesh, but some fraction of the light passes through this layer and arrives at the second layer. Spatial resolution of the detector also depends on fiber diameter and pitch. The fiber material does not absorb all of the

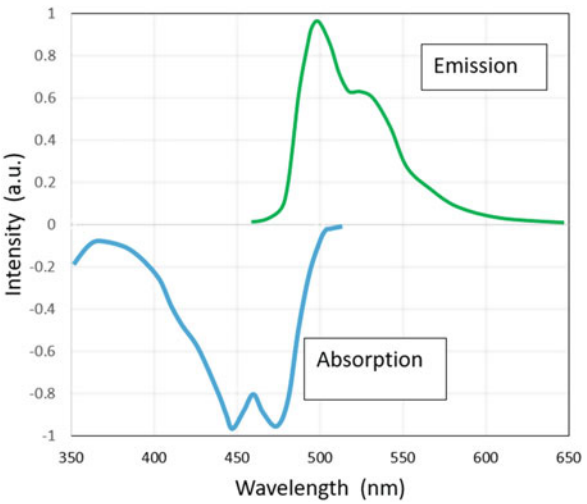

Fig. 4.30 Absorption and emission spectra of the WLSF Y7 produced by Kuraray

Table 4.4 Specifications of the WLSFs produced by Kuraray

WLSF type	Color	Emission peak (nm)	Absorption peak (nm)	Attenuation length (m)	Shifting characteristics
Y-7(100)	Green	490	439	>2.8	Blue to green
Y-8(100)	Green	511	455	>3.0	Blue to green
Y-11(200)	Green	476	430	>3.5	Blue to green
B-2(200)	Blue	437	375	>3.5	UV to blue
B-3(200)	Blue	450	351	>4.0	UV to blue
O-2(100)	Orange	550	535	>1.5	Green to orange
R-3(100)	Red	610	577	>2.0	Green to red

light arrived on it because it has an absorption length of 0.4 mm at a 450 nm wavelength. Some fraction of the light passes the fibers without interaction, and some is reflected from the surface of the fibers. Also, the surface of the ZnS(Ag)/^{6}LiF scintillator is highly reflective, and the light that is not absorbed by WLSFs may return to the source or other fibers after reflection off the scintillator surface. The designs like that shown in Fig. 4.20 were used at the POWGEN beamline at SNS [43]. Some other groups at SNS used the design similar to that shown in Fig. 4.20, but the WLSFs with a square cross section of 0.5 mm (Saint-Gobain BCF-92MC) were used with no gap between them [50]. The smaller fraction of the scintillation light that passed the first layer of WLSF arrived on the second fiber layer. The WLSFs with smaller diameters of 0.25 mm were used in the new designs to simultaneously improve neutron absorption, light collection, and spatial resolution (Fig. 4.29).

WLSFs can be connected to the photosensors in different ways. In the POWGEN detectors shown in Fig. 4.24, each WLSF has a total length of 150 cm. However, the

ZnS(Ag)/^{6}LiF scintillators used in this detector are 77 × 38 cm. Therefore, only 38 and 77 cm of the total length of fibers are used to read out the scintillator. The remaining 112 and 73 cm parts of the fibers are used for transporting light to the photosensors. However, these extra lengths of the fibers add parasitic self-absorption of the fluorescence light and must be minimized. One of the advantages of the flat panel detector shown in Fig. 4.25 is that it minimizes the extra length of the fibers.

Choice of the WLSF heavily depends on the detector design, and a large variety of fiber specifications are commercially available from at least two companies (Kuraray and Saint-Gobain).

4.2.5.3 Photosensor Selection

The first scintillation detectors based on Anger logic used single PMTs as photosensors [1]. These PMTs were later used in neutron Anger cameras with LG and ZnS(Ag)/^{6}LiF scintillators. The early neutron detectors developed at the ISIS Neutron and Muon Source used ZnS(Ag)/^{6}LiF scintillators and single PMTs for readout [29]. Large numbers of pixels were read out by smaller numbers of single PMTs using the fiber coding method. No WLSFs were used in these detectors, and scintillator pixels were connected to the PMTs using clear fibers and the fiber coding method. When the multichannel PMTs became available, they were used to replace single PMTs in some neutron imaging detectors. The work performed at ORNL [33] used a multichannel PMT with 96 individual anodes (Philips XP1704) to read out a 2D neutron detector with a ZnS(Ag)/^{6}LiF scintillator. The x and y coordinates were determined by 1D Anger logic using a resistive charge divider. The multichannel PMTs (mainly Hamamatsu tubes) were used later in many other neutron detectors [34]. The multichannel PMTs allow for the use of many more channels at a time and require much less space. Using multichannel PMTs, each WLSF can be connected to the individual PMT input without needing fiber coding.

The problems with vacuum-based PMTs were associated with their high cost, large size, and sensitivity to magnetic fields. Additionally, the multichannel PMTs had a relatively large inter-channel cross talk that created problems in many applications. The next generation of the photosensors, SiPMs, have much smaller sizes, lower cost, and immunity against magnetic field. They are manufactured as single elements, 1D arrays, or 2D arrays (Hamamatsu, Onsemi). A potential problem with SiPMs is their much higher dark count rates as compared with vacuum-based PMTs. This problem is inherent to the avalanche generation in silicon detectors, and the magnitude of the dark count rate is proportional to the sensitive area of the sensor (Table 4.5). The SiPMs are being used in neutron detectors based on LG scintillators, as well as in the detectors with ZnS(Ag)/^{6}LiF scintillators and WLSFs [36, 51].

Table 4.5 shows specifications of several single and multichannel light sensors of interest. The multichannel PMT with 8 × 8 anode array (Hamamatsu H14220) has been widely used in WLSF-based neutron imaging systems, including the SNS Gen-2 system. The 2D SiPM with 8 × 8 array (Onsemi SiPM ARRAYC-60035-64P-PCB) is used in the GS20 scintillator-based Anger cameras, including one

Table 4.5 Specifications of the different multichannel photosensors used in neutron detectors

Sensor	Hamamatsu SiPM S13363-3050NE-16	Hamamatsu PMT H14220	Onsemi SiPM ARRAYC-60035-64P-PCB	Hamamatsu SiPM S12572-010	Hamamatsu SiPM S13360-1350PE
Pixel size (mm^2)	3 × 3	6 × 6	7 × 7	3 × 3	1.3 × 1.3
Pixel pitch (mm^2)	3.2 × 3.2	6 × 6	7.2 × 7.2	6 × 6	2.1 × 2.1
Array	1 × 16	8 × 8	8 × 8	1 × 1	1 × 1
Array size (mm^2)	3.2 × 51.4	48.5 × 48.5	57.4 × 57.4	6 × 6	2.1 × 2.1
Gain	1.7×10^6	1.5×10^6	3×10^6	1.35×10^5	1.7×10^6
Dark current (nA) (counts)	50 (0.5 Mcps)	0.1 (1 kcps)	618 (3 Mcps)	100 (1 Mcps)	9 (90 kcps)
Spectral range (nm)	320–900	300–700	300–950	320–900	320–900
Peak wavelength (nm)	450	420	420	470	470
Detection efficiency (%)	40	30	30–40	10–25	40
Rise time (ns)	–	0.52	1	–	–
Cost	$250–$300	–	–	–	–

cps counts per second

developed at SNS. The 1D SiPM with 1 × 16 pixel array (Hamamatsu S13363-3050NE-16) is being considered for the next generation (Gen-3) flat panel detector with WLSFs and the ZnS(Ag)/^{6}LiF scintillator. The single-pixel SiPM (Hamamatsu SiPM S12572-010) was used in the work by the National Institute of Standards and Technology group for the 1D neutron detector [45], and another single-pixel SiPM (Hamamatsu SiPM S13360-1350PE) was used in the small test prototype of the SNS Gen-3 detector. The last SiPM was used to evaluate the effect of the SiPM dark count rate on detector performance, and it was concluded that no significant deterioration occurs.

4.2.6 Current Status and Future Perspectives

Testing and evaluation of the Gen-2 detector is in progress. The evaluation is performed using 2D position encoding electronics based on the resistive charge division concept. The first test images have been acquired with this system (Fig. 4.31). The test image was acquired using a detector sensitive area of 32 × 38 cm^2, and the full sensitive area of the Gen-2 detector is 77 × 38 cm^2. The

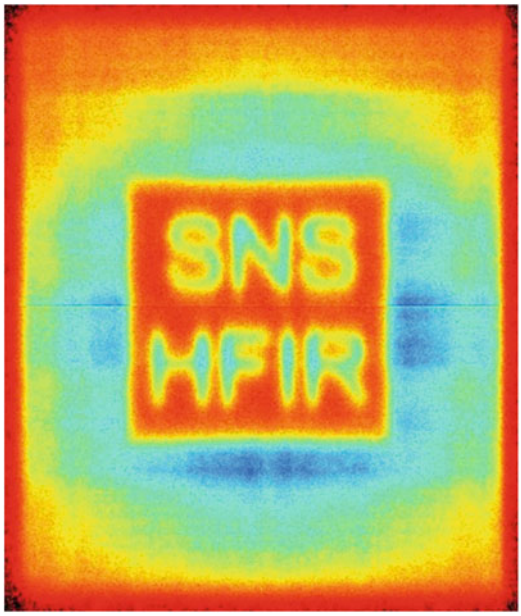

Fig. 4.31 First image acquired with Gen-2 detector using resistive charge division position encoding method

size of the imaged mask was 16 × 16 cm^2. The image was acquired using moderated ^{252}Cf with 25 meV average neutron energy. Some artifacts are noticeable that can be removed by flat field correction, which has not been applied yet. Further evaluation and optimization of this detector is in progress. The other areas of current research are optimization of the scintillator and fiber characteristics to improve light conversion and collection efficiency, as well as selection and evaluations of the new SiPMs for Gen-2 detector to substitute currently used PMTs.

4.2.7 Conclusion

The current background on WLSF-based neutron detectors indicates that significant potential exists for improving the detection efficiency and spatial resolution of these detectors. This potential can be realized by improving detector design and optimizing parameters of ZnS(Ag)/^{6}LiF scintillators to increase light collection. Multichannel SiPM technology is a developing area, and SiPMs will further improve and have wider applications in neutron detectors. Compact, inexpensive, and efficient detectors will become available.

References

1. H.O. Anger, Scintillation camera. Rev. Sci. Instrum. **29**, 24–33 (1958)
2. S.R. Cherry, J.A. Sorenson, M.E. Phelps, *Physics in Nuclear Medicine*, 3rd edn. (Saunders, Philadelphia, 2003), p. 523
3. G. Kemmerling et al., System for small-angle neutron scattering experiments. IEEE Trans. Nucl. Sci. **48**(4), 1114–1117 (2001)
4. J.D. Richards, et al., Development of a neutron-sensitive anger camera for neutron scattering instruments, in *IEEE Nuclear Science Symposium and Medical Imaging Conference Record* (2010, NSSMIC 5874079), p. 1771–1776
5. J. Schelten et al., Development of a linear position-sensitive neutron detector. Nucl. Inst. Methods **205**, 319–330 (1983)
6. C.C. Wilson, T. Zaleski, The performance and future prospects of the Anger camera PSD for single crystal diffraction at ISIS. Phys. B Condens. Matter **180–181**, 993–996 (1992)
7. S. Kumar et al., Performance of a position-sensitive neutron scintillation detector based on silicon photomultipliers. IEEE Trans. Nucl. Sci. **67**(6), 1169–1174 (2020)
8. S. Jaksch et al., Recent developments SoNDe high-flux detector project. JPS Conf. Proc. **22**, 011019-1-8 (2018)
9. G.F. Knoll, *Radiation Detection and Measurement*, 3rd edn. (Wiley, Hoboken, 2000), p. 802
10. https://scintacor.com/products/6-lithium-glass/
11. https://et-enterprises.com/
12. R.A. Riedel et al., Design and performance of a large area neutron sensitive anger camera. Nucl. Inst. Methods **A794**, 224–233 (2015)
13. K. Kandiah, A pulse processor for x-ray spectrometry with Si(Li)-detectors. IEEE Trans. Nucl. Sci. **NS-22**, 2058–2065 (1975)
14. P.M. De Lurgio et al., 2-D scintillation position-sensitive neutron detector, in *IEEE Nuclear Science Symposium Conference Record*, vol. N14-129, (2005), pp. 648–653
15. T.K. Johnson, C. Nelson, D.L. Kirch, A new method for the correction of gamma camera nonuniformity due to spatial distortion. Phys. Med. Biol. **41**(10), 2179–2188 (1996)
16. A. Morozov et al., SiPM-based neutron Anger camera with auto-calibration capabilities. J. Instrum. **14**, P03016-1-11 (2019)
17. W. Siman, S.C. Kappadath, Performance characteristics of a new pixelated portable gamma camera. Med. Phys. **39**(6), 3435–3444 (2012)
18. V.N. Solovov, Position reconstruction in a dual phase xenon scintillation detector. IEEE Trans. Nucl. Sci. **59**(6), 3286–3293 (2012)
19. C. Fiorini, F. Perotti, Small prototype of Anger camera with submillimeter position resolution. Rev. Sci. Instrum. **76**, 044303-1-8 (2005)
20. L. Coates et al., A suite-level review of the neutron single-crystal diffraction instruments at Oak Ridge National Laboratory. Rev. Sci. Instrum. **89**, 092802-1-9 (2018)
21. https://neutrons.ornl.gov/sites/default/files/SNAP_spec_sheet_0.pdf
22. https://neutrons.ornl.gov/sites/default/files/TOPAZ_spec_sheet_0.pdf
23. https://neutrons.ornl.gov/sites/default/files/MaNDI_spec_sheet.pdf
24. https://neutrons.ornl.gov/sites/default/files/DEMAND_spec_sheet.pdf
25. C.L. Wang, R.A. Riedel, Improved neutron-gamma discrimination for a (6)Li-glass neutron detector using digital signal analysis methods. Rev. Sci. Instrum. **87**, 013301-1-8 (2016)
26. G. Ehlers et al., Modern trends in neutron scattering instrument technologies. Instruments **6**(3), 22-1-16 (2022)
27. https://www.rmdinc.com/
28. V. Nagarkar, et al., Hemispherical detector for neutron scattering, in *Presentation at IEEE-NSS/MIC Milan*, 10 Nov 2022 (2022). Abstract
29. N.J. Rhodes, M.W. Jonson, C.W.E. Eljk, The future of scintillator detectors in neutron scattering instrumentation. J. Neutron Res. **4**, 129–133 (1996)

30. G. Mauri et al., Enhanced position resolution for ZnS:Ag/6LiF wavelength shifting fibre thermal neutron detectors. Eur. Phys. J. Plus **136**(286), 1–26 (2021)
31. M.L. Crow, J.P. Hodges, R.G. Cooper, Shifting scintillator prototype large pixel wavelength-shifting fiber detector for the POWGEN3 powder diffractometer. Nucl. Inst. Methods **A529**, 287–292 (2004)
32. D.P. Hutchinson, V.C. Miller, J.A. Ramsey, Neutron scintillators using wavelength shifting fibers. J. Neutron Res. **4**, 123–127 (1996)
33. D.P. Hutchinson et al., Optical readout for imaging neutron scintillation detectors. Proc. SPIE **4785**, 262–267 (2002)
34. M. Katagiri, Development status of position-sensitive neutron detectors for J-PARC in JAERI—A comprehensive overview. Nucl. Inst. Methods **A529**, 254–259 (2004)
35. T. Nakamura et al., A half-millimetre spatial resolution fibre-coded linear position-sensitive scintillator detector with wavelength-shifting fibre read-out for neutron detection. Nucl. Inst. Methods **A606**, 675–680 (2009)
36. J.B. Mosset et al., Evaluation of two thermal neutron detection units consisting of ZnS/6LiF scintillating layers with embedded WLS fibers readout witha SiPM. Nucl. Inst. Methods **A764**, 299–304 (2014)
37. W. Kockelmann et al., Time-of-flight neutron imaging on IMAT@ISIS: A new user facility for materials science. J. Imaging **47**(4), 1–22 (2018)
38. W. Worstell, O. Johnson, V. Zavarzin, Development of a high-resolution PET detector using LSO and wavelength-shifting fibers, in *IEEE Nuclear Science Symposium and Medical Imaging Conference Record* (1995), 21–28 Oct 1995, p. 1756–1760
39. N.J. Rhodes et al., Pixelated neutron scintillation detectors using fibre optic coded arrays. Nucl. Inst. Methods **A392**, 315–318 (1997)
40. T. Nakamura et al., An empirical formula for calculating the spatial resolution of a wavelength-shifting fibre detector coupled with a ZnS/6LiF scintillator for detecting thermal neutrons. J. Instrum. **9**(C11020), 1–7 (2014)
41. G.W. Fraser, X- and gamma -ray imaging using microchannel plates. Nucl. Instrum. Methods Phys. Res. **A221**, 115–130 (1984)
42. M.J. Cieslak, K.A.A. Gamage, R. Glover, Critical review of scintillating crystals for neutron detection. Crystals **9**(9), 480-1-27 (2019)
43. C.L. Wang et al., Eliminating of ghosting artifacts from wavelength-shifting fiber neutron detectors. Rev. Sci. Instrum. **84**, 013308-1-6 (2013)
44. C.L. Wang et al., Wavelength-shifting-fiber scintillation detectors for thermal neutron imaging at SNS, in *IEEE Nuclear Science Symposium Conference Record*, vol. HE4-3, (2011), pp. 4877–4882
45. A. Osovizky et al., Design of an ultrathin cold neutron detector. Nucl. Inst. Methods **A893**, 1–9 (2018)
46. A. Osovizky et al., 6LiF:ZnS(Ag) mixture optimization for a highly efficient ultrathin cold neutron detector. IEEE Trans. Nucl. Sci. **65**(4), 1025–1032 (2018)
47. K.T. Al-Rasoul, N.K. Abbas, Z.J. Shanan, Structural and optical characterization of Cu and Ni doped ZnS nanoparticles. J. Electrochem. Sci. **8**, 5594–5604 (2013)
48. V. Ramasamy, K. Praba, G. Murugadoss, Synthesis and study of optical properties of transition metals doped ZnS nanoparticles. Spectrochim. Acta A Mol. Biomol. Spectrosc. **96**, 963–971 (2012)
49. R. Wojcik et al., Embedded waveshifting fiber readout of long scintillators. Nucl. Inst. Methods **A342**, 416–435 (1994)
50. T. Hosoya et al., Development of a new detector and DAQ systems for iBIX. Nucl. Inst. Methods **A600**, 217–219 (2009)
51. M. Hildebrandt, J.B. Mosset, A. Stoykov, Evaluation of ZnS:6LiF and ZnO:6LiF scintillation neutron detectors readout with SiPMs. IEEE Trans. Nucl. Sci. **65**(8), 2061–2067 (2018)
52. T.E. Peterson, L.R. Furenlid, SPECT detectors: the Anger Camera and beyond. Phys. Med. Biol. (IOP Publishing). **56**(17), R145–R182 (2011). https://doi.org/10.1088/0031-9155/56/17/r01

Chapter 5
Other Detectors

Yacouba Diawara and Richard Riedel

Abstract This chapter describes other detectors used in scattering facilities or under development. These other detectors include semiconductor-based neutron beam monitors and detectors, vacuum-based neutron detectors, image plates, charge-coupled devices (CCDs), and pixelated detectors. This chapter presents also the midterm plans to develop detector-critical parameters for future instrument needs by 2030.

In addition to the gaseous and wavelength shifting fiber detectors along with the Anger cameras described in the previous chapters, many other neutron detectors are either being used in neutron scattering facilities or are being developed by research and development groups for many critical applications with gaps or unmet needs. The current focus is on the development of neutron detectors exhibiting high detection efficiency, a high counting rate, and position resolution at a reduced cost. Improvements in these detector characteristics will enable enhanced materials science and lead to more discoveries as novel detector technologies and instrumentation become available. Developing a complex neutron detection system is a lengthy process given the design and fabrication time for each component, the effort of integration, and the time needed for characterization design and deployment of these cutting-edge detectors for current and future instruments. This chapter describes other detectors used in scattering facilities or under development. These other detectors include semiconductor-based neutron beam monitors and detectors, vacuum-based neutron detectors, image plates, charge-coupled devices (CCDs), and pixelated detectors. This chapter finally presents the midterm plans to develop detector-critical parameters for future instrument needs by 2030.

Y. Diawara (✉) · R. Riedel
Spallation Neutron Source, Oak Ridge National Laboratory, Oak Ridge, TN, USA
e-mail: yacouba.diawara@yahoo.com

Y. Diawara (ed.), *Neutron Detectors for Scattering Applications*, Particle Acceleration and Detection, https://doi.org/10.1007/978-3-031-36546-1_5

5.1 Solid-State Neutron Beam Monitors

At neutron scattering facilities, the neutron intensity fluctuates over time depending on the characteristics of the nuclear fuel burn protocol or proton beam to the spallation target, as well as moderator performance. This fluctuation necessitates continuous and reliable monitoring of the neutron beam intensity to obtain normalization data for the instruments. The desired characteristics of these beam monitors are low efficiencies, high counting rate capabilities, high timing resolution (especially for instruments with time-of-flight [TOF] design), and radiation hardness.

Neutron beam monitors are low-efficiency detectors in which only a fraction of the incident beam is absorbed or scattered; the remainder is transmitted. Therefore, beam monitors are an important diagnostic tool in neutron facilities because they monitor the neutron flux, beam distribution, and pulse timing to ensure that the beam conditions reliably conform to what is expected. For example, measuring the neutron flux at the sample is important to correctly analyze the scattering data gathered on other instrument detectors. A beam conditions monitor can address the following issues:

- provide information about the beam flux, which is necessary to normalize scattering data
- detect early signs of beam instabilities
- possibly allow for protection of equipment during instabilities and accidents
- provide feedback to the machine for the optimization of beam conditions
- improve counting statistics at high neutron energies
- facilitate moderator studies

Generally, neutron beam monitors have low efficiency (10^{-1} to 10^{-8}). This low attenuation allows the monitor to transmit most of the incident beam (i.e., high transmission coefficient). Because various neutron instruments possess different requirements, a large variety of neutron beam monitors are used to fulfill these specifications. Multiwire proportional counters are widely used detectors in neutron scattering facilities. They are ^{3}He or nitrogen gaseous detectors. These pulse counters operate well in low to moderate counting rate applications, but they are easily saturated by high-intensity beams.

Existing single-neutron beam monitors address some of the moderate counting rate applications, but in many cases, beam intensities (such as 100,000 counts per second) exceed the counting rate capability of wire chambers or multiwire proportional counters. Higher-speed detector technologies are needed to address these counting rate limitations. Additionally, neutron beam monitors should provide fast time resolution and very strong gamma ray rejection, as well as be position-sensitive for beam profiling.

5.1.1 Principle of Operation

The beam monitor can be used to detect either thermal neutrons via nuclear reactions or fast neutrons via recoil interactions, as described by the following reactions:

$$^{10}\mathrm{B} + \mathrm{n} \rightarrow {}^{7}\mathrm{Li} + {}^{4}\mathrm{He} + 2.3\ \mathrm{MeV} + 0.48\ \mathrm{MeV}\ \gamma \tag{5.1}$$

$$^{3}\mathrm{He} + \mathrm{n} \rightarrow {}^{3}\mathrm{H} + {}^{1}\mathrm{H} + 0.764\ \mathrm{MeV} \tag{5.2}$$

$$^{6}\mathrm{Li} + \mathrm{n} \rightarrow {}^{4}\mathrm{He} + {}^{3}\mathrm{H} + 4.8\ \mathrm{MeV} \tag{5.3}$$

where n represents a neutron, and γ represents gamma rays.

Neutrons are not directly ionizing, and they usually need to be converted into charged particles before they can be detected. Semiconductor-based neutron beam monitors consist of a thin neutron converter to convert neutron radiation to a charged particle. A common feature of the reactions in Eqs. (5.1), (5.2), and (5.3) is that the products are ejected in opposite directions and generally give rise to ionization tracks that extend several micrometers from the neutron conversion location. In lithium or boron, for example, the combined ranges of the alpha and triton particles are on the order of 130 μm or 3 μm, respectively [1].

The semiconductor-based neutron beam monitor can be based on a neutron reactive layer (such as ^{6}Li or ^{10}B, or boron-doped silicon) deposited in the entrance window of a charged particle detector. The monitor can act as neutron convertor. This semiconductor device structure can be a rectifying junction type: metal–semiconductor, homojunction, or heterojunction. The generated charge particles in the neutron reactive layer will be absorbed into the semiconductor, creating electron–hole (e–h) pairs, which are drifted toward the collecting electrode for registration of individual neutrons. The charge velocities in the semiconductor can be fast enough to obtain sub-nanosecond charge transit time, and the signal registration is performed with a preamplifier, a shaper, and a dual threshold constant fraction discriminator, followed by a baseline restorer, counter, and a time stamper. The compactness and light weight of such a detection system are attractive traits for a portable device designed to accommodate many instruments.

5.1.2 Detector Structure

The neutron conversion into an individual signal is a process that can be divided into three major steps:

- The incident neutron on the neutron reactive layer on the semiconductor generates charged particles.

- The charged particles create carriers, which are transported through the semiconductor to the electrodes. Optionally, an internal amplification by avalanche phenomenon within the semiconductor can be seen.
- Extraction of the generated carriers in current pulses represent each neutron.

Each of these three steps needs to be optimized to meet the beam monitor requirements.

The semiconductor-based neutron beam monitoring system uses neutron reactive thin film on semiconductor rectifying junctions to convert neutrons into charged particles before they can be detected. Schottky, P-N (P-type and N-type), P-I-N (P-type, intrinsic, and N-type), avalanche, or heterojunctions designed to generate charge carriers in the depletion region are rectifying junctions' devices to fulfill the neutron beam monitor requirements.

The following section describes the silicon P-I-N, or PIN, structure, which is mostly preferred because of its fast response time. Its use for high-speed applications, such as for high-rate beam monitors, is attractive. The structure consists of a neutron reactive layer on top of a P-I-N structure.

A silicon P-I-N structure is made of P and N regions separated by a highly resistive intrinsic (I) layer.

- The P-layer is doped with boron, a trivalent impurity. For the neutron beam monitoring application, the boron-doped layer is a degenerate semiconductor (P^+), with the Fermi level located in the valence band. It can serve as the low-efficiency neutron conversion layer.
- The I-layer is intrinsic (undoped) with a width that can be tailored to match the charge particle range created upon neutron capture. In reverse bias mode, this intrinsic layer is fully depleted and free of any mobile charge carriers.
- The N-layer is doped with phosphorous, a pentavalent impurity with a high concentration to form an ohmic contact.

Figure 5.1 depicts the P-I-N band structure. The carriers, electrons, and holes are generated in the intrinsic layer. The electrons are drifted toward the N side, and the holes are drifted toward the P side. The intrinsic thickness can be used to control many parameters of the beam monitor, such as the efficiency (e.g., through the charged particle range), speed (e.g., through the carrier transit time), full depletion bias, and the capacitance.

5.1.3 Charge Generation

Upon neutron capture in the thin reactive layer at the semiconductor device entrance window, the charged particle energies, ranging from approximately 0.8 keV to 4.8 MeV, are created with a range varying from few micrometers for boron to approximately 130 μm for lithium [1]. The charge created by these energies then ionizes and excites the atoms along the charge's path until its energy is exhausted. A

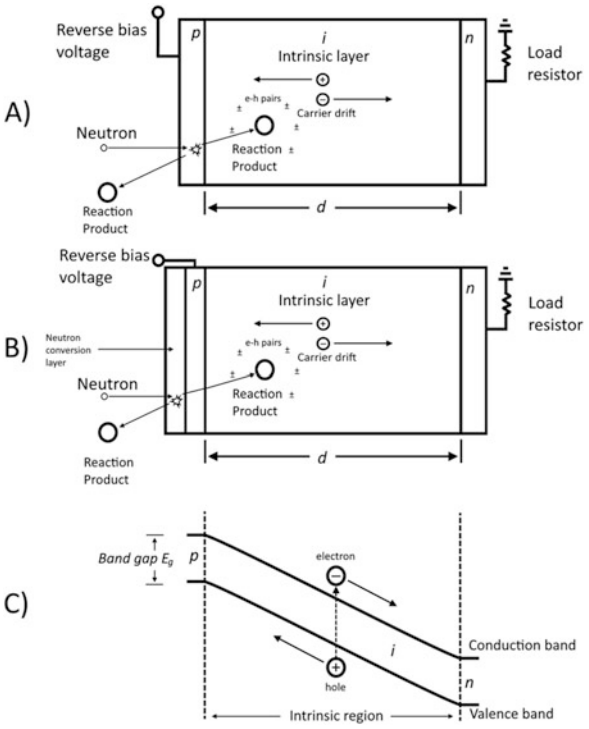

Fig. 5.1 Schematic of the P^+-I-N device and its band structure. The (**a**) P^+ or (**b**) thin neutron converter serves as a low-efficiency neutron reactive layer. (**c**) represents the energy diagram of the P-I-N structure

common feature in these nuclear reactions is that the products are ejected in opposite directions and generally produce ionization tracks that extend several micrometers into the semiconductor. The charge in the opposite direction of the intrinsic layer may be lost, thus reducing the neutron signal amplitude. Figure 5.2 shows the ionized impurity concentration profiles at the electrodes and the electric field profile across the intrinsic layer.

In most semiconductor-based detectors, an ionization energy (E_i) ranging from 1.0 to 10 eV is required to create an electron–ion pair depending on the semiconductor material, as shown in Fig. 5.3. The ionization energy increases with the increase in the semiconductor bandgap, and their values are many times below the ionization energies of gases (such as ^{3}He or BF_3) used for neutron conversion, justifying the semiconductor's superior performance in energy resolution.

The maximum number of primary electrons, η, created by the charged particle in the semiconductor is given by Eq. (5.4):

$$\eta = \frac{E}{E_i} \tag{5.4}$$

where E is the kinetic energy of the charged particle(s) in electron volts, and E_i is the ionization energy.

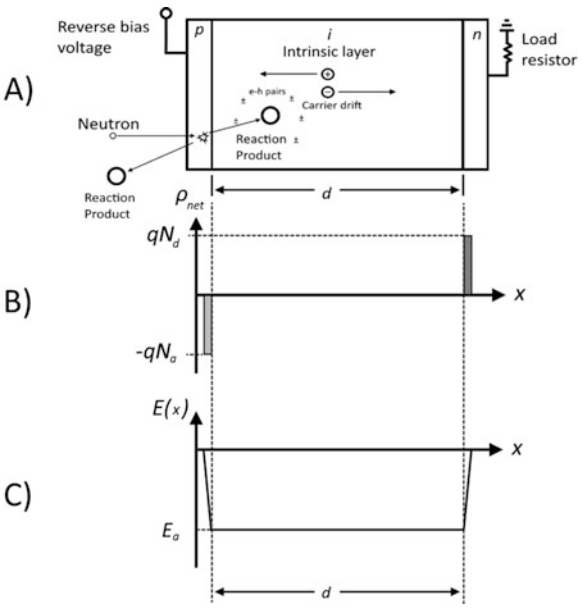

Fig. 5.2 Figure indicating the neutron converter on a P-I-N junction and the uniform built-in field. (**a**) A P-I-N structure under a reverse bias, (**b**) charge density profile indicating abrupt junctions, and (**c**) electric field profile in the junction

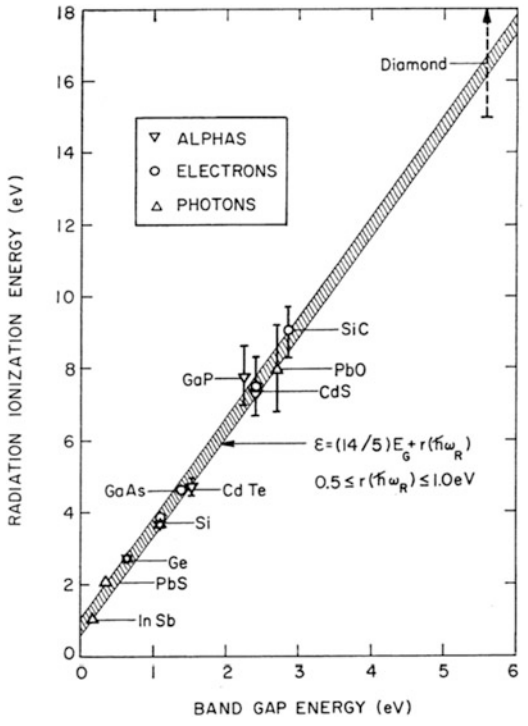

Fig. 5.3 Energy required for creation of an e–h pair as a function of the bandgap of various semiconductors [2]

Table 5.1 Mean ionization energy and maximum number of primary electrons per neutron for semiconductors using a ^{6}Li-based neutron reactive layer

Semiconductors	Ionization energy (eV)	Primary electrons released by a neutron ($\times 10^6$)
Silicon	3.6	1.33
Germanium	2.9	1.65
Silicon carbide	7.28	0.66
Diamond	13.0	0.37
Gallium arsenide	4.3	1.11

For example, the mean energy to produce an e–h pair in silicon is 3.6 eV, and a ^{6}Li reactive thin layer on a silicon P-I-N structure will release several primary electrons ($\eta = 4.8$ MeV/3.6 eV) of approximately 1.33 million electrons (or 0.21 pC), which is well above the noise (including dark current and electronic noise). Other semiconductors with rectifying junctions can also be considered, as shown in Table 5.1. Notably, germanium needs a cooling system because of its small gap, but it produces the highest signal. Diamond, however, exhibits the smallest signal while offering the lowest dark current.

5.1.4 Biasing Conditions

The semiconductor junction represented in Fig. 5.1 is a reverse-biased junction in which the P^+-side of the junction is made negative with respect to the N-side. The P and N regions act as electrodes, and the depletion layer (w) in the intrinsic region acts as dielectric. The depletion region behaves as a capacitor (C) since the charges are built up on either side of the intrinsic layer, which constitutes the capacitor thickness in full depletion mode. The junction or depletion capacitance is given by Eq. (5.5):

$$C = \frac{\epsilon A}{w} \tag{5.5}$$

where ϵ is the silicon electric permittivity, A the detector area, and w is the depletion thickness, which depends on the acceptor (N_A) and donor (N_D) doping levels and the reverse bias voltage (V_r) [3], as shown in Eq. (5.6):

$$w = \sqrt{\frac{2 \in (N_A + N_D)}{qN_A N_D}(V_{bi} + V_r)} \tag{5.6}$$

V_{bi} is the built-in voltage across the depletion region, and q is the electron charge.

When an external reverse bias voltage (V_r) is applied to the detector, the potential difference across the junction is enhanced because the bias is entirely across the depletion layer (i.e., depletion zone, void of free charge carriers). The electric field (E) across the depletion layer is given by Eq. (5.7):

$$E = \frac{V_{\text{bi}} + V_{\text{r}}}{w} \tag{5.7}$$

As the reverse bias voltage increases, the depletion region grows, and the capacitance decreases [4], as shown in Eq. (5.8):

$$C = \frac{\varepsilon A}{w} = A.\sqrt{\frac{q\varepsilon N}{2(V_{\text{r}} + V_{\text{bi}})}} \tag{5.8}$$

where q is the elementary charge, and N the effective doping concentration in the intrinsic layer. The capacitance decreases proportionally to the square root of the reverse bias until the depletion region extends to the entire volume (i.e., full depletion) of the detector, which corresponds to the intrinsic layer. Beyond the full depletion voltage, the capacitance is constant, as shown in Fig. 5.4.

Small capacitance exhibits interesting detector characteristics, such as a good energy resolution and a faster slew rate (i.e., rise time).

The junction width increases with the increase in reverse bias until it reaches the intrinsic ($w = d$, where d is the silicon intrinsic thickness). The voltage at this point is called the *full depletion* voltage, V_{fd}, and can be written as Eq. (5.9):

$$V_{\text{fd}} = \frac{d^2}{2 \in \rho\mu} \tag{5.9}$$

where μ is the mobility of electrons in N-type (or holes in P-type) bulk, and ρ the resistivity of the bulk.

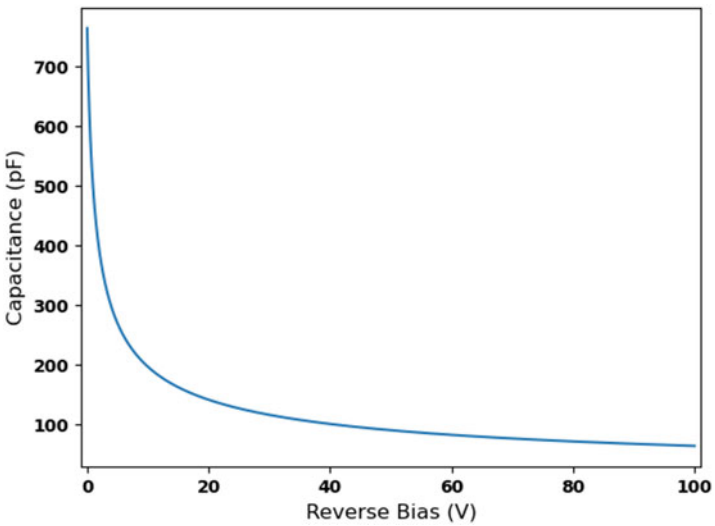

Fig. 5.4 Silicon P-I-N junction capacitance variation with the reverse bias

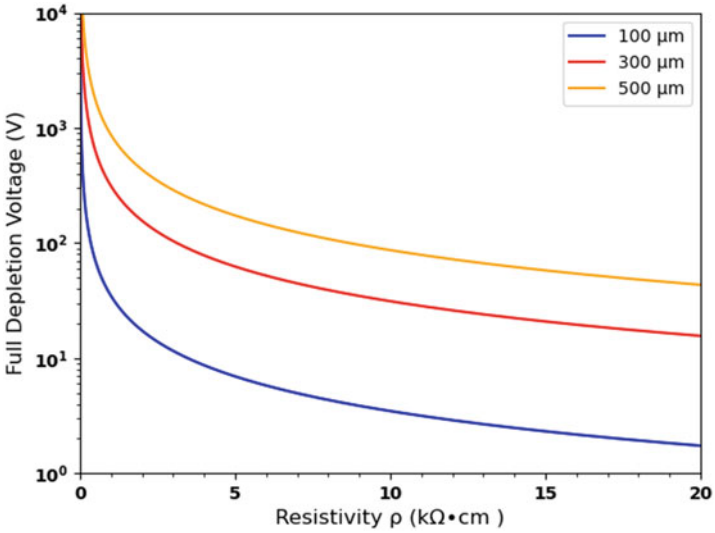

Fig. 5.5 Full depletion voltage as a function of the silicon resistivity

For a 300 µm thick silicon detector with a 5 kΩ·cm resistivity, the full depletion voltage is approximately 60 V, as shown in Fig. 5.5.

5.1.5 Charge Collection

The operation of a fully depleted silicon device as a neutron detector relies on its ability to collect the charge generated by ionization. In principle, upon a neutron capture, the fully depleted silicon junction collects the charge created by the ionizing charged particle inside the intrinsic region.

The passage of an ionizing particle creates e–h pairs, which separately drift toward the electrodes under the electric field. The absence of free carriers in the intrinsic layer avoids recombination processes of the generated charge. The collection of holes or electrons appears as a current pulse. The current signal is induced by the charge moving inside the fully depleted detector, where the diffusion current is negligible. The drift current density is proportional to the charge released by the ionization caused by the passage of the particle through the detector. The total induced current (J) is the superposition of the electron-induced current (J_e) and the hole-induced current (J_h), as well as the integration over time, which equals the total charge (Q) deposited in silicon (Eq. 5.10):

$$J = J_e + J_h = qE\left(n\mu_n + p\mu_p\right) = \frac{dQ}{dt} \tag{5.10}$$

where n is the carrier density of electrons, and p is the carrier density of holes.

Because the electric field is uniform throughout the intrinsic layer, the current is constant until the charge reaches the electrodes, which is the transit time (t_t). The transit time needed to detect the whole signal depends on the drift length (in the intrinsic layer) and on the strength of the applied electric field (E_a), as shown in Eq. (5.11):

$$t_t = \frac{d}{v_d} = \frac{d}{\mu E_a} \tag{5.11}$$

where μ represents the carrier mobility of electrons or holes. The linear region of $v_d = \mu E_a$ in Fig. 5.6 represents the slope and corresponds to the mobility shown in Eq. (5.11).

At high electric fields, the saturation drift velocity is reached, and it represents the maximum velocity a charge carrier in a semiconductor can reach in the presence of very high electric fields.

For most semiconductors, the saturation velocity is approximately 10^7 cm/s. Equation (5.11) gives the transit time (t_t) corresponding to the time taken by a carrier to transit through a semiconductor sandwiched between two electrodes.

The minimal transit time is reached at the saturation velocity. For a 10 μm thick silicon intrinsic layer, the drift time is about is approximately 0.1 ns. In counting mode, each neutron will result in individual pulses or signals with a 100 ps duration.

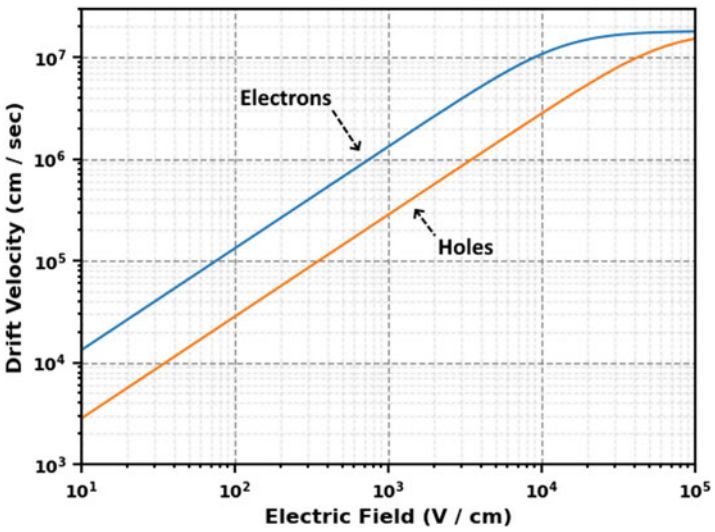

Fig. 5.6 Drift velocity vs. electric field for holes and electrons in silicon

Sub-nanosecond transit times are also observed for most of the semiconductors considered for neutron beam monitors. The maximum counting rate (i.e., speed) of these semiconductor-based neutron beam monitors is limited by the carrier's transit time across the intrinsic layer.

Thinner semiconductor layers result in picosecond-range electron transit times (t_t) and timing resolution, which are important features for high-rate neutron beam measurements, as shown in the Table 5.2.

As a second example, a thin (0.1 μm) ^{10}B layer (5.4×10^{-3}efficiency) can be deposited into the entrance window of an epitaxial SiC layer as a charged particle sensor. Silicon carbide is extremely radiation-hard, chemically inert, and has a wide bandgap (2.2–3.27 eV at 300 K), allowing for low-leakage currents for low-noise, high-temperature operation. Additionally, it possesses a high thermal conductivity, which enhances heat dissipation, a high electric breakdown field, and a high electron saturation drift velocity. The SiC semiconductor radiation detectors offer many advantages for beam monitoring in harsh environments (7×10^{14} fast neutrons/cm^2 and elevated temperature or humidity operations) without deterioration. The SiC rectifying junctions that use thick epitaxial layers ($L = 20$ μm) with a saturated drift velocity ($V_d = 2 \times 10^7$ cm/s) results in a 100 ps transit time (10^9 counts per second counting rate capability). Such a beam monitor measures a neutron beam with intensities up to 10^{12} neutrons per second.

Table 5.2 Key parameters of semiconductors that can be used for neutron beam monitors

	Saturation drift velocity at 300 K (cm/s)	Transit time at constant velocity (ns)	Beam monitor efficiency for 100 μm thickness (%)	Highest achievable counting rate (cps) at 10% linearity	Radiation hardness to neutrons
Silicon	1.5×10^7	0.67	8.5×10^{-3}	1.6×10^8	10^{15}/cm^2 MeV neutron [5]
Germanium	6×10^6	1.67	4.4×10^{-2}	6.0×10^7	3×10^9/cm^2 fast neutron [4]
Silicon carbide	2×10^7	0.5	8.3×10^{-3}	2×10^8	2×10^{15}/cm^2 MeV neutron [6]
Single-crystal diamond	2.7×10^7	0.37	1.28×10^{-2}	2.7×10^8	10^{16}/cm^2 MeV neutron [7]
Gallium arsenide	4×10^7	0.26	1.54×10^{-1}	3.8×10^8	10^{15}/cm^2 MeV neutron [8]

The radiation hardness depends on the impurities' type and concentration, as well as the irradiation rate

cps counts per second

5.1.6 Solid-State Beam Monitor Efficiency

Transparent materials along the entire neutron beam path (detector housing and all other detector inner components) are important. These materials should exhibit low neutron scattering properties. In most cases, the beam is being monitored while the experiments take place. Thus, the goal is to transmit the incident neutron beam (preferably over 99%) with no measurable effect on the experiments.

Figure 5.7 depicts the absorption values of selected semiconductor materials. For thicknesses up to 100 μm, the transmission to thermal neutrons is over 99%. Additionally, their low scattering properties have a negligible effect on the measurements owing to their thin layers and low cross section values.

A low-sensitivity neutron converter (or a high-transmission property) is highly desirable. The neutron beam monitor efficiency can be tailored by selecting an adequate neutron reactive layer on the semiconductor entrance window, as shown in Table 5.3. Boron is the P-type dopant of choice in a standard silicon rectifying junction. Even if near-degenerate boron-doped silicon does not contain enough

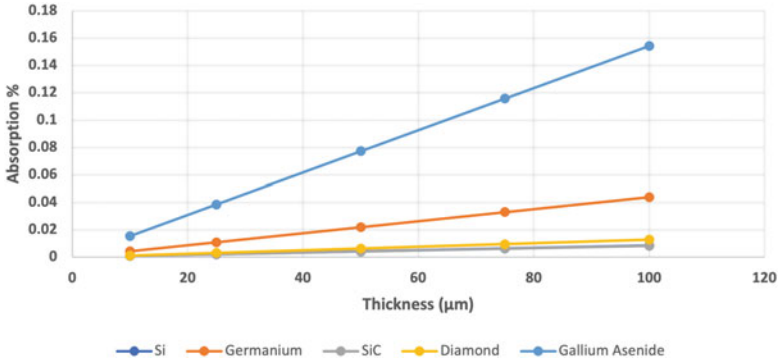

Fig. 5.7 Thermal neutron absorption variation as a function of selected semiconductor thicknesses

Table 5.3 Cross section and efficiency of selected neutron reactive layers for beam monitor applications

Material	Density (g/cm^3)	Atoms/cm^3	Macro cross section (1/cm)	Absorption efficiency (% absorption efficiency)			
				0.1 μm	0.5 μm	1 μm	5 μm
^{10}B	2.34	1.30×10^{23}	500	0.0050 (0.50%)	0.0247 (2.47%)	0.0488 (4.88%)	0.2213 (22.13%)
Natural boron	2.34	1.30×10^{23}	100	0.0010 (0.10%)	0.0050 (0.50%)	0.0099 (0.99%)	0.0488 (4.88%)
^{6}LiF	2.64	6.12×10^{22}	57.5	0.0006 (0.06%)	0.0029 (0.29%)	0.0057 (0.57%)	0.0283 (2.83%)
Gadolinium	7.9	3.03×10^{22}	1504	0.0149 (1.49%)	0.0724 (7.24%)	0.1396 (13.96%)	0.5285 (52.85%)

neutron-absorbing nuclei, it still can give reasonable neutron detection efficiency (up to 10^{-5}), which still can be used for beam monitoring applications. The efficiency can be tailored by selecting an appropriate layer thickness on the entrance window. A standard silicon P^{+}(0.1 μm)-I-N^{+} photodiode detects a neutron beam with 9.9×10^{-4}efficiency, but 0.1 μm of ^{10}B on the same device provides 0.5% efficiency.

5.1.7 Signal Processing

The neutron beam monitoring system uses advanced electronic features to have the characteristics of high counting rate and time resolution, which are required in neutron scattering facilities. The schematic in Fig. 5.8 describes the basic electronic components of the neutron beam monitor system. The electronic readout chain should adequately address the dead time and pileup, as well as the baseline restoration.

Because this beam monitor is designed to operate in pulse mode, it generates current pulses that are individually counted to determine the number of neutron events detected, as shown in Fig. 5.9. The signal is from a 500 μm thick P^{+}-I-N^{+} detector using a 20 ns shaper. The detector was tested using a californium source placed approximately 5 cm from the center of the tube.

Each of the electronic components plays an important role in signal processing and analysis.

The preamplifier is designed (for large capacitance owing to the large required detector dimensions) to receive current signals from the detector and amplify them to the required level for further processing. It establishes the best signal-to-noise ratio for the neutron beam monitor's readout.

The amplifier's shaping of the pulse plays a critical role in preserving the spectroscopic and timing (or count rate) information. The shaper of the high-rate beam monitor is designed by considering two major functions, which are to amplify the small pulses from the preamplifier to larger amplitudes and to apply the shaping required for sub-nanosecond pulse acquisition at high counting rates with the best signal-to-noise ratio. The integrated baseline restoration circuit is used to reach the stable counting characteristic over a broad range of counting rates.

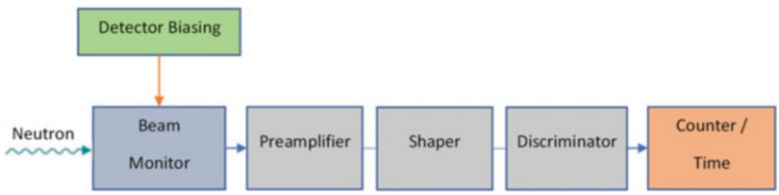

Fig. 5.8 Schematic of electronic circuitry chain used in neutron beam monitoring for fast signal processing time with low probability of pileup at high counting rates

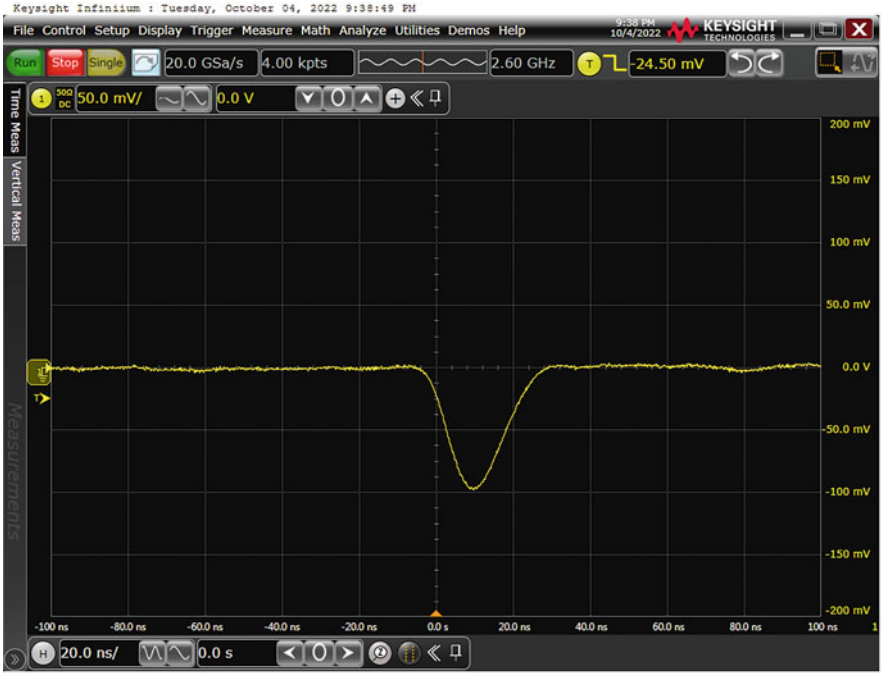

Fig. 5.9 Pulse output from a silicon-based neutron beam monitor displayed on a digital storage oscilloscope. The timescale setting was 20 ns per division

The discriminator circuit is designed to deliver a digital output signal after the amplifier. A constant fraction discrimination is employed to achieve the required time resolution with signals of broad amplitude distribution, which is common to neutron beam monitors. Among the circuit's features is a dual threshold discrimination, which provides the selection of a narrow energy range (pulse height analysis) for registration, with good rejection against events other than neutrons, such as gamma rays.

The digitized sub-nanosecond pulses from the dual thresholds are analyzed to provide spectral information for radionuclide identification purposes and temporal information (a timestamp of the event or TOF of the particle), as well as other optional parameters describing each pulse. Such timestamp-based digital data acquisition also allows for designing novel data acquisition beam monitors. These new detection systems are compact and much simpler than traditional hardware solutions (without a loss of precision) and thus are well-suited for neutron scattering facilities and in the field.

5.1.8 TOF Spectrum

Figure 5.10 depicts the TOF spectrum of a gaseous beam monitor and a ^{6}Li (1 μm)/silicon-based beam monitor mounted approximately 30 cm behind the gas beam monitor. The neutron beam is from a spallation neutron source, and both detectors are positioned to have their active area in line with the neutron beam that emerges from the apertures. The vertical lines are theoretical positions of the 200 and 111 aluminum absorption features. The gas beam monitor has an efficiency measured at 1.05×10^{-5} for the incoming beam. Assuming a typical 5% beam absorption through the monitor, this implies a 1.1×10^{-5}efficiency for the outgoing beam. The plot of the results shown in Fig. 5.10 is with 50 μs bins. Recognizable TOF spectrums are seen from both monitors, which match within the limits of the scatter. Some signs of a prompt pulse are shown at approximately 4.8 Å. The ratio of this silicon-based monitor counts to gas monitor counts is 180, indicating the silicon-based monitor has an efficiency of 1.98×10^{-3} at 1.8 Å. This large ratio in efficiencies is the reason why the gas monitor spectrum in Fig. 5.10 has more statistical scatter than the silicon-based monitor spectrum.

The TOF measurements were also performed on two different silicon-based neutron beam monitors, as shown in Fig. 5.11. One of the monitors was a standard silicon P-I-N photodiode using a heavily boron-doped layer in the entrance window. The other monitor used a silicon P-I-N photodiode with a 1 μm thick ^{6}LiF coating. In both cases, the neutron beam also passed through a ^{3}He-based gas beam monitor, with a thermal efficiency of 0.0047, for comparison with the first monitor. A neutron chopper limited the neutron wavelengths to a range of 0.5–3.7 Å. A reasonable correspondence in spectrum shape between the silicon-based and gas-based monitors was observed for neutron wavelengths greater than 2 Å. The silicon-based monitors displayed a peak in the TOF spectrum at wavelengths below 0.5 Å, outside

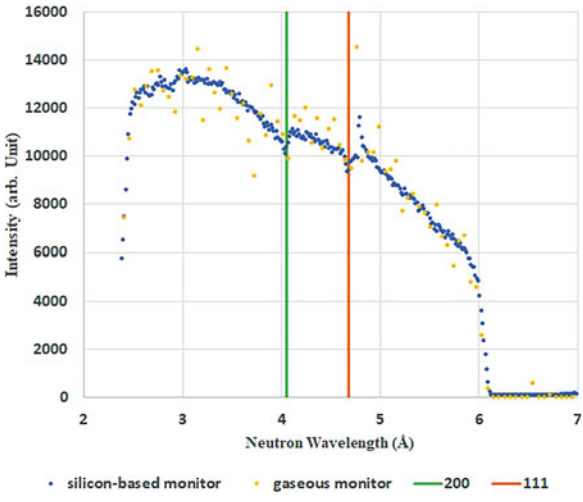

Fig. 5.10 TOF spectrum of a gaseous monitor and a silicon-based neutron beam monitor obtained at the spallation neutron source reflectometry beamline (BL-4B)

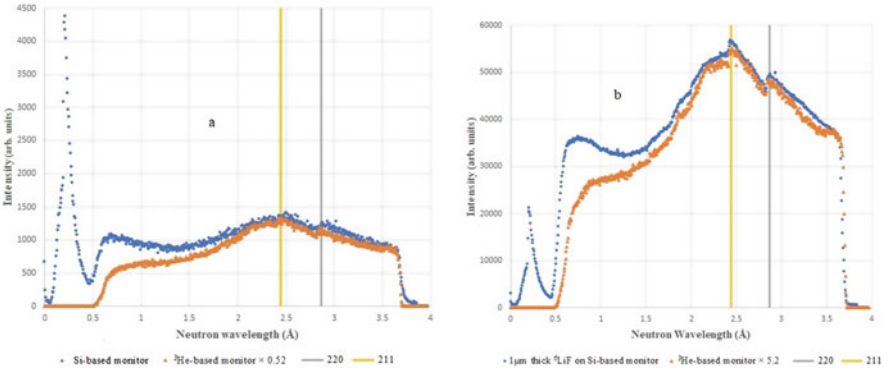

Fig. 5.11 TOF spectrum of a ^{3}He-based neutron beam monitor compared to (**a**) a silicon-based and (**b**) a ^{6}LiF coated on a silicon-based neutron beam monitors obtained at a beamline (BL-3) at the Oak Ridge National Laboratory's Spallation Neutron Source

of the range of admitted wavelengths. This peak can be attributed to gamma ray detections. Below 2 Å, the silicon-based beam monitors displayed more counts than the trend from the gas-based monitor. The cause of this increase in counts is uncertain. Above 2 Å, the silicon-based monitor with the boron-doped layer had a TOF spectrum whose amplitude corresponded with expectations for a ^{3}He gas-based monitor with 0.0025 thermal neutron efficiency. For the silicon-based monitor with the ^{6}LiF coating, the correspondence was to a gas-based monitor with 0.025 thermal neutron efficiency. Improving the gamma ray rejection of silicon-based monitors is one of the remaining challenges in their development.

5.1.9 Beam Profiling

In addition to the neutron beam monitoring, a beam profile measurement with a position-sensitive beam monitor is important in many experiments. This measurement can be achieved by the same semiconductor-based devices described in previous sections because the semiconductor technology allows micrometer-scale patterning of electrodes (strip and pixel detectors). The charge, instead of being measured on a metallic electrode like a point detector, is collected on a segmented detector in many subdetectors that can be read out separately or by interpolation. Having the charge split on more than one readout electrode allows the researcher to determine the ratio of charges on the individual electrode and to measure the centroid, which gives a better spatial resolution. Many research and development efforts are devoted to various readout options for 2D neutron beam monitors. Among the options are resistive charge division, diode strip detectors, strip detectors with a double-sided readout, or a pixelated readout.

5.2 Semiconductor Neutron Detectors

With the goal of making a device similar to silicon full depletion detectors, crystalline neutron-sensitive materials must have carrier lifetimes and mobilities large enough that the charges from neutron conversion can be collected on a bias electrode at the surface of the same material. As a bulk device, much greater sensor thickness could potentially be used to provide much greater detection efficiencies. Despite the inherent difficulties of synthesizing such materials, two neutron-sensitive crystalline materials were recently reported. These promising materials are BN [9, 10] and $LiInSe_2$ [11, 12]. Although both materials have shown evidence of scintillation [13, 14], it is unclear what advantage these scintillators would have over extant neutron scintillators. More interesting is the possibility of a bulk solid-state detector with capture efficiencies much larger than amorphous convertor films. Crystalline films of BN show efficiencies of 58% for thermalized neutrons from a californium source when compared with a reference detector [10]. The $LiInSe_2$ material, which can be operated as a wide-gap semiconductor, has also shown promise as a neutron-sensitive, bulk solid-state detector.

A new room-temperature semiconductor, $LiInP_2Se_6$ (LIPSe), was recently reported in Nature [15]. This semiconductor is the first direct-conversion neutron sensor that exhibits a full energy peak because it has efficient hole and electron collection. As a semiconductor, it collects the generated e–h pairs directly, providing higher spatial resolution over scintillators. Many recent research and development efforts [16, 17] are currently focused on studying LIPSe electronic properties and the charge carrier characteristics because of its interesting features as a direct-conversion neutron semiconductor.

5.3 Gaseous and Vacuum-Based Neutron Detectors

In the attempt to achieve a very high count rate detector, prototypes of neutron detectors using gas electron multiplier foils have been developed using ^{10}B convertor layers [18]. The detector has an extremely high count rate (10^7 neutrons/[cm^2·s]) capability with a full width at half maximum (FWHM) resolution of approximately 1.2–1.5 mm. Currently, efficiencies are approximately 20% for thermal neutrons. Although not a thin film structure, neutron-sensitive microchannel plates (MCPs), which contain gadolinium and ^{10}B [19], have been used for many years as a neutron convertor. Recent studies using a neutron-sensitive MCP coupled to a Timepix sensor have allowed the analysis of material composition using the Bragg edge technique in radiography applications [20]. Systems coupled to a Timepix sensor have achieved resolutions of 15 μm and, with interpolation, can achieve approximately 10 μm [21]. Like the gas electron multiplier foil detector, the MCP-based detector is well suited for the very high count rates encountered at imaging

instruments. Evidence exists of gain degradation in MCP-based detectors when exposed to high particle flux [22].

5.4 Image Plates and CCD-Based Neutron Detectors

Although wavelength shifting fiber detectors and Anger cameras have been used in many newly commissioned instruments at TOF neutron sources, some newly commissioned Laue diffractometers have made use of CCD cameras and image plates. These applications include the Laue diffractometer IMAGINE at Oak Ridge National Laboratory's High Flux Isotope Reactor, which uses a cylindrical image plate, lasers, and linear CCD sensors similar to a detector described in reference [23]. In a similar vein, two Laue diffractometers outfitted with ZnS(Ag)/^{6}LiF scintillator plates and area-intensified CCD detectors were commissioned at the CYCLOPS (Cylindrical CCD Laue Octagonal Photo Scintillator) instrument at the Institut Laue-Langevin [24] and the FALCON (Fast Acquisition Laue Camera for Neutrons) instrument at Helmholtz Zentrum Berlin [25]. Improvements in frame speed open the possibility of dynamic measurements, especially where periodic phenomenon are being measured. CCD-based scintillator detectors also continue to play an important role in radiography and imaging, where resolutions $<$100 μm are routinely required. Thin screens containing ZnS(Ag)/^{6}LiF or gadolinium oxides are used depending upon the required resolution [26].

5.5 Future Directions

This last section highlights the required next generation of neutron detector development in four critical applications where gaps or unmet instrument needs are observed. Plans to continue these development efforts within the next decade will be important because they will provide instruments focused on scientific leadership in materials science and engineering, which are essential for future discoveries.

Detectors are critical components needed in scattering facilities to operate under high neutron brightness and to exhibit specific characteristics that can enable many new scientific discoveries for the neutron science community.

Many of the instrument's applications require the recording of an image of the neutron signal in one, two, or three dimensions. Important characteristics required from neutron detectors are high position resolutions of the sub-millimeter to a few micrometers, excellent position linearity and stability, electrical stability, high–count rate capability, and insensitivity to gamma ray background.

Most of the current detectors meet the requirements of the various instruments. Nonetheless, there are four detector technologies that need further development to meet the desired instrument specifications. Their improvement could lead to significant progress in these valued science areas. These four technologies will improve

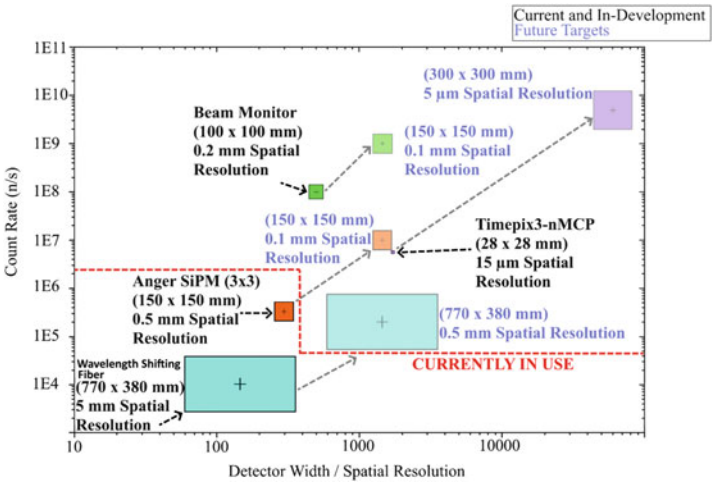

Fig. 5.12 (*Below dashed red line*) Detectors in use at the Spallation Neutron Source and High Flux Isotope Reactor at Oak Ridge National Laboratory are situated at the bottom, signifying in the chart low count rate performance. The size of box symbol is proportional to the area of the 2D detector. The required performance of each of the four proposed detectors is labelled as (*purple*) "Future Targets" by 2030. SiPM stands for silicon photomultiplier

four areas that need further development, as described in the following list. Fig. 5.12 summarizes the performance of current detectors, as well as the targeted performance for the four detector technologies by 2030.

- Improve spatial resolution: Powder diffraction and crystallography applications are innovative avenues of research in pursuit of superior materials and an understanding of biological processes involved in human diseases. The new generation of scintillator-based detector technologies will improve the spatial resolution by developing brighter and faster scintillators to enable more challenging science.
- Increase count rate capability: Fast (nanosecond time resolution), high dynamic range detectors ($>10^8$), and insensitive to gamma rays ($<10^{-7}$) are characteristics that will be needed for neutron reflectometry and small-angle scattering, which are used to study nanostructures and magnetic properties at surfaces and interfaces. Detectors with such features will enable the performance of complete reflectometry experiments on nano systems. Complete reflectometry includes TOF reflectometry, off-specular scattering, and grazing-incidence small-angle neutron scattering geometry in one shot.
- Better imaging detectors: Detector technology to meet requirements for advanced neutron imaging (e.g., Bragg edge imaging, resonance imaging, wavelength-dependent grating interferometry, and polarized imaging) will be critical for supporting materials and energy research. These detectors will require high position (micrometer) and timing (nanosecond) resolution capabilities to accurately record the 2D radiographs of all scattering and reaction processes occurring

Table 5.4 Typical detector operational parameters for some major instrument types

	Resolution (FWHM)	Distortion	Efficiency (at 2 Å)	Counting rate	Gamma ray sensitivity (^{60}Co)	Active area
Powder diffractometer	0.5 × 2 mm	–	>70%	200 kcps	$<1 \times 10^{-6}$	0.3 m^2
Single crystal	0.1 mm	<0.05 mm	>65%	5 Mcps	$<1 \times 10^{-6}$	225 cm^2
Reflectometer	0.5 mm	–	>65%	5 Mcps	$<1 \times 10^{-6}$	400 cm^2
Beam monitor	0.1 mm	–	10^{-5}	100 Mcps	$<1 \times 10^{-6}$	225 cm^2
Imaging	5 μm	–	>50%	5 Gcps	$<1 \times 10^{-6}$	900 cm^2

cps counts per second

in a sample. The spatial and temporal resolutions of the detection system are the critical parameters defining the accuracy of wavelength-dependent neutron transmission measurements needed for obtaining the stress distribution, microstructure, nano- to mesoscale defects, magnetic domains in advanced materials, electrode chemistry and performance in lithium batteries, and water distribution in plants and fuel cells.

- Better beam monitors: Neutron beam monitors are low-efficiency detectors where only a fraction (approximately 1%) of the incident beam is absorbed or scattered; the remainder is transmitted. Beam monitors are an important diagnostic tool in neutron facilities because they monitor the neutron flux, beam distribution, and pulse timing to ensure that the beam conditions reliably conform to what is expected. They also provide information about the beam flux, which is necessary to normalize scattering data. Higher-speed detector technologies are needed to address the current counting rate limitations in many instruments. The future generation of neutron beam monitors should provide fast time resolution (sub-nanosecond), very strong gamma ray rejection, and be position-sensitive for beam profiling.

Parameters that will be considered when choosing next-generation detector technology are spatial resolution, distortion, efficiency, count rate, gamma ray sensitivity, uniformity, and active area. Table 5.4 shows target operational values by 2030 for four detector technologies where unmet needs are observed.

The beam monitor project is research sponsored by the Laboratory Directed Research and Development Program of Oak Ridge National Laboratory, managed by UT-Battelle, LLC, for the US Department of Energy.

References

1. US Department of Energy Office of Science, *Report of the Basic Energy Sciences Workshop on Neutron and X-ray Detectors*, Gaithersburg, MD, USA, 1–3 Aug 2012, p. 46
2. C.A. Klein, Bandgap dependence and related features of radiation ionization energies in semiconductors. J. Appl. Phys. 39, 2029 (1968). https://doi.org/10.1063/1.1656484
3. S.M. Sze, M.K. Lee, Semiconductor Devices: Physics and Technology, 3rd edn. (Wiley, 2012)
4. H.W. Kraner et al., Fast neutron radiation damage of high-purity germanium detectors. IEEE Trans. Nucl. Sci. 22(1), 149–159 (1975)
5. Z. Li, Radiation hardness/tolerance of Si sensors/detectors for nuclear and high energy physics experiments. SLAC National Accelerator Laboratory, Stanford University. https://www.slac.stanford.edu/econf/C020909/zlpaper.pdf
6. J.M. Rafí et al., Electron, neutron, and proton irradiation effects on SiC radiation detectors. IEEE Trans. Nucl. Sci. **67**, 2481–2489 (2020)
7. K. Ferry, High field transport in wide-band-gap semiconductors. Phys. Rev. B **12**, 2361–2369 (1975)
8. S. Manolopoulos, et al. Radiation Hardness of GaAs P-I-N Diodes to Neutron Irradiation. In *Gallium Arsenide and Related Compounds 3rd International Workshop: Proceedings*, San Miniato, Italy, 21–24 March 1995, pp 144–151
9. A. Maity, T.C. Doan, J. Li, J.Y. Lin, H.X. Jiang, Realization of highly efficient hexagonal boron nitride neutron detectors. Appl. Phys. Lett. **109**, 072101 (2016). https://doi.org/10.1063/1.4960522
10. A. Maity, S.J. Grenadier, J. Li, J.Y. Lin, H.X. Jiang, Hexagonal boron nitride neutron detectors with high Detection efficiencies. J. Appl. Phys. **123**, 044501 (2018). https://doi.org/10.1063/1.5017979
11. Z.W. Bell et al., Neutron Detection with LiInSe2. (2015) In *SPIE Optical Engineering + Applications Proceedings Volume 9593 Hard X-Ray, Gamma-Ray, and Neutron Detector Physics XVII*, San Diego, CA, USA, 2015; 95930D. https://doi.org/10.1117/12.2189418
12. E. Herrera et al., LISe pixel detector for neutron imaging. Nucl. Instrum. Methods Phys. Res., Sect. A **833**, 142–148 (2016)
13. R. Engels, G. Kemmerling, J. Schelten, Boron nitride, a neutron scintillator with deficiencies, in *IEEE Nuclear Science Symposium Conference Record*, vol. 3 (2005), pp. 1318–1322. https://doi.org/10.1109/NSSMIC.2005.1596563
14. B. Wiggins et al., Scintillation properties of semiconducting $^{6}LiInSe_2$ crystals to ionizing radiation. Nucl. Instrum. Methods Phys. Res., Sect. A **801**, 73–77 (2015)
15. D.G. Chica et al., Direct thermal neutron detection by the 2D semiconductor $^{6}LiInP_2Se_6$. Nature **577**(7790), 346–349 (2020)
16. E. Lukosi et al., Methylammonium lead tribromide semiconductors: Ionizing radiation detection and electronic properties. Nucl. Instrum. Methods Phys. Res., Sect. A **927**, 401–406 (2019)
17. D.S. Hamm et al., Semiconducting lithium indium diselenide: Charge-carrier properties and the impacts of high flux thermal neutron irradiation. Appl. Phys. Lett. **112**, 242104 (2018). https://doi.org/10.1063/1.5028269
18. M. Klein, C.J. Schmidt, CASCADE, neutron detectors for highest count rates in combination with ASIC/FPGA based readout electronics. Nucl. Instrum. Methods Phys. Res., Sect. A **628**(1), 9–18 (2011)
19. W.B. Feller, R.G. Downing, P.L. White, Neutron field imaging with microchannel plates. Proc. SPIE **4141**, 291 (2000)
20. G. Song et al., Characterization of crystallographic structures using Bragg-edge neutron imaging at the spallation neutron source. J. Imaging **3**(4), 65 (2017)
21. A.S. Tremsin et al., Optimization of high-count rate event counting detector with microchannel plates and quad Timepix readout. Nucl. Instrum. Methods Phys. Res., Sect. A **787**, 20–25 (2015)

22. A. Lehmann et al., Improved lifetime of microchannel-plate PMTs. Nucl. Instrum. Methods Phys. Res., Sect. A **766**, 138–144 (2014)
23. B. Schillinger et al., A new fast and large area neutron detector using a novel image plate readout technique. App. Rad. Isotopes **61**, 451–454 (2004)
24. B. Ouladdiaf et al., CYCLOPS – A reciprocal-space explorer based on CCD Neutron detectors. J. Appl. Crystallogr. **44**, 392–397 (2011)
25. G.N. Iles, S. Schorr, Commissioning the Neutron Laue Diffractometer in Berlin. *Acta Crystallogr. A Found. Adv.* ***70***(a1), C1742 (2014). https://doi.org/10.1107/S2053273314082576
26. N. Kardjilov et al., A highly adaptive detector system for high resolution neutron imaging. Nucl. Instrum. Methods Phys. Res., Sect. A **651**, 95–99 (2011)

Appendices

Y. Diawara (ed.), *Neutron Detectors for Scattering Applications*, Particle Acceleration and Detection, https://doi.org/10.1007/978-3-031-36546-1

Appendix A: Reactor-Based Neutron Sources

Country	United States	United States	Canada	France	France	Germany	Germany	Australia	Korea	Japan
Neutron source	HFIR	NBSR	NRU	HFR	ORPHEE	BENSC	FRM-II	OPAL	HANARO	JRR-3 M
Organization	Oak Ridge National Laboratory	National Institute of Standards and Technology	Atomic Energy of Canada Limited	Institut Laue-Langevin	Laboratoire Leon Brillouin	Helmholtz-Zentrum Berlin	Technische Universitat Munchen	Australian Nuclear Science and Technology Organization	Korea Atomic Energy Research Institute	Japan Atomic Energy Agency
Power (MW)	85	20	120	58	14	10	20	20	24 (present) 30 (designed)	20
Flux (n-cm^{-2}-s^{-1})	1.5×10^{15}	3×10^{14}	3×10^{14}	1.5×10^{15}	3×10^{14}	2×10^{14}	8×10^{14}	3×10^{14}	2×10^{14}	3×10^{14}
Number of cold/hot sources	1/0	1/0	0/0	2/1	1/1	1/0	1/1	1/0	1 (planned)/0	1/0
Number of instruments	9 (present) + 6 (planned by 2012)	24	5	26	22	22	20 (present) + 10 (under construction)	6	6	24
Existing neutron imaging instrument		BT-2				CONRAD	ANTARES		NR-port	TNRF and TNRF
Facility operating since	1967	1970	1957	1972 (refurbished 1993)	1980	1973	2004	2006	1997	1990

Reference: Neutron Imaging and Applications – A Reference for the Imaging Community, Springer, 2009, Table 2.1 (reproduced)
HFIR High-Flux Isotope Reactor, *NBSR* National Bureau of Standards Reactor, *NRU* National Research Universal Reactor, Chalk River, Canada, *HFR* High-Flux Reactor at ILL, *ORPHEE* reactor at LLB, *BENSC* Berlin Neutron Scattering Centre, *FRM-II* Forschungsneutronenquelle Heinz Maier-Leibnitz, *OPAL* Open Pool Australian Light-water Reactor, *HANARO* High-flux Advanced Application Reactor, *JRR-3 M* Japan Research Reactor No. 3 Modified. Consult the websites for these facilities to obtain additional information and current details. A number of smaller research reactors, primarily at universities, are not listed here

Appendix B: Spallation-Based Neutron Sources

Country	United States	United States	United States	U.K.	Switzerland	China	Europe	Japan	Japan
Neutron source	IPNS	LANSCE	SNS	ISIS	SINQ	CSNS	ESS	KENS	JSNS
Organization	Argonne National Laboratory	Los Alamos National Laboratory	Oak Ridge National Laboratory	Rutherford Appleton Laboratory	Paul Scherrer Institute	Institute of High Energy Physics	Undecided	High Energy Accelerator Research Organization	Japan Atomic Energy Agency
Proton energy (MeV)/Current (μA)	450/15	800/70	1000/1400	800/200	590/1500	1600	1333/7500	500/9	3000/333
Proton beam power	7 kW	56 kW	1.4 MW	160 kW	1 MW	100 kW	5 MW	4.5 kW	1 MW
Repetition rate (Hz)	30	20	60	50/10 (2 targets)	Continuous	25	16 (long pulse)	20	25
Target material	Depleted Uranium	Tungsten	Mercury	Tantalum	Zircaloy	Tungsten	Mercury	Tungsten	Mercury
Moderator	S-CH_4/L-CH_4	L-H_2/H_2O	L-H_2/H_2O	L-H_2/L-CH_4/H_2O	L-D_2/D_2O	H_2OL-CH_4L-H_2	L-H_2	S-CH_4/H_2O	L-H_2
Number of instruments	12	7	24 (beam ports)	22 (TS1)7 (TS2)	15		20 (beam ports)	15	23 (beam ports)
Existing neutron imaging instrument					NEUTRA and ICON				
Facility operating since or planned to operate in	1981 (closed 2008)	1983	2006	1985 (TS1) 2008 (TS2)	1996	2014	Under planning	1980 (closed 2005)	2008

Reference: Neutron Imaging and Applications – A Reference for the Imaging Community, Springer, 2009, Table 2.2 (reproduced)
IPNS Intense Pulsed Neutron Source, *LANSCE* Los Alamos Neutron Science Center, *SNS* Spallation Neutron Source, *ISIS*, *SINQ* Swiss Spallation Neutron Source, *CSNS* Chinese Spallation Neutron Source, *ESS* European Spallation Source, *KENS* Koh-Energy-ken Neutron Source, *JSNS* Japanese Spallation Neutron Source. Consult the websites for these facilities to obtain additional information and current details

Appendix C: Derivation of E_F for Direct Geometry Spectrometers

Inelastic scattering $\Delta E = E_i - E_f$ (endothermic if $E_i > E_f$ exothermic if $E_i < E_f$)

Direct geometry - neutron beam choppers set E_i, E_f determined from TOF

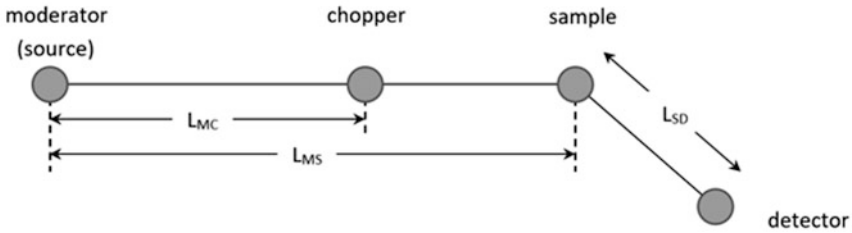

$T = L/v = L\sqrt{m_n/2E_K}$ (from $E_K = \frac{1}{2}m_n v^2$)

$T_{chopper} = T0 + L_{MC}\sqrt{m_n/2E_i}$ $\quad$ $T_{detector} = T0 + L_{MS}\sqrt{m_n/2E_i} + L_{SD}\sqrt{m_n/2E_f}$

$E_f = \frac{1}{2}m_n [L_{SD}/(T_{detector} - T0 - L_{MS}\sqrt{m_n/2E_i})]^2$

$\Delta E = E_i - E_f = E_i - \frac{1}{2}m_n [L_{SD}/(T_{detector} - T0 - L_{MS}\sqrt{m_n/2E_i})]^2$

L_{SD}, L_{MS}, T0 all known parameters, E_i (determined by chopper settings)

$T_{detector}$ = TOF

Note: uncertainties exist for all these quantities, it is the job of the instrument designer to ensure uncertainties are small enough to not affect data quality.

Appendix D: Derivation of E_I and E_F for Indirect Geometry Spectrometers

Inelastic scattering $\Delta E = E_i - E_f$ (endothermic if $E_i > E_f$ exothermic if $E_i < E_f$)

Indirect geometry - E_i determined from TOF, E_f fixed by Bragg scatter from analyzer crystal

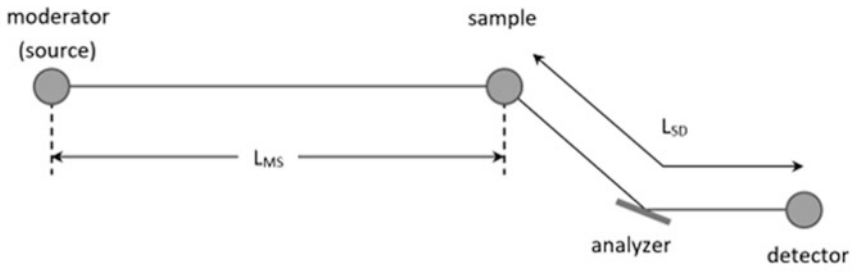

$E_f = (1/2m_n)\,[h/2d_A \sin\theta)^2$ where d_A is lattice spacing of analyzer crystal

$T = L/v = L\sqrt{m_n/2E_K}$ (from $E_K = \frac{1}{2}m_n v^2$)

$T_{detector} = T0 + L_{MS}\sqrt{m_n/2E_i} + L_{SD}\sqrt{m_n/2E_f}$

$E_i = \frac{1}{2}m_n\,[L_{MS}/(T_{detector} - T0 - L_{SD}\sqrt{m_n/2E_f})]^2$

$\Delta E = E_i - E_f = \frac{1}{2}m_n\,[L_{MS}/(T_{detector} - T0 - L_{SD}\sqrt{m_n/2E_f})]^2 - E_f$

L_{MS}, L_{SD}, T0 all known parameters, E_F (determined from analyzer crystal)

$T_{detector}$ = TOF

Note: uncertainties exist for all these quantities, it is the job of the instrument designer to ensure uncertainties are small enough to not affect data quality.

Index

Y. Diawara (ed.), *Neutron Detectors for Scattering Applications*, Particle Acceleration and Detection, https://doi.org/10.1007/978-3-031-36546-1